# Development and Qualification of Deployable Membranes for Space Applications

Vom Fachbereich Produktionstechnik

der

UNIVERSITÄT BREMEN

zur Erlangung des Grades
*Doktor-Ingenieur*
genehmigte

Dissertation

von

Patric Seefeldt

Gutachter:

Prof. Dr. Claus Braxmaier
Fachbereich Produktionstechnik,
Universität Bremen

Prof. Dr. Andreas Rittweger
Fachbereich Produktionstechnik,
Universität Bremen

Bremen, 10.04.2018

# Abstract

Deployment systems for innovative space applications such as solar sails require technology for a controlled and autonomous deployment in space. Before employing such technology for a dedicated mission, it is necessary to demonstrate its reliability with a Technology Readiness Level (TRL) of six or higher. On the example of the design implemented in the Gossamer-1 project of the German Aerospace Center(DLR), a stowing and deployment process for large deployable membranes mainly considered for solar sailing is analyzed and tested. It is based on a combination of zig-zag folding and coiling of triangular sail segments spanned between crossed booms.

Possible membrane materials are evaluated and a deployment technique is explored through theoretical analysis and tests in order to verify their functionality for large membrane space systems.

The requirements for membranes that are exposed to the space environment are studied and the materials are analyzed regarding their resistance against atomic oxygen, radiation and their thermal properties. The folding geometry and force progressions are described mathematically. Load introduction aspects, the stress-strain state and the billowing of the deployed membrane are analyzed with finite element models. The folding lines were examined with microscopes, and their impact on thermal behavior is shown by analytical analysis. The membrane and deployment mechanisms were manufactured and integrated in an ISO 8 clean room environment, and the deployment process was verified in an extensive test campaign. It ranged from component level to system level and included mechanical vibration, static acceleration, fast decompression, thermal vacuum and laboratory deployment tests.

It is shown that state-of-the-art aluminum-coated polyimide foils are sufficient for a demonstration of deployment technology in an Low Earth Orbit (LEO) and that coating systems based on a combination of aluminum, silicon oxide and titanium oxide enhance the membrane properties for solar sails. The model of the deployment force progression under zero gravity shows a tendency that the loads are transferred along the cathetus of the sail segments. The finite element models show generally low stresses in the deployed membrane and interface forces on the order of several Newtons for a $25\,\mathrm{m}^2$ membrane. The analysis of the folding lines reveals that coatings in this region are damaged, and that hot spots can occur due to multiple reflections. The verification testing showed the general suitability of the membrane and of the deployment strategy itself.

Materials, mechanisms, and a stowing and deployment strategy are presented that enable the controlled and autonomous membrane deployment for space sails. While the analysis presented is applied on a sail with an edge length of about 5 m, it allows an analysis of other configurations as well. This is of particular interest because currently-considered solar sails are about one order of magnitude bigger. With the environmental tests conducted, the membrane-related aspects of the deployment technology are on TRL six for a $25\,\mathrm{m}^2$ LEO deployment demonstrator. The deployment strategy is scalable and materials are available that can be used for bigger solar sails as well. With respect to membrane-related aspects there is nothing to prevent the development of full-scale solar sails.

# Zusammenfassung

Entfaltungssysteme für innovative Raumfahrtanwendungen wie Solarsegler erfordern Technologien für eine kontrollierte und autonome Entfaltung im Weltraum. Vor dem Einsatz dieser Technologien für eine bestimmte Mission muss ihre Zuverlässigkeit mit einem Technologie-Reifegrad von sechs oder höher nachgewiesen werden. Am Beispiel des im Gossamer-1 Projektes des Deutschen Luft- und Raumfahrtzentrums (DLR) umgesetzten Designs wird ein Verstauungs- bzw. Entfaltungsprozess für große entfaltbare Membranen, hauptsächlich zur Verwendung als Solarsegel, analysiert und getestet. Dieser basiert auf einer Kombination von Zig-Zag-Faltung und Aufrollen.

Um die Funktionalität für membranbasierte Raumfahrtsysteme nachzuweisen, werden mögliche Materialien bewertet und eine Entfaltungstechnik analysiert und getestet.

Die Anforderungen an Membranen, die der Weltraumumgebung ausgesetzt sind, werden studiert und sie werden hinsichtlich ihrer Widerstandsfähigkeit gegenüber atomarem Sauerstoff und Strahlung sowie ihrer thermalen Eigenschaften untersucht. Die Entfaltungsgeometrie und die Kraftverläufe werden mathematisch beschrieben. Lasteinleitungsaspekte, der Spannungs-Dehnungszustandes sowie das Durchwölben der entfalteten Membran werden mit Finite-Element-Methoden analysiert. Die Faltenlinien wurden mittels Mikroskopie untersucht und der Einfluss auf das Thermalverhalten wird analysiert. Die Membran und Entfaltungsmechanismen wurden hergestellt, unter ISO 8 Reinraumbedingungen integriert und der Entfaltungsprozess wurde in einer umfassenden Testkampagne verifiziert. Diese reichte von der Komponentenebene bis zur Systemebene und umfasste Vibrations-, statische Beschleunigungs-, Thermal- Vakuum- und Entfaltungstests im Labor.

Es wird gezeigt, dass für eine Entfaltungsdemonstration, in einem niedrigen Erdorbit, aluminiumbeschichtete Polyimidfolien ausreichen und dass Beschichtungssysteme basierend auf Aluminium, Siliziumoxid und Titanoxid die Eigenschaften eines Solarsegels verbessern. Die Modellierung der Kraftverläufe ohne Gravitationseinwirkung zeigt während der Entfaltung eine Tendenz, dass Kräfte entlang der Katheten der Segelsegmente geleitet werden. Die Finite-Elemente-Modelle zeigen generell niedrige Spannungen in der entfalteten Membran und geringe Kräfte, in der Größe einiger Newton für ein $25\,\mathrm{m}^2$ Segel, in deren Anbindungsstellen. Die Analyse der Faltenlinien zeigt eine Beschädigung der Beschichtung in diesen Regionen und lokale Temperaturerhöhungen durch Mehrfachreflektionen. Die Verifikationstests weisen die generelle Eignung der Membran- und der Entfaltungsstrategie nach.

Materialien, Mechanismen und eine Strategie zum Verstauen und Entfalten, die eine kontrollierte und autonome Entfaltung von Membranen für Weltraumsegel ermöglichen, werden präsentiert. Während die gezeigte Analyse auf ein Segel mit einer Seitenkante von 5 m angewendet wird, erlaubt diese auch die Analyse anderer Konfigurationen. Dies ist von besonderem Interesse, da die derzeit in Betracht gezogenen Solarsegler in etwa eine Größenordnung größer sind. Mit den durchgeführten Umgebungstests sind die membranbezogenen Aspekte, für einen $25\,\mathrm{m}^2$ Entfaltungsdemonstrator in einem niedrigen Erdorbit, auf einem Technologie-Reifegrad von sechs. Die Entfaltungsstrategie ist skalierbar und Materialien zum Bau größerer Segel sind verfügbar, so dass größere Solarsegel entwickelt werden könnten.

# Contents

# Chapter 1

# Introduction

The development of solar sail technology in Europe and specifically at the DLR goes back to the 1990s when the first solar sail breadboards were tested using a 20 m × 20 m sail in a joint DLR, NASA/JPL and ESA project, followed by several development and study projects like ODISSEE (Leipold et al. (1)) and GEOSAIL (Agnolon (2)). The ground demonstration is presented in Leipold et al. (3) and the study activities are summarized in Leipold et al. (4).

In 2010 a deployment mechanism for a CubeSat drag sail was developed on bread board level (Seefeldt (5), Seefeldt et al. (6)). The breadboard is shown in Figure 1.1(a). In the following years it was possible to further develop this mechanism together with the student group Space Sailors, and finally demonstrate the drag sail deployment successfully on the Rocket Experiments for University Students (REXUS) 13 sounding rocket. The drag sail mechanism and the test of the sounding rocket is presented in Wolff et al. (7) and the deployment is shown in Figure 1.1(b). Now in 2017, the drag sail is integrated on the FH Aachen University of Applied Sciences CubeSat Compass 2 waiting for its launch within the QB 50 project Thoemel et al. (8) within the year.

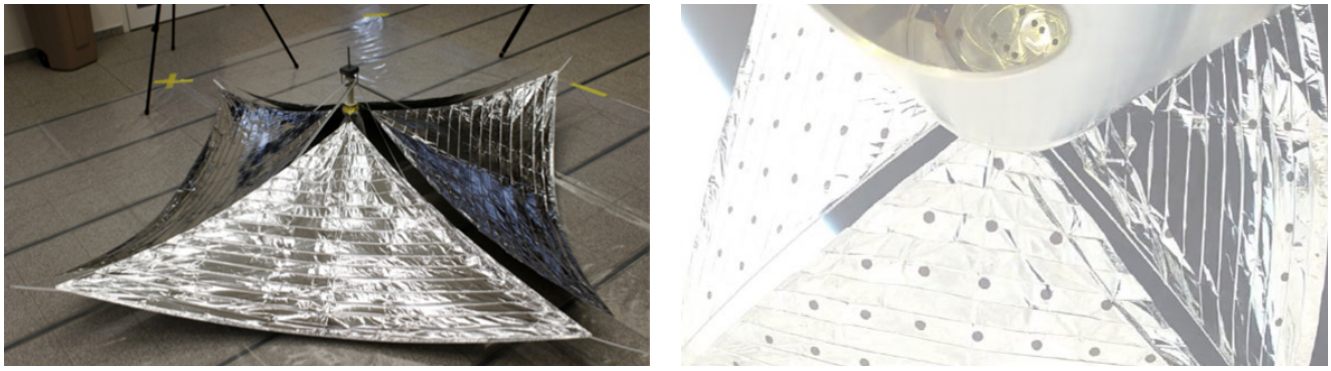

(a) CubeSat drag sail bread board.

(b) Deployment of the Space Sailors drag sail on a REXUS sounding rocket Wolff et al. (7).

Figure 1.1: Precursor CubeSat drag sail development.

The studies of previous projects and the experience with the CubeSat drag sail showed that for the further development of large deployable gossamer structures, especially in Europe, a focus on the qualification testing and verification in the environment expected in space is necessary. The main focus of the work presented here is on the design, analysis and verification testing of a membrane mainly considered as a solar sail. In this context, the stowing and deployment strategy with the mechanisms involved is of particular importance. It was recognized that previous strategies had disadvantages with respect to controlling and automatizing the deployment. A technique for a controlled deployment is proposed and the deployment process is analyzed and mathematically modeled. Several membrane-specific aspects are studied and the membrane, as well as its deployment mechanism and the deployment process, was verified in an extensive test

campaign. These analyses and tests show that the materials, mechanisms and the deployment process are to a great extent suitable for the space applications considered, but it also shows critical points that may require further investigation.

The German Aerospace Center (DLR) has pursued the further development of scalable deployment technology for gossamer spacecraft, suitable for autonomous and controlled deployment within the Gossamer-1 project. The work presented here mainly contributed to this project and in consequence is described mainly on the example of the Gossamer-1 configuration. However, the analyses and conclusions can also be transferred to other projects. A summary of the developments within the Gossamer-1 project was published in the reviewed scientific journal Advances in Space Research (Seefeldt et al. (9)). The aim was to develop a deployment system for space applications with a focus on solar sailing and secondary use cases as a flexible photovoltaic array and drag sail. The development was carried out for a $5\,\mathrm{m} \times 5\,\mathrm{m}$ technology demonstrator that should in principal allow for up-scaling to $50\,\mathrm{m} \times 50\,\mathrm{m}$. The satellite has an estimated mass of about 30 kg, and the compact launch configuration has a maximum width of approximately 790 mm and a height of 500 mm. The sail is based on a crossed boom configuration using previously developed Carbon Fiber Reinforced Plastic (CFRP) booms with four triangular sail segments. An artist's rendering of this demonstrator is provided in Figure 1.2(a). The project was initiated with the goal of demonstrating the technology in a LEO. Currently, several aspects were verified by environmental testing and therefore the membrane related technology is at least close to TRL six.

Within the ESA Deployable Membrane and ADEO projects, the Gossamer-1 technology has been adapted and further developed for the drag sail application together with industrial partners. The sail system utilizes the same CFRP booms and coated polyimide foils. The ADEO system design aims for passive attitude stabilization with a pyramidal shaped sail with a drag area of $25\,\mathrm{m}^2$ and a deployment actuation implemented in a de-orbit module that would be mounted onto the main satellite bus. Then first results of the project are presented in Sinn et al. (10) and an artist's rendering is shown in Figure 1.2(b). The development is being carried out in a consortium consisting of the companies High Performance Space Structures GmbH, Hoch Technologie Systeme GmbH, Etamax Space GmbH and DLR.

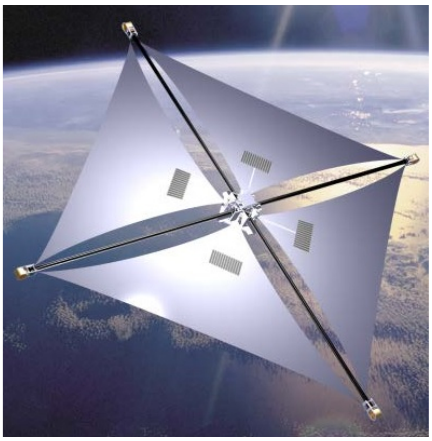

(a) DLR project Gossamer-1 demonstrator, artist's rendering.

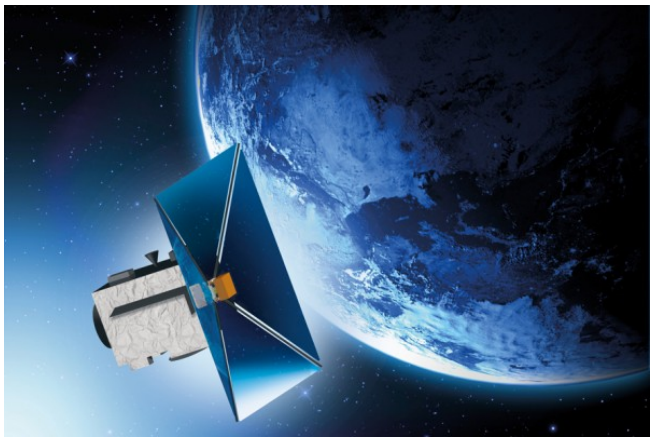

(b) ESA project ADEO, artist's rendering (Sinn et al. (10)).

Figure 1.2: Gossamer technology development in recent projects.

After reviewing several projects in a state-of-the-art summary provided in Chapter 2 an evaluation of possible membrane materials follows in Chapter 3. The main requirements for the materials are described and possible membrane materials, as well as coatings, are studied. Membrane materials are selected for the Gossamer-1 LEO mission and for a future solar sail mission. In Chapter 4, possible stowing and deployment strategies are analyzed and a strategy for large membrane space systems is presented. The deployment process is analyzed by a mathematical

description of the deployment geometry and forces. This content was published in the reviewed scientific journal Advances in Space Research (Seefeldt (11)). In the framework of the Gossamer-1 project, the required deployment mechanisms were developed. These mechanisms are presented in Chapter 5. For the Gossamer-1 design, several membrane specific aspects are analyzed in Chapter 6. It includes the determination of load cases, load introduction considerations, a prediction of the behavior of the deployed membrane and an investigation of the folding lines. The chapter ends with a design description of the Gossamer-1 sail membrane. The membrane manufacturing and integration is presented in Chapter 7.1 followed by a description of the verification testing of that hardware in Chapter 7.2. The tests ranged from component level to system level and included mechanical vibration, static acceleration, fast decompression, thermal vacuum and laboratory deployment tests.

# Chapter 2

# State of the art applications of deployable membranes

This chapter outlines the state of the art and provides examples of applications, missions and projects in the field of deployable gossamer systems. Deployable membrane structures offer new kinds of space applications in innovative fields such as

- solar sails,
- drag sails,
- deployable membrane antennas,
- flexible solar cell arrays.

In addition, thin membranes are used for Multilayer Insulation of spacecrafts and sun shielding. In consequence, the considered materials in the different fields of application often originate from MLI manufacturing.

The development of gossamer structures has a long history in the field of solar sailing. A solar sail utilizes the solar radiation pressure on the sail as a means for the propulsion of space probes. Huge deployable membranes have been developed in this field. Solar sail projects are described in Section 2.1.

In the last decade the field of nano- and pico-satellites rapidly developed by employing the CubeSat standard. On the one hand, CubeSats further increase the space debris problem due to a high ballistic coefficient. On the other, they are perfect platforms for developing new technologies. As a result, various CubeSat projects are exploring possibilities for deploying drag sails and other structures. The technologies used in this field demand high efforts in miniaturization, and in consequence those systems are not easily scalable for bigger satellites. Activities in the field of drag sails are presented in Section 2.2.

Deployable membranes are also used in the field of membrane antennas. In this field the requirements regarding the geometry of the antenna and the surface quality clearly dominate. Therefore, the designs presented in former projects show well-spanned membranes with sophisticated load introduction strategies. A few examples are given in Section 2.3.

New solar generators based on flexible thin-film solar cells are also in need of deployment strategies and technologies. A few projects in the solar sail area attached solar cells to the sail membrane in order to combine those technologies. The thin-film solar cells are much thicker than the membranes considered in the other fields of application described. Furthermore, electrical requirements need serious consideration when creating huge solar electric generators. Some projects that investigated such generators are presented in Section 2.4.

## 2.1 Solar sails

Solar sails make use of solar radiation pressure as spacecraft propulsion. Therefore, a solar sail does not require any propellant that ultimately limits the lifetime of a spacecraft. They are considered to be an effective propulsion system for long term missions, e.g. the exploration of the solar system. The constant but small acceleration leads to significant $\Delta v$ over time. In order to have sufficient acceleration, huge lightweight sails are required (typically larger than $20\,\mathrm{m} \times 20\,\mathrm{m}$ depending on the spacecraft's mass). There is a wide range of considered possible missions. A few examples are:

- near Earth object rendezvous (Peloni et al. (12)),
- Lagrange point orbits (Bookless and McInnes (13)),
- solar polar missions (Leipold et al. (14))
- non-Keplerian orbits (McInnes (15)), e.g artificial Lagrange point (McInnes (16)),
- heliopause missions (Carl G. Jr. (17)) .

The theoretical basis for solar sailing was first discovered in the 1860s when James C. Maxwell published his theory of electromagnetism, pointing out the fact that electromagnetic radiation exerts a pressure on objects. The first idea for solar sailing in space ranges back to Bernal (18), who published an essay highlighting that the repulsive effect of the Sun's radiation can be used for propelling spacecraft. The first actual technological approach and the first designs for solar sails were initiated by NASA's Jet Propulsion Laboratory (JPL) for a comet rendezvous mission in 1976. The historical background and the principles of solar sailing are described in Colon (19). The following paragraphs present some projects aimed at the application of solar sails.

### 2.1.1 Exemplary solar sail projects

In Europe the first comprehensive ground demonstrations were made testing a $20\,\mathrm{m} \times 20\,\mathrm{m}$ breadboard sail in a joint DLR, NASA/JPL and ESA project in the 1990s (see Figure 2.1), followed by several development and study projects like ODISSEE Leipold et al. (1) and GEOSAIL Agnolon (2). The ground demonstration is presented in Leipold et al. (3) and the study activities are sum-

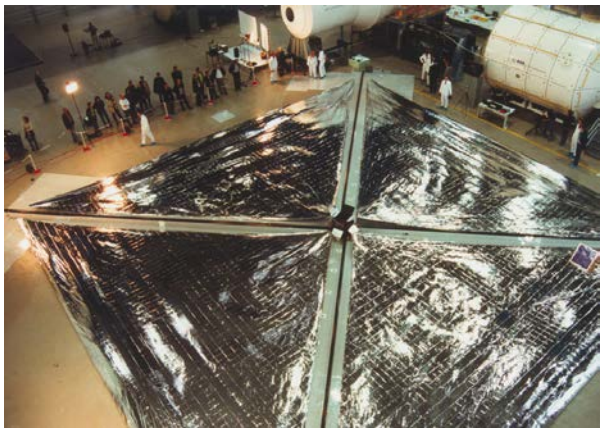

Figure 2.1: ESA/DLR deployment demonstration of a $20\,\mathrm{m} \times 20\,\mathrm{m}$ solar sail in 1999 (Agnolon (2))

marized in Leipold et al. (4). Leipold et al. (20) presents another concept for a heliopause explorer mission. Based on the previous work described and recent developments, DLR start another effort

to develop a scalable solar sail technology within the Gossamer-1 project that has mainly driven the work presented here.

In the USA, the development of solar sail technology was pursued in a collaboration between NASA and the company L'Garde. The development is based on inflatable truss booms. Some information about the development can be found in L'Garde publications in Lichodziejewski et al. (21) and Lichodziejewski et al. (22). The development resulted in the Sunjammer solar sail demonstrator that aims to deploy a steerable 35 m × 35 m sail. Further information is published on their website by Space Service Holdings Inc. (23) The sail is shown in Figure 2.2.

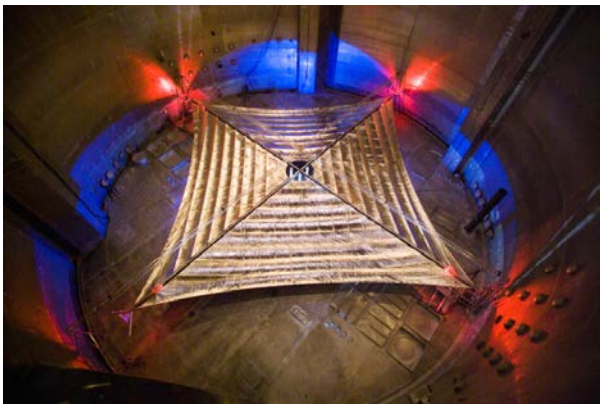

Figure 2.2: NASA's Sunjammer sail in a vacuum chamber (Space Service Holdings Inc. (23)).

JAXA's IKAROS solar sail, described in Tsuda et al. (24), is up to now the largest launched and tested sail. It combines solar sailing with electric propulsion. Therefore, it is also an example of employing flexible solar cells for space applications. The IKAROS sail was launched on an interplanetary trajectory. A sail of 14 m × 14 m was deployed employing centrifugal forces by spinning up the spacecraft.

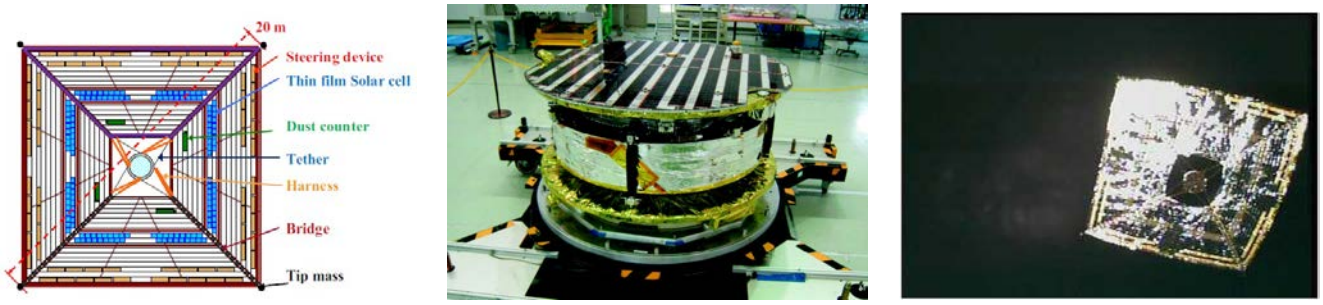


(a) Schematic (b) Launch configuration (c) Deployed in space

Figure 2.3: JAXA's IKAROS solar-power sail (Tsuda et al. (24)).

## 2.2 Drag sails

The increasing amount of space debris is becoming more and more of a threat to space flight. The situation is illustrated in Figure 2.4(a) and 2.4(b) provides an overview of the evolution of tracked space debris.

In consequence, ESA initiated the Clean Space program dedicated to preserving Earth's orbital environment so that a safe operation of satellites remains possible. As part of this program the above mentioned projects Deployable Membrane and Architectural Design and Testing of a De-orbiting Subsystem were initiated by ESA in 2015.

With the increasing amount of debris in LEO, the idea grew to increase the drag area by deploying lightweight membrane structures at the end of a satellite's lifetime (Matloff (25), Harkness (26)). Today these devices are often referred to as drag sails (e.g. Bonin et al. (27)), exo-brakes (e.g. Murbach et al. (28)) or aero-brakes (e.g. Matloff (25)). In his Ph.D. thesis, Harkness (26) provides a good study of de-orbit devices. His work covers aerodynamic and solar pressure simulations, shape and size optimization, assessments of aerodynamic loads and conceptual designs.

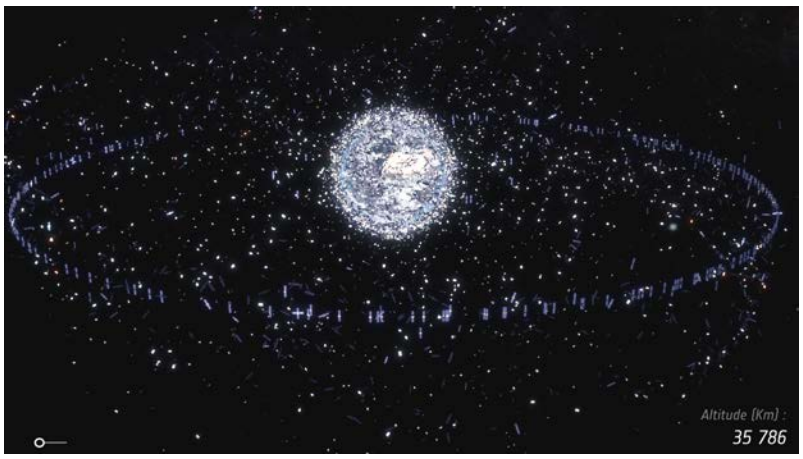


(a) Illustration of space debris, note that there is an agglomeration in commonly used low orbits and in the geostationary orbit.

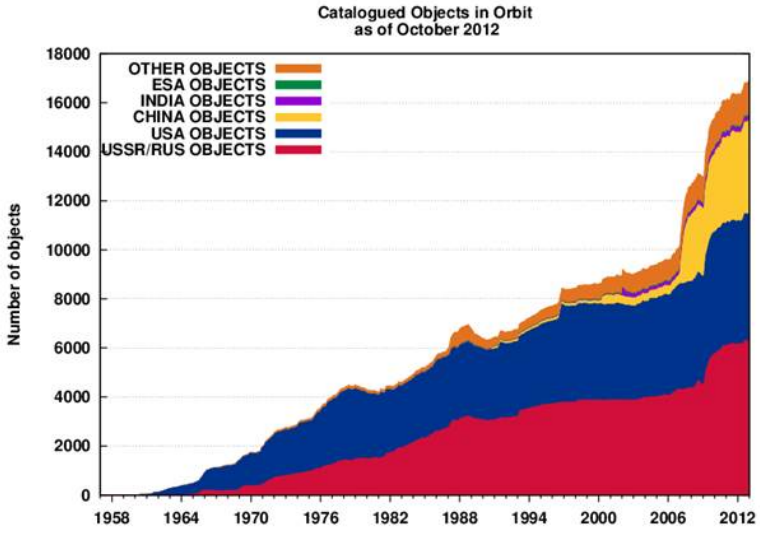


(b) Space debris evolution from 1958 to 2012 differentiated by the country responsible.

Figure 2.4: Visualization of the space debris problem ESA (29).

The EU FP7 project Deploytech University of Surrey (30) presents the know-how and results gathered from different space sail projects conducted in Europe in recent years. The following paragraphs present some projects aimed at the application of drag sails.

### 2.2.1 Exemplary drag sail projects

Seefeldt et al. (6) presented a concept for a triple CubeSat with a drag sail and a flexible thin-film photovoltaic array. In the following years this concept was further developed together with many motivated students. In 2013, the Space Sailors student group tested this drag sail within the REXUS program of the German Aerospace Center (DLR). The project was supported by

the Faculty of Aerospace Engineering of the FH Aachen University of Applied Sciences, various institutes of the RWTH Aachen and several companies as well as the Institute of Space Systems at DLR Bremen. Employing DLR's Gossamer-1 technology the sail membranes were manufactured and the sail was successfully tested on the sounding rocket REXUS14 as presented in Wolff et al. (7). The deployed $2\,m^2$ drag sail is shown in Figure 1.1. A dedicated CubeSat mission for demonstrating this sail in orbit is currently being developed at FH Aachen within the QB50 project. The sail design and manufacturing is supported and supervised by DLR Bremen. The deployment module was sized according to the CubeSat standard to $10\,cm \times 10\,cm \times 10\,cm$. Within this cube, bi-stable metal leaf spring booms and the sail segments are coiled on two spools. The energy for the deployment is stored mechanically in the spring tapes. The sail material is a $7.5\,\mu m$ thick polyimide film which is coated with aluminum.

In the further process, the space sailors' drag sail is currently integrated on a CubeSat (see Figure 2.5), which is developed at the FH Aachen University of Applied Sciences (31) in the Compass 2 project. The drag sail will fly in a sun synchronous orbit at an altitude of 350 to 400 km. The de-orbiting duration is calculated to be somewhere between 24 to 43 hours depending on the Sun's activity (Wolff et al. (7)) and the attitude behavior of the sail. The sail technology is derived from the DLR's Gossamer-1 project.

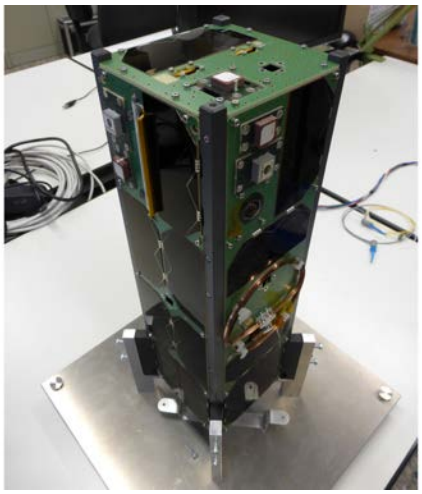

(a) Compass-2 satellite

(b) Compass-2 Drag sail with coiled sails and deployed booms

Figure 2.5: Drag sail CubeSat Compass-2 FH Aachen University of Applied Sciences (31) of the FH Aachen University of Applied Sciences. The sail segments were manufactured together with students at the DLR's Institute for Space Systems in Bremen.

The De-Orbit Sail presented in Hillebrandt et al. (32) is a three unit CubeSat ($30\,cm \times 10\,cm \times 10\,cm$) developed within the EU FP-7 program by a consortium of universities, research facilities, and industries. It deploys a $25\,m^2$ sail. The concept employes DLR's CFRP shell booms and a Kapton foil with a thickness of $7.5\,\mu m$. Figure 2.6 shows the laboratory deployment of the sail.

Figure 2.6: Laboratory deployment of the De-Orbit Sail with aluminum coated foil (Hillebrandt et al. (32)).

NASA's Marshall Space Flight Center and NASA's Ames Research Center developed a sail deployed from a three unit CubeSat as presnted in Johnson et al. (33). After the first sail was lost due to a problem with the launcher in 2008, the NanoSail-D2 was successfully launched in 2010. The "D" in the name stands for deploy, de-orbit, demonstration and drag which summarized the mission goals. The sail is made of a 7.5 $\mu$m thin reflective polyimid foil called CP-1. In Figure 2.7 an artistic impression of the deployed sail is shown. Due to a failure of the on-board cameras there is no picture of the sail in orbit. The satellite provided orbit data that allowed scientists to witness the de-orbit behavior of the sail system.

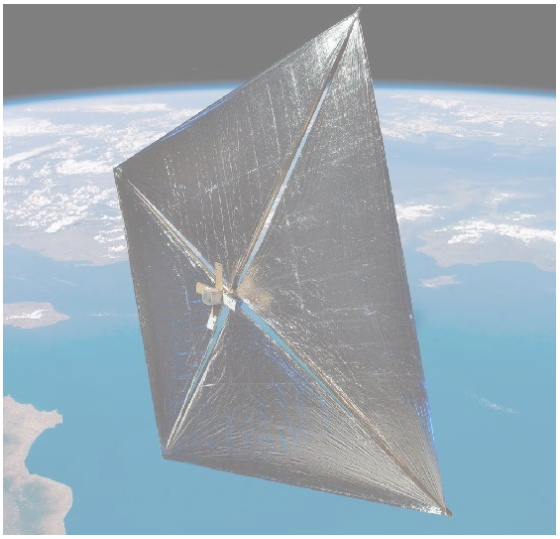

Figure 2.7: Deployment of NanoSail-D2 Johnson et al. (33).

Te KnightSat 2, presented in Pfisterer et al. (34), is another Drag Sail CubeSat developed at the University of Central Florida. The drag sail which is applied as a payload on the KnightSat 2 is also referred to as Attitude Control and Aerodynamic Drag Sail (ACADS). It was developed as an experimental payload. In Figure 2.8 the deployed ACADS attached on KnightSat 2 is shown. The sail's stowage box has four outside windows that are opened at the beginning of the sail deployment. Inside the box are electronics which control the sequence of the deployment, a pressure vessel which inflates the four folded booms and the sail which is also stored in four segments. The sail is made of 3 $\mu$m Kapton. The booms are made of Sub-Tg resin-impregnated Vectran fabric. This is pliable when heated and becomes rigid when it is cooled. The booms have a reflective coating to prevent a loss of rigidity once deployed. A circular hole in the center of the sail decreases the shadowing of the solar panels. The deployed sail will have an area of 10 $\mathrm{m}^2$ and a weigh of 2.1 kg. Simulations revealed that the satellite will de-orbit approximately 50 times faster with the sail than without.

Bonin et al. (27) presents the Canadian Advanced Nanospace eXperiment 7 (CanX-7) CubeSat that is built at the Institute for Aerospace Studies and Space Flight Laboratory of the University of Toronto. The primary mission of the CanX-7 is to demonstrate de-orbiting technology suitable for CubeSats. As a secondary payload, CanX-7 was launched in 2016 into an orbit altitude of about 800 km. During a period of 6 months it will operate a secondary payload provided by COM DEV Ltd. After this period the drag sail will be deployed. The special feature of this drag sail is that it has four individual sail modules. Each of them has a different task, shown in Figure 2.9. The whole sail area will be approximately 5 $\mathrm{m}^2$. The deployment mechanism of the CanX-7 sail works on the basic principle of stored mechanical energy. Therefore, tape springs coiled on a reel are used. The sail consists of a 12.7 $\mu$m Kapton film with aluminum coating on both sides.

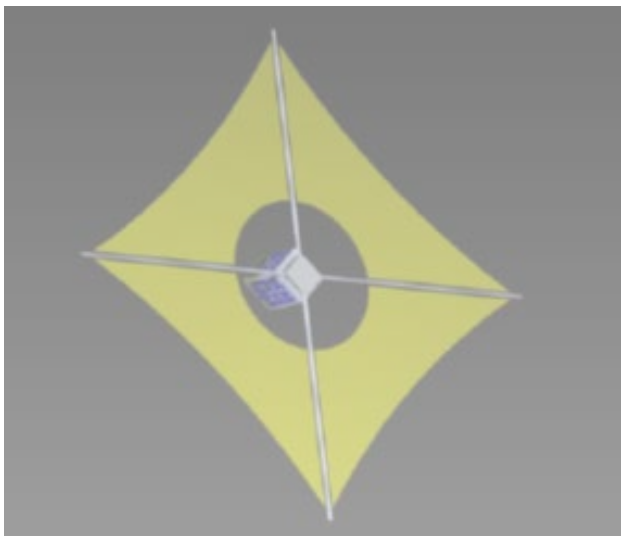

Figure 2.8: KnightSat 2 with the attached ACADS (Pfisterer et al. (34)).

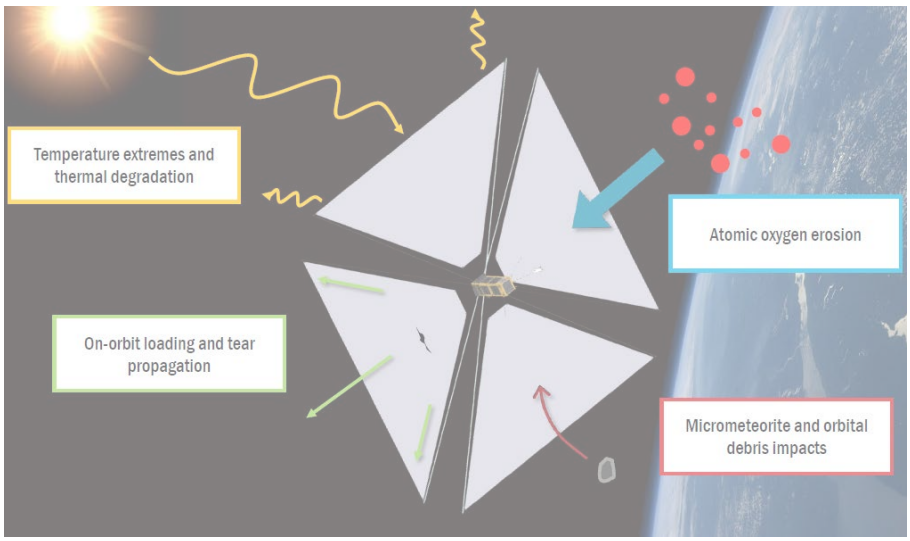


Figure 2.9: CanX-7 Spacecraft (Bonin et al. (27)).

## 2.3 Membrane antennas

Freeland et al. (35) identifies mobile communication, Earth observation radiometry, active microwave sensing, space-orbiting very-long-baseline interferometry, and space-based radar as possible applications for deployable membrane antennas. Overviews about the past development of membrane antennas are given in Freeland et al. (36) and Im et al. (37).

### 2.3.1 Exemplary membrane antenna projects

In the late 1980s, the first ideas and experiments were developed by L'Garde Inc. and NASA to employ thin membranes and deployable structures for antenna applications for mobile communications, Earth observation radiometry and radars. A first in-orbit demonstrator was launched in 1996 on board STS-77 (Freeland et al. (35)) deploying a 14 m diameter inflatable parabolic reflector with a supporting torus and three inflatable struts (see Figure 2.10). This first demonstrator was inflated by gaseous nitrogen provided by the host spacecraft. However, it was observed that the deployment process was difficult to control.

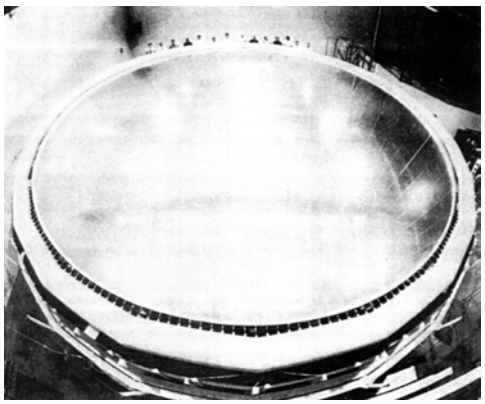

(a) on ground

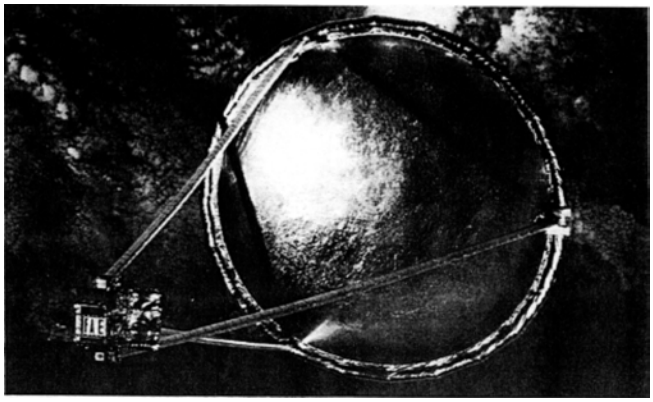

(b) in space

Figure 2.10: Large inflatable deployable antenna developed by L'Garde Inc. and NASA in 1996 (Freeland et al. (35)).

In 2002, Huang presented in Huang (38) deployable planar antennas for Synthetic Aperture Radar (SAR) as shown in Figure 2.11. The membrane consists of three layers. On the top layer, micro strip antennas are integrated. The middle layer is the ground plane with a set of aperture coupling slots, and the bottom layer has power divider lines that excite the top-layer patches. The membrane material used is a 0.13 mm thick Kapton coated with 5 $\mu$m of copper. The three membrane layers are separated 1.27 cm between the top radiator layer and the middle ground-plane layer, and 0.635 cm between the middle layer and the bottom transmission-line layer.

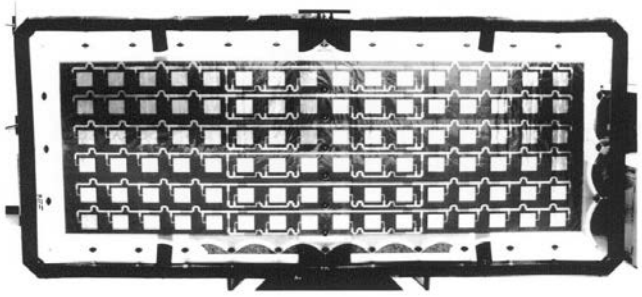

(a) Inflatable L-band SAR array

(b) Ka-band inflatable reflectarray

Figure 2.11: Development of membrane antennas presented by Huang (38).

Adaptive membranes are being developed for very demanding applications. These membranes are able to actively control the surface shape of the membrane in order to counteract wrinkles and eigenmode shapes, excited due to movements of the spacecraft or external distortions. In a study by JPL/NASA Fang et al. (39) and Fang et al. (40), this is achieved by including feedback controlled flexible actuators at the back of the reflector. The need for adaptive gossamer reflectors for space telescopes and their corresponding requirements are also investigated by Gorinevsky and Hyde (41).

In Europe, Contraves Space (today part of RUAG Space) and ESA have been developing inflatable structures for reflector antennas as well as sun shields since the 1970s. In the 1980s, this development resulted in a 6 m diameter reflector antenna. In the following years the development continued to be pursued, resulting in the 10 m $\times$ 12 m reflector presented in Freeland et al. (36).

It is shown in Figure 2.12.

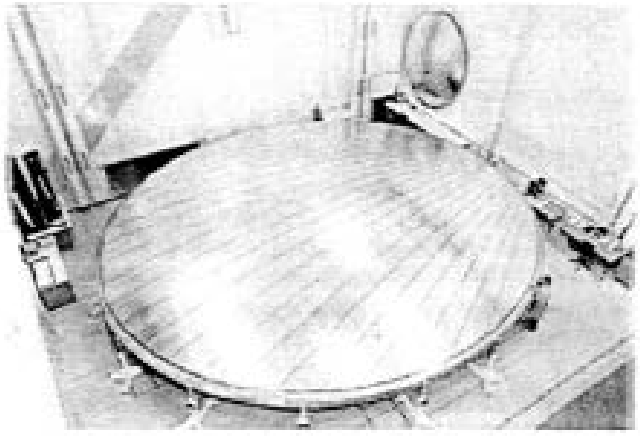

Figure 2.12: 10 m × 12 m offset reflector developed by Contraves Space (see Freeland et al. (36)).

In the late 1990s and early 2000s, possibilities for large active antennas (40 $m^2$ and more) were investigated. These antennas were meant to be used for Earth observation radar. In the joint ESA/DLR study, Very Large Stable Membrane Antenna Architectures (Straubel (42) and Straubel (43)), the potential of large lightweight deployable SAR antennas was evaluated and breadboards, shown in Figure 2.13, were built.

(a) Straubel (42) oval, flexible frame concept.

(b) Straubel (43) 1:3 sub-scale model of a deployable SAR antenna (model size 6 m x 1.4 m).

Figure 2.13: DLR deployable antenna bread boards.

In addition to deployable membrane antennas, Datashvili et al. (44) presents an alternative approach to deployable antennas. The SMART reflector is developed by the Munich University of Technology and Wacker-Chemie GmbH. The deployable reflector employs a novel carbon fiber reinforced silicone material, which is flexible enough to allow compact stowing, but in the deployed configuration it is stiff and provides a high surface quality.

## 2.4 Flexible photovoltaic arrays

An extensive description of the photovoltaic developments is provided in Luque and Hegedus (45), and a more compact summary of the development until 1998 is provided in Jones and Spence (46). As a very short summary it can be stated that one trend of space photovoltaics is the

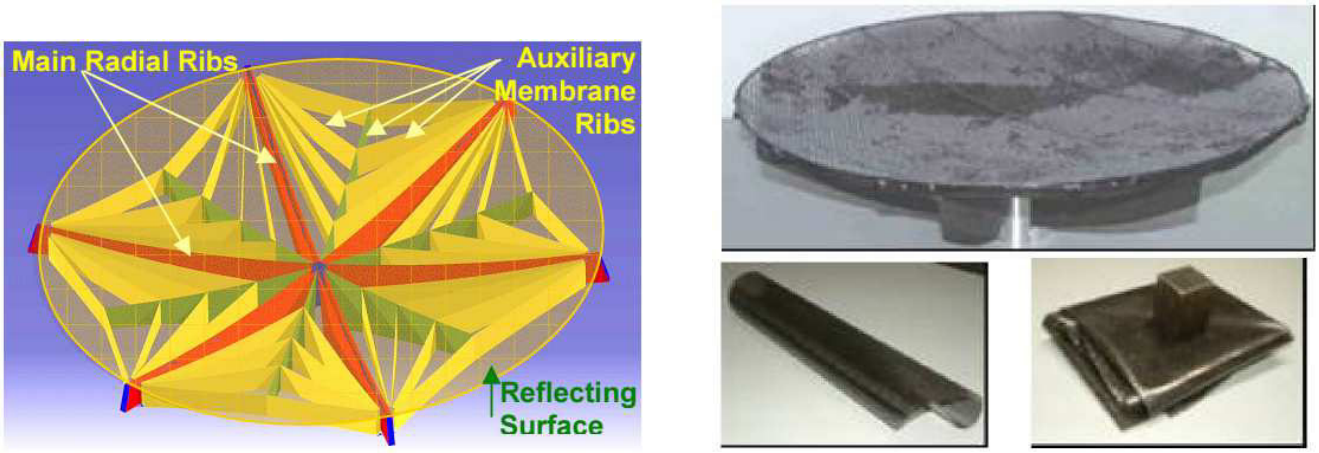


(a) CAD model of the SMART reflector

(b) Laboratory model of the SMART reflector

Figure 2.14: Datashvili et al. (44) SMART deployable reflector.

use of high efficient (about 30%) triple-junction cells on rigid structures. For these cells, indium gallium phosphide (InGaP), gallium arsenide (GaAs) or indium gallium arsenide (InGaAs) and germanium (Ge) are fabricated on a germanium substrate. When it comes to applications that require huge solar arrays, a different approach is pursued. In this case flexible blanket systems are employed. That does not necessarily mean that the photovoltaic cell itself provides flexibility, but the substrates on which they are mounted and electrically interconnected are. In cases when the flexibility of the cell itself is required, amorphous silicon and other thin-film photovoltaics are employed.

In recent years thin film solar cells were recognized as a possible alternative for electrical power generation in space. The focus was on Copper Indium Gallium Selenide (CIGS) based solar cells. The first concepts to employ thin film solar cells on spacecrafts were developed in the late 1990s and early 2000s by NASA, as presented by Dhere et al. (47). CIGS cells have roughly 12 % efficiency, which is one third of the efficiency of triple-junction cells. Yet, as they are very lightweight, there is a potential to develop deployable flexible solar arrays that provide a high power-to-mass ratio ($> 100\,\mathrm{W/kg}$ Otte et al. (48)). Due to the efficiency, the required area that needs to be deployed is roughly three times bigger compared to conventional solar arrays. In order to use the CIGS cells for space applications, it is required to adjust the thermal properties of the cells, for instance the $\alpha_s/\epsilon_{ir}$ ratio, so that the cells do not get to hot when irradiated by the Sun. Furthermore, when operated in LEO, they have to withstand the environment, e.g. ATOX. This is achieved through additional coatings. Shimazaki et al. (49) investigated $SiO_2$ and combined $Al_2O_3/SiO_2$ coatings. He increased the emissivity from 0.18 to 0.77 with a coating thickness of approximately $2\,\mu\mathrm{m}$. Within the PIPV project similar results were achieved, as presented by Günthner et al. (50) and Pscherer et al. (51). The focus was also on creating a mechanically stable coating that can be used for flexible solar generators that need to be rolled for stowing. Figure 2.15 shows a CIGS solar cell with a combined Silicon $Al_2O_3/SiO_2$ coating of $1\,\mu\mathrm{m}$ thickness.

### 2.4.1 Exemplary flexible photovoltaic projects

Solar arrays with flexible blankets have been in use for a long time to meet the power requirements of innovative space systems. Prominent examples include the Hubble space telescope and the International Space Station (ISS). Each Hubble array has a size of $12\,\mathrm{m} \times 2.5\,\mathrm{m}$ and a weight of 290 kg. They were coiled into a cylinder of about 30 cm in diameter (ESA (52)). The two arrays provide 4 kw of electricity (Shayler and Harland (53)). The ISS arrays have a size of $35\,\mathrm{m} \times 12\,\mathrm{m}$ producing about 15 kW of electricity (NASA (54)).

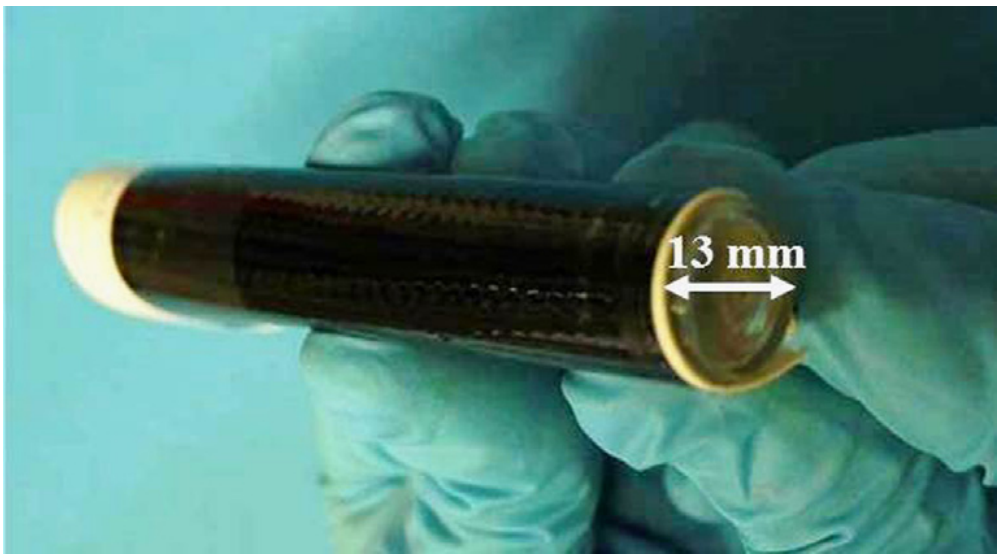


Figure 2.15: Coated CIGS solar cell bending test (Pscherer et al. (51)).

(a) Coilable Hubble space telescope photovoltaic arrays (ESA (55)).

(b) Zig-zag folded ISS solar arrays (NASA (56)).

Figure 2.16: State of the art systems employing flexible blanket photovoltaics.

More recently, the development of huge solar arrays based on flexible blankets has been further perused in the United States leading, for example, to the Ultra-Flex and Mega-Flex concepts as presented in Jones and Spence (46) and shown in Figure 2.17.

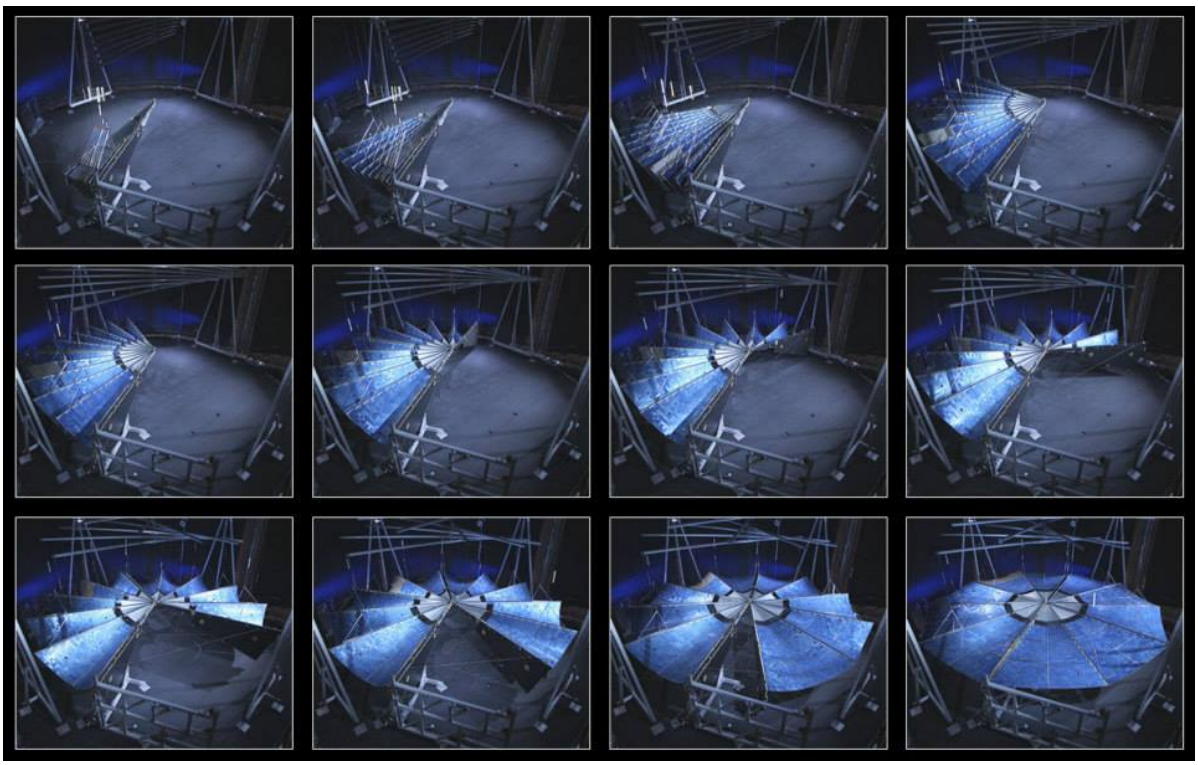

Figure 2.17: Mega-Flex deployment demonstration of a 10 m diameter array in the Glenn vacuum chamber Alliant Techsystems Inc. (ATK) (57).

In the field of thin-film photovoltaics, the above-mentioned PIPV project also led to the development of thin-film photovoltaic array concept for a first demonstration mission. Seifart et al. (58) present the design and test of a concept for large CIGS based solar arrays (2 m x 10 m), and Langendorf et al. (59) show a first flight design for an in-orbit verification mission. Figure 2.18 shows a CAD model of the flight design and the prototype. With a total thickness of roughly 30 $\mu$m, including protective layers, these cells can be rolled up to a diameter of 25 mm without damaging the cells or the interconnections.

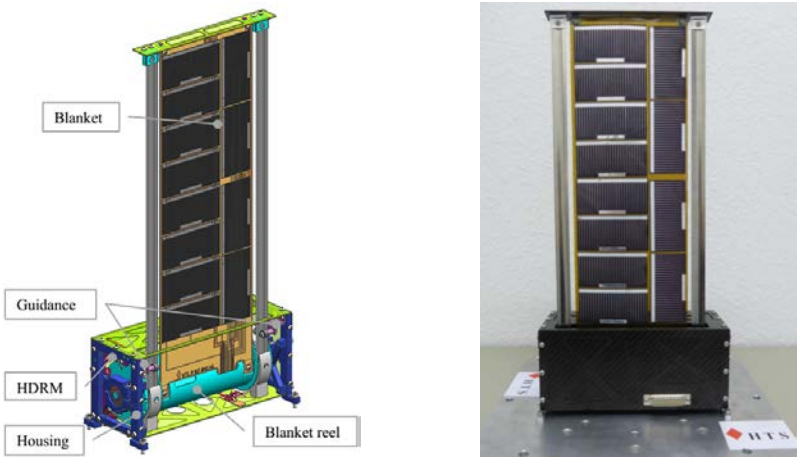


(a) CAD Model (b) Prototype

Figure 2.18: Langendorf et al. (59) deployable solar array with CIGS photovoltaics

JAXA's IKAROS sail has thin-film photovoltaics integrated into the sail. The photovoltaics are placed between two folding lines so that they are only rolled up and not folded. Folding the cells would indeed destroy them. The sail with its photovoltaics is shown in Figure 2.19.

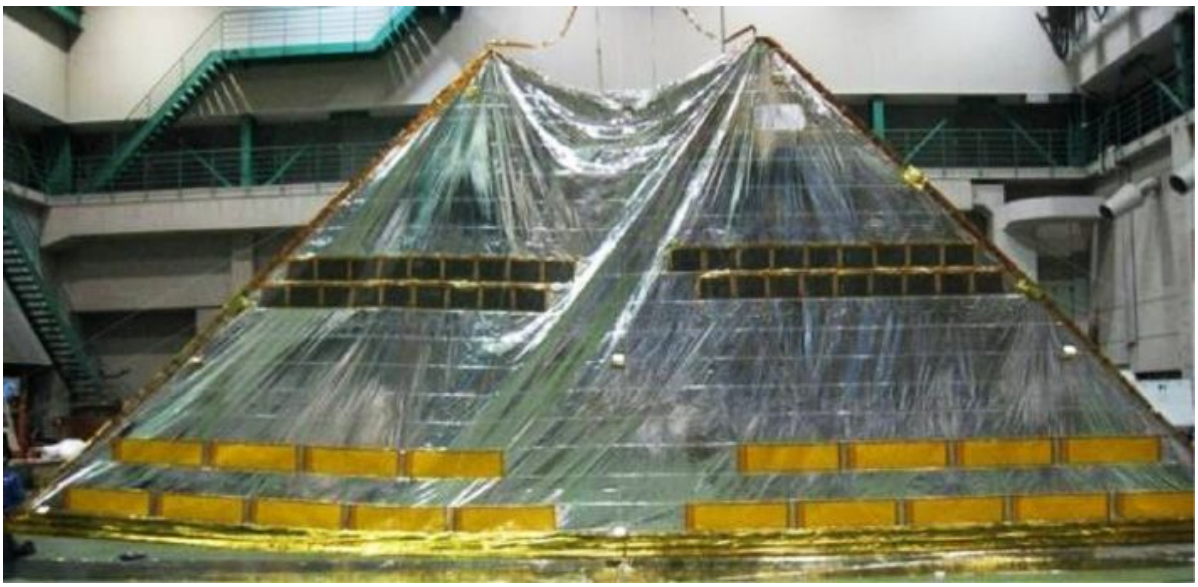

Figure 2.19: JAXA's IKAROS Design (Tsuda et al. (24)).

## 2.5 Conclusion

All of the above projects in the field of solar sails and drag sails employ designs based on a sail membrane divided into four separate segments. However, the chosen deployment mechanisms and strategies vary significantly. The European community has focused on concepts employing rollable CFRP booms with mechanisms that employ electrical motors. The mechanisms actively deploy the booms and thereby simultaneously the sail segments. NASA's / L'Garde's concepts are based on inflatable booms with sails connected not only at the tip of the boom, but also on several points along the boom. JAXA's IKAROS project is not based on booms at all, but instead employs centrifugal forces in a spin deployment. The spacecraft was set into rotation. Masses mounted on the outer edges of IKAROS were pulled away from the center, thereby deploying the sail. The stowing and deployment techniques employed by the various CubeSat projects cannot be easily transferred to solar sail applications with membranes that are one to two orders of magnitude larger. This is further discussed in Chapter 4.

Summarizing the developments presented in the field of deployable membrane antennas, these aim for smaller deployed membranes compared to solar sails or drag sails (up to 10 m in diameter in Huang (38) and Datashvili et al. (44)). However, the development is ongoing and bigger structures are being considered and built on the breadboard level (Straubel (42), Fang et al. (40)). The membranes consist of several layers, are much thicker compared to the solar sail and drag sail applications, and need to fulfill several electric functions. The requirements regarding the surface accuracy are significantly more demanding compared to other applications ($< 1$ mm RMS in Freeland et al. (35) and Huang (38)). Due to that reason, sophisticated mechanical analysis of membrane structures is present in this field.

Huge solar arrays as those being used on the ISS are already using flexible blankets instead of stiff arrays. The solar cells themselves cannot be folded, but flexible thin-film cells can be coiled (e.g the Hubble telescope arrays). Just considering these two examples, ISS and Hubble, it seems only be only consistent to combine folding and coiling in a next step. This step was made by JAXA's IKAROS project. The electrical contacting and harnessing significantly increases the complexity of the membrane compared to a pure sail membrane without electrical functions. The progress made with flexible thin-film CIGS photovoltaics, for which efficiency has constantly increased over the years, could very well lead to a new kind of cheap (material saving) and flexible solar array for future space applications.

# Chapter 3

# Evaluation of membrane materials

The projects introduced in Chapter 2 all employ polyimid as a base or substrate material. Brand names of polyimid foils are Kapton, Upilex and CP1. Polyimide is especially characterized by its superior high thermal and chemical stability (low out-gassing). These foils are also known in the field of Multilayer Insulation (MLI). For MLI the foils are coated with different thin films in order to provide protection from the space environment and to adjust the thermal-optical properties. Specifications of such materials are available e.g. in the Sheldahl Red Book, Multek Corporation (60). The following sections analyze the environment in which spacecraft have to operate and their effects on polyimide substrates and coatings.

## 3.1 Material Requirements

The requirements for spacecraft depend strongly on their field of application or their location of application, respectively. While Gossamer-1 is supposed to demonstrate a deployment in LEO (orbit height between 200 to 800 km), a solar sail would operate in interplanetary space.

### 3.1.1 Atomic oxygen resistance

If a mission in an LEO is considered, Atomic Oxygen (AO) corrosion is one main degradation factor. AO is produced by the photo-dissociation of molecular oxygen in the upper atmosphere by solar radiation of a wavelength of about 243 nm (Banks et al. (61)). At LEOs, space vehicles orbit the Earth at velocities of between 7.4 km/s and 7.9 km/s. This is a direct result of the Vis-Viva equation for an elliptical orbit between 200 km and 700 km. The Vis-Viva equation is a formulation of the energy conservation for orbital energy and it is used to describe the orbit velocity (Fortescue et al. (62, p.88)). Considering a maximum velocity of approximately 8 km/s, the mass of one oxygen atom $m_{AO}$ of $2.66 \cdot 10^{-26}$ kg yields kinetic energy of

$$E_{AO} = \frac{1}{2} \cdot m_{AO} \cdot v_{AO} = 8.5 \cdot 10^{-19}\,\mathrm{J} = 5.3\,\mathrm{eV}\ . \tag{3.1}$$

With additional thermal energy of 0.1 eV (De Rooij (63)), the total energy of one oxygen atom is at maximum 5.4 eV. The flux of AO as a function of altitude is shown in Figure 3.1. Note that there is a high deviation of the flux caused by the solar activity. If the energy of the impacting AO exceeds the bonding energy of atoms or molecules of the impacted material, this leads to a sputtering process, which results in mass loss of the bombarded material. The materials employed either have to be AO resistant or the mass loss or erosion of the material needs to be sufficiently small. For the evaluation of AO resistance of materials, the experimentally determined Erosion Yield (EY) is available for many materials. It defines the amount of material loss per oxygen atom. Combining the EY with the atomic oxygen flux (see Figure 3.1) $\Phi_{AO}$ allows an estimation

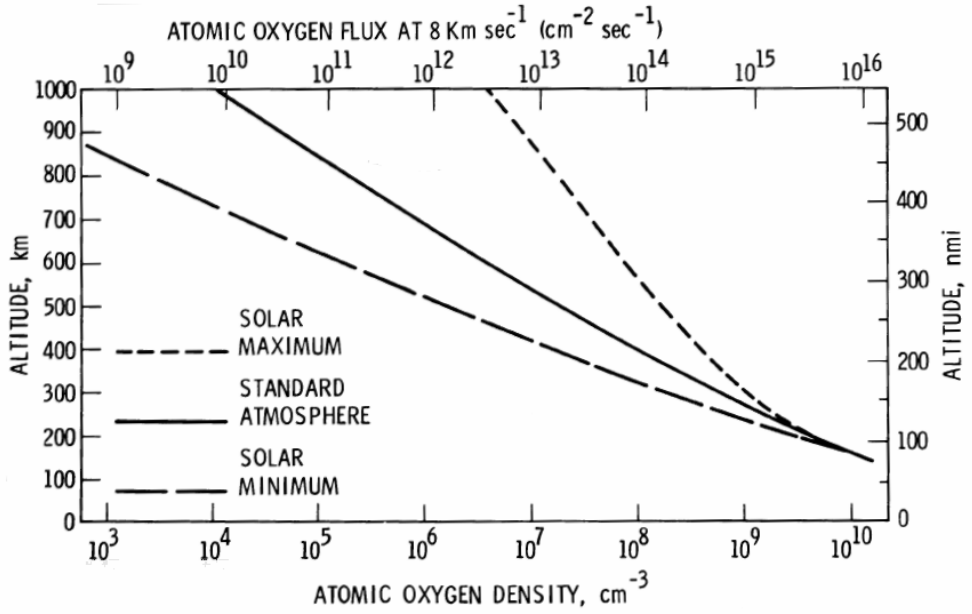


Figure 3.1: Atomic Oxygen density in Low Earth Orbit Rooij (64).

of the material loss per time, which is a measure for the decrease in material thickness. For a given mission time $T_m$ the decrease in material thickness is

$$\Delta t_{AO} = EY \cdot \Phi_{AO} \cdot T_m \ . \tag{3.2}$$

The material used must be thickened by the amount of $\Delta t_{AO}$ to compensate for the material loss through the mission time.

### 3.1.2 Electromagnetic radiation

All of the materials used for space applications have to be evaluated regarding their behavior under electromagnetic radiation (ECSS (65), ASTM International (66)). It is known from many evaluation tests that particle and electromagnetic radiation can significantly degrade materials and lead to changes in their mechanical behavior, e.g. embrittlement of plastic materials. The materials employed have to be sufficiently radiation resistant with respect to their mechanical properties. Polymers in LEO are also susceptible to high intensities of the VUV radiation. According to Minton et al. (67) and Grossman and Gouzman (68) it causes their degradation through multiple photochemical processes, i.e. VUV radiation is energetic enough to break their bonds such as C-C, C-O and functional groups. This in turn can lead to a delamination between a substrate and its coating when gas bubbles form between the layers. In the further process this can lead to a destruction of the coating and subsequently to a destruction of the substrate that is then exposed directly to the space environment. Therefore a shielding of plastic materials in such an environment is often necessary. The depth of penetration of electromagnetic radiation into a material can be evaluated by the Beer-Lambert law, which describes the decrease in the intensity of an electromagnetic wave in a material (Tipler and Mosca (69, p. 1415-1417)). If a material is supposed to shield, for example, 99% of the intensity $I_\lambda$, the Beer-Lambert law can be transformed

to determine the required material thickness according to the penetration depth $d$ as

$$I_\lambda = I_{\lambda,0} \cdot e^{-\alpha_\lambda \cdot t} \stackrel{!}{=} (1 - 0.99) \cdot I_{\lambda,0}$$
$$\Rightarrow d = -\frac{ln(0.01)}{\alpha_\lambda} \ . \tag{3.3}$$

The absorption coefficient $\alpha_\lambda$ depends on the wavelength. If a material provides a certain absorption throughout a wavelength range, the lowest $\alpha_\lambda$ within this wavelength range is used to determine a material thickness that provides a certain shielding throughout this wavelength range.

### 3.1.3 Proton radiation

Beyond the LEOs the main source of materials properties change is caused by corpuscular and electromagnetic radiation. Corpuscular radiation is mainly produced by the Sun. Solar wind consists of charged particles, mainly protons and electrons. They originate from coronal mass ejections and solar flares. Electrons with energies from about 0.01 eV up to a few hundredths eV come from coronal mass ejections. Flares are the sources of electrons with energies from 1 MeV up to hundreds of MeV. The solar protons carry energies from 0.2 keV to a few tenths keV in the solar wind and in coronal mass ejections. Protons with energy up to a few GeV are produced in solar flares Kezerashvili and Matloff (70). The solar wind is then caught by the Earth's magnetic field and constitutes a unique environment. Therefore, when for instance Geostationary Orbit (GEO) is considered, the influence of the so-called trapped protons and electrons cannot be neglected.

The effect of proton irradiation on aluminum coated polyimide was extensively studied by Sznajder et al. (71, 72). He showed that protons of energy around 8 keV get trapped in the aluminum layer. There they recombine with free electrons to hydrogen and form bubbles on the aluminum surface. The subsequent effect of the hydrogen formation is a decrease of reflectance. Dachwald et al. (73) showed that this has a huge impact on possible solar sail missions.

The penetration depth of protons, or more general ions, is a complex field of research that is not addressed here. Fortunately, this research led to a software tool named Stopping and Range of Ions in Matter (SRIM) that can be used to calculate the depth of penetration of protons (Ziegler (74)). If a material is supposed to protect from protons of a certain energy, this tool allows the determination of the required thickness for a variety of materials and material combinations. High energy protons just fly through thin coating layers without significantly damaging it, while protons with lower energy get trapped inside these layers.

### 3.1.4 Thermal requirements

The environmental effects described are changing the thermo-optical properties of the material surfaces (Verkhovtseva et al. (75), Heltzel et al. (76), Sharma and Sridhara (77), Sznajder et al. (71)). The thermo-optical properties of materials are defined by a pair of parameters: the solar absorption coefficient $\alpha_\mathrm{S}$ and the thermal emission coefficient $\epsilon_\mathrm{t}$. Both values are derived from spectral reflection $R(\lambda)$ that is measured with spectrometers according to ECSS (78). Therefore the average specular absorption weighted with the solar spectrum $S(\lambda)$ between 250 nm and 25000 nm wavelength is calculated as

$$R_\mathrm{S} = \frac{\int_{250\,\mathrm{nm}}^{2500\,\mathrm{nm}} R(\lambda) \cdot S(\lambda)\, d\lambda}{\int_{250\,\mathrm{nm}}^{2500\,\mathrm{nm}} S(\lambda)\, d\lambda} \ . \tag{3.4}$$

For a nontransparent material $\alpha_\mathrm{S}$ is defined as

$$\alpha_\mathrm{S} = 1 - R_\mathrm{S} \ . \tag{3.5}$$

The wavelength range considers 96% of the solar spectrum total energy. Consequently, $R_S$ is also a good measure for the overall reflectance of the solar sail and therefore for its propulsion capabilities. $\epsilon_t$ is the infrared emittance, calculated as the average specular absorption weighted with the blackbody emittance spectrum $E_\lambda(\lambda)$ at 300 K in the infrared spectrum, between 3 $\mu$m and 20 $\mu$m wavelength, as

$$\epsilon_t = \frac{\int_{3\,\mu m}^{20\,\mu m} (1 - R(\lambda)) \cdot E_\lambda(\lambda) d\lambda}{\int_{3\,\mu m}^{20\,\mu m} E_\lambda(\lambda)\, d\lambda} \tag{3.6}$$

The equations consider a non-transparent sample. If the sample is transparent, the transmission must also be subtracted when calculating the absorption. The change of these properties is a result of the change of the specular reflectance.

In order to evaluate materials for the Gossamer-1 LEO demonstration a hot and cold case is established, and equilibrium temperatures are calculated. The equilibrium temperature of a spacecraft depends on the balance between the heat received from external and internal sources, and the head that is radiated to space (Fortescue et al. (62, p. 361)). The cold case is calculated in the shadow of the Earth at a height of 800 km and the hot case is calculated considering the sail at the subsolar point at 300 km. In the cold case only the edge of the sail is directed toward the Earth while in the hot case, the complete sail area is directed toward the Earth. Figure 3.2 illustrates the considered configuration. The mean earth radius $r_e$ is $6.371 \cdot 10^6$ m (Boyle (79)). The space background temperature of about 3°K is neglected for the calculation of the equilibrium temperature.

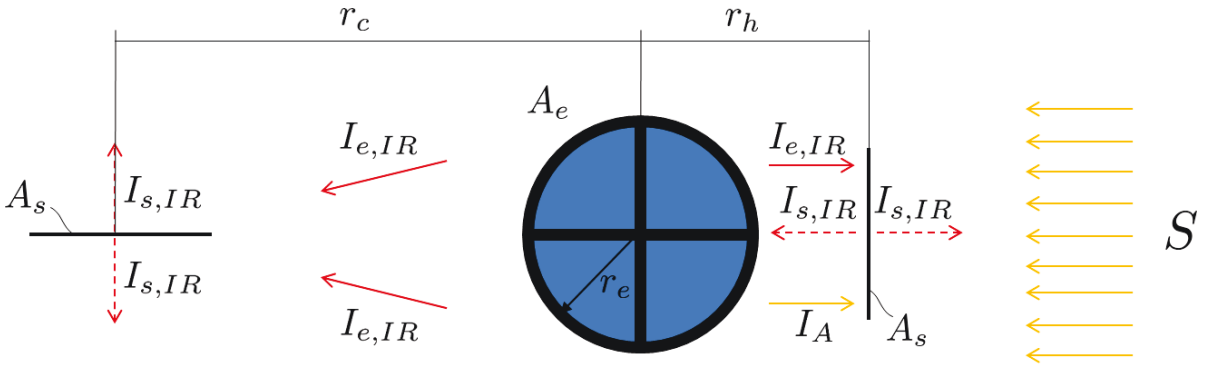


Figure 3.2: Illustration of the cold case (left) and the hot case (right) with surface areas $A$ of the sail and the Earth, intensities $I$ ($IR$ - infrared, $S$ - sun) emitted or reflected from the earth and sail, the Earth radius $r_e$ and the solar constant $S$. The sail is at radius $r_c$ for the considered cold case and at radius $r_h$ for the hot case considered.

For the cold case, 200 W/m$^2$ infrared emission of Earth $I_{e,IR}$ is considered (Donabedian and Gilmore (80, pp. 340-341)) and the orbit radius $r_c$ is $7.171 \cdot 10^6$ m (earth radius + height). Considering the view factor $F_{e,s_c}$ according to Chung and Naraghi (81) as

$$F_{e,s_c} = \frac{A_s}{A_e} \cdot \frac{1}{\pi} \cdot \left[ tan^{-1}\left( \frac{1}{\sqrt{\left(\frac{r_c}{r_e}\right)^2 - 1}} \right) - \frac{\sqrt{\left(\frac{r_c}{r_e}\right)^2 - 1}}{\left(\frac{r_c}{r_e}\right)^2} \right] , \tag{3.7}$$

the cold case Temperature $T_c$ is calculated as

$$T_c = \left( \frac{2 F_{e,s_c} A_e I_{e,IR}}{2 \sigma A_s} \right)^{\frac{1}{4}} \tag{3.8}$$

Here, $\sigma$ is the the Boltzmann constant, $A_e$ is the Earth's surface (sphere with radius $r_e$), $A_s$ is the sail surface (one side) and $I_{e,IR}$ is the intensity of Earth's infrared emission.

For the hot case, the view factor $F_{e,s_h}$ is calculated as

$$F_{e,s_h} = \left(\frac{r_e}{r_h}\right)^2 , \tag{3.9}$$

and the hot case temperature is given by

$$\begin{aligned} T_h &= \left(\frac{q_s + q_a + q_{IR}}{2\epsilon_t \sigma A_s}\right)^{\frac{1}{4}} \\ &= \left(\frac{A_s \alpha_S S(1+0.3) + \epsilon_t F_{e,s_h} A_e I_{e,IR}}{2A_s \epsilon_t \sigma}\right)^{\frac{1}{4}} . \end{aligned} \tag{3.10}$$

It considers heat transfer from the Sun $q_s$, 35% Earth albedo $q_a$, $200\,\mathrm{W/m^2}$ infrared emissions from Earth $I_{e,IR}$, and the solar constant $S$ with $1350\mathrm{W/m^2}$ (Donabedian and Gilmore (80, pp. 340-341)). The orbit radius $r_h$ is $6.671 \cdot 10^6\,\mathrm{m}$. The cold- and hot-case temperatures are shown in Figure 3.3 for different $\alpha_S/\epsilon_t$ ratio.

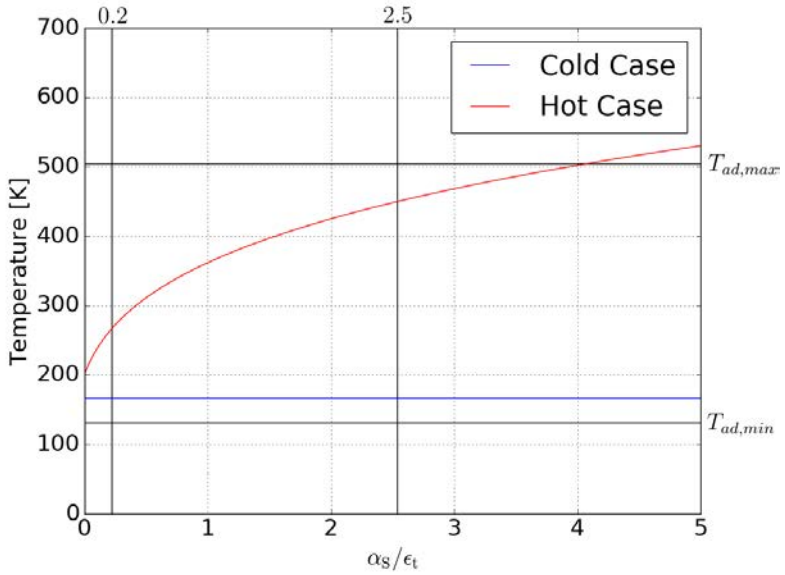


Figure 3.3: Hot- and cold-case temperature as a function of $\alpha_S/\epsilon_t$. A coating combination of aluminum, silicon dioxide and titanium dioxide has a ratio of 0.2 while the aluminum coating was measured with a ratio of 2.5 (see Subsection 3.3.4). The diagram also shows the tested maximum temperature $T_{ad,max}$ and minimum temperature $T_{ad,min}$ of the adhesive.

The specific requirements of a solar sail are driven by the long-term character of the missions with small but constant acceleration in interplanetary space. Furthermore, a lot of solar sail missions consider trajectories that come close to the Sun ($< 0.5\,\mathrm{AU}$) (see list of possible missions in Section 2.1), and this drives thermal requirements. Consequently the membranes considered must be very thin and thus lightweight, as well as provide high thermal limits. For the evaluation of solar sail materials equilibrium temperature $T_{ip}$ (in interplanetary space) as function of the distance from the sun is calculated as

$$T_{ip} = \left(\frac{\alpha \cdot I_S}{2 \cdot \epsilon \cdot \sigma} \cdot cos(\theta)\right)^{\frac{1}{4}} \tag{3.11}$$

with the Sun's radiation intensity $I_S$

$$I_S = \frac{P_S}{4 \cdot \pi \cdot r_s^2} . \tag{3.12}$$

Here, $P_S$ is the total radiated solar power and $r_s$ is the distance from the sun or the radius of an orbit around the Sun, respectively. $I_S$ is equal to the solar constant $S$ at 1 AU distance from the Sun. Figure 3.4 shows the temperature evaluated for different angles of incidents $\theta$ and a different $\alpha_S/\epsilon_t$ ratio.

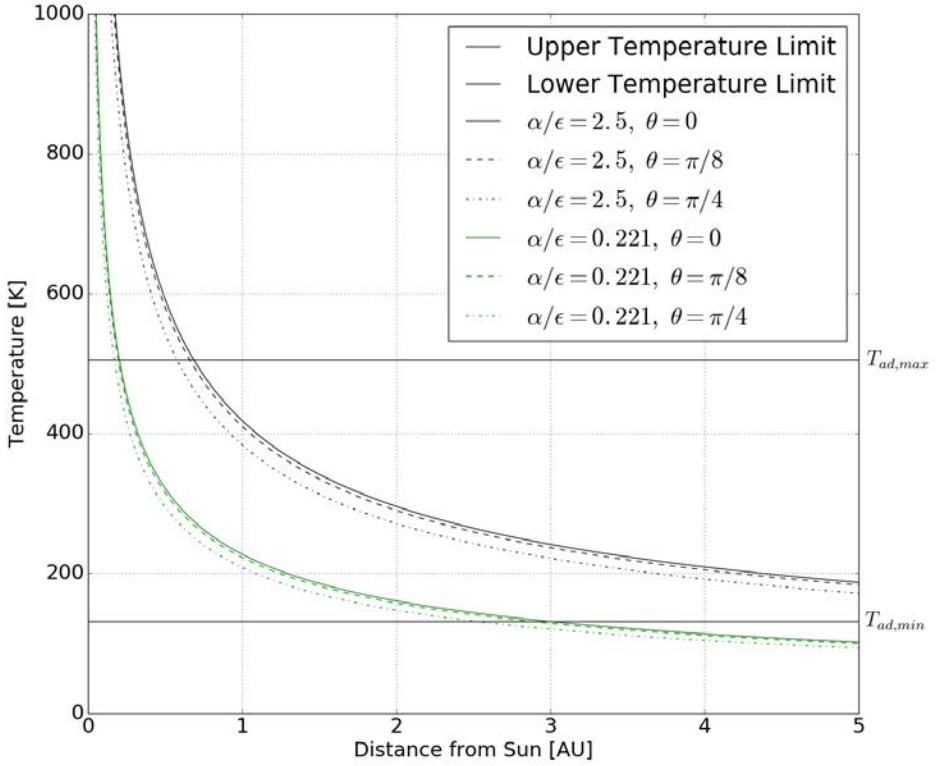


Figure 3.4: Temperatures as a function of the distance to the Sun for the $\alpha_S/\epsilon_t$ ratio of 0.221 (aluminum, silicon dioxide and titanium dioxide) and 2.5 (aluminum) for different angles of incident $\theta$. For properties of coating combinations, see Subsection 3.3.4.

### 3.1.5 Electrostatic requirements

The main concern with respect to the membranes considered here is that they expose huge areas that are subject to surface charging. Surface charging occurs when electrically-charged particles (ions, electrons) in the space environment accumulate on the surface. Additionally, Vacuum Ultra Violet (VUV) and high energetic photons can expel electrons from the materials thereby causing a positive charging of the surface. The commonly associated hazard to such surfaces charging is a so-called Electrostatic Discharge (ESD). It is a sudden discharge between surfaces of different electrical potential, either through contact or plasma. Such discharges can, for example, damage electronics or photovoltaics. Electrostatic charging can of course also accrue during on-ground handling. For the membranes considered here this has another negative effect. The adhesion due to the charging of a membrane (e.g. uncoated polyimide) makes it difficult to accurately fold and coil the membrane during the stowing process, and causes additional forces when trying to deploy such a charged membrane. Requirements regarding the electrical properties of devices operating in a space environment can be found in the ECSS (82) standard. According to that standard, the maximum electrical potential should be less then 100 V, and the maximum current density should be no more then 10 nA/cm$^2$. This allows a first estimation of the required resistance assuming the complete sail being one square membrane (not considering that it is split into segments with

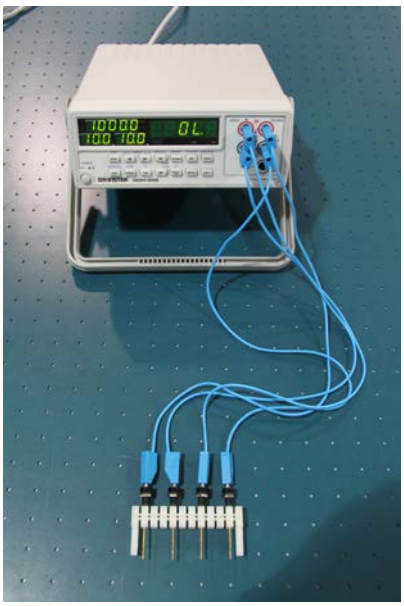

Figure 3.5: Equipment for resistance measurement using the four-point method.

multiple grounding points) as

$$\begin{aligned} R \cdot A \leq & \frac{100\,\mathrm{V}}{10\,\mathrm{nA/cm^2}} \\ \Rightarrow R_{5\mathrm{m}^2} &= 2 \cdot 10^5\,\Omega \\ \Rightarrow R_{50\mathrm{m}^2} &= 2 \cdot 10^4\,\Omega \end{aligned} \tag{3.13}$$

In the case that the membrane is a square, resistance $R$ is equal to surface resistance $R_\square$. The surface resistance is the ratio of the specific electrical resistance to the thickness of the surface considered. A more precise requirement that might be evaluated for the final design is that the grounding contact is less then $10^6\Omega$. A good design may have at most such a maximum resistance between any outer point of the membrane and the grounding point at the center of the sail.

According to Smits (83) the surface resistance can be measured by a standard four-point resistance measurement. Figure 3.5 shows the used equipment for the resistance measurement. It should be noted that there are more sophisticated ways and equipment for sheet resistance measurements, but it is believed that for the purpose of a first resistance evaluation with respect to its ESD behavior and for material comparison, a rough measurement is sufficient.

## 3.2 Thin-film substrates

In Table 3.1, different polyimide substrate materials are compared. The following material parameters are taken into account:

- glass transition temperature $T_g$,
- ultimate tensile strength $\sigma_{uts}$,
- total mass loss $TML$,
- coefficient of thermal expansion $CTE$.

Upilex-S is a heat resistant polyimide film produced by the company UBE. With a glass transition temperature above 500°C and a tensile strength of 657 MPa, it has superior material properties. The total mass loss with respect to outgassing is small, as it is for all polyimide materials. Additionally the material has a low thermal expansion. There are also other modifications of the Upilex foil available. The Upilex-VT, for example, has a modified surface that has thermoplastic properties, which allows heat bonding. The UBE films are available in four thicknesses: 25, 50, 75, and 125 $\mu$m (UBE Compant Ltd. (84)) and until recently a thicknesses of 7.5 $\mu$m was also available (UBE Compant Ltd. (85)), but was taken out of production for unknown reasons.

DuPont Kapton is available in various modifications. Widely used is Kapton HN, which has good thermal and mechanical properties. The ultimate tensile strength at room temperature is 231 Mpa, and its glass transition is at 360°C. While the material is widely used for example for MLI and photovoltaic blankets, the material properties of the Upilex are clearly superior. The total mass loss is comparable to the Upilex-S material, but the CTE is higher. The minimal thickness available is 7.5 $\mu$m. One modification is the Kapton PV9100 type has a higher temperature resistance (623°K), but is only available down to a thickness of 25 $\mu$m.

CP1 is a relatively new product that was established in the past few years by the company NeXolve. Its glass transition temperature is 263°C and its tensile strength at room temperature is only 87 Mpa. Additionally, it has a relatively high $CTE$. For the materials compared here these are clearly the worst properties, but the material is the only one available down to a thickness of 2.5 $\mu$m. Considering that it still has good thermal properties and that the expected loads transferred to a solar sail membrane are low, this material would allow for an extremely lightweight membrane. The material has a very low total mass loss.

The information about the cryogenic behavior of the materials is very limited. Yano and Yamaoka (86) provide information about the Upilex-S and Kapton. Comparable values for the Upilex-S are also given in Songhan Plastic Technology Co., Ltd. (87). The values show that while the tensile strength does not change significantly, the elongation at break decreases significantly from about 42% at 25°C to 10% at −269°C. As can be expected, the material gets brittle for cryogenic temperatures but still provides tensile strength and some elasticity.

Table 3.1: Glass transition temperature $T_g$, ultimate tensile strength $\sigma_{uts}$, total mass loss $TML$, and coefficient of thermal expansion $CTE$ of polyimide thin films.

| Material Type | $T_g$ [°C] [K] | $\sigma_{uts}$ [MPa][*2] | $TML$ [%] | $CTE$ [ppm/°C | Minimal Thickness |
|---|---|---|---|---|---|
| UBE Upilex-S 7.5 $\mu$m | $\geq$ 500 | 657 | 0.85 | 12[*1] | 7.5 |
| DuPont Kapton HN 25 | $\geq$ 360 | 231 | 0.96 | 20 | 7.5 |
| NeXolve CP1 | 263 | 87 | 0.74 | 51 | 2.5 |

[*1] Value taken from 25 $\mu$m Upilex-S

[*2] At room temperature

## 3.3 Thin film coatings

Thin film coatings on membranes for space applications are known from MLI materials. They are used to adjust thermal-optical properties and as protection from the space environment. Commonly used are coatings such as aluminum, silver and gold as well as indium tin oxide oxide as offered by Multek Corporation (60). In precursor DLR projects in the field of solar sailing, the use of silicon dioxide and titanium dioxide coatings on top of an aluminum coating was considered and patented by Görlich and Lura (88), but not further studied. In further pursuing this work, the focus of the studies presented here is on coating combinations of these materials. Furthermore, both sides of the sail should have the same thermo-optical properties and therefore the same coating. In principle a design could provide a high spectral reflectance, possibly throughout the spectrum, on the side directed towards the sun and a radiator backside. This is a good design

in case the attitude of the sail is well controlled and attitude maneuvers always ensure that the backside is not directed toward the Sun. For an uncontrolled sail such as Gossamer-1 or first solar sails, such a design is not suitable as it involves the risk that the backside is directed toward the Sun which could lead to temperatures that exceed material limits.

### 3.3.1 Aluminum

For metals, the binding energy of atoms is much higher than the energy of the AO of 5.3 eV. According to Ziegler (74) aluminum has a binding energy of 28.36 eV and thereby does not degrade due to AO. This is also stated in ECSS (89). Therefore, a thin Al-layer may be considered as a perfect protection coating against AO exposure.

Aluminum provides limited shielding against VUV radiation. Employing the Beer-Lambert law with an absorption coefficient $\alpha_\lambda$ for a wavelength of 30 nm (Rakić (90)) yields to a coating thickness of 1.5 $\mu$m in order to shield 99% of the intensity of that wave length.

The aluminum coating provides a good mirror-like reflective surface and is therefore often considered as solar sail material. The studies of Sznajder et al. (71, 72) showed that under proton radiation, the reflectivity decreases or the solar absorptance increases, respectively. A recombination of the protons with free electrons in the aluminum layer forms hydrogen bubbles. A pure aluminum coating is therefore not suitable for solar sailing.

Aluminum has a relatively high $\alpha_S/\epsilon_t$ ratio. It strongly depends on the surface quality and also on the quality of the measurement. It was measured at 2.5, but values in the order of 5 are also possible (UBE Compant Ltd. (85)). The above-mentioned proton degradation can further increase the ratio due to the loss of reflectance which increases the absorptance.

As a conductor, aluminum has very low electrical resistance. The measured surface resistance is about 243 $\Omega_\square$ (see Table 3.3).

### 3.3.2 Silicon dioxide

As stated in Minton et al. (67), silicon dioxide ($SiO_2$) is relatively unreactive to AO. For instance, $SiO_2$-coated polyimide surfaces with a thickness of 130 nm have demonstrated erosion yields against AO as low as $\sim 0.1 - 0.2\%$ of unprotected polyimide. Shimamura et al. (91) state an EY of $0.42 \cdot 10^{-25}\,\mathrm{cm^3 AO^{-1}}$ for this material.

With respect to VUV protection, $SiO_2$ shield short wavelength in a narrow wavelength bend around 30 nm to 100 nm. According to Kitamura et al. (92) the absorption coefficient is $0.23 \times 10^6$ at 30 nm.

$SiO_2$ does not have free electrons. In consequence, a hydrogen recombination as it appears in aluminum is not present. In order to protect a layer underneath from proton irradiation, the minimum $SiO_2$ thickness calculated with the SRIM software (Ziegler (74)) is at least 280 nm thick.

Coated polyimide films are investigated in the context of their thermo-optical properties change under space conditions in Silverman (93). It has been indicated that $SiO_2$ coating changes its solar absorptance and thermal emittance slightly. Considering that $SiO_2$ is quartz glass, it is known from everyday life that it is transparent in the visible spectrum but not in the infrared spectrum (greenhouse effect). In the infrared spectrum it mainly absorbs and reflects. According to haltec GmbH (94) the infrared emissivity of quartz glass is about 0.75. An $SiO_2$ layer on top of a metallic surface is known as second surface mirror. This principle is frequently used to build radiators for spacecraft Donabedian and Gilmore (80, pp. 140–141). It is illustrated in Figure 3.6. It should be noted that the standard second surface mirrors are much thicker then the coatings considered here, up to 0.25 mm.

$SiO_2$ is an electrical non-conductive material and cannot provide suitable antistatic properties with respect to ESD protection (Gouzman et al. (95)).

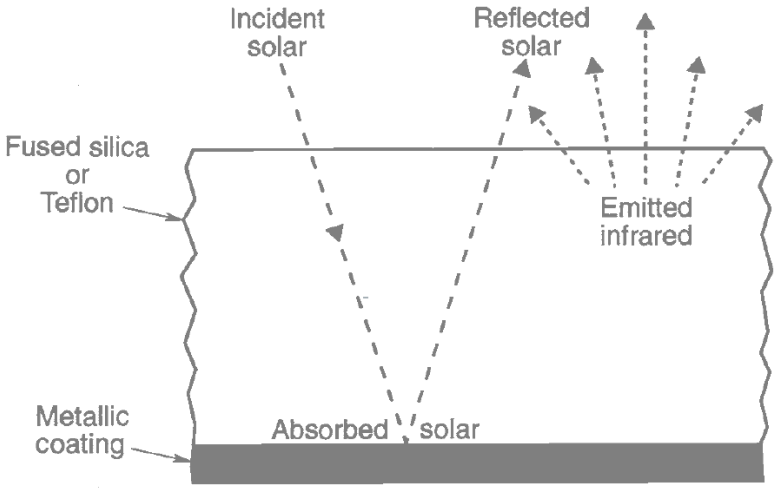


Figure 3.6: Illustration of a second surface mirror Donabedian and Gilmore (80, p. 143)

### 3.3.3 Titanium dioxide

It has been observed in Gouzman et al. (95) that titanium dioxide ($TiO_2$) coatings crack during AO exposure. However the chemical composition of the coating has not been changed and cracking does not induce the substrate degradation. Banks et al. (96) state an EY of $1.01 \cdot 10^{-25}, \mathrm{cm}^3\mathrm{AO}^{-1}$.

The samples which have additional protective $TiO_2$ coating exhibit substantially less mass loss against VUV radiation (Minton et al. (67)) than without the coating. The $TiO_2$ coating reduces the flux of VUV radiation that can reach the substrate and as consequence the release of volatile products. The mass loss of the $TiO_2$ coatings thicker than 6.0 nm exposed to VUV radiation is negligible ( according to Minton et al. (67) for radiation in the wavelength range 110 - 200 nm, approx. 8 solar constants, exposure time of 900 min.) It has been measured in Minton et al. (67) that $TiO_2$ thickness of 12.5 nm absorbs only 30% of the incident VUV radiation. The rest of it is transferred to the substrate and as a result it causes photodegradation and possibly a delamination between the coating and the substrate. With an absorption coefficient of $10^6\,\mathrm{cm}^{-1}$ in the wavelength range of 200-300 nm (Jellison Jr. et al. (97)), a 100 nm thick $TiO_2$ coating could almost completely block incident UV radiation in that range (Gouzman et al. (95)).

$TiO_2$ does not have free electrons, and in consequence a hydrogen recombination as it appears in aluminum is not present. In order to protect an underneath layer from 8 keV protons the minimum $TiO_2$ thickens calculated with the SRIM software (Ziegler (74)) is 175 nm thick.

$TiO_2$ is often used in white paint for thermal control surfaces in a thermal design. Such paints are diffuse reflectors with an $\alpha_S$ of about 0.2 and an $\epsilon_t$ of about 0.9 (Donabedian and Gilmore (80)). As a thin coating it appears transparent but causes changes in the reflectance throughout the spectrum from short Ultra Violet (UV) to long Infrared (IR).

Titanium dioxide is a wide band semiconductor that can prevent an ESD. Daniyan et al. (98) measured the sheet resistance of thin (tens of nm) $TiO_2$ layers covered glass and ITO substrates. The typical resistance value of the layers made through the use of a commercial $TiO_2$ powder on glass substrate is $2.23 \times 10^3\ \Omega\ \mathrm{sq}^{-1}$ and on Indium Tin Oxide (ITO) it is approximately 10 $\Omega$ $\mathrm{sq}^{-1}$. The values were measured at room temperature. That experimental results indicate that the resistance strongly depends on type of the substrate.

### 3.3.4 Coating combination

Considering the various requirements for solar sail material a combination of coatings is required. Therefore samples were investigated regarding thermal-optical properties and electrical resistance.

The samples were manufactured by the Fraunhofer FEP in a magnetron sputtering process with the coFlex® 600 film coating machine. It is a so called roll-to-roll process, where the substrate material comes on a roll and is directly fed into the machine, and the coated material is coiled on a roll again. This method is particularly suitable for mass production, which is required for the amounts of foil needed to build a solar sail or even a small deployment demonstrater like the Gossamer-1. The maximum width of the roll that can be processed in this machine is 700 mm. The properties of the coated material are summarized in Table 3.3. The spectral reflectance of the different coatings is shown in Figure 3.7. It needs to be pointed out that a coating thickness of $SiO_2$ and $TiO_2$ of more then 200 nm, for a single as well as a combined coating, is brittle and tends to crack. Thicker coatings should therefore be avoided. For wavelength in the order of the coating thickness interference phenomena between the incoming wave and the reflected wave are present. This leads to oscillations of the measured spectral reflectance in the measured near UV range and possibly for shorter wavelength as well.

For the solar sail, a specular reflective surface is required, and the only viable option for this is an aluminum coating. The pure aluminum coating has a low electrical resistance but a high $\alpha_S/\epsilon_t$ ratio that leads to high temperatures. In addition, it does not provide good VUV protection of the substrate and protons degrade the surface by recombining with the free electrons to hydrogen.

An additional 100 nm $SiO_2$ coating on top of the aluminum only slightly changes the reflectance in the visible spectrum and in consequence, $\alpha_S$ does not change significantly. This is expected because $SiO_2$ is not only transparent in the visible spectrum but also the coating thickness of 100 nm is small compared to the wavelength and therefore all longer wavelengths easily pass through this layer without wave interference phenomena within the coating layer. In the infrared spectrum, the reflectance drops significantly in the wavelength range between 7600 nm to 15000 nm, which shows the good emitting properties of $SiO_2$. In consequence, $\epsilon_t$ increases by a factor of 10 and thereby the $\alpha_S/\epsilon_t$ ratio is significantly decreased. As an electrical isolator, $SiO_2$ rapidly increases the electrical resistance. Apparently, for very thin coatings on the order of a 100 nm, the current is still transferred through the $SiO_2$ layer into the aluminum, while for a coating thickness of 500 nm the $SiO_2$ completely isolating the aluminum.

An additional 100 nm of $TiO_2$ coating on top of the aluminum slightly changes the reflectance in the visible spectrum. Even for such a thin coating layer the reflectivity of between 500 nm and 1500 nm already significantly decreases, and thereby solar absorptance $\alpha_S$ increases. The decrease of reflectance in this wavelength range is of course a significant disadvantage for the performance of a solar sail. Thicker $TiO_2$ should therefore be avoided. In the infrared spectrum the additional 100 nm $TiO_2$ lead to a very constant 85% reflectance nearly throughout the whole infrared spectrum. That also means that the material has a certain capability of emitting in the infrared spectrum. This decreases the $\alpha_S/\epsilon_t$ ratio overall compared to a pure aluminum coating, but not as strong as $SiO_2$. With $TiO_2$ as a semiconductor the electrical resistance is very low. Especially for thin coatings on top of the aluminum, electrical currents are transferred through both materials. It is even lower than the one measured for the pure aluminum coating. This can be explained when considering that the formation of aluminum oxide, which has a higher resistance, is prevented. Aluminum and $TiO_2$ are coated in one vacuum process. That means that during the manufacturing process, the generation of aluminum oxide is avoided and after the manufacturing, the aluminum is shielded from the atmospheric oxygen by the $TiO_2$. When the coating gets thicker an electrical current is increasingly transferred through the $TiO_2$ that results in an increase in the electrical resistance.

A coating combination of 100 nm $SiO_2$ and 100 nm $TiO_2$ on top of the aluminum only slightly decreases the reflectance in the visible spectrum or increases $\alpha_S$, respectively. The $TiO_2$ infrared reflective properties throughout the infrared spectrum also yields a more homogenous reflectance of the coating combination with an overall decrease in the infrared reflectance or increase in $\epsilon_t$, respectively. An interesting observation is that the coating combination leads to an increase of

$\epsilon_t$ by a factor of 20. That is more than one of the single coatings on top of the aluminum could achieve, even for thicker coatings. The $TiO_2$ top layer provides limited, but for ESD protection sufficient, electrical conductivity.

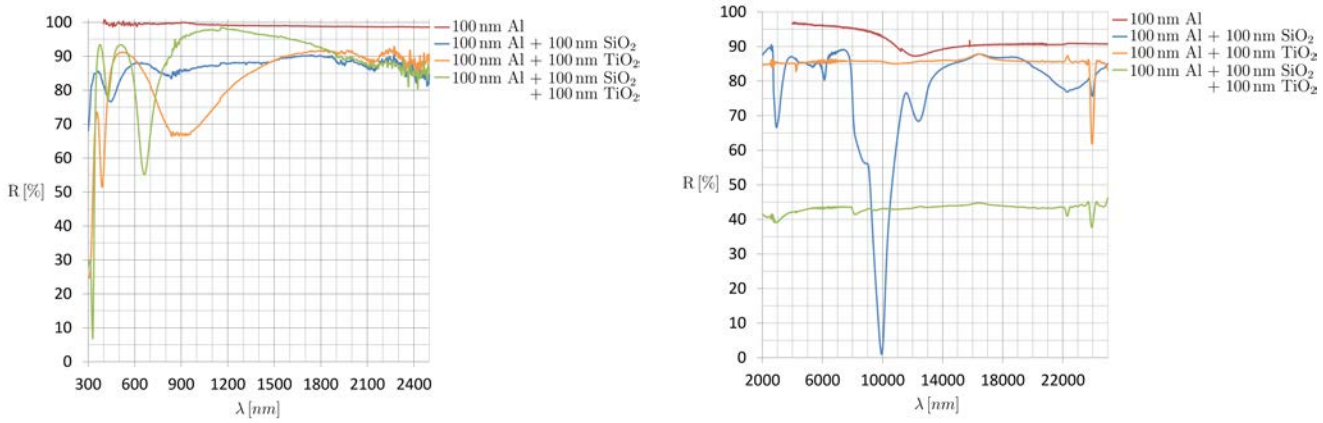


(a) Reflectance Near Ultraviolet (NUV)-Visible-NIR.

(b) Reflectance IR.

Figure 3.7: Spectral reflectance of different coating combinations.

Table 3.2: Atomic oxygen erosion yield and absorption coefficients for Al, $SiO_2$ and $TiO_2$

| Material Type | EY [$cm^3AO^{-1}$] | $\alpha_\lambda$ [$cm^{-1}$] for ($\lambda$ [nm]) |
|---|---|---|
| $SiO_2$ | $0.42 \cdot 10^{-25}$ | $0.23 \cdot 10^6$ (30.0) |
| $TiO_2$ | $1.01 \cdot 10^{-25}$ | $1.00 \cdot 10^6$ (200) |
| Aluminum | 0 | $0.03 \cdot 10^6$ (30.0) |

Table 3.3: Thermal properties and surface resistance of aluminum based coating combinations (Al, $SiO_2$ and $TiO_2$)

| Material Type | $\alpha_S$ | $\epsilon_t$ | $\alpha_S/\epsilon_t$ | $R_\square$ [$k\Omega_\square$] |
|---|---|---|---|---|
| Al | 0.066 | 0.026 | 2.538 | 243 |
| Al+100 nm$SiO_2$ | 0.127 | 0.275 | 0.462 | 409 |
| Al+500 nm$SiO_2$ | 0.122 | 0.244 | 0.500 | $\infty$ |
| Al+100 nm$TiO_2$ | 0.173 | 0.143 | 1.209 | 0.155 |
| Al+500 nm$TiO_2$ | 0.469 | 0.128 | 3.664 | 1.5 |
| Al+100 nm$SiO_2$+100 nm$TiO_2$ | 0.125 | 0.566[1] | 0.221 | 403 |
| Al+200 nm$SiO_2$+200 nm$TiO_2$ | 0.285 | 0.324 | 0.880 | 2910 |

## 3.4 Membrane bonding

The sail is manufactured from pre-coated polyimide foils. A welding process of thermoplastic materials (e.g. the Upilex-VT) is therefore not applicable because the coatings cannot be removed from the foil. Adhesive bonding was therefore considered from the beginning. Acrylic adhesives are known to be low out-gassing and temperature resistant. The transfer adhesive tape 966 with adhesive 100 from the company 3M is an adhesive that has been use for MLI manufacturing at the DLR for many years. Due to the good processability and thermal stability, all bonding processes during the membrane manufacturing are made with this tape. The data sheet specifies a temperature range between $-40°C$ and $232°C$. While the real application limits are still unknown,

[1] A measurement at DLR gave an $\epsilon_t$ value of 0.171.

the material has generally been proven in tests (see Section 7.2.1) to be applicable in a temperature range between −142°C and 232°C. Anyway, the limiting factor for the endurable temperatures is the adhesive, therefore these limits are also shown in Figures 3.3 and 3.4.

## 3.5 Conclusion

The evaluated coatings have a significant impact on the materials properties. It is possible to adjust several parameters in accordance with the possible requirements of one specific mission. A clear selection of one space sail material is difficult and, if at all, only possible for a particular mission. Gossamer-1 is a short-term mission in the LEO environment, while a solar sail mission would be long-term and in interplanetary space. In addition, financial aspects had to be taken into account in the Gossamer-1 project. In consequence, one question is can a low-cost LEO deployment demonstrator employ a relatively cheap off-the-shelf product like aluminum coated Upilex-S instead of foils with customized coatings. Furthermore, an attempt is being made to select a material and in particular a possible coating system that enhances the sail performance and could potentially enable solar sail missions that lead much closer to the Sun.

Aluminum coated polyimide foils are frequently used in LEO environment as MLI. The aluminum coating provides perfect protection of the polyimide against atomic oxygen and limited shielding against VUV radiation. It is therefore out of question that aluminum coated polyimide would survive a short-term mission of several month in this environment. The high $\alpha_S/\epsilon_t$ ratio results in high temperatures that need careful evaluation. The hot and cold case considered would appear, if at all, only for seconds during a real mission in LEO. Most of the time the temperatures are more moderate. The limiting factor seems to be the adhesive used for the manufacturing of the sail segments, however the absolute application limits are not yet known. As shown in Figure 3.3, the thermal limits of the adhesive are not exceeded for $\alpha_S/\epsilon_t$ smaller four. The cold case temperature is below the temperature range specified in the datasheet, but it was shown in precursor projects that it is still usable (DLR (99)). The reflective properties are not of interest as long as the sail is not utilized as a solar sail. Anyway, in low earth orbit the amount of particle radiation is negligible. Therefore, Gossamer-1 and other LEO demonstrators can use aluminized polyimides like the Upilex-S.

The high $\alpha_S/\epsilon_t$ and insufficient VUV shielding of the foil are very critical for solar sail missions, especially for those with a trajectory that leads close to the Sun. Furthermore, protons would decrease the reflectance of the aluminum over time and therefore the solar sail's propulsion capabilities. Additional oxide coatings also decrease the reflectance of the sail, and which coating thickness is really required as shielding and for the adjustment of thermal-optical parameters must be carefully evaluated. An upper limit for the coating thickness is the mechanical stability of the coating layer, which is only given for a thickness up to 200 nm with the manufacturing techniques currently employed. In order to provide limited electrical conductivity the top layer of the coatings considered here must be $TiO_2$. According to Equation 3.3 a 100 nm $TiO_2$ would shield 99.995% of the VUV radiation and for wavelength about 30 nm the $SiO_2$ would even provide additional shielding. An SRIM simulation shows that protons $< 8$ keV are shielded, which is a significant amount of the protons in interplanetary space. Still there are protons between 8 keV and 10 keV that get trapped in the aluminum and can cause degradation. Protons with an energy higher than 10 keV get trapped in the polyimide and can also cause degradation in this material. This degradation would decrease the mechanical properties of the polyimide over time, but this is considered to be a relatively slow process. Furthermore, the stress in the material is very low (see Chapter 6). The low $\alpha_S/\epsilon_t$ would potentially enable missions in a distance of 0.2 AU, which is within Mercury's sun orbit. The additional coating decreases reflectance $R_S$ to 87.5%, but considering the overall improvement that seems to be a good trade.

# Chapter 4

# Stowing and Deployment Strategy

Studies investigating how to stow membranes for space applications go back to the 1980s. Miura (100) already stated general requirements for the packaging of membranes for space applications. He recognized that besides all of the theoretical possibilities of folding membranes, it is most important that the "automatization of it cannot be attained unless the deployment process is simple and reliable to a considerable degree of extent. Thus simplification of the process is the utmost important requirement". This consideration has also driven the development presented here.

Miura (100) further described that folding and deployment are two phases of a reversible process. Reversible means that the chosen stowing strategy must allow an autonomous deployment in space. It should be supplemented after the stowed sail has withstood all launch loads, namely shock, vibrations and fast decompression. Such a qualification process is described in Chapter 7.2 and is presented in Seefeldt et al. (101). Furthermore the sail structure, which might not have reached its full stiffness during the deployment process, needs to withstand all deployment forces. Finally, the deployed membrane must be stabilized, e.g by the supporting structure or centrifugal forces.

In Section 4.1 an overview of commonly considered stowing techniques is provided. With respect to the differentiation of folding strategies, Miura (100) distinguished one-dimensional and two-dimensional folding techniques. The differentiation is made by the in-plane dimensions of the membrane that shrink due to the folding process. Due to the size of the membranes considered, it is of course always necessary to reduce both dimensions. As described in Section 4.1.1, this can be achieved by combining two one-dimensional folding processes or by employing an additional coiling of the previously folded membrane. The techniques described in Section 4.1.2 allow a simultaneous stowing of both dimensions.

In all projects described in Chapter 2 the sail membrane was split into triangular segments. This is a direct consequence of the necessity of supporting structures like booms. Furthermore, it significantly improves the manageability of the membrane on the ground during the integration process. Splitting the membrane into several segments or to dispense with this step is therefore another important aspect of the stowing strategy.

A new variation of a stowing and deployment strategy based on folding and coiling is presented in Section 4.2. In contrast to the other strategies, this one allows a slow and controlled deployment.

## 4.1 Stowing strategies overview

Frequently considered stowing strategies are summarized in Figure 4.1. Guest and Pellegrino (102) describe patterns allowing the wrapping of a membrane around a central hub, and De Focatiis and Guest (1
present different folding patterns based on the folding of tree leaves. Double zig-zag folding patterns sometimes referred to as frog-leg folding were employed, for example, by Leipold et al. (3)

and Stohlman et al. (104). A combined folding and central coiling of a sail membrane split into four triangular segments was implemented by Tsuda et al. (24) for JAXA's IKAROS sail and for a Cubesat sail by Wolff et al. (7).

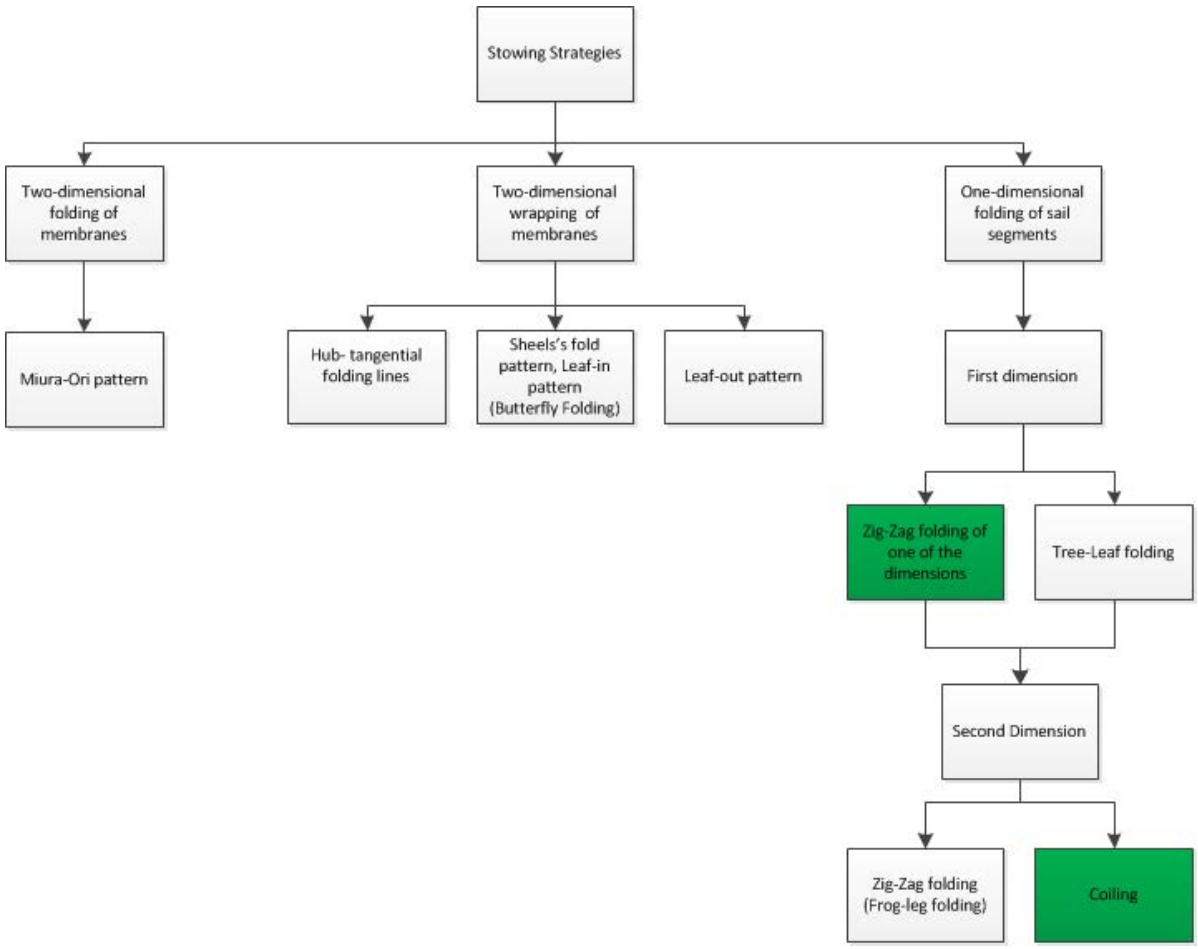


Figure 4.1: Overview of frequently considered stowing and deployment strategies.The strategy considered here is based on the green highlighted combination.

### 4.1.1 One-dimensional folding and coiling combinations

The most frequently considered stowing strategies use triangular sail segments and employ two stowing steps in which one dimension at a time is stowed.

Zig-zag folding parallel to the height (Figure 4.2(a)) or parallel to the hypotenuses (Figure 4.6(a)) of the triangular segment is commonly used. It is employed in all drag sail and solar sail projects presented in Chapter 2. An alternative to the zig-zag folding is the tree-leaf folding or L-folding as shown in Figure 4.2(b). These folding patterns are extensively described in De Focatiis and Guest (103) and Furuya et al. (105). After the first folding process, a folded membrane strip results as shown in Figure 4.6(b) (bottom, left).

In former projects like the ESA/DLR deployment demonstrator in 1999 (Agnolon (2)) additional zig-zag folding for the second dimension was used. As this is also a common origami pattern, the combination of two zig-zag foldings is often refereed to as frog-leg folding. Such a stowing strategy is also employed by the Deorbitsail drag sail CubeSat (Stohlman et al. (104)). Figure 4.4 shows the Deorbitsail stowing. In order to stow the folded sail, some kind of sail container is required. It should be pointed out that this stowing strategy presents one challenge. When the sail package is released, the sail is not under tension until the booms are fully deployed and thus a controlled deployment is more difficult to achieve.

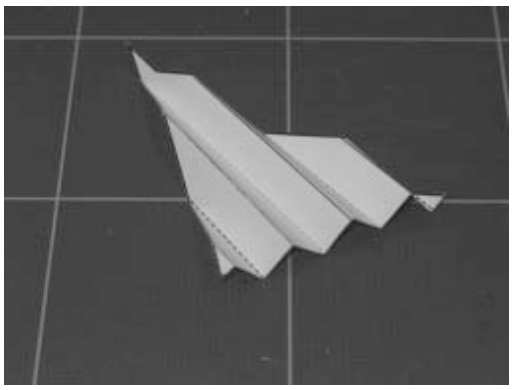

(a) Zig-zag folding Furuya et al. (105).

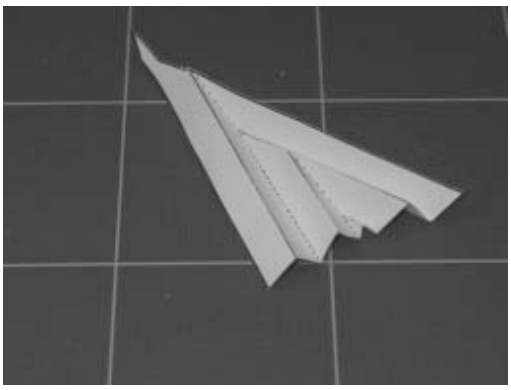

(b) Tree-leaf folding or L-folding Furuya et al. (105).

Figure 4.2: Examples for one-dimensional folding patterns.

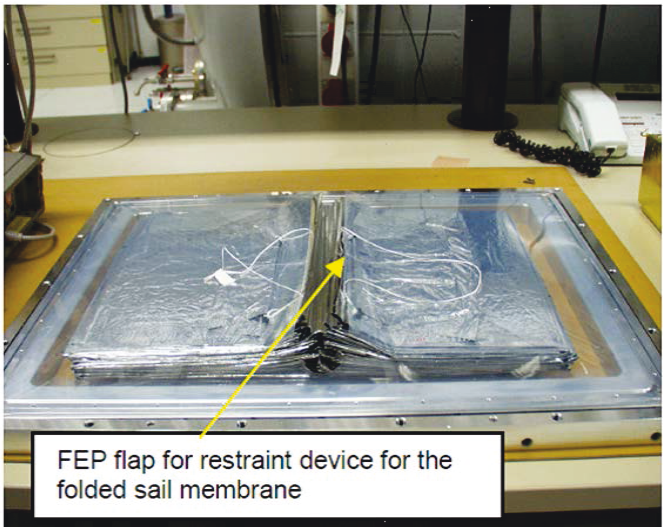


Figure 4.3: Double-folded triangular sail segment of the ESA/DLR solar sail demonstrator (Leipold et al. (4)).

An example from the solar sail field of application is IKAROS where the sail segments were coiled onto one single hub (Tsuda et al. (24)). In Figure 4.6 the space sailor stowing strategy is shown. The IKAROS deployment is shown in 4.5. The zig-zag folded segments are folded over in the second dimension. Finally, all folded segments are coiled onto one spool.

In recent CubeSat projects, the need for a most compact sail package resulted in a stowing strategy that allows stowing on one central hub. An example is the Space Sailors project (Wolff et al. (7)).

### 4.1.2 Two-dimensional folding and coiling combinations

Wrapping the membrane around a central hub is one example of a simultaneous stowing of both membrane dimensions. In this case the sail membrane cannot be split into several segments. It is a combined folding and coiling process. The folding is along spiraling crease lines which are tangential to the hub. Hub-tangential folding lines are described in Guest and Pellegrino (102). The simplest one is to fold along tangential lines as shown in Figure 4.7. These simple patterns can also be combined with tree-leaf folding as presented in De Focatiis and Guest (103).

The leaf-in pattern also refereed to as Scheels Folding or Butterfly Folding also uses leaf folding patterns for the hub-tangential folding lines. The leaves point inwards towards the center. The

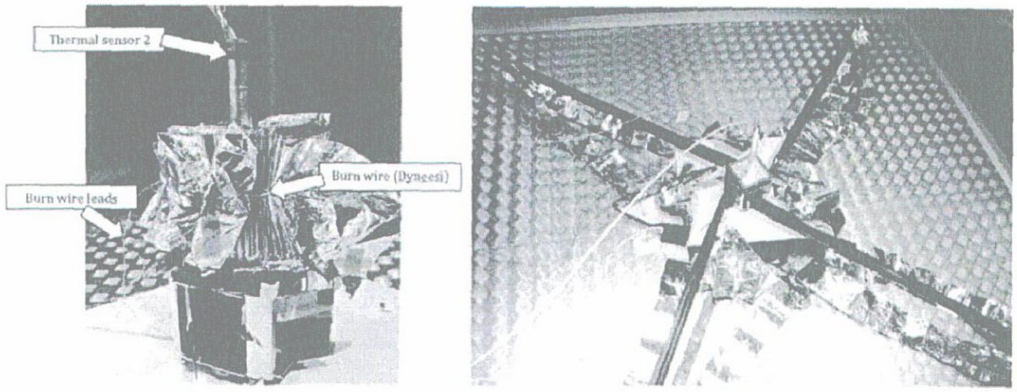


Figure 4.4: Double folded triangular sail segments of the Deorbitsail (Stohlman et al. (104)).

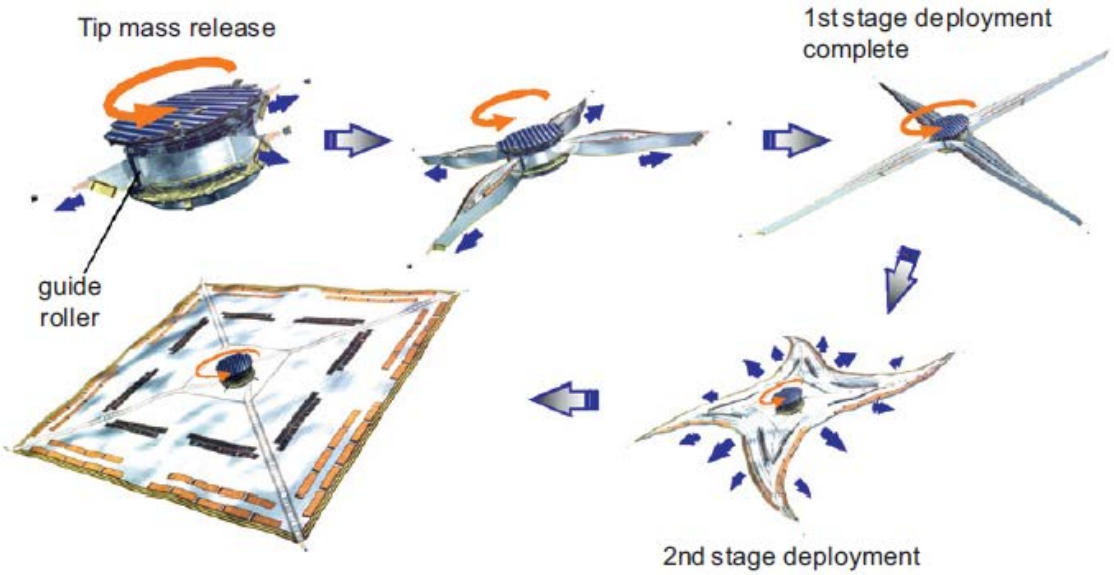


Figure 4.5: IKAROS deployment sequence (Tsuda et al. (24)).

pattern is shown in Figures 4.8(a) and 4.8(b).

For the leaf-out pattern, the leaves point outwards from the center. To reduce the size of the folded structure to a minimum, it must achieve the maximum of overlaps in the folding panels. The optimum shape is an $n$-sided polygon. A typical deployment is shown in Figures 4.9(a) and 4.9(b).

Other variants of leaf patterns are the skew leaf-in pattern and leaf-in pattern. They are achieved by a change in angle $\alpha$ where the number of leaves are the same. Furthermore, the structure of the leaf-in pattern is in contrast to the skew leaf-in pattern unable to fold fully closed. The angle can be varied according to the following formula:

$$\alpha = r \cdot \left(\frac{\pi}{2} - \frac{\pi}{n}\right), \quad 0 \leq r \leq 1 \tag{4.1}$$

Figure 4.10(b) shows that the deployment of the skew leaf-in pattern is smoother than the leaf-in pattern.

Miura's folded map is an extreme form of skew leaf-in pattern for $n \to \infty$. The pattern was applied for the stowing of solar arrays (Miura (100)).

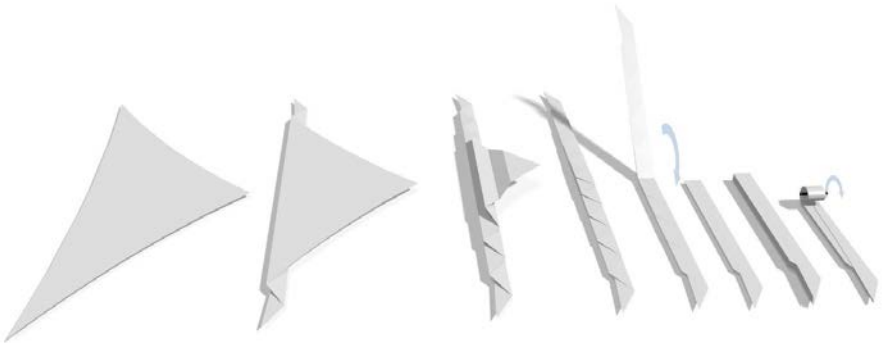

(a) Stowing strategy Space Sailor project.

(b) Manufacturing and stowing of the Space Sailors' drag sail.

Figure 4.6: The CubeSat drag sail of the REXUS student group Space Sailors.

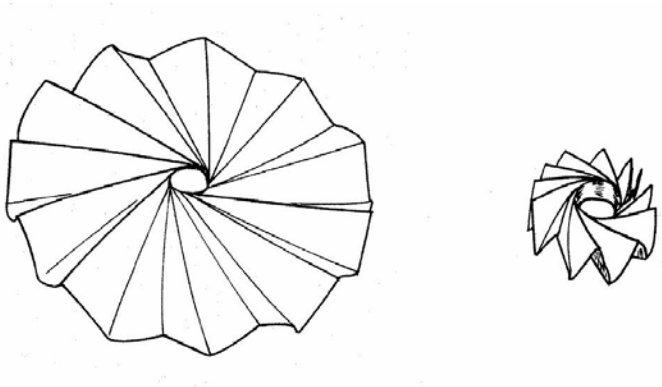

Figure 4.7: Simple wrapping pattern (Guest and Pellegrino (102)).

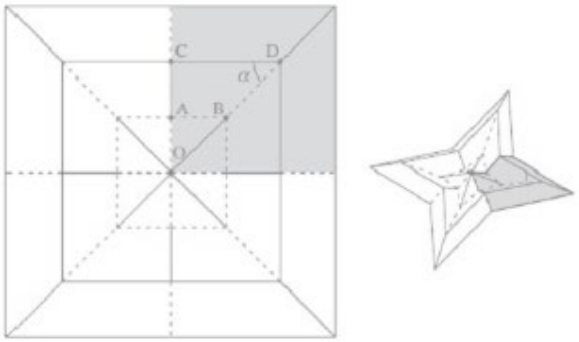


(a) Leaf-in folding pattern.

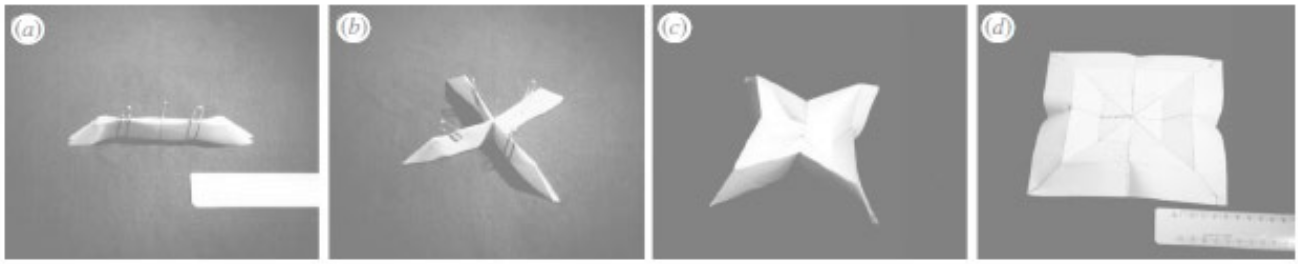


(b) The Deployment of the Leaf-in pattern.

Figure 4.8: Leaf-in folding for a rectangle with four leaves and three segments on either side of the midrib (De Focatiis and Guest (103)).

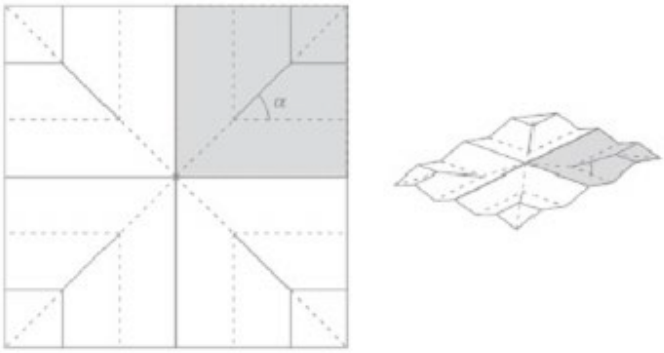


(a) Leaf-out folding pattern.

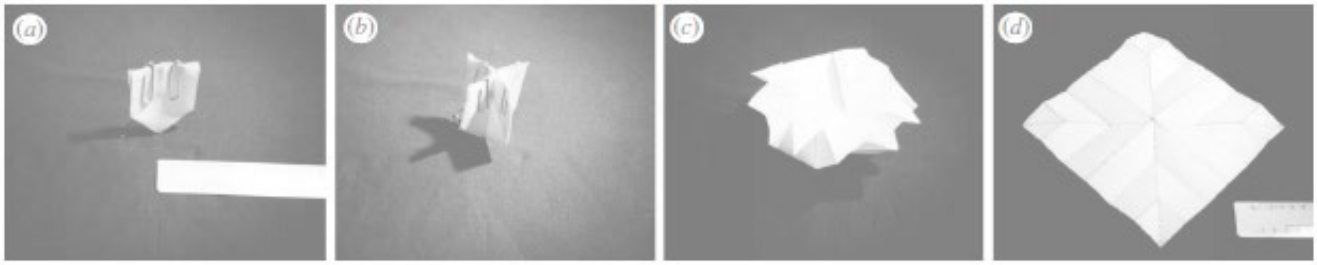


(b) The Deployment of the Leaf-out pattern.

Figure 4.9: Leaf-out folding for an rectangle with four leaves and three segments on either side of the midrib (De Focatiis and Guest (103)).

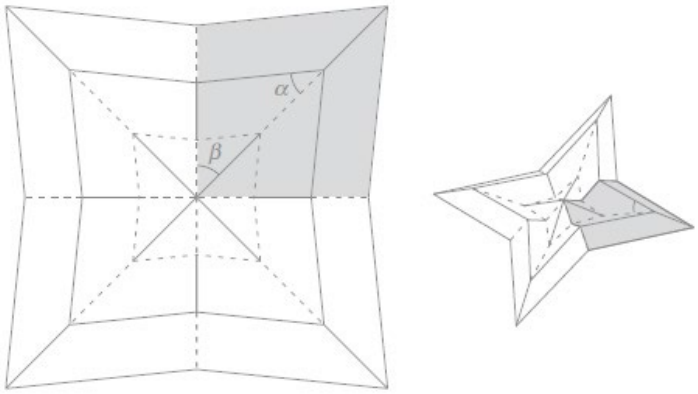


(a) Skew Leaf-in folding pattern.

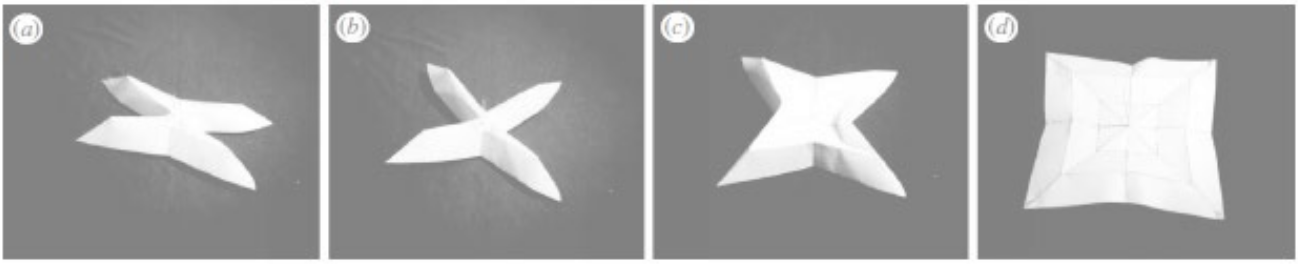


(b) The deployment of the skew leaf-in pattern.

Figure 4.10: Skew leaf-in folding for a rectangle with four leaves ($n = 4$), three segments on either side of the midrib, $r = 8/9$ and $\alpha = 40°$. The pattern shown is defined by $n = 4$ (De Focatiis and Guest (103)).

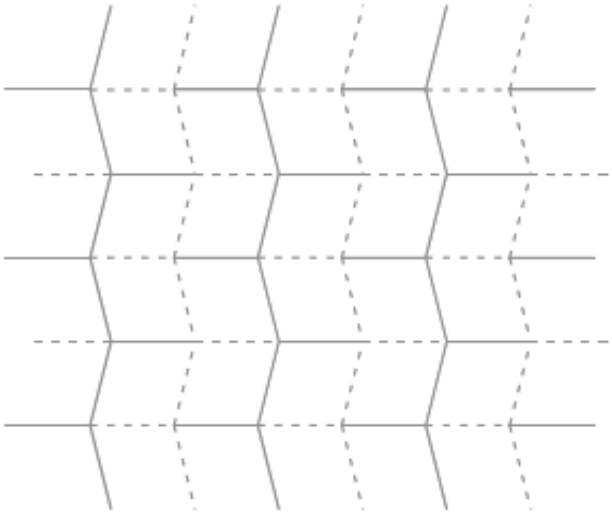

Figure 4.11: Miura's folding pattern (Miura (100)).

## 4.2 A stowing and deployment technique for large membrane space systems

This section provides the technical description including a mathematical model of a new innovative deployment strategy for large membranes. The here presented content was published in the reviewed scientific journal Advances in Space Research (Seefeldt (11)).

One of the first considerations for a stowing technique was that rectangular, non-folded areas for the photovoltaics, were needed. Additionally, it was required that the photovoltaic strings are mounted such that they were lying face to face on each other. This resulted from electrical insulating considerations. Therefore, the specific peculiarities of the photovoltaics alone already caused the consideration of a combined folding and coiling strategy.

In a first attempt, the sail deployment mechanism was supposed to be part of the central spacecraft unit. Therefore the stowing strategy shown in Figure 4.12 was chosen, where each sail segment was coiled on one spool. While a derivation of this strategy, for which all folded segments

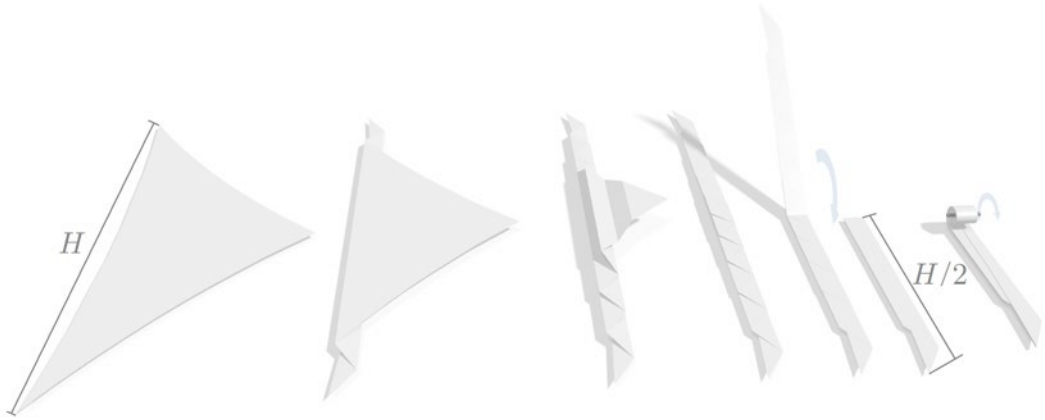


Figure 4.12: First idea for a sail stowing strategy with deployment mechanisms mounted on the central spacecraft unit.

were coiled on one spool, was successfully employed for a CubeSat sail (see Wolff et al. (7)), it was not compliant with the requirement of a controlled deployment. The folded sail segments have a length of $H/2$, where $H$ is the hypotenuse of the sail segment. When the booms are deployed to this length, the complete sail segment slides off of the spool. One can observe this behavior during the deployment of a $2\,\mathrm{m}^2$ sail on a REXUS sounding rocket shown in Figure 4.13. The two small pictures in the second row show the booms not yet fully deployed but with the complete sail segments already off the spool and not tensioned.

What is not a problem with a small $2\,\mathrm{m}^2$ sail in a highly dynamic deployment process (deployment time less than a second) becomes difficult to handle with a sail off several tenths or even hundredths of square-meters deployed in about 20 to 30 minutes or even longer. Considering one of the segments is a rectangular triangle representing one quarter of the full sail allows an estimation of the length not spanned along the hypotenuse. If the booms are deployed to a length of half the sail segments hypotenuse length $H/2$, the distance $d$ between the boom tips is

$$d = \sqrt{2 \cdot \left(\frac{H}{2}\right)^2} \approx 0.7 \cdot H \ . \tag{4.2}$$

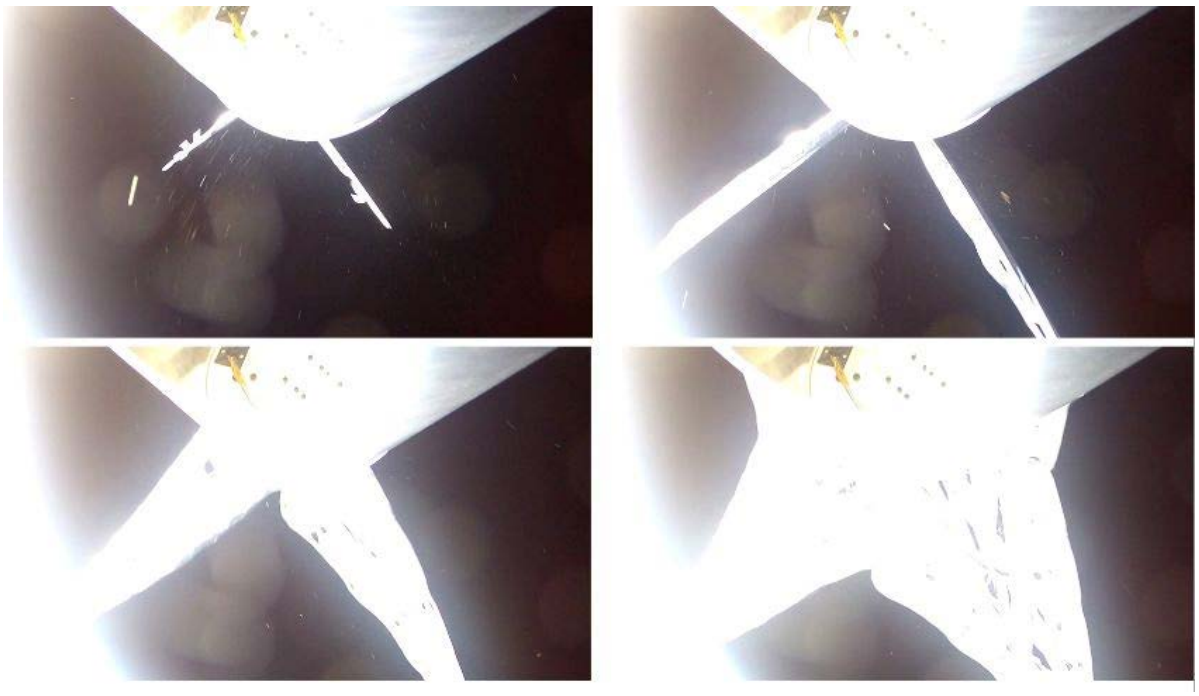

Figure 4.13: Space Sailor's drag sail deployment.

In other words, $0.3H$ is not tensioned at this point and is free to drift due to e.g. drag and get potentially twisted and jammed with itself or other spacecraft parts. Considering Gossamer-1 with a 5 m × 5 m, this results in 1.5 m free sail length and for a 50 m × 50 m sail it is of course 15 m. This obvious disadvantage led to a rethinking of the stowing and deployment technique.

Taking that under the given geometric constraints (e.g. crossed booms) triangular sail segments are chosen, it is apparently necessary to deploy the full length of the hypotenuse at the end of the deployment process.

Pursuing the goal of having a controllable configuration during the deployment, the main difference with the Gossamer-1 deployment strategy is that the membrane is stowed on four deployment units that, during deployment, move away from the central unit (the center of the deployed sail). Figure 4.14 illustrates the deployment process. By uncoiling the booms, the deployment units move outwards, thereby deploying the sail segments simultaneously. After the sail deployment is completed, the sail segments are separated from the deployment mechanism and the deployment units are jettisoned. The triangular segments are first zig-zag folded and then coiled onto two spools starting from the outer edges (see Figure 4.16). The spools are mounted on two neighboring BSDUs (see Figure 4.14(a)).

### 4.2.1 Mathematical model of the stowing process

For the analysis, a paper model scaled 1:30 of one sail segment was made, as shown in Figure 4.16. The figure also provides the symbols used and coordinate systems.

When implementing the zig-zag folding, the result is a sail stripe with $n_f$ folding lines and $n_f + 1$ layers of foil. The hypotenuse is coiled on the spool, together with all of the other layers of the folded sail to a spiral like geometry as

$$l_{h_{coiled}} = \begin{pmatrix} l_{h,x_s} \\ l_{h,y_s} \end{pmatrix} = \begin{pmatrix} r(\alpha) \cdot cos(\alpha) \\ r(\alpha) \cdot sin(\alpha) \end{pmatrix} . \tag{4.3}$$

The cathetus translates into a zig-zag line running up and down along width $w$ of the folded sail segment with pitch angle $\phi$. The slope $tan(\phi)$ in the case presented here is one because the

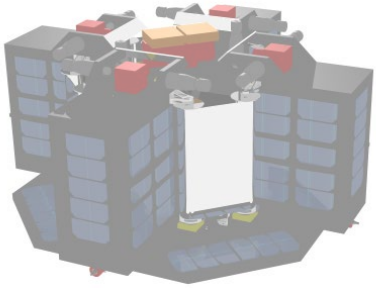

(a) Launch configuration

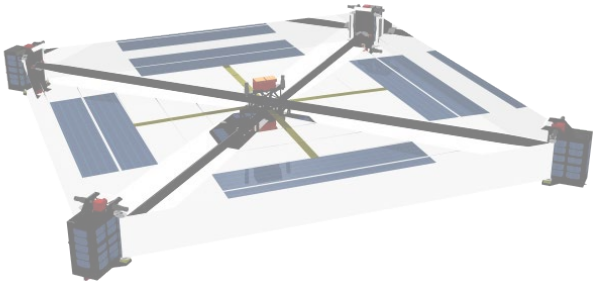

(b) During deployment

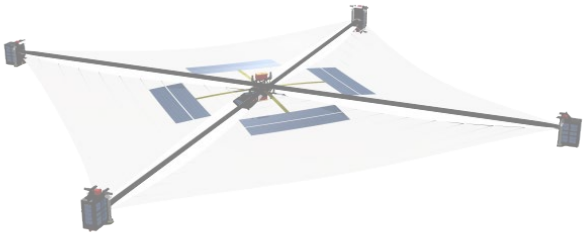

(c) Deployed

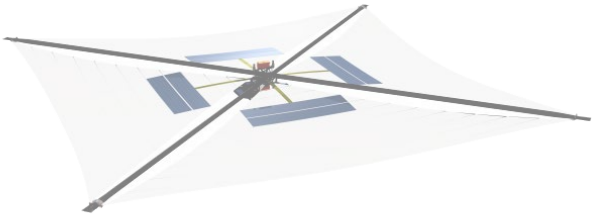

(d) Deployed and mechanisms jettisoned

Figure 4.14: Gossamer-1 deployment sequence.

sail segment represents an isosceles right triangle. The alternating point appears at $y_f = 0$ and $y_f = w$ in a $x$-distance of every $w$ (isosceles right triangle).This zig-zag line may be described as

$$l_c(x_f) = \frac{w}{\pi} \cdot cos^{-1}\left[cos\left(\frac{2 \cdot \pi}{2 \cdot w} \cdot x_f\right)\right] . \tag{4.4}$$

This gives an algebraic expression without the need for piecewise affine linear mapping. When coiling this sail stripe, the zig-zag line segments translate into a helix which alternates up and down along the sail coil height respectively the width $w$. A helix with varying radius $r$ and an alternating slope is described by

$$l_{c_{coiled}} = \begin{pmatrix} l_{c,x_s} \\ l_{c,y_s} \\ l_{c,z_s} \end{pmatrix} = \begin{pmatrix} r(\alpha) \cdot cos(\alpha) \\ r(\alpha) \cdot sin(\alpha) \\ l_{c,z_s}(\alpha) \end{pmatrix} . \tag{4.5}$$

The varying radius is influenced by several parameters like:

- the materials thicknesses (foil, photovoltaic, harness, adhesive),
- the folding pattern by which several layers add up to the total thickness,
- the sail package that is not fully compressed.

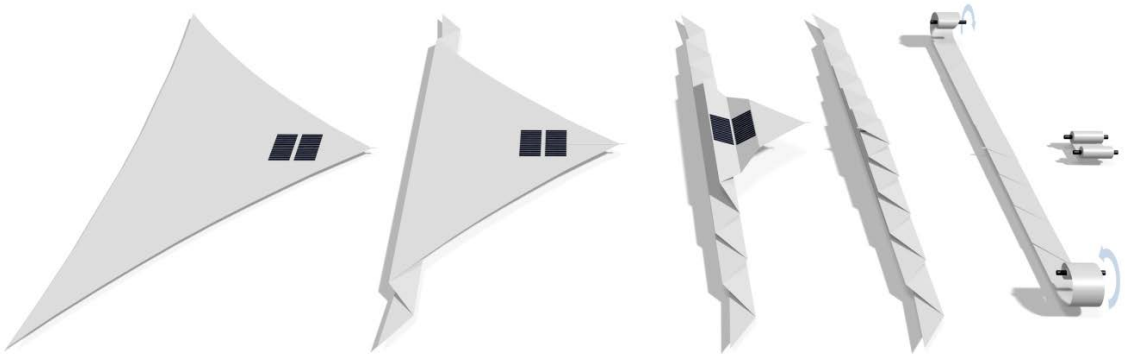

Figure 4.15: Gossamer-1 sail stowing strategy for one of the four segments.

When summarizing the volume according to Table 6.1, it is found that the material that is coiled on the spool would ideally occupy a volume of $1.436 \cdot 10^{-4}\,\mathrm{m}^3$. In reality, when coiling the sail on the Gossamer-1 spool with a radius of 17.5 mm (the inner radius of the coil), it is found that the outer radius is about 30 mm. With a folding width of 230 mm this equals a volume coiled on two spools of $8.576 \cdot 10^{-4}\,\mathrm{m}^3$. Due to the sail segment that is not fully compressed, the real volume is about six times bigger than the theoretical one. From the above stated parameters, this is clearly the most dominant one. In consequence, the mathematical model of thickness $t$ of the folded segment can be simplified as shown in Figure 4.17(a) into a linear variation with slope $m$ as

$$\frac{dt}{d\left(\frac{H}{2} - x_f\right)} = m\,. \tag{4.6}$$

When coiling the folded sail segment onto a spool, the thickness of the folded sail segment translates into a change of radius and $x_f$ translates into an arc length. The spiral geometry is shown in Figure 4.17(b). This leads to the following approach for a mathematical model of the spiral:

$$\begin{aligned} \frac{dt}{d\left(\frac{H}{2} - x_f\right)} \overset{!}{=} \frac{dr}{\sqrt{dr^2 + r^2 d\alpha^2}} &= c \cdot m \\ \Leftrightarrow \frac{dr}{r} &= \frac{m \cdot c}{\sqrt{1 - (m \cdot c)^2}} d\alpha \end{aligned} \tag{4.7}$$

The factor c is introduced here as a correction factor that takes into account that the sail package is not fully compressed. It is used to fit the spiral to the empirically evaluated geometry of the folded and coiled sail. The volume achieved after coiling is bigger than the one of the folded membrane, and much bigger than the volume that would be occupied by the material alone.

By separation of variables and integration, the mapping from angle to radius is achieved, which leads to a logarithmic spiral that is described as

$$r(\alpha) = r_i \cdot e^{\pm \frac{m \cdot c}{\sqrt{1-(m \cdot c)^2}} \cdot \alpha}\,. \tag{4.8}$$

The sign of the exponent indicates the coiling direction which differs for the two spools used for the coiling. The factor before the exponential factor defines the inner radius of the coil which is the radius $r_i$ of the spool on which the folded sail is coiled on.

In the further analysis it is assumed that the uncoiling points of the hypotenuse and the cathetus are always on the radius $r$ according to Equation 4.8. In this respect, the thickness of the folded sail package is neglected. Factor $c$ is calculated such that for the maximum coiling angle the maximum radius as well as the maximum coiled hypotenuse length are achieved.

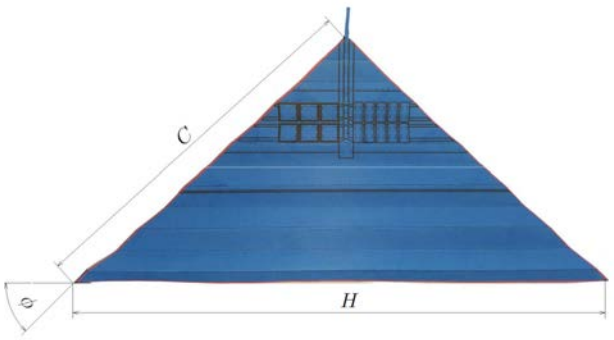


(a) Sail segment uncoiled and unfolded (deployed).

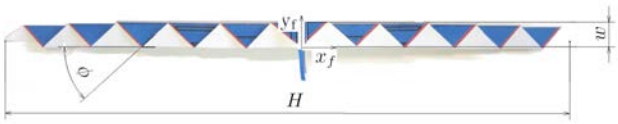


(b) Folded segment.


(c) Coiled segment with folding openings on the inside of the coil as used for the Gossamer-1 project.

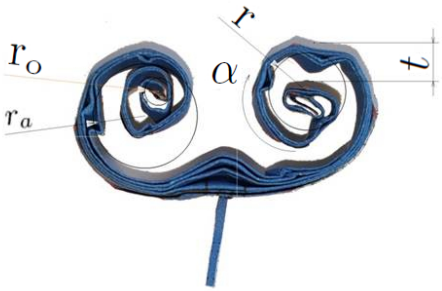


(d) Alternatively coiled segment with folding openings on the outside of the coil.

Figure 4.16: Paper model of a sail segment, scale 1:30 with symbols for the basic dimensions.

When coiling the folded sail segment on the spool, the layers of multiple windings are lying on top of each other. If it would be taken very exactly, one would have to differentiate between the first rotation on the circular spool and the next rotations where the layers are coiled on each other. Although it is not presented here it can be stated that the computation is also possible taking different and more complex descriptions of spiral geometries into account. The impact on the results in Section 6.3.2 is negligibly small, while the mathematical description becomes more confusing.

Taking Equation 4.7 into account, the function of the zig-zag line according to Equation 4.4 can be described as a function of the coiling angle $\alpha$ by taking into account that

$$d\left(\frac{H}{2} - x_f\right) = \sqrt{dr^2 + r^2 \cdot d\alpha^2}, \tag{4.9}$$

and thereby

$$\begin{aligned}
\frac{H}{2} - x_f &= \frac{1}{\sqrt{1-(m\cdot c)^2}} \int_0^\alpha r(\alpha)\, d\alpha \\
&= \frac{1}{\sqrt{1-(m\cdot c)^2}} \int_0^\alpha r_i \cdot e^{\pm\frac{m\cdot c}{\sqrt{1-(m\cdot c)^2}}\cdot\alpha}\, d\alpha \\
&= \pm\frac{r_i}{m\cdot c} \cdot \left(e^{\pm\frac{m\cdot c}{\sqrt{1-(m\cdot c)^2}}\cdot\alpha} - 1\right) \\
\Leftrightarrow x_f &= \frac{H}{2} \mp \frac{r_i}{m\cdot c} \cdot \left(e^{\pm\frac{m\cdot c}{\sqrt{1-(m\cdot c)^2}}\cdot\alpha} - 1\right) \ .
\end{aligned} \tag{4.10}$$

The zig-zag line as a function of coiling angle $\alpha$ is achieved by replacing variable $x_f$ in Equation

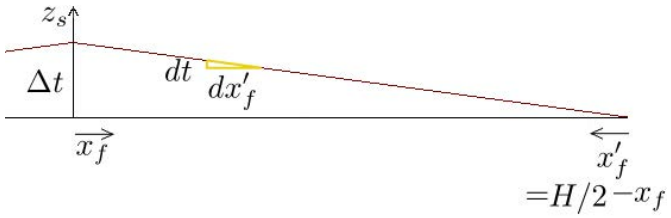


(a) Simplified geometry of the folded sail with linearly varying thickness.

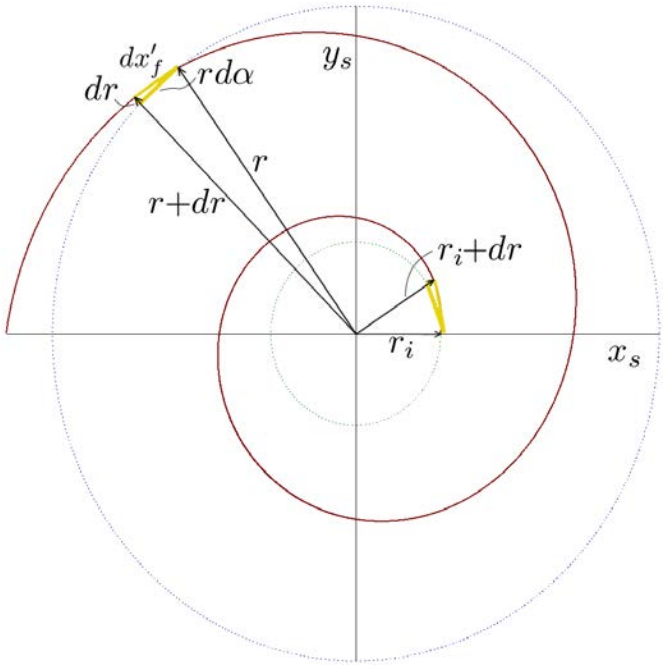


(b) Simplified spiral geometry of the coiled sail.

Figure 4.17: Geometry simplification for the transformation from the folded to the coiled configuration.

4.4 accordingly, it is

$$l_{c,z_s}(\alpha) = \frac{w}{\pi} \cdot cos^{-1}\Bigg\{cos\Bigg[\frac{\pi \cdot H}{w \cdot 2} \mp \frac{\pi \cdot r_i}{w \cdot m \cdot c} \cdot \left(e^{\pm \frac{m \cdot c}{\sqrt{1-(m \cdot c)^2}} \cdot \alpha} - 1\right)\Bigg]\Bigg\} - \frac{w}{2} \,. \tag{4.11}$$

The last term moves the zero point to the middle of the spool (see Figure 4.18), which is the considered mounting position of the inner edge.

With Equations 4.8 and 4.11 the folded and coiled cathetus of the sail segment is described by the helix with alternating slope according to Equation 4.5.

The previously derived equations apply for both coiling directions shown in Figure 4.16(c) and 4.16(d). Two adjacent booms deploy with an angle $\Theta$ of 90°. A sail segment is spanned in between these two booms as shown in Figure 4.18.

The deployed length of the segment's cathetus $c$ as a function of the spool rotation angle $\alpha$ is

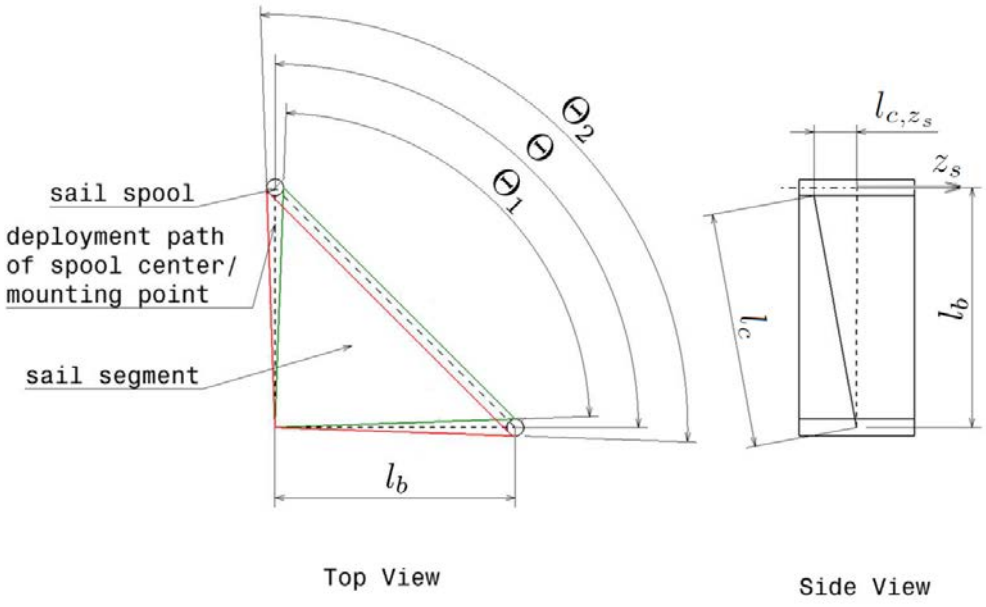


Figure 4.18: Deployment Geometry. Two booms with a sail spool on each side deploy under an angle of $\Theta = 90°$. The sail segment is deployed between the two sail spools with an angle of $\Theta_1$ or $\Theta_2$ depending on the coiling direction.

given by the arc length of the helix with alternating slope according to Equation 4.5 as

$$\begin{aligned}
|l_c| &= \int_{\alpha_{max}}^{\alpha} \left[ \left( \frac{\mathrm{dl_{c,x_s}}}{\mathrm{d}\alpha} \right)^2 + \left( \frac{\mathrm{dl_{c,y_s}}}{\mathrm{d}\alpha} \right)^2 + \left( \frac{\mathrm{dl_{c,z_s}}}{\mathrm{d}\alpha} \right)^2 \right]^{\frac{1}{2}} \mathrm{d}\alpha \\
&= \int_{\alpha_{max}}^{\alpha} \left[ \frac{r_i^2}{1-m^2} \cdot e^{\frac{2 \cdot m}{\sqrt{1-m^2}} \cdot \alpha} \cdot \right. \\
&\quad \left\{ \left( m \cdot c \cdot cos(\alpha) - \sqrt{1-(m \cdot c)^2} \cdot sin(\alpha) \right)^2 \right. \\
&\quad + \left( m \cdot c \cdot sin(\alpha) - \sqrt{1-(m \cdot c)^2} \cdot cos(\alpha) \right)^2 \\
&\quad \left. \left. + \frac{c^2}{1-m^2} \right\} \right]^{\frac{1}{2}} \cdot d\alpha \\
&= \frac{\sqrt{2} \cdot r_i}{m \cdot c} \cdot \left( e^{\frac{m \cdot c}{\sqrt{1-m^2}} \cdot \alpha} - e^{\frac{m \cdot c}{\sqrt{1-m^2}} \cdot \alpha_{max}} \right) .
\end{aligned} \tag{4.12}$$

The deployed length of the segment's hypotenuse $h$ as a function of the spool rotation angle $\alpha$ is given by the arc length of the logarithmic spiral in the $x$-$y$ plane according to Equation 4.5 as

$$\begin{aligned}
|l_h| &= \int_{\alpha_{max}}^{\alpha} \left[ \left( \frac{\mathrm{dl_{h,x_s}}}{\mathrm{d}\alpha} \right)^2 + \left( \frac{\mathrm{dl_{h,y_s}}}{\mathrm{d}\alpha} \right)^2 \right]^{\frac{1}{2}} \mathrm{d}\alpha \\
&= \frac{r_i}{m \cdot c} \cdot \left( e^{\frac{m \cdot c}{\sqrt{1-(m \cdot c)^2}} \cdot \alpha} - e^{\frac{m \cdot c}{\sqrt{1-(m \cdot c)^2}} \cdot \alpha_{max}} \right) .
\end{aligned} \tag{4.13}$$

The idea of the deployment strategy presented is to always span the sail between the booms during the deployment process. In a first approximation, the dimensions of the spool are not taken into account. That means the sail is deployed along the dashed lines shown in Figure 4.18. The deployed length of the cathetus and the hypotenuse correspond to the geometry of the triangular

segment as

$$\rho = \frac{|l_c|}{|l_h|} = \frac{C}{H} = \frac{1}{sin(\Theta)} = \sqrt{2} \ . \tag{4.14}$$

When investigating the geometry in more detail, the dimensions of the spool need to be taken into account. The uncoiling point moves up and down the spool along the spool's $z-$axes according to the helix with alternating slope (see Figure 4.18 Side View). The projection of the deployed cathetus $l_c$ into the $x$-$y$ plane (sail plane) is given by

$$l_{c,xy} = \sqrt{|l_c|^2 - l_{c,z}^2} \ . \tag{4.15}$$

The deployed cathetus is slightly longer for $z \neq 0$ compared to the cathetus of the triangle projected into the $x$-$y$ plane. In turn, a little more hypotenuse is uncoiled than what can be spanned between the booms. This effect indicates a tendency of the deployment forces to be transferred through the tensioned cathetus instead of the hypotenuse. For further analysis, it must be differentiated between the coiling directions with respect to the point at which the cathetus and the hypotenuse is uncoiled from the spool.

For the coiled segment with the folding openings on the outside of the coil (see Figure 4.16(d)), it is found that the uncoiling point is on the side of the spool that shows away from the deployed sail segment. The geometry is highlighted in red in Figure 4.18 and the symbols have the additional index 2. Angle $\Theta_2$ is slightly bigger than angle $\Theta$ between the booms (here 90°). This effect indicates that during the deployment with this coiling direction, there is a tendency that the deployment forces are transferred through the hypotenuse. This would introduce an unwanted bigger bending load to the boom. In consequence, the other coiling direction was chosen for the Gossamer-1 project. It is analyzed in more detail in the following paragraphs.

For the coiled segment with the folding openings on the inside of the coil (see Figure 4.16(c)), the uncoiling point is on the side of the spool that shows to the deployed sail segment. The geometry is highlighted in green in Figure 4.18 and the symbols have the additional index 1.

Angle $\Theta_1$ is slightly smaller than Angle $\Theta$ between the booms (here 90°). This effect indicates that during the deployment with this coiling direction, there is a tendency that the deployment forces are transferred through the cathetus. The geometry is shown in Figure 4.19. The constant tangent angle $\gamma$ of the logarithmic spiral is expressed as

$$\gamma = tan^{-1}\left(\frac{\sqrt{1-(m\cdot c)^2}}{m\cdot c}\right) \ . \tag{4.16}$$

For the blue highlighted triangle, the law of sines is applied as

$$\frac{l_{c,xy}}{sin(\gamma-\delta)} = \frac{l_b}{sin(\pi-\gamma)} = \frac{r(\alpha)}{sin(\delta)} \ . \tag{4.17}$$

With some mathematical transformation and considering that

$$sin(\gamma-\delta) = sin(\gamma)\cdot cos(\delta) - cos(\gamma)\cdot \sin(\delta) \ , \tag{4.18}$$

this allows angle $\delta$ to be described as

$$\delta = arccot\left(\frac{l_{c,xy} + r\cdot cos(\gamma)}{r\cdot sin(\gamma)}\right) \tag{4.19}$$

and the boom length as

$$l_b = l_{c,xy}\cdot\frac{sin(\pi-\gamma)}{sin(\gamma-\delta)} \ . \tag{4.20}$$

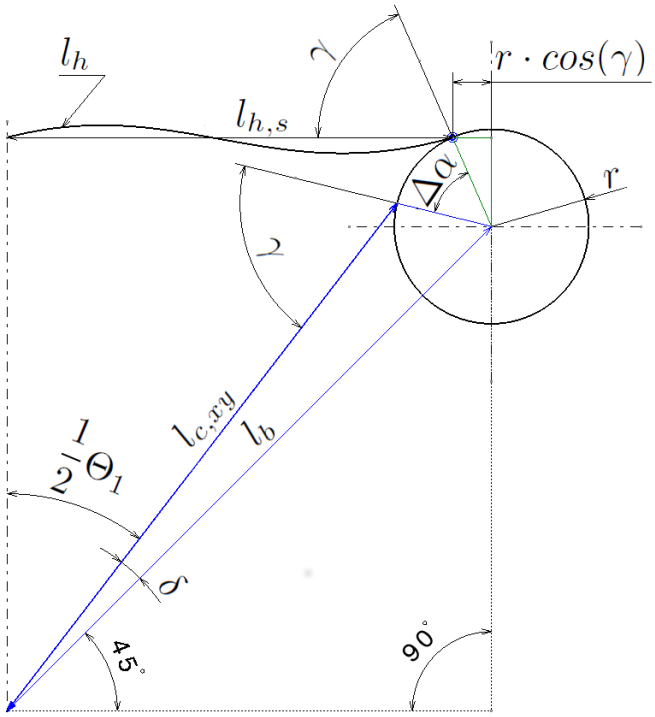


Figure 4.19: Details of the deployment geometry. A half sail segment during deployment is shown it is uncoiled to the left from a spool with the radius $r$ of the coiled sail segment.

The length that can be spanned between the two sail spools (see Figure 4.19, green highlighted triangle) is expressed as

$$l_{h,s} = l_b \cdot cos\left(\frac{\pi}{4}\right) - r \cdot cos(\gamma) \ . \tag{4.21}$$

The uncoiling point of the hypotenuse differs from that of the cathetus by angle $\Delta\alpha$ described by

$$\Delta\alpha = \frac{\pi}{4} + \delta \ . \tag{4.22}$$

With Equations 4.13, 4.21 and 4.22 the additional length that cannot be tensioned is given by

$$\Delta l_h = l_h(\alpha + \Delta\alpha) - l_{h,s} \ . \tag{4.23}$$

### 4.2.2 Deployment forces

In order to uncoil the sail, a certain torque $T_b$ must be exceeded to rotate the spool. This torque might be due to friction as well as an intentionally introduced brake torque and can be a function of the spool rotation angle $\alpha$. The brake force is obtained dividing the brake torque by the radius as

$$F_b(\alpha) = \frac{T_b(\alpha)}{r(\alpha)} \ . \tag{4.24}$$

The point of force application is at the uncoiling point of the spool. At this point deployment force $F_D$ is applied to the spool. The geometry of the forces during deployment that are transferred through the membrane onto the spool and thereby also onto the boom are shown in Figure 4.20. The forces transferred through the membranes and spools on the two sides of the boom are

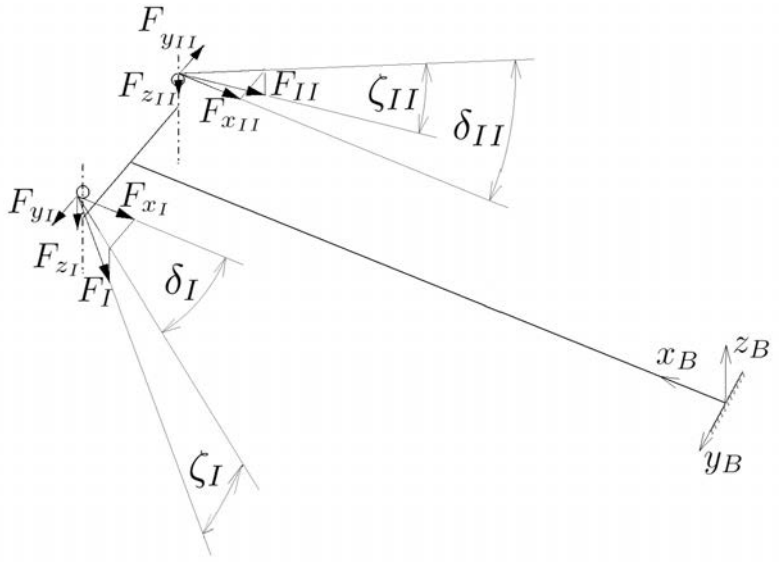


Figure 4.20: Geometry of the forces applied through the membrane to the spool for uncoiling the membrane.

differentiated by the subscripts $I$ and $II$. The component that pulls tangentially at the spool (in the $x$-$y$ plane) is uncoiling the sail segment. Because the uncoiling point moves up and down the sail spool, there is also a force component acting in $z$-direction along the spool axis. The corresponding angle of that force component out of the sail plane is calculated by

$$\zeta = arcsin\left(\frac{l_{c,z}}{l_c}\right) \ . \tag{4.25}$$

The absolute value of the total force is given by

$$F_D = \frac{F_b \cdot sin(\gamma)}{cos(\zeta)} \tag{4.26}$$

and the force vector in the boom coordinate system is given by

$$\vec{F}_D = \begin{pmatrix} F_x \\ F_y \\ F_z \end{pmatrix} = \begin{pmatrix} F_D \cdot cos(\zeta) \cdot cos(\delta) \\ F_D \cdot cos(\zeta) \cdot sin(\delta) \\ F_D \cdot sin(\zeta) \end{pmatrix} \ . \tag{4.27}$$

The vector of the deployment moments $\vec{M}_D$ at the boom mounting point is given by the cross product of force $\vec{F}_S$ with the vector of lever arms $\vec{L}$. The moment vector is expressed as

$$\begin{aligned} \vec{M}_D &= \vec{L} \times \vec{F}_D \\ &= \begin{pmatrix} L_x \\ L_y \\ L_z \end{pmatrix} \times \begin{pmatrix} F_D \cdot cos(\zeta) \cdot cos(\delta) \\ F_D \cdot cos(\zeta) \cdot sin(\delta) \\ F_D sin(\zeta) \end{pmatrix} \end{aligned} \tag{4.28}$$

Here, $L_x$ equals $l_b$ and $L_z$ equals $l_{c,z}$. $L_y$ is a geometric parameter depending on the accommodation and design of the considered system.

## 4.3 Conclusion

With Section 4.2.1 a mathematical model of the stowing and deployment geometry is established. The representation of the coiled geometry with a spiral (see Figure 6.8(b)) and a helix (see Figure

6.8(a)) is idealized. When coiling a real membrane, the folded layers are coiled on different radii. The layers directed more to the inside of the coil have a smaller arc length then the ones that are more outside. At the same time, the length of the folded sail segment is of course the same for the inside and outside layers. This can only be resolved by wrinkling the inner layers during the coiling process. This effect is also visible in the paper model shown in Figures 4.16(c) and 4.16(d) (one example is highlighted with a red circle). For thin foils, this is not a major problem and could very well be excepted. A disadvantage for a solar sail might be that the reflectivity of the foil might decrease by the wrinkling, which would reduce the efficiency of the solar sail. For a thick layer like the flexible photovoltaic, which cannot wrinkle without getting broken, this is more problematic. An approach to deal with that problem was to have small photovoltaic areas with areas of thin foil in between them that can be wrinkled to compensate for the length difference during the coiling process.

While the focus of the presented work was the analysis of the Gossamer-1 stowing and deployment strategy, the coiling of the sail in the opposite direction (see Figure 4.16(d)) was also briefly introduced. The main reason to choose the coiling direction was the reduction in the boom load. Nevertheless, coiling the folded sail segments such that the opening of the folds is directed to the outside would lead to a more compact stowing volume because the folded sail segment can be coiled a little further, as the interface is located on the outside of the coil (compare Figures 4.16(c) and 4.16(d).

The analysis presented establishes a model for a deployment technique that aims for a mechanically stable and thereby controllable deployment. It can be used to combine the deployment geometry with the forces introduced by the deployment mechanisms (see Chapter 5) in order to describe the progression of deployment loads (see Chapter 6).

# Chapter 5

# Deployment mechanisms

The deployment strategy chosen in Section 4.2 requires that the sail spools move away from the center of the sail. In principle there are two ways to achieve this. The sail spools are either fixed mounted on the boom tips and the booms are pushed out from the center of the spacecraft or they are mounted on deployment units that deploying the booms while moving away from the sail center. The letter one was used in the Gossamer-1 project as already shown in in Figure 4.14. The deployment units move away from the sail center, thereby booms and sail segments are deployed at the same time.

The main reason for this deployment was a better utilization of the boom stiffness during deployment. The weakest point of the coilable booms during their deployment is the uncoiling point at which the cross section is not developed. From the point where the boom cross section is fully compressed the cross section slowly increases through several meters. After one meter the cross section and stiffness is close to the one of a fully deployed boom. A boom guiding supports the boom in this weak area, but only through about 25 cm at this point the boom can barely carry any loads. For a deployment driven from the center of the sail, the point of load introduction from the sail deployment moves further away from this weakest point, which leads to even higher banding loads due to the bigger leaver arm.

Another advantage of using deployment units is an easy way of jettisoning this units after the deployment is completer. This is considered for a solar sail being on an earth escape trajectory. By jettisoning all deployment units a very lightweight sail craft with a low area specific sail loading or a height specific acceleration is achieved. The performance of the current technology is outlined in Appendix B.

In the following paragraphs the sub-components and mechanisms that finally enabling the deployment of the chosen concept are described. A complete description of the Gossamer-1 mission and hardware is given in Seefeldt et al. (9) and the engineering model of the boom deployment mechanism is presented in Straubel et al. (106).

## 5.1 Deployment unit overview

Figure 5.1 shows one deployment unit (without the sails) during the deployment process, including the jettisoning of the deployment unit. For further clarification, details of the mechanisms are shown in Figure 5.2.

In the stowed configuration, shown in Figure 5.1(a), launch locks secure the deployment units, also refered to as Boom and Sail Deployment Unit (BSDU), at the sail center at the main spacraft bus, also refered to as Central Spacecraft Unit (CSCU) (see section 5.3). At the beginning of the deployment those locks are released. The deployment is driven by an additional belt that is coiled on the boom hub together with the boom. At the very end of the boom, a small piece of Velcro is connecting the belt to the boom. The boom and in consequence the sails are deployed by pulling

the belt from the boom hub, thereby uncoiling the boom as well. The deploying boom pushes the BSDU away from the CBSU, which in consequence leads to an uncoiling of the sail segments. During deployment (Figure 5.1(b)) the load is transferred through friction between belt and boom and with progressing deployment more and more through the Velcro.

The uncoiling of the belt and thereby the deployment is driven by a Belt Winding Mechanism (BWM) employing an electrical motor. To prevent uncontrolled deployment of the booms and sails, e.g. by stored elastic energy, the boom hub and the sail spools need to have a brake mechanism, described in the following dedicated paragraphs.

To achieve the jettisoning-function of the BSDU, the Boom Sail Fixation Ring (BSFR) provides the interface between the outer sail corners and the boom. During sail deployment, the BSFR is attached to the BSDU and the boom runs through the ring-like shape of the BSFR. Once the sail is fully deployed (Figure 5.1(c)) the BSFR is locked on the boom and is mechanically separated from the BSDU (Figure 5.1(d)). At this point the BWM drive unit can be engaged again to further deploy the remaining coiled boom, either for just a short distance (Figure 5.1(d)) or thereafter to move the BSDU off the boom completely (Figure 5.1(e) and 5.1(f)).

As the sail's outer corners are not attached to the BSDU but to the BSFR, the BSDU no longer has to carry sail loads. At the final stage of the deployment the tip of the boom is deployed by transferring the deployment load purely through the Velcro. This Velcro loading applies until Figure 5.1(e). At this point the Velcro passes the pulley and the Velcro loading transforms from shear loading into peel loading (compare Figure 5.2(a)), which separates both parts without decelerating the BSDU much. The BSDU and boom are separated completely, and the BSDU maintains the previously gained kinetic energy and floats away as indicated by Figure 5.1(f).

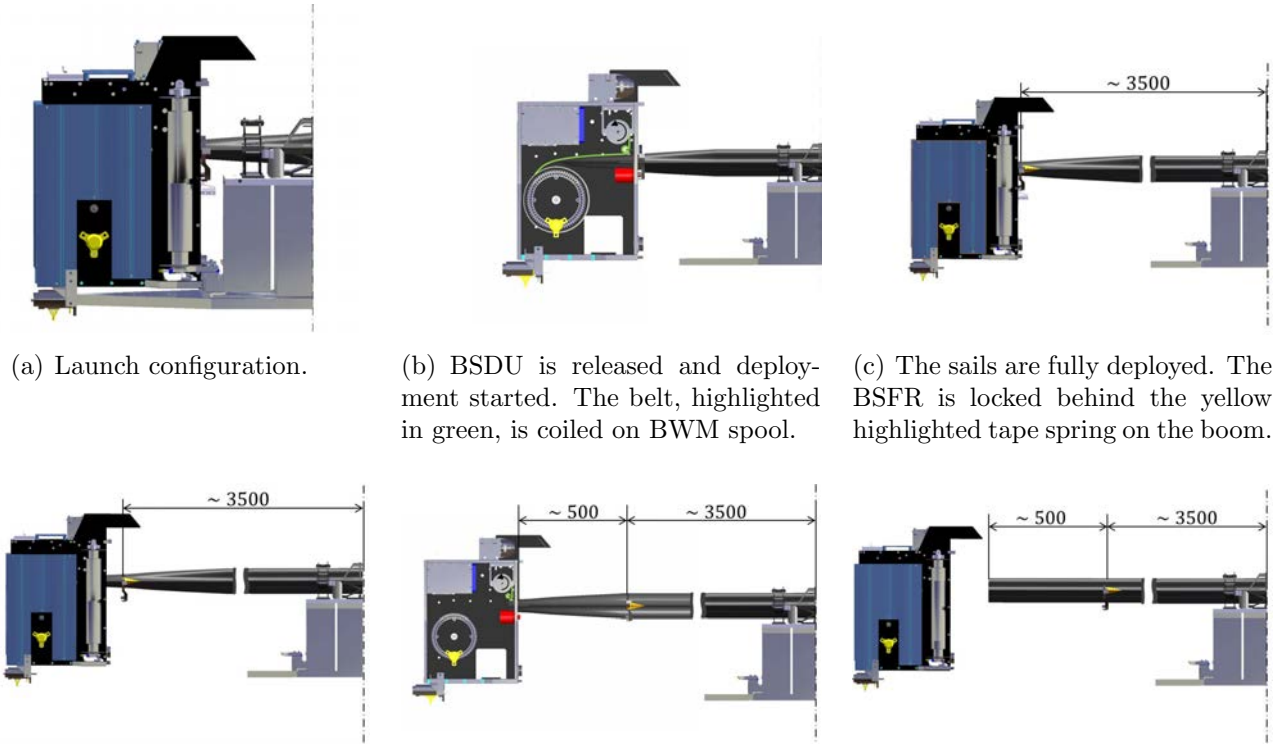


(a) Launch configuration.

(b) BSDU is released and deployment started. The belt, highlighted in green, is coiled on BWM spool.

(c) The sails are fully deployed. The BSFR is locked behind the yellow highlighted tape spring on the boom.

(d) The BSFR is separated and the remaining boom is deployed.

(e) The belt, connected by Velcro, is separating from the boom.

(f) The BSDU is jettisoned and drifting away.

Figure 5.1: BSDU deployment sequence. In order to keep a clear representation, only one BSDU and no sail segments are shown.

The main drive of the BSDU is the Belt Winding Mechanism. As explained above, the BWM pulls off a 0.03 mm thick stainless steel belt, that is coiled up together with the boom. The BWM itself consist of an electrical motor, a spool on which the belt is coiled on and a freewheel. Figure

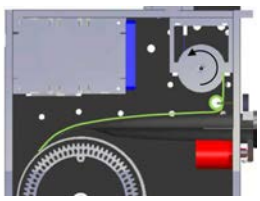

(a) View from the side. Belt (green) coiled on BWM spool.

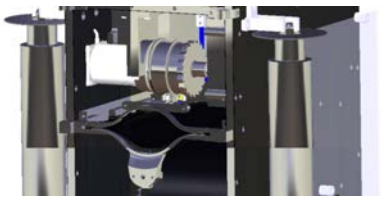

(b) View from CSCU to BSDU. BWM BSDU drive and BSFR.

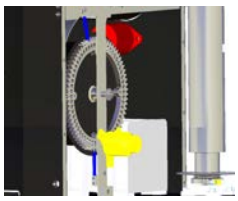

(c) Boom hub with gear and engaging spring plates (blue). The pin-puller (yellow) can lock into holes on the side of the gear (see section sec:launchlock).

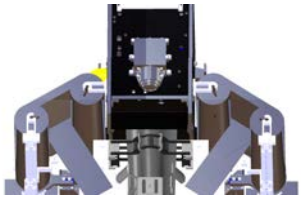

(d) View from top. Camera mounted on the top plate and stowed sail segments on each side (see section 5.2)

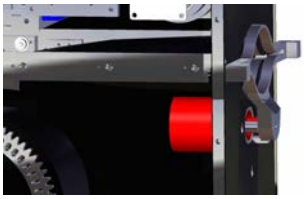

(e) BSFR and its separation mechanism (red).

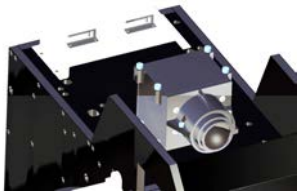

(f) BSDU top with camera and blue-tooth antennas for the wireless communication with the main Bus on the CSCU

Figure 5.2: BSDU Details

5.2(b) shows the BWM in detail. The motor, shown in light gray, is mounted on the left and with a bracket in the middle. The winding spool is located on the right, it is directly mounted on the output shaft of the gearbox employing a feather key. The freewheel is made of a gear with pitched teeth that is part of the winding spool and an engaging copper beryllium spring plate (blue part). The belt, which is highlighted in green in Figure 5.2(a), is guided by a diverting pulley to the BWM spool.

The motor for the winding mechanism has to overcome torques induced by the boom hub, the boom guidance and the sail spool. Besides the required actuation torque a further critical point is that motors used under vacuum conditions easily overheat. In consequence the life cycle is very important. For the deployment (Phase 4) the motor has to run with low speed but for a relative long period of time of approximately 10 minutes. After a longer break (Phase 5), jettison will take place with high motor speed for a short period.

The motor VSS32 with a GPL32 gear box of the company Phytron was chosen for the engineering model. For the qualification model the company produced a customized Version of the VSS32 with a GPL22. In order to withstand the high mechanical launch loads the design of motor and gearbox was made more robust. That led to a slight increase in size which was compensated by the smaller GPL22, so that it still fits into the dedicated space inside the BSDU. Change of the gear box led to a change of the transmission ratio from 50:1 to 49:1. The motor can run 6 rpm up to 7.5 min for the deployment and 30 rpm up to 1 min for the jettison. A torque budget, derived from force measurements with the engineering models, is given in Section 7.2.3, (Table 7.2).

To ensure that the belt is always under tension, so that it does not slip off the winding spool, the design includes a freewheel. This is especially required during launch as the vibration loads might lead to a rotation of the winding spool even if the motor is turned off.

The BSFR as shown in Figure 5.2(e) is the boom-sail interface. During deployment (Phase 4) the boom is sliding through the BSFR. At the point where the sails are fully deployed, the sails

must be fixated to the booms. This is achieved by fixating the BSFR at this certain position to the boom by employing tape springs that are glued onto the boom as shown in Figure 5.2(b). During deployment the BSDU with the BSFR is moving across the tape spring until the BSFR locks in right behind the spring. After the ring is locked to its final position, the separation (Phase 5) between BSFR and BSDU takes place. This is achieved by employing the Ejection and Release Mechanism (ERM) E250 STD from TiNi Aerospace Inc.. The mechanism is highlighted in red in Figure 5.2(e). The mechanism opens the mounting of the BSFR to BSDU. Finally, the BSDU can move further, deploying the last centimeters of the booms leaving the BSFR with the mounted sail at the fixation point.

## 5.2 Sail spool mechanism

As explained in Subsection 4.2, the sail is divided into four segments as shown in Figure 4.15. Each of the quadrants is folded and coiled on two sail spools, which are mounted on two adjacent BSDUs (see Figure 5.2(d)). An overview of the sail spool design is given in Figure 5.3(a). The principle was patented Seefeldt and Spietz (107). When uncoiling the sail segment, the spool with the sail interface rotates around the truss-like structure connected to the BSFR (Figure 5.3(b)). After the sail segment is uncoiled, the truss-like structure directly mounts the sail through the sail interface to the BSFR (Figure 5.3(c)). After the separation from the BSFR (Phase 5), the BSDU with the sail spools drives further along the booms, thereby separating the sail spool from the truss like structure that is mounting the sail to the BSFR (Figure 5.3(d)).

During launch, a gear wheel on the sail spool's underside is used to lock the spool with a corresponding counterpart mounted on the CSCU. A leaf spring engaging the gear adds an oscillating break torque of approximately 0.035 Nm at maximum. This is required during deployment to ensure that the sail does not slip off of the spool by itself. The mechanism allows a complete stop within the deployment process and still has the partly-deployed sail safely mounted.

### Spool brake

The spool brake utilizes the deformation of spring that engages a gear on the bottom of the spool. The geometry is shown in Figure 5.4. When the spool rotates, the spring is deflected from the neutral position (0) to the point of maximum deflection (1) where it snaps back to the next tooth, maintaining a minimum deflection (2). When the spool is further rotated, the spring is again further deflected until it snaps to the next tooth and so on.

The maximum deflection of the spring is given by

$$\begin{aligned} W_{max} &= \sqrt{R^2 - (R - \Delta z)^2} \\ &= \sqrt{-\Delta z^2 + 2 \cdot R \cdot \Delta z}\ . \end{aligned} \tag{5.1}$$

According to the Euler-Bernoulli static beam equation, the relation between the beam's or the spring's deflection and the load is given by

$$\begin{aligned} F_{max} &= \frac{3 \cdot E \cdot I}{l_s^3} \cdot W_{max} \\ &= \frac{3 \cdot E \cdot I}{l_s^3} \cdot \sqrt{-\Delta z^2 + 2 \cdot R \cdot \Delta z)}\ . \end{aligned} \tag{5.2}$$

The maximum brake torque is given by

$$T_{max} = F_{max} \cdot R\ . \tag{5.3}$$

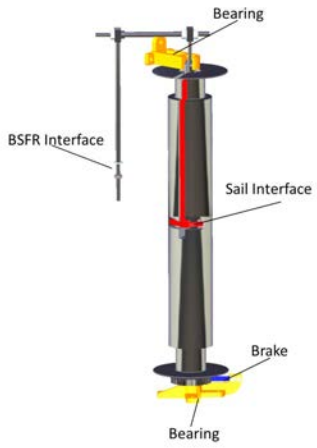


(a) Overview of the SSM components.

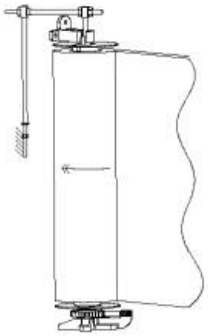

(b) Uncoiling sail segment from spool.

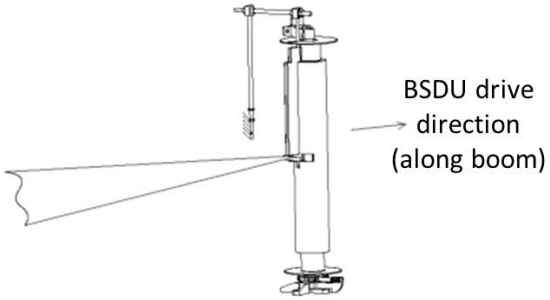


(c) Segment is uncoiled and mounted through the interface to the BSFR (which is then separated from the BSDU).

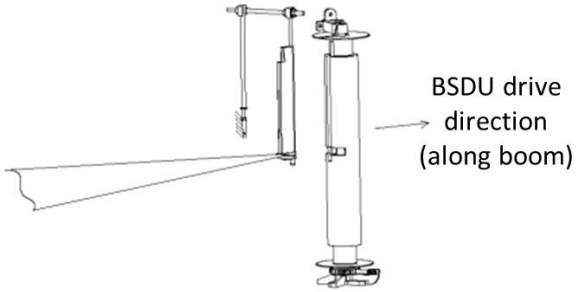


(d) The sail spool (connected to the BSDU) moves further, thereby completely separating from the interface that mounts the sail to the BSFR.

Figure 5.3: Sail spool and separation sequence.

The rotation angle to the maximum deflection point of the gear is

$$\alpha_{max} = cos^{-1}\left(\frac{R - \Delta z}{R}\right) . \tag{5.4}$$

With the number of gear teeth $n_z$ the circular pitch of the gear's outer diameter is

$$p = \frac{2 \cdot \pi \cdot R}{n_z} . \tag{5.5}$$

When the spring snaps to the next tooth it cannot reach the initial neutral position (see Figure 5.4), it still has a small deflection $W_{min}$, and introduces force $F_{min}$. The arc length on the radius $R$ to the first maximum deflection point is

$$u_{max} = R \cdot \alpha_{max} . \tag{5.6}$$

From there the spring snaps back one circular pitch $p$, so the arc length to the minimum deflection point is

$$u_{min} = u_{max} - p = R \cdot \alpha_{min}$$

and by this the minimum deflection angle is

$$\alpha_{min} = \frac{u_{min}}{R} = \frac{u_{max} - p}{R} . \tag{5.7}$$

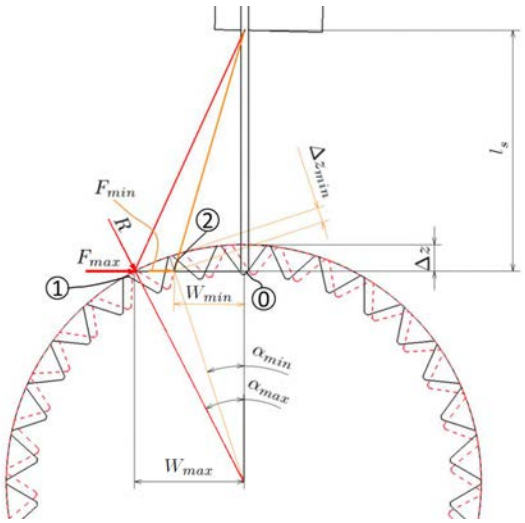


Figure 5.4: Simplified geometry of the brake, consisting of a spring that engages a gear. The red dashed line represents the position at which the spring snaps back to the next gear tooth.

The minimum deflection of the spring is given by

$$W_{min} = tan(\alpha_{min}) \cdot (R - \Delta z) \ . \tag{5.8}$$

Employing the Euler-Bernoulli static beam equation and back substituting Equations 5.7, 5.6 and 5.4, the minimum force is calculated as

$$\begin{aligned} F_{min} &= \frac{3 \cdot E \cdot I}{l^3} \cdot W_{min} \\ &= \frac{3 \cdot E \cdot I}{l_s^3} \cdot tan(\alpha_{min}) \cdot (R - \Delta z) \\ &= \frac{3 \cdot E \cdot I}{l_s^3} \cdot tan\left( \frac{R \cdot cos^{-1}(\frac{R-\Delta z}{R}) - p}{R} \right) \\ &\quad \cdot (R - \Delta z) \ . \end{aligned} \tag{5.9}$$

For the minimum engagement depth $\Delta z_{min}$, the following geometric relation can be employed:

$$\begin{aligned} cos(\alpha_{min}) &= \frac{R - \Delta z}{R - \Delta z_{min}} \\ \Rightarrow \Delta z_{min} &= \frac{R - \Delta z - R \cdot cos(\alpha_{min})}{cos(\alpha_{min})} \ . \end{aligned} \tag{5.10}$$

The radius at this point is

$$R_{min} = R - \Delta z_{min}, \tag{5.11}$$

and the minimum brake torque is

$$T_{min} = F_{min} \cdot R_{min} \ . \tag{5.12}$$

In accordance with the Euler-Bernoulli static beam equation, the force linearly increases from the minimum value to the maximum value with increasing deflection. At the maximum point the

force is suddenly reduced to the minimum value as the spring snaps back. Such a sawtooth wave for the force may be described as

$$F_R(\alpha) = F_{min} + \frac{F_{max} - F_{min}}{\pi} \cdot cot^{-1}\left[cot\left(\frac{n_z}{2} \cdot \alpha\right)\right] \tag{5.13}$$

and for the torque it is

$$T(\alpha) = T_{min} + \frac{T_{max} - T_{min}}{\pi} \cdot cot^{-1}\left[cot\left(\frac{n_z}{2} \cdot \alpha\right)\right] \ . \tag{5.14}$$

## 5.3 Launch locks

During launch, all mechanisms are locked in order to provide a mechanically stable configuration of all parts. An overview of the locking mechanisms employed is given in Figure 5.5.

The Boom Hub will be locked by employing a pin puller P5 manufactured by TiNi Aerospace, Inc.. Figure 5.2(c) shows the boom hub with the pin-puller highlighted in yellow. It is mounted on the outer wall and the pin is locked into one of the holes located around the boom hub gear wheel. In order to simplify the integration, 60 holes allow locking of the hub, so that it is not necessary to reach one designated end position. Instead, the hub can be locked every 6° of rotation, so that after coiling the boom the nearest locking position can be employed. In order to avoid clamping of the locked pin (e.g. due to thermal expansion), a cone shape for the pin and the holes was chosen.

The BSDU itself is locked to the main structure of the central unit by employing a TiNi Aerospace Frangibolt actuator FC4. This is the main mounting point of the BSDU, positioned on the outer side of the BSDU/CBSU assembly. In addition, the BSDU is mounted on the side directed to the CSCU by additional pins that slide into counter part sleeves on the CSCU side.

Additionally a form-fitting locking element ensures the locking of the sail spools by engaging with the gear and a groove on the sail spool (see Figure 5.5 on the right). Please refer to Section 5.2 and the patent Seefeldt and Spietz (107) for further details.

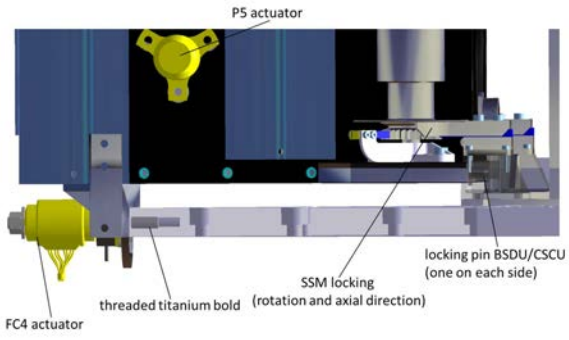


Figure 5.5: BSDU launch locks

## 5.4 Conclusion

For the proposed deployment strategy, mechanisms have been designed within the Gossamer-1 project that enable the deployment and thereby allow the further study of the deployment

process. The development includes a spool mechanism onto which the folded sail is coiled. This mechanism provides a brake that prohibits a premature uncoiling and allows a separation of the sail after the deployment. This is required in order to achieve a most lightweight sail craft by jettisoning of the deployment mechanisms. For the further analysis of deployment loads, the brake force of the spool mechanism is described mathematically.

# Chapter 6

# Membrane analysis and design

The various design aspects summarized in Section 6.1 implicate multiple analyses in different fields that are necessary to provide an overall picture of the sail membrane and its behavior in different configurations and environments throughout its lifetime. Some important aspects are discussed in the following sections. After the principle design aspects are discussed, possible load cases are determined in Section 6.3. This is followed by considerations regarding the load introduction in corners of a triangular segment in Section 6.4, and a mechanical analysis of the deployed configuration is presented in Section 6.4.1. As a very specific point of folded membranes, the constitution of folding lines is analyzed in more detail in Section 6.5. Another focus is on the shape of the folding lines and its impact on the thermal design. The chapter ends with a presentation of the Gossamer-1 membrane design in Section 6.2 and a conclusion on that design and the prepared analysis as well as open points in Section 6.6.

## 6.1 Overview of possible design aspects

The membrane design is influenced by various aspects ranging from general considerations like membrane geometry and stabilization by adequate spanning of the membrane, to load transmission and joining techniques. In cases where different functions must be fulfilled by the membrane, it is also possible to use several layers. An example would be a membrane for thin-film photovoltaics that has electrical aspects that need to be considered. Figure 6.1 provides an overview of those design aspects that are further described in the next paragraphs.

The projects presented in Chapter 2 employed two general techniques for tensioning the membrane and thereby stabilizing the geometry. The membranes were either employing a supporting structure (booms) between which the membranes are spanned or the stabilization of the membrane's shape was achieved by centrifugal forces (spin). The Gossamer-1 project and its drag sail spin-offs used CFRP booms. The supporting structure can either be inflated or is deployed by mechanisms like the ones used for the Gossamer-1 project (see Chapter 5).

In combination with the method for spanning the membrane, a corresponding geometry has to be chosen. The projects presented in the survey that use booms to span the sail have a rectangular shape. It is obvious that such a sail can be tensioned with mounting points at the edges of the sail or by several, or even continuous mounting along the rectangular diagonals. As explained in Chapter 4, most projects considered the use of four triangular membrane segments that together form a rectangular sail. In addition, circular membranes wrapped around a cylindrical hub might have good deployment behavior for a spin deployment (Furuya et al. (105)). Considerations regarding the load introduction within the Gossamer-1 project are presented in Section 6.4.

An adequate load transmission needs to consider where the membrane is mounted (e.g. at the corners or along the edge), as well as through which interface the load is transferred to the membrane. If rectangular sails are considered, Fernandez et al. (108) differentiate between some

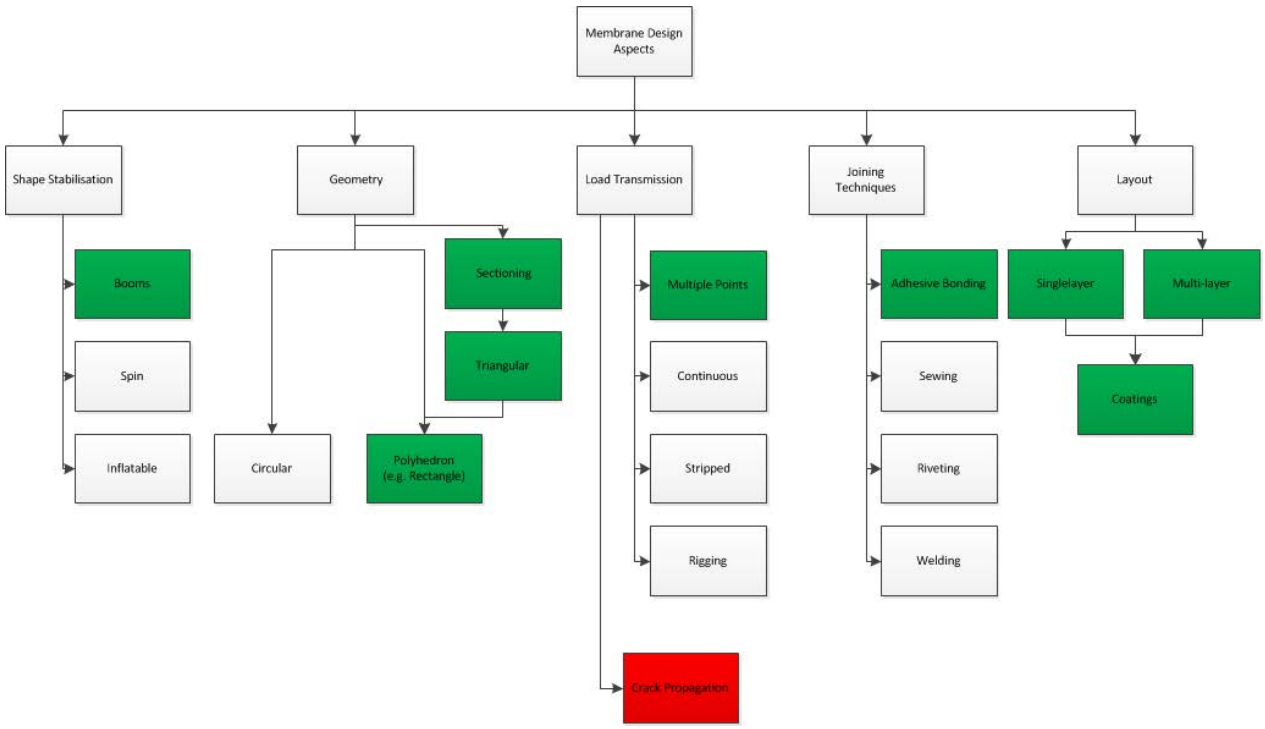


Figure 6.1: Aspects of membrane design. The green highlights correspond to the Gossamer-1 design. The red highlighted crack propagation analysis has not yet been investigated but is considered to be an important design driver.

general sail suspension techniques as shown in Figure 6.2.

Instead of mounting the sail to the booms, the IKAROS project used masses mounted to the sail at the corners that spanned the sail by centrifugal forces. The mounting corresponds to a five point suspension. The IKAROS sail was built out of four segments connected to one rectangular sail. Sakamoto et al. (109) present a tensioning strategy employing a boundary with a cable web. With Figure 6.3 he also provides an overview of strategies for tensioning rectangular membranes. The goal of the cable web boundary and the shear compliant boundary is to avoid the wrinkling of the membrane due to the tensioning.

In addition, adequate interfaces are required for the load transmission. Dalla Vedova et al. (110) presents three options for a load transfer into the corners of triangular membrane segments shown in Figure 6.4.

The membranes considered here consists of a substrate coated with different materials and, in the case of thin-film solar cells, a multilayer membrane fulfills different mechanical and electrical functions.

The propagation of cracks due to the impact of micrometeorites or space debris was identified as an important design driver, but it was not investigated in the work presented here. It is a specific analysis that requires mechanical testing in order to determine specific material parameters. The first results of an analysis implemented by the company HPS within the ADEO project indicate that for the low pretension of the membranes considered here and the overall low stress in the membrane no crack propagation is present. Local destruction due to an impact would therefore be confined. It also indicates that a strong tensioning of the membrane could lead to a strong crack propagation and therefore the destruction of the sail. Besides the reduction in boom loads, this is another indicator that a low tension state is more beneficial for the space sails. This topic clearly needs further analysis to determine, for example, a maximum stress at which the crack propagation starts.

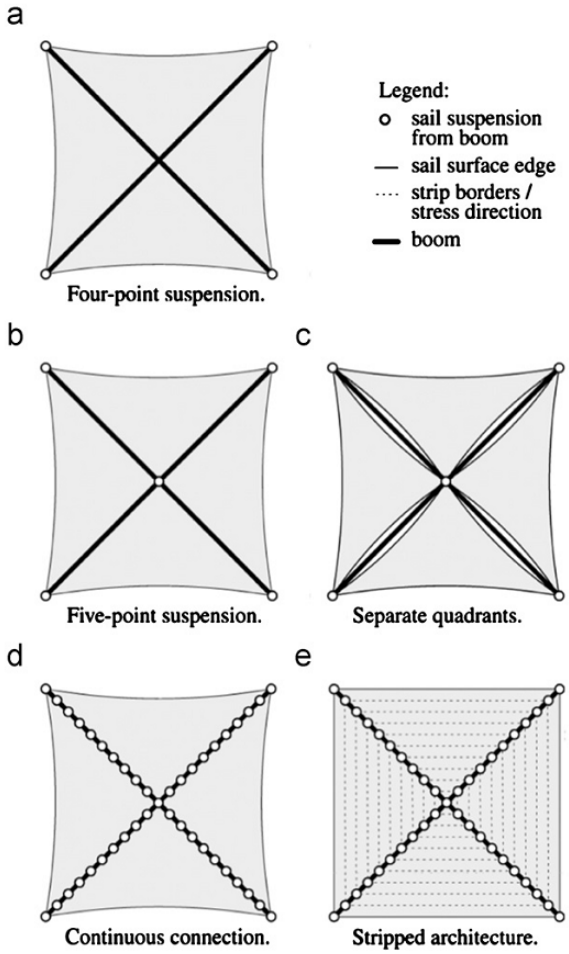


Figure 6.2: Sail suspension techniques for solar sails according to Fernandez et al. (108)

## 6.2 Design of the Gossamer-1 membrane

The sail consists of an aluminum coated polyimid foil. It is an off-the-shelf product of the company UBE called Upilex-S. The material is available on a roll with a maximum width of 1016 mm and a thickness of 7.5 $\mu$m. In consequence, the sail is manufactured out of four sheets that are bonded to each other. In addition, all edges are reinforced by folding the edges over and bonding them with adhesive. Bonding is done with the transfer adhesive tape 966 with adhesive 100 from the company 3M. The adhesive tapes have a width of 10 mm and 20 mm with an adhesive thickness of 60 $\mu$m. The sail design is shown in Figure 6.5 and Tables 6.1 and 6.2 provide a volume and mass budget.

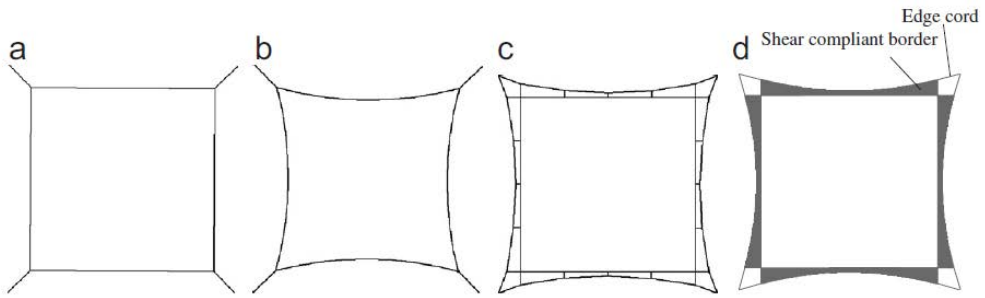


Figure 6.3: Existing membrane designs. (a) Membrane only design, (b) conventional catenary design, (c) Miura–Natori design, (d) shear compliant border design.Sakamoto et al. (109)

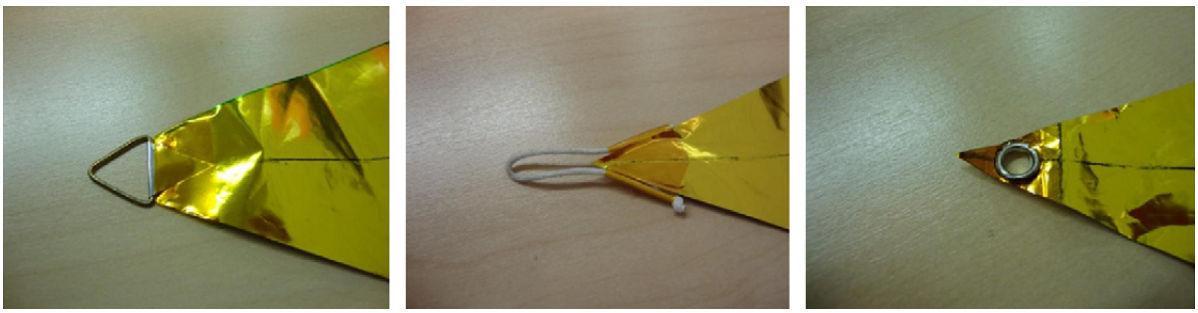

Figure 6.4: Load transmission at the sail corner. Attachments/fasteners: Rigid triangle, taped string along border, eyelet on corner reinforcement according to Vedover Dalla Vedova et al. (111).

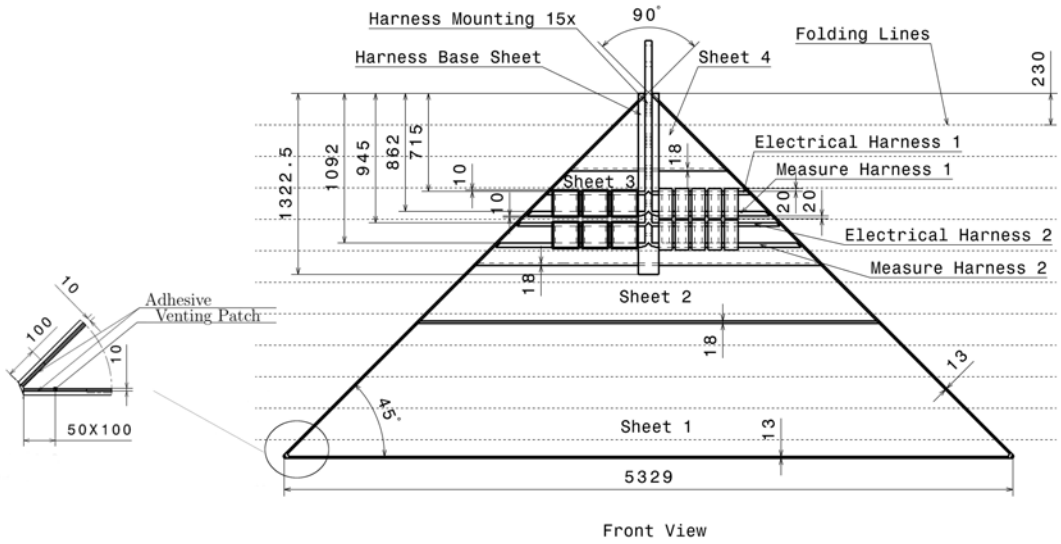


Figure 6.5: Drawing of the sail consisting of four main sheets, an insulating harness base sheet, the harness and photovoltaic modules. In addition, the folding lines are shown.

The design with respect to some parts of the analysis has changed slightly. In order to improve the manufacturing process and the handling, the photovoltaics are implemented on one dedicated sheet (sheet 3). On both sides of the photovoltaic segment, two smaller sheets (sheets 2 and 4)

are connected and the segment is complemented by one more big sheet (sheet 1). The bonding areas are always implemented with an overlap of three millimeters in order to avoid the adhesive protruding over the bonding area. This can lead to an unwanted bonding of foil layers during the stowing process that can interfere with the later deployment.

The edges are always reinforced by folding them over and bonding them with the adhesive. In order to ensure that trapped air can be vented, a patch made of the same foil that leaves a venting hole is applied every 100 mm. For the purpose of electrically isolating the flexible Printed Circuit Board (PCB) harness from the conductive aluminum coated areas, a harness base sheet is added between the aluminum coated foil and the harness. This base sheet is currently a pure polyimide Upilex-S foil (12.5 $\mu$m thickness) without any coating. For future flight hardware, an $SiO_2$ coating as protection from space environment should be considered. In the areas with photovoltaics, a cutout in the aluminum coated foil is provided. This is part of the thermal design of the photovoltaics. The backside of the photovoltaic is Kapton coated with $SiO_2$, which provides better infrared emissivity. Consequently, the backside of the modules cannot be shielded by the aluminum coated Upilex-S that has a high $\alpha_S/\epsilon_t$ ratio, and therefore a high equilibrium temperature. The harness is mounted to the main foil through flexible foil hinges. On the one hand, this allows a tensioning of the foil without (or at least reduced) interaction with the harness, and on the other hand, it ensures that mechanical loads are not carried by the harness (strain-relief).

The interfaces with the sail were made of a flexible PCB material (copper coated polyimide) and stainless steel cable that consists of multiple wires, as shown in Figure 6.6. Shim rings of 0.1 mm thickness were placed between the sail foil and the more rigid PCB and everything was bonded with the transfer adhesive. The cable is made of $7 \times 19$ single wires and can withstand force of 152 N (see Car (112)). The wires are crimped with sleeves of 1.2 mm diameter that are 10 mm long. The interfaces were not analyzed for their total load bearing capacity, but it can be stated that these interfaces are stronger then the Upilex-S foil, and therefore the interfaces are not a weak link in the design.

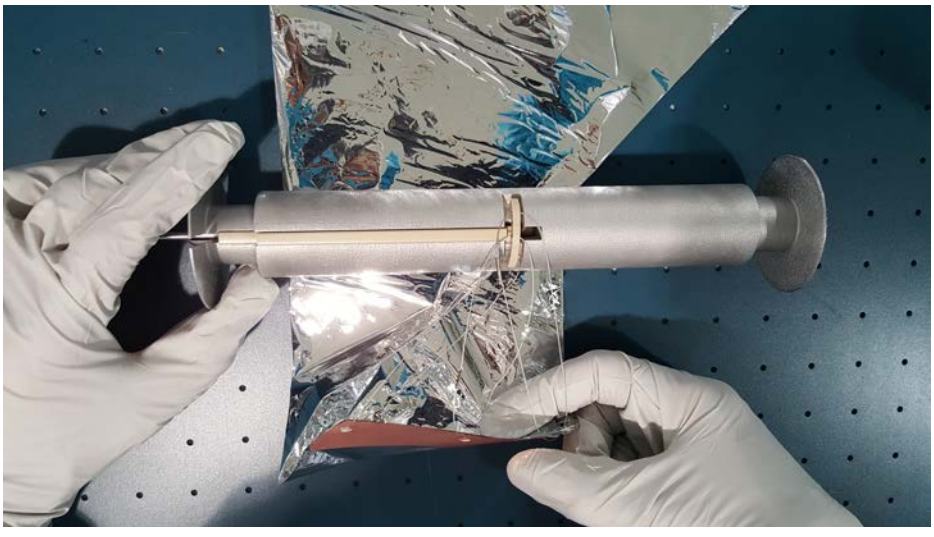

Figure 6.6: Sail interface made of flexible PCB material and stainless steel cables.

Table 6.1: Volume of sail parts used for one segment that is coiled on two spools.

| Component | Coiled Fraction | Area [$m^2$] | Thickness [m] | Volume [$m^3$] |
|---|---|---|---|---|
| Upilex-S foil | $\sim 1$ | 7.361 | $7.5 \cdot 10^{-6}$ | $5.521 \cdot 10^{-5}$ |
| Photovoltaic ZSW | 1 | 0.240 | $132 \cdot 10^{-6}$ | $1.728 \cdot 10^{-5}$ |
| Photovoltaic Solarion | 1 | 0.220 | $132 \cdot 10^{-6}$ | $1.584 \cdot 10^{-5}$ |
| Harness | 0.41 | 0.408 | $67 \cdot 10^{-6}$ | $2.734 \cdot 10^{-5}$ |
| Harness Base Sheet | 0.5 | 0.198 | $25 \cdot 10^{-6}$ | $4.950 \cdot 10^{-6}$ |
| Adhesive | 0.95 | 0.477 | $60 \cdot 10^{-6}$ | $2.862 \cdot 10^{-5}$ |
| Harness Mounting Hinges | 0 | 0.009 | $7.5 \cdot 10^{-6}$ | $6.750 \cdot 10^{-6}$ |
| Total | | | | $1.640 \cdot 10^{-4}$ |
| Total coiled | 0.88*1 | | | $1.436 \cdot 10^{-4}$ |

*1 Mean value

Table 6.2: Mass of sail parts

| Component | Density [$kg/m^3$] | Mass [kg] |
|---|---|---|
| Upilex-S foil | 1546.67 | 0.085 |
| Photovoltaic ZSW | 1401.52 | 0.024 |
| Photovoltaic Solarion | 1401.52 | 0.022 |
| Harness | 2384.91 | 0.065 |
| Harness Base Sheet | 1470.00 | 0.007 |
| Adhesive | 1012.00 | 0.029 |
| Harness Mounting Hinges | 1546.67 | 0.010 |
| Total | 1475.61*1 | 0.242 |

*1 Mean value calculated with the volume given in Table 6.1

## 6.3 Load cases

The membrane need to withstand different loads throughout its lifetime, including

- launch loads,
- deployment loads,
- mission loads (solar radiation pressure, atmospheric drag), and
- loads during laboratory tests.

These load cases are determined and analyzed for the design implemented in the Gossamer-1 project in the following sections.

### 6.3.1 Launch loads

In the normal process, a satellite is designed to withstand the mechanical loads it is subjected to by the selected launch vehicle. However, for a secondary payload that has to maintain launch vehicle flexibility throughout the design process, this procedure needs to be advanced in order to enable multiple possible launch vehicles. A virtual launch vehicle is defined in Grundmann et al. (113)with a launch load envelope that results from a launch vehicle survey based on the planned launch of Gossamer-1 within the framework of the QB50 project. The survey considers

the Cyclone-4, Dnepr, Shtil (-1), Shtil-2R, Shtil-2.1, VEGA, Falcon-9, PSLV (including PSLV-CA, PSLV-XL), Eurockot Rokot-KM, Ariane 5 ASAP (micro and mini) and Soyuz ASAP-S (micro and mini) launchers. The launch loads of the virtual launch vehicle are given in A.

Structural analysis made within the Gossamer-1 project (Hillebrandt et al. (114)) analysis revealed amplification factors at the interfaces between the overall structure, subcomponents and mechanisms. These amplification factors were used for the dimensioning of the mechanisms. Instead of taking vibration loads for each mechanism design into account, a representative local static load is considered. The maximum loads are driven by the random vibrations. The representative local static load is calculated by considering a three sigma environment of the vibration loads multiplied with the amplification factor $A_F$. The $G_{rms}$ value, the one sigma value, is chosen according to a launch load envelope (Grundmann et al. (113)), and its value is $12.4\,g$. The acceleration to be considered in the mechanism design is calculated according to equation 6.1.

$$a_m = 3 \cdot G_{rms} \cdot A_F \tag{6.1}$$

Table 6.3 provides the amplification factors for the sail spools with the stowed sail segments. Because the exact mounting position and orientation of Gossamer-1 on the launcher is also uncertain, the maximum amplification factor across all three axes was considered in the mechanism design process.

Table 6.3: Amplification factors for the sail spools with the stowed sail segments.

| Mechanism | $A_{Fx}$ | $A_{Fy}$ | $A_{Fz}$ | $A_{Fmax}$ |
|---|---|---|---|---|
| Sail Spool | 2.56 | 3.03 | 3.36 | 3.36 |

The Structural aspects of the stowed sail segments are not analyzed by simulation. The simulation of a configuration with multiple folded and coiled layers that are partly wrinkled is obviously difficult. Instead of using simulations, the integrity of the stowed sail segments under launch loads needs to be verified through testing (see Section 7.2.2).

### 6.3.2 Deployment loads for the Gossamer-1 configuration

In the following paragraphs, the model for the stowing and deployment geometry established in Section 4.2 will be applied on the design presented in Section 6.2. By combining the deployment geometry with the deployment mechanism forces (see Section 5.2) the progression of the deployment loads is predicted.

With the width $w$ of the folded sail segment, the function of the zig-zag folding line according to Equation 4.4 is described as

$$l_c(x_f) = \frac{0.23\,\mathrm{m}}{\pi} \cdot cos^{-1}\left[cos\left(\frac{\pi}{0.23\,\mathrm{m}} \cdot x_f\right)\right] \ . \tag{6.2}$$

Figure 6.7 shows a plot of this function.

The maximum thickness of the folded sail segment in the areas to be coiled consists of 12 layers Upilex-S foil, two layers of photovoltaics, the harness, the harness base sheet and up to three layers of adhesive. Note that the thickness is not constant along the width of the folded sail. Considering the thickness of the different layers of the sail (see Table 6.1), the maximum thickness is approximately $626 \cdot 10^{-6}$m. In the design presented here, the harness in the center of the sail with a width of $5 \cdot 10^{-2}$m is not coiled. The maximum length of the hypotenuse coiled on one spool is therefore calculated as

$$l_{h,max} = \frac{H}{2} - \frac{5 \cdot 10^{-2}\mathrm{m}}{2} = 2.666\,\mathrm{m} \ . \tag{6.3}$$

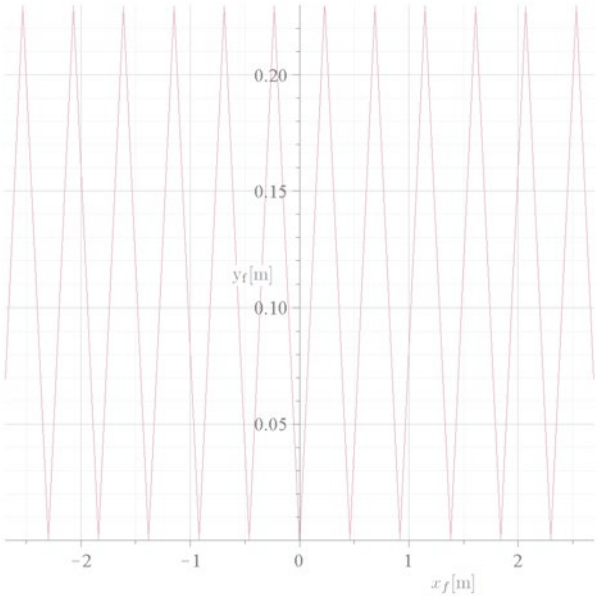


Figure 6.7: Zig-zag line of the folded cathetus.

The minimum thickness is considered to be one layer of Upilex-s foil ($7.5 \cdot 10^{-6}$ m). The mathematical model presented here considers a linear distribution of thickness along the coiled length (see Equation 4.7). The slope $m$ is calculated as

$$\begin{aligned} m &= \frac{dt}{dx} \\ &= \frac{\Delta t}{l_{c,max}} \\ &= \frac{626 \cdot 10^{-6}\,\text{m} - 7.5 \cdot 10^{-6}\text{m}}{2.666\,\text{m}} = 2.32 \cdot 10^{-4}\ . \end{aligned} \tag{6.4}$$

As mentioned before, the folded and coiled sail is far from being compressed to a state where the layers lie directly on top of one another. The folded sail is coiled on a spool with an outer radius $r_{max}$ of 30 mm. In order to take this into account, factor $c$ is calculated accordingly. In order to do this, two relations can be used. First, for the maximum coiling angle $\alpha_{max}$ the maximum radius is reached. This is described as

$$\begin{aligned} r(\alpha_{max}) &= r_i \cdot e^{m \cdot c \cdot \alpha_{max}} = r_o \\ \Leftrightarrow c &= \frac{1}{m \cdot \alpha_{max}} \cdot ln\left(\frac{r_o}{r_i}\right)\ . \end{aligned} \tag{6.5}$$

Secondly, for this maximum coiling angle the hypotenuse is coiled up to a length of $l_{h,max}$. This is described by calculating the arc length of the spiral according to Equation 4.13 as

$$\begin{aligned} l_{h,max} &= \frac{r_i \cdot \sqrt{1+m^2}}{m} \cdot (e^{m \cdot c \cdot 0} - e^{m \cdot c \cdot \alpha_{max}}) \\ \Leftrightarrow \alpha_{max} &= 114.91\,\text{rad} \\ \Rightarrow c &= 20.2\quad . \end{aligned} \tag{6.6}$$

The coiling direction differs for the two spools a sail segment is coiled on. The coiling direction is considered by the sign of $m \cdot c$. For the left coil in Figure 4.16(c), the sign is negative, and for the right coil it is positive. The right spiral is described by

$$r(\alpha) = 1.75 \cdot 10^{-1} \cdot e^{4.6896 \cdot 10^{-2} \cdot \alpha}\,[\text{m}] \tag{6.7}$$

Figure 6.8(b) exemplary shows the plot of this function.

The zig-zag line for the helix with alternating slope according to Equation 4.11 is given by

$$\begin{aligned} f_c(\alpha) =& 7.32 \cdot 10^{-2} \\ & \cdot cos^{-1}(cos(50.97 \cdot e^{4.69 \cdot 10^{-3} \cdot \alpha} - 87.72)) \\ & - 1.15 \cdot 10^{-1} \,[\mathrm{m}] \end{aligned} \tag{6.8}$$

and the complete function of the helix with alternating slope that represents the folded and coiled cathetus is thereby given according to Equation 4.5. Figure 6.8(a) gives an impression of the helix for the first rotations.

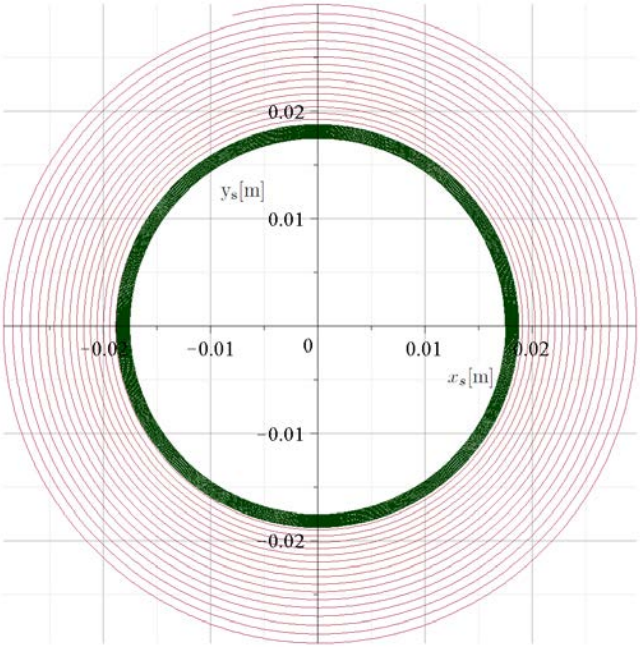


(a) SSpiral that represents the coiled hypotenuse of the sail segment. The red curve shows the function adjusted by factor $c$ according to the maximum radius $r_{max}$, achieved in the real coiling process, and for comparison the spiral for $c = 1$ that represents the ideal coiled sail that has the same volume as the folded segment.

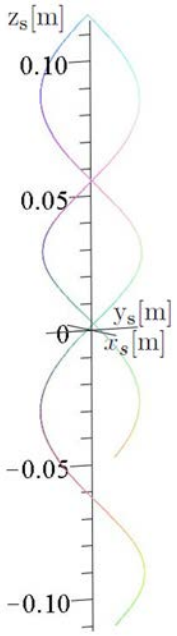


(b) Helix representing the folded and coiled cathetus.

Figure 6.8: Geometry of the coiled sail.

The deployment forces for the mechanism described in Section 5.2 are calculated for two copper beryllium springs that engage the gear. The parameters according to the Gossamer-1 design are given in Table 6.4.

The geometrical moment of inertia is calculated by

$$I = \frac{w_s \cdot t_s^3}{12} = 1.40625 \cdot 10^{-15} \,[\mathrm{m}^4] \,. \tag{6.9}$$

With Equation 5.1 and 5.2 the maximum spring force is calculated as

$$\begin{aligned} F_{max} = & 2 \cdot \frac{3 \cdot 125 \cdot 10^9 \cdot 1.40625 \cdot 10^{-15}}{(16 \cdot 10^{-3})^3} \cdot \\ & \sqrt{2 \cdot 16 \cdot 10^{-3} \cdot 2 \cdot 10^{-3} - (2 \cdot 10^{-3})^2} \,[\mathrm{N}] \\ = & 1.99 \,[\mathrm{N}] \,. \end{aligned} \tag{6.10}$$

and with Equation 5.8 and 5.9 the minimum spring force is calculated as

$$\begin{aligned} F_{min} = & \frac{3 \cdot 125 \cdot 10^9 \cdot 1.40625 \cdot 10^{-15}}{(16 \cdot 10^{-3})^3} \cdot \\ & tan\left[\frac{16 \cdot 10^{-3} \cdot sin^{-1}\left(\frac{16 \cdot 10^{-3} - 2 \cdot 10^{-3}}{16 \cdot 10^{-3}}\right)}{16 \cdot 10^{-3}} - \right. \\ & \left. \frac{\frac{2\pi \cdot 16 \cdot 10^{-3}}{30}}{16 \cdot 10^{-3}}\right] \cdot (16 \cdot 10^{-3} - 2 \cdot 10^{-3})\,[\mathrm{N}] \\ = & \, 1.1\,[\mathrm{N}]\ . \end{aligned} \tag{6.11}$$

Table 6.4: Parameter of the deployment mechanism for the calculation of deployment forces.

| Parameter | Symbol | Value [Unit] |
|---|---|---|
| Young's modulus | $E$ | $125 \cdot 10^9$ [Pa] |
| Spring width | $w_s$ | $5 \cdot 10^{-3}$ [m] |
| Spring length | $l_s$ | $16 \cdot 10^{-3}$ [m] |
| Spring thickness | $t_s$ | $0.15 \cdot 10^{-3}$ [m] |
| Spool radius | $r_i$ | $17.5 \cdot 10^{-3}$ [m] |
| Number of gear teeth | $n_z$ | 30 |
| Gear outer radius | $R$ | $16 \cdot 10^{-3}$ [m] |
| Gear engaging depth | $\Delta z$ | $2 \cdot 10^{-}3$ [m] |

The spring force as a function of rotation angle $\alpha$ is described by Equation 5.13 as

$$F_R(\alpha) = 1.1\,[\mathrm{N}] + \frac{1.99 - 1.1}{\pi} \cdot \cot^{-1}[\cot(15 \cdot \alpha)]\,[\mathrm{N}] \tag{6.12}$$

and the torque is described by Equation 5.14 as

$$\begin{aligned} T(\alpha) = & \, 15.4 \cdot 10^{-3}\,[\mathrm{Nm}] \\ & + \frac{31.84 \cdot 10^{-3} - 15.4 \cdot 10^{-3}}{\pi} \\ & \cdot cot^{-1}[cot(15 \cdot \alpha)]\,[\mathrm{Nm}]\ . \end{aligned} \tag{6.13}$$

With Equation 4.23, the analysis of the deployment geometry revealed that the hypotenuse of the deployed part of the sail segment, and thereby the folded layers alongside, are not under tension. For the geometry at hand, Figure 6.10 shows the length that is not tensioned. When the segment is fully coiled to angle $\alpha_{max}$ the slag is maximal, because the additional length of the cathetus deployed due to an offset of the uncoiling point from the sail plane (see Figure 4.18)has the biggest impact at the beginning of the deployment. Every time the uncoiling point reaches the maximum offset from the sail plane, another peak of the slack is visible. But due to the bigger overall dimensions of the deployed sail, the slack decreases. The point when the sail segment is fully deployed and slips off of the sail spool is not represented in the function. It is only then that the slack is zero.

Assuming that this slack is not compensated by manufacturing tolerance or an unsymmetrical deployment, the load during deployment is transferred through the cathetus of the sail segment. While the membrane is uncoiling, the deployment force necessary to overcome the brake torque is changing with radius $r(\alpha)$ according to Equation 4.24. This leads to a general increase in the total

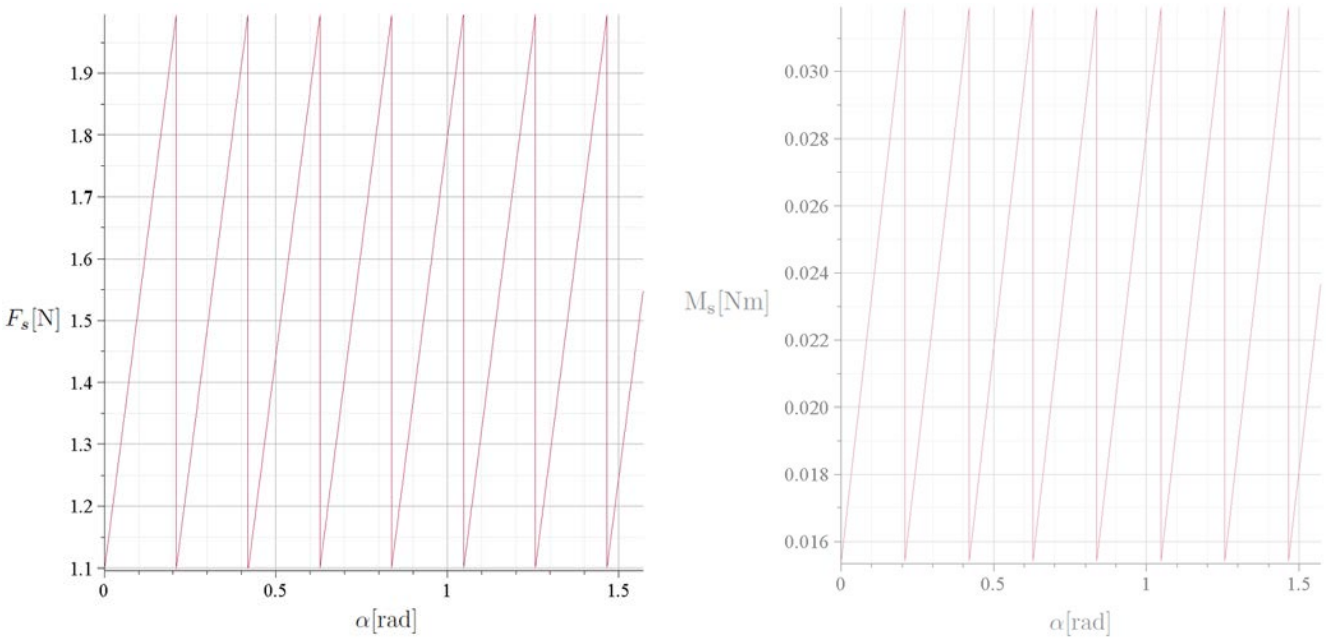


(a) Spring force.

(b) Spring torque.

Figure 6.9: Sail spool brake force and torque are generated by a leaf spring that engages into a gear on the spool (see Section 5.2).

forces throughout the deployment. The force components are calculated according to Equations 4.26 and 4.27. The deployment forces are introduced on both sides of the boom (see Figure, subscripts $I$ and $II$). Ideally both spools would deploy the sail segments in a symmetrical manner. In this case the $x$- and $z$-components of the deployment forces on each side would add up while the $y$-components cancel each other out. This would significantly decrease the bending load due to the $y$-component. However, the function of the forces shows oscillations due to the oscillation of the brake torque as well as the zig-zag folding, and it is unlikely in a real deployment that the phase of this oscillation would fully match. Assuming that the deployment of the sail segments would generally be simultaneously and thus at least in a good approximation synchronized there could still be a slight difference in the spool rotation. This would mean that while on the one side of the boom only the minimum brake force is present (the spring already snapped to the next gear tooth), the brake force on the other side of the boom is close to the maximum. Additionally the maximum forces are not significantly decreased by a small offset.

In order to get a more realistic impression of the combined loads that are transferred from both sail spools to the boom a small offset of $-0.001\,\text{rad}$ for $\alpha$ is assumed for the calculation of $F_{D_{II}}$. This small offset reflects that very small deviations of the geometry, e.g in the order of $1/100\,\text{mm}$ on the circumference of the gear, have a strong impact on the accumulation of forces. As this is very well within the order of expected manufacturing and assembling tolerances, this needs to be taken into account in the model. The progression of both deployment forces is shown in Figures 6.11(a) and 6.11(b). In all curves, a fast oscillation due to the brake force is present. While the main component in $x_b$-direction (see Figures 6.11(a) and 6.11(b), red curves) shows the general increase due to the smaller uncoiling radius, the other components are decreasing because the angles $\zeta$ and $\delta$ (see Figure 4.20) are decreasing with progressing deployment. The z-component (see Figures 6.11(a) and 6.11(b), blue curves) additionally shows an oscillation due to the zig-zag folding. Every time a maximum distance from the sail plane is reached ($z_s = \pm 0.5w$), a maximum of that force component is present.

The sum of both forces $F_{D,I}$ $F_{D,II}$ is presented in Figure 6.12. The sum of the forces reflects the progression of its components described previously. It should be pointed out that due to the

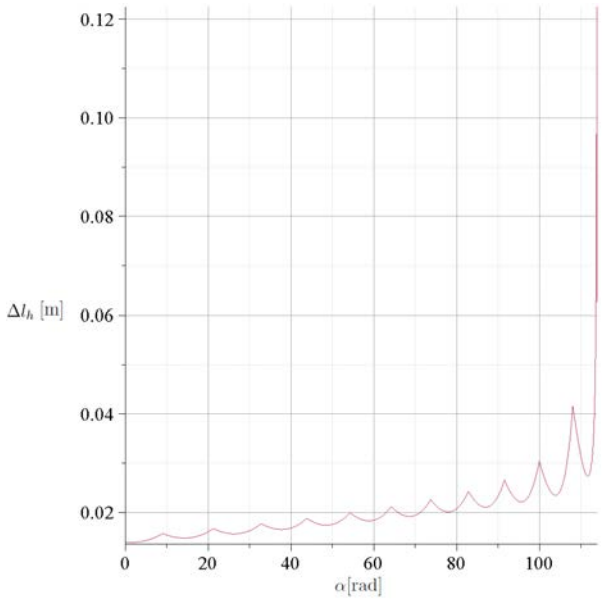


Figure 6.10: Slack of the deployed hypotenuse.

offset of the spool rotations, the $y_b$-components of the forces are not compensating for each other.

In order to calculate the torque and bending moments on the boom, the lever arm needs to be specified. The $x_b$-component corresponds to the length of the deployed boom according to Equation 4.20, the $z$-component corresponds to the uncoiling point of the cathetus according to Equation 4.11, and the $y_b$-component is a geometry parameter that purely depends on the Gossamer-1 design. The lever arm is expressed as

$$\vec{L} = \begin{pmatrix} l_b \\ 0.109\,[\mathrm{m}] \\ l_{c,z}(\alpha) \end{pmatrix} \tag{6.14}$$

The torque and bending moments are calculated according to Equation 4.28. The progression of the moments is shown in Figures 6.13(a) and 6.13(b). As it is for the forces, the fast oscillation due to the brake force is also present in the progression of the moments. Due to the varying offset of the uncoiling point from the sail plane, a torque around the $x_b$-axis (see Figure 6.13(a) and 6.13(b), red curves) is present that additionally oscillates according to the zig-zag folding. It decreases because the $y_b$- and $z_b$-components of the forces or the angles $\zeta$ and $\delta$ (see Figure 4.20) are decreasing throughout the deployment. The moment around the $y_b$-axis (see Figures 6.13(a) and 6.13(b), green curves) is the smallest and it would be the only moment if the offset of the spool rotation would not have been taken into account. The moment around the $z_b$-axis (see Figures 6.13(a) and 6.13(b), blue curves) reflects the additional oscillation due to the zig-zag folding in the same way as it is for the $z_b$-component of the forces.

When summarizing the moments, the influence of the offset is fully reflected in the results, which are presented in Figure 6.14. Without the offset of the spool rotation the torque around the $x_b$-axis as well as the bending moment around the $z_b$-axis (blue curves) would have been zero, which would give the wrong impression with respect to the real process. With the offset in the spool rotation, a torque about the $x_b$-axis (see Figure 6.14, red curve) and bending moment around the $z_b$-axis (see Figure 6.14, blue curve) is present in addition to the bending moment about the $y_b$-axis (see Figure 6.14, green curve). All torques show fast oscillation due to the spool brake force. The torque also oscillates according to the zig-zag folding and in accordance with the above-described force progressions decreases throughout the deployment. The biggest moment appears about the $z_b$-axis and increases throughout the deployment because of the increase of the

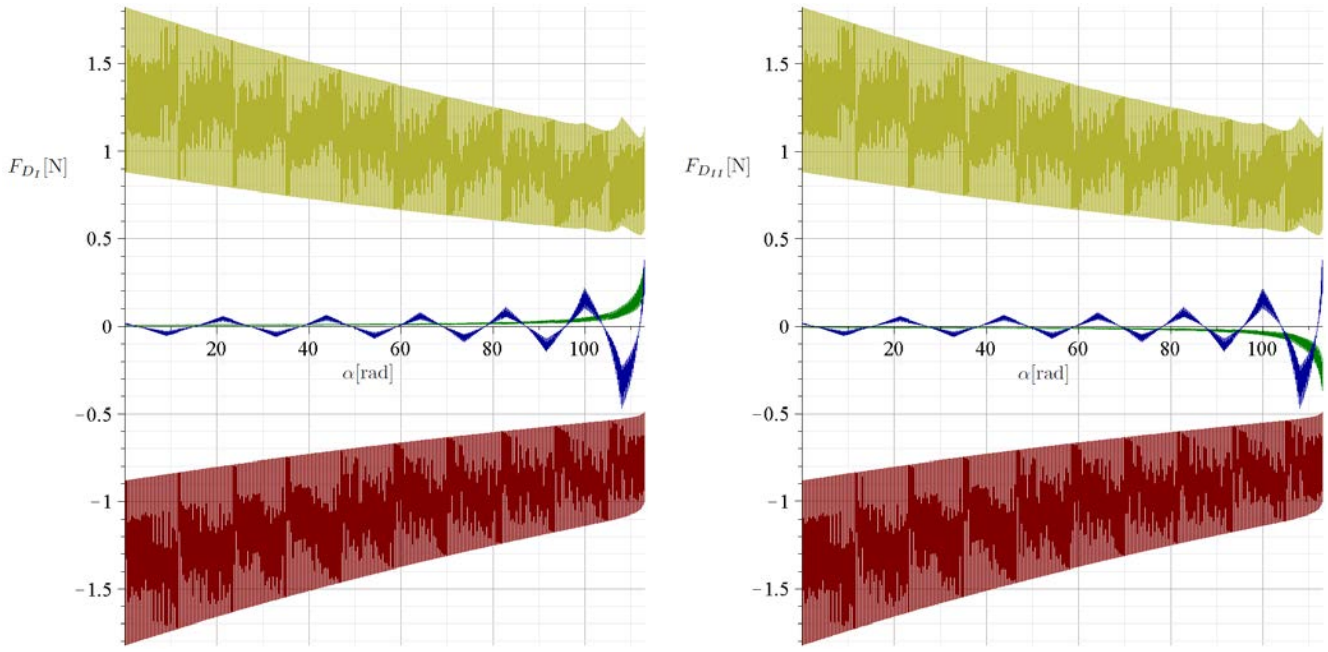


(a) Deployment force $F_{D_I}$.

(b) Deployment force $F_{D_{II}}$.

Figure 6.11: Calculated deployment force (yellow) and its components (red: $x_b$-component, green: $y_b$-component, blue: $z_b$-component).

$x_b$-component of the forces. The bending moment about the $y_b$-axis, which would be the only one if an ideally synchronized deployment would have been assumed, is small compared the other moments. It also oscillates according to the zig-zag folding (not fully visible in Figure 6.14) and decreases throughout the deployment.

### 6.3.3 Solar radiation pressure

For a solar sail, it is assumed that the main load case is the radiation pressure acting on the sail. In principle, a mission could include specific maneuver, for example an attitude change, docking, or the separation of a payload, which would require additional analysis.

The following equations describe the radiation pressure which is the fundamental physical principle for solar sailing. More detailed descriptions are provided by McInnes Colon (19, 35-36) describes the equations and its impact on solar sailing in more detail. The relativistic energy-momentum relation for a photon with a rest mass $m_0$ equal to zero directly connects the energy of a photon $E_\mathrm{p}$ to its momentum $p_\mathrm{p}$ by the speed of light $c$ as

$$\begin{aligned} E_\mathrm{p}^2 &= m_0^2 \cdot c^4 + p_\mathrm{p}^2 \cdot c^2 = p_\mathrm{p}^2 \cdot c^2 \\ \Rightarrow p_\mathrm{p} &= \frac{E_\mathrm{p}}{c} \ . \end{aligned} \tag{6.15}$$

The intensity of an electromagnetic wave is defined as its energy per time and area. Dividing the intensity by the speed of light leads, according to Equation 6.15, to a momentum per time and area. Momentum per time is by definition a force and force per area is pressure. The intensity divided by the speed of light is the so-called radiation pressure. For the intensity of the Sun $I_\mathrm{S}$ it is described as

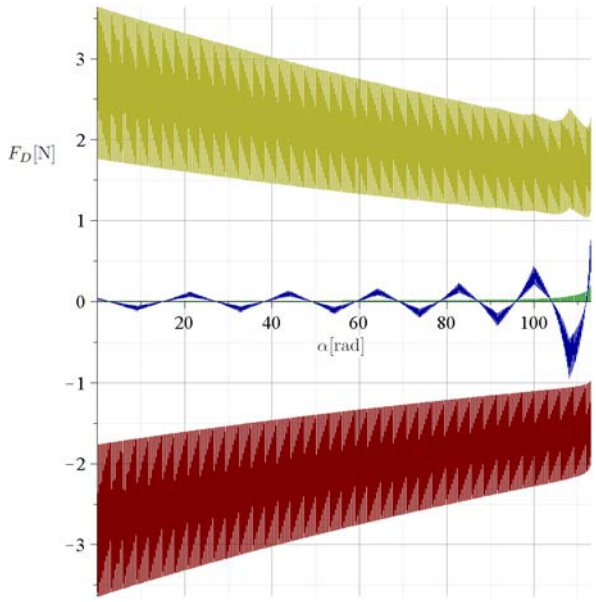


Figure 6.12: Calculated total deployment force $F_D$ (yellow) and its components (red: $x_b$-component, green: $y_b$-component, blue: $z_b$-component)

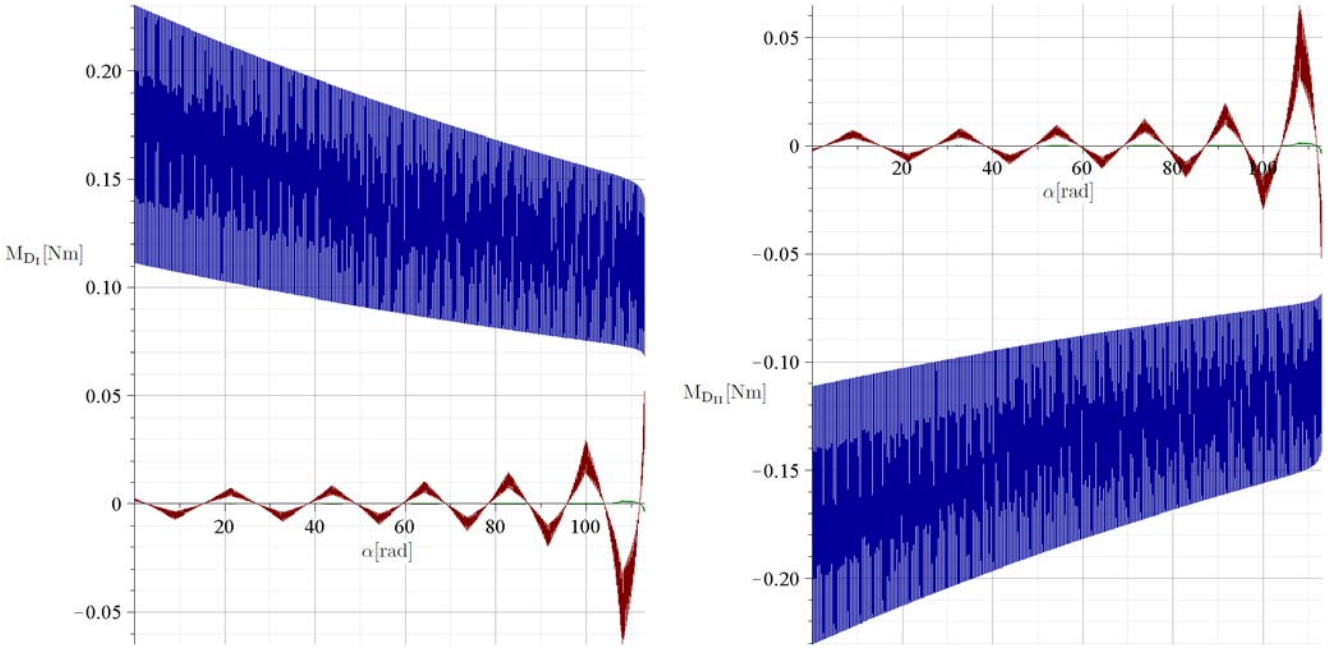


(a) Deployment moment $M_{D_I}$.

(b) Deployment moment $M_{D_{II}}$.

Figure 6.13: Calculated deployment moment and its components (red: $x_b$-component, green: $y_b$-component, blue: $z_b$-component).

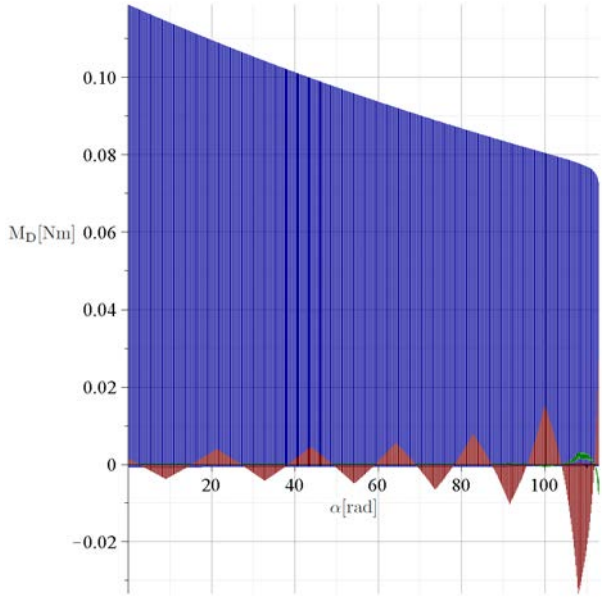


Figure 6.14: Calculated total deployment moments (red: $x_b$-component, green: $y_b$-component, blue: $z_b$-component).

$$p_{\mathrm{S}} = \frac{I_{\mathrm{S}}}{c} \ . \tag{6.16}$$

If the energy of the electromagnetic wave is absorbed by an irradiated material the momentum according to Equation 6.15 is transferred into the direction of the wave propagation. In case the wave is reflected, another momentum transfer appears into the direction of the reflected wave. For a perfect reflection on a perpendicularly irradiated surface that is fixed mounted and not accelerated the transferred momentum doubles as well as the radiation pressure because after the reflection the momentum points in the opposite direction. As a small remark, it should be pointed out that in the case of an accelerated solar sail the energy conservation is maintained by a change of energy of the reflected photon. The photon reflected has therefore also a smaller momentum and a longer wavelength (Planck relation).

The electromagnetic radiation is either specular reflected ($\rho_s$), diffuse reflected ($\rho_d$ ), absorbed ($\alpha_{\mathrm{S}}$) by a material or transmitted through a material ($\tau$). This is described with the fractions of the respective phenomenon as

$$\begin{aligned} 1 &= \rho_s + \rho_d + \alpha_{\mathrm{S}} + \tau \\ &\approx \rho_s + \rho_d + \alpha_{\mathrm{S}} \end{aligned} \tag{6.17}$$

The transmitted radiation is just not interacting with the material. For the material considered here, this part is considered to be negligibly small. The incoming wave that is specular reflected superimposes a force directed along the surface normal vector $\vec{e}_n$. The incoming wave of the diffuse reflectance causes a force directed along the Sun vector $\vec{e}_{\mathrm{S}}$, while the diffuse reflectance causes a resulting force directed along $\vec{e}_n$. Considering a Lambert's distribution, the integral through the hemisphere resulting in the factor of 2/3. The absorbed radiation causes a force acting along $\vec{e}_{\mathrm{S}}$. Thereby, the solar radiation force is described as $I_{\mathrm{S}}$, the speed of light $c$ and the surface area $A$ as

$$\vec{F}_{\mathrm{S}} = -\frac{I_{\mathrm{S}} \cdot A \cdot (\vec{e}_{\mathrm{s}} \cdot \vec{e}_n)}{c} \cdot \left[ (\alpha_s + \rho_d) \cdot \vec{e}_{\mathrm{S}} + \left( 2 \cdot \rho_s + \frac{2}{3} \rho_d \right) \cdot \vec{e}_n \right] \ . \tag{6.18}$$

The angle of incidence is here described as the scalar product of the unit vectors $\vec{e}_{\mathrm{S}}$ and $\vec{e}_n$. For the highly specular reflective foils considered here the diffuse reflectance may also be neglected. In this case, the solar radiation force for a perpendicular irradiated surface is described more simply as

$$\vec{F}_{\mathrm{S}} = \frac{I_{\mathrm{S}}}{c} \cdot A \cdot (1 + r_s) \cdot \vec{e}_s \ , \tag{6.19}$$

and the pressure is

$$p_{\mathrm{S,res}} = \frac{I_{\mathrm{S}}}{c} \cdot (1 + r_s) \ . \tag{6.20}$$

The pressure as a function of the distance to the sun for the different reflectance $r_s$ is presented in Figure 6.15.

### 6.3.4 Atmospheric drag

For a sail in a LEO the drag force caused by the residual atmosphere is the dominant force. The pressure coefficient in a flow with density $\rho_a$ and speed $v_a$ is defined as

$$C_p = \frac{p - p_\infty}{\frac{1}{2} \rho v_a^2} \ . \tag{6.21}$$

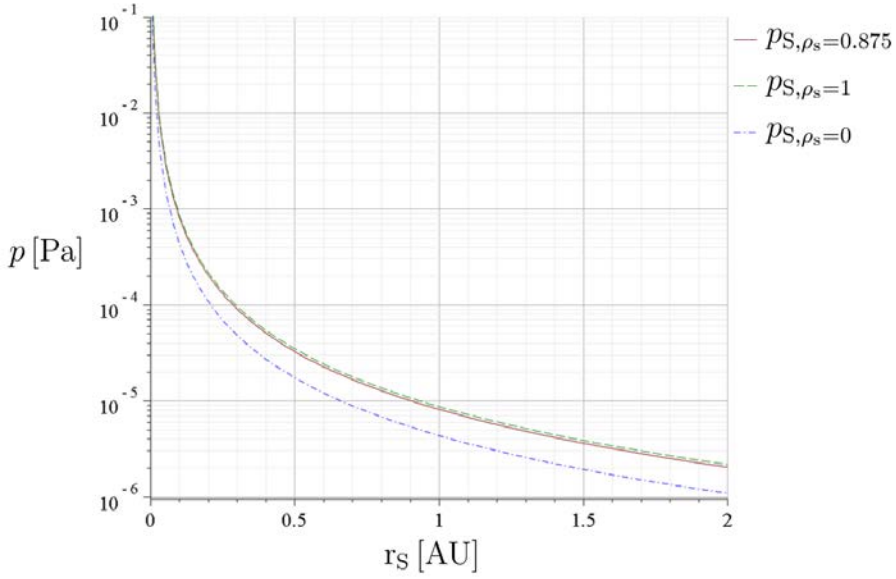


Figure 6.15: Solar radiation pressure as a function of the distance to the Sun for a reflectance of $Al/SiO_2/TiO_2$ of 0.875 (see Section 3.3.4), a perfect reflector ($\rho_s = 1$) and for a perfect absorber ($\rho_s = 0$).

Here, $p$ is the pressure building up at the sail (or another object) and $p_\infty$ is the pressure of the undisturbed flow (far away from the object). For hypersonic molecular flows the Newtonian flow theory is applicable (Anderson (115)). This theory can be used to calculate the pressure or the flow coefficient, respectively. Furthermore, drag coefficients are provided in different books in the field of astronautical engineering (e.g. Wertz et al. (116)). Some of these coefficients are calculated based on the observed decay of satellites. According to the Newtonian flow, the pressure coefficient of a flat plate is descried as

$$C_p = 2 \cdot sin^2(\alpha_a) \ . \tag{6.22}$$

Here $\alpha_a$ is the angle between the flow and the plate. The pressure and force components tangential to the flow are associated with "drag" and the components perpendicular to the flow are associated with "lift". For a plate, the coefficients according to the Newtonian flow are described as

$$C_d = C_p \cdot sin(\alpha_a) \ , \tag{6.23}$$

and

$$C_l = C_p \cdot cos(\alpha_a) \ \ . \tag{6.24}$$

Considering that in vacuum $p_\infty$ is 0, the corresponding pressure is described as

$$p = \frac{1}{2} \cdot \rho \cdot v_r^2 \cdot C_p \ . \tag{6.25}$$

The drag component of the pressure is given by

$$p_d = \frac{1}{2} \cdot \rho \cdot v_a^2 \cdot C_\mathrm{D} \ , \tag{6.26}$$

and the lift component is

$$p_l = \frac{1}{2} \cdot \rho \cdot v_a^2 \cdot C_\mathrm{L} \ . \tag{6.27}$$

Velocity $v_a$ does not always equal orbit velocity $v_o$. Considering an atmosphere that rotates with the Earth's angular velocity $\omega_\mathrm{E}$ (see Griffin and French (117)), the orbit velocity and the atmosphere velocity are superimposed as

$$v_a = v_o + \omega_\mathrm{E} \cdot r_o \cdot \cos i \tag{6.28}$$

Here, $r_o$ is the orbit ratio and $i$ is the orbit inclination. For Gossamer-1 an orbit with a high inclination close to 90° was likely. In this case the orbit velocity is indeed the velocity of the flow. It is calculated according to the Vis-viva equation as

$$v_a = v_o = \sqrt{\mu \cdot \left(\frac{2}{r_o} - \frac{1}{a}\right)} \tag{6.29}$$

For a perpendicular plate or sail, respectively, the pressure coefficient equals the drag coefficient and it can be estimated according to the Newtonian flow as 2. According to ECSS (118) the Jacchia-Bowman semi-empirical atmospheric model 2006 (JB2006) should be used for an estimation of the atmospheric density. For a drag force estimate, the density is used according to the table data provided in that standard, and intermediate values are interpolated linearly. The drag force for circular orbits ($r_o = a$) is shown in Figure 6.16.

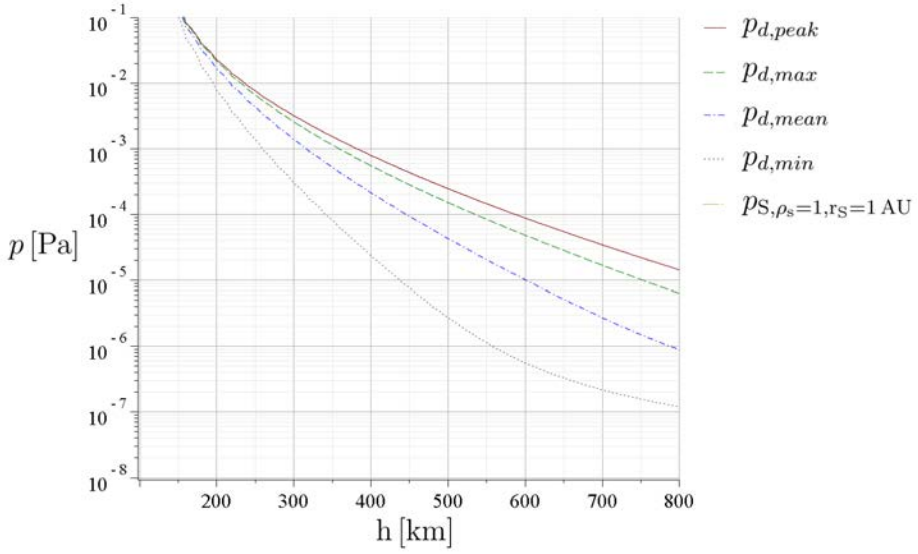


Figure 6.16: Pressure due to drag on a surface directed into the flight direction on a circular polar orbit for different atmospheric densities according to the JB2006 model (ECSS (118)) as a function of the orbit height.

## 6.4 Load introduction considerations

Two designs for the sail segment's load introduction being considered. One sail design provides curved edges with a cable, also referred to as rigging, guided in a pocket along the edges as illustrated in Figure 6.17, and a second design with straight edges without a rigging. While the first segment is tensioned through the rigging, the second is tensioned directly through the corners of the sail segment. A stainless steel cable of 0.09 mm made of $1 \times 7$ wires was considered (see Car (112)) as cable. The Young's modulus of the foil was considered with 9.893 Gpa and for the cable with 200 GPa. The poison ratio of all materials is approximated at 0.3.

In order to get an impression of the stress-strain state of the sail under pressure loads the two configurations were transferred to an ANSYS finite element model. The results are shown in Figure 6.18.

The sail with the straight edges is tensioned directly at the corners that are cut off to a length of about 30 mm. The pretension with a reaction force of about 2 N is applied through a displacement of the edge of 0.1 mm along the angle bisecting. Wrinkles appear due to the tensioning. If the

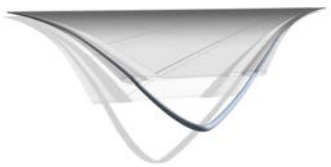

Figure 6.17: Sail corner with rigging guided in a pocket along the sail edges.

elements are not sufficiently small to map the wrinkle geometry no convergence is found. In order to reduce the computational effort, only half of the sail is modelled with 176312 SHELL181 elements. The elements' size ranges between 1 mm and 20 mm. In a first step the configuration is pretensioned by the displacement, and in a second load step, pressure of $9.1\,\mu\mathrm{Nm}^{-2}$ is applied to the surface. The pressure is an approximation for the solar radiation pressure at 1 AU for a fully reflective surface.

The curved edge sail employed BEAM188 for the rigging and ANSYS SHELL181 shell elements. The young modulus was considered with $2 \cdot 10^{11}$ Pa. Along the edges the elements were contacted with COTA176 elements applied on the beam elements, and TARGET170 elements along the shell edge. In a first loadstep the sail is pretensioned by a displacement such that the reaction force is again 2 N, and in a second loadstep pressure of $9.1\,\mu\mathrm{Nm}^{-2}$ is applied. The coefficient of friction between rigging and the sail membrane pocket is estimated with 0.3. The radius of the curved edges is 20 m. Out-of-plane forces combined with contact elements lead to convergence problems. The model had to be set up carefully with respect to the contact algorithms and the contact parameters. The mesh has a total of 41365 nodes and 38809 elements.

Due to the rigging, the tensioning loads are introduced along the entire edge of the sail. In consequence, the tension state of the sail is more even compared to the load introduction in the corners of the sail. The stress in the sail tensioned through the rigging is smaller because the forces are mainly transferred through the rigging and not through the sail membrane. With the rigging the formation of wrinkles is avoided. This is a consequence of the fact that with this kind of load introduction there are no areas that are have pressure loads when tensioning the sail (no negative principle stress). The wrinkles appearing when tensioning the sail through the corners are small, and the main deformation appears at the load introduction point and is a deformation in the plain of the sail.

When analytically investigating the load distribution, it is found that forces along the sail edges follow the Euler-Eytelwein belt friction equation. Figure 6.19 shows the relation of the normal force $F_N$ and the friction Force $F_R$ that are transferred to the sail along the sail edge on a differential element of the edge. The equilibrium of foces is described as

$$dF_R - (F + dF) \cdot cos\left(\frac{d\varphi}{2}\right) + F \cdot cos\left(\frac{d\varphi}{2}\right) = 0 \ , \tag{6.30}$$

and

$$dF_N - (F + dF) \cdot sin\left(\frac{d\varphi}{2}\right) - F \cdot sin\left(\frac{d\varphi}{2}\right) = 0 \ . \tag{6.31}$$

Considering that

$$cos\left(\frac{d\varphi}{2}\right) = 1 \ , \tag{6.32}$$

$$sin\left(\frac{d\varphi}{2}\right) = \frac{d\varphi}{2} \ , \tag{6.33}$$

and neglecting terms of higher order leads to

$$dF_N = F d\varphi \ , \tag{6.34}$$

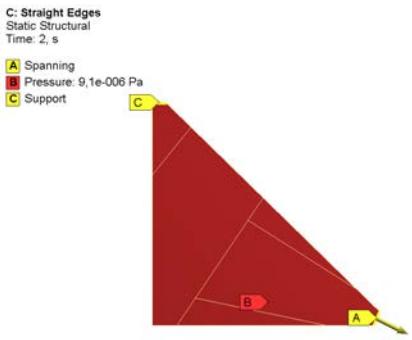


(a) Straight edges model, spanned by displacement.

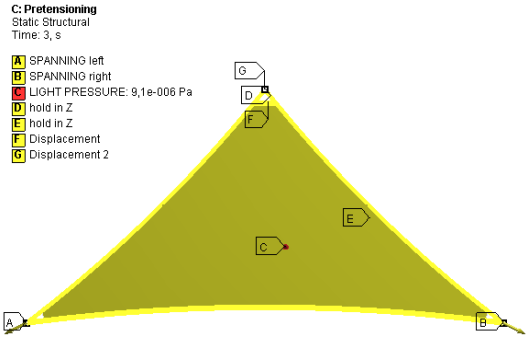


(b) Rigging model, spanned by displacement.

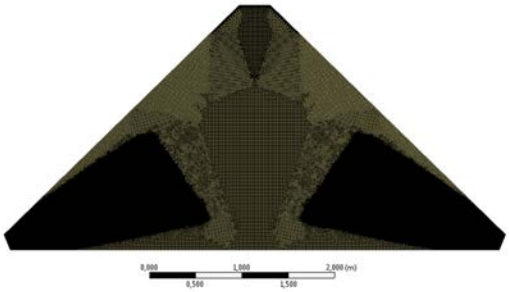

(c) Mesh for straight edge model.

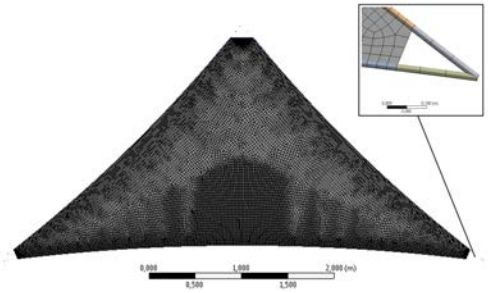

(d) Mesh for rigging model.

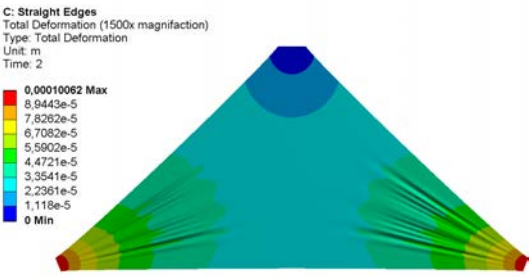


(e) Straight edge model total displacement.

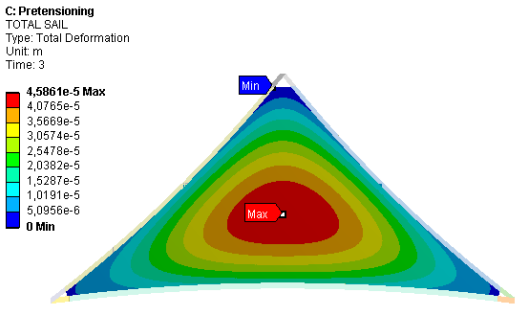


(f) Rigging model total displacement.

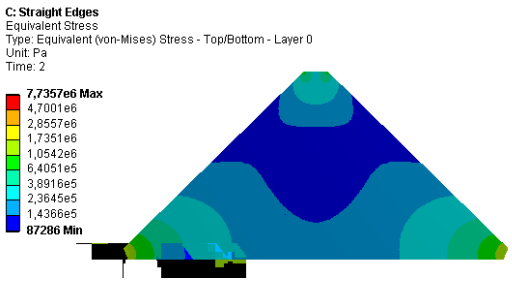


(g) Straight edge model von-Mises stress.

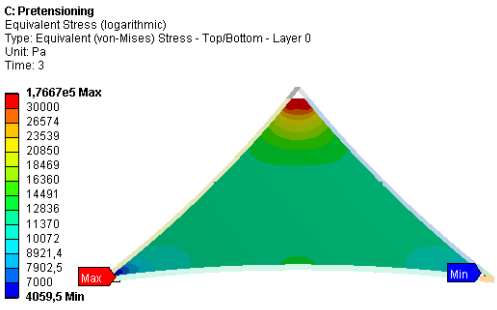


(h) Rigging model von-Mises stress.

Figure 6.18: Comparison of load introduction at the sail corners (left side) and through a rigging with curved edges (right side).

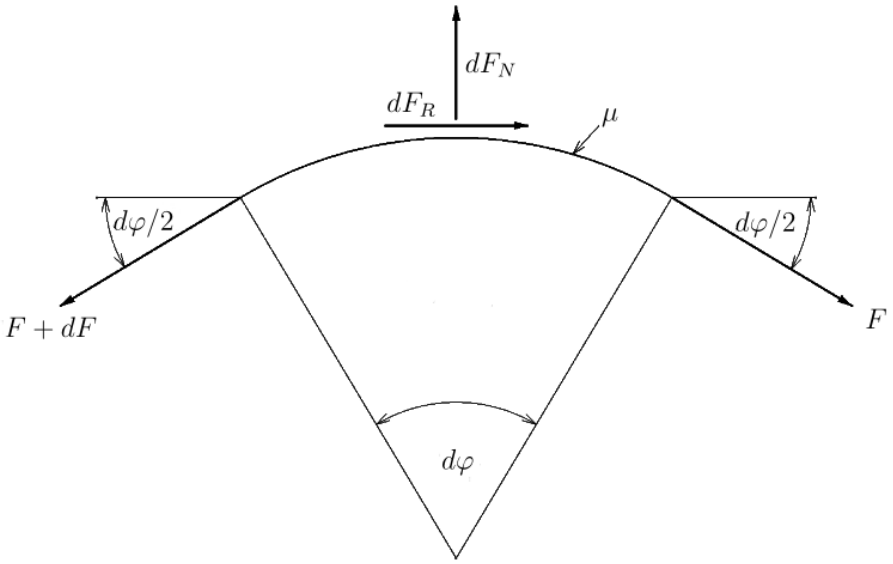


Figure 6.19: Friction between rigging and sail segment.

and

$$dF = dF_R = \mu dF_N \ = \mu F d\varphi. \tag{6.35}$$

Here, it was taken into account that the ratio of friction force and normal force is usually describe by the empirically determined friction coefficient $\mu$. Separation of variables and integration results in the well known Euler-Eytelwein belt friction equation as

$$F = F_R = \mu \cdot F_N = \mu \cdot F_0 \cdot e^{-\mu \cdot \varphi} \ . \tag{6.36}$$

Here, $F_0$ is the force applied at the sail corner, and $\varphi$ is the angle of the curved edge.

For the case presented here the axial forces in the rigging are shown in Figure 6.20. Force $F_{N,b}$ in the rigging along the bottom edge follows the function according to Equation 6.36 as

$$F_{N,b} = 1.535 \cdot e^{-0.3 \cdot \varphi} \ . \tag{6.37}$$

The function describes the force along the edge from one of the corners to the middle of the edge. The minimum fore appears in the middle of the edge at a distance of 2.423 m and the corresponding angle of 0.121 rad as

$$F_{N,b_{min}} = 1.535\,\mathrm{N} \cdot \mathrm{e}^{-0.3 \cdot 0.121} = 1.481 \ . \tag{6.38}$$

The force in the side edge follows the Euler-Eytelwein equation as

$$F_{N,b} = 0.925 \cdot e^{-0.3 \cdot \varphi} \ . \tag{6.39}$$

In order to verify that the force distribution of the finite element model also corresponds to the Euler-Eytelwein equation for different friction coefficients, two more simulations with friction coefficients of 0.5 and 15 were made and compared. The comparison is shown in Figure 6.21. The agreement of the two models is confirmed again. Therefore, future finite element models can be significantly simplified by directly considering the force distribution according to the Euler-Eytelwein equation.

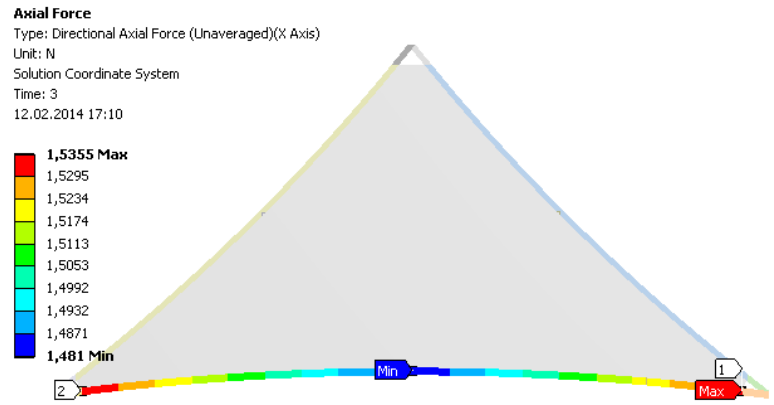


(a) Rigging force along the bottom edge ("hypothenuse").

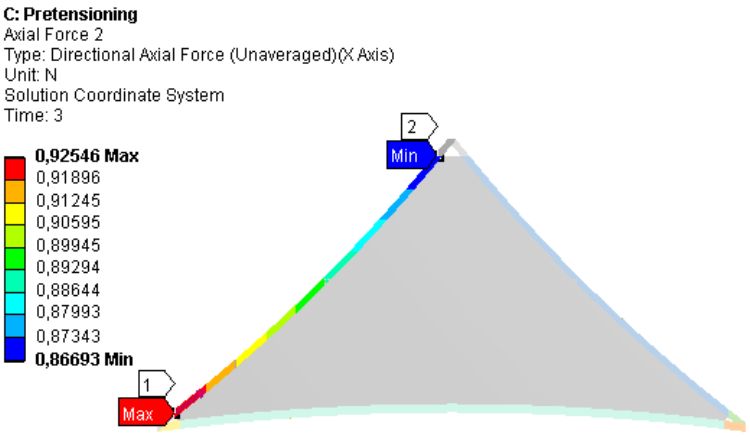


(b) Rigging force along the side edge ("cathetus").

Figure 6.20: Axial force in the rigging that slides along the edges of the sail segment with a friction coefficient of 0.3.

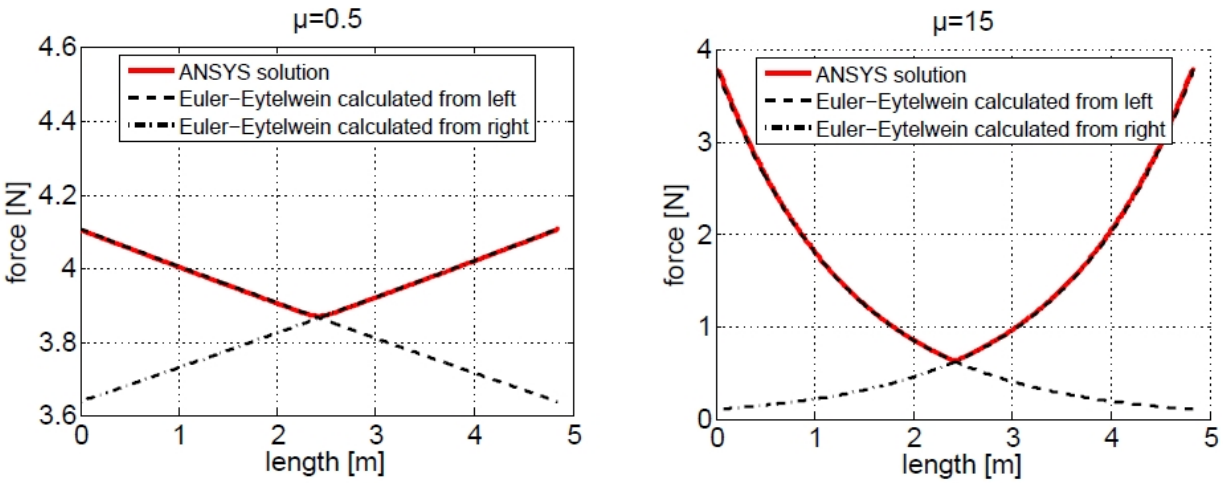


Figure 6.21: Axial force in the bottom rigging (red line) in comparison with the belt friction equation (black dashed line). Calculated with a low coefficient of friction of 0.5 on the left. Calculated with a high coefficient of friction of 15 on the right.

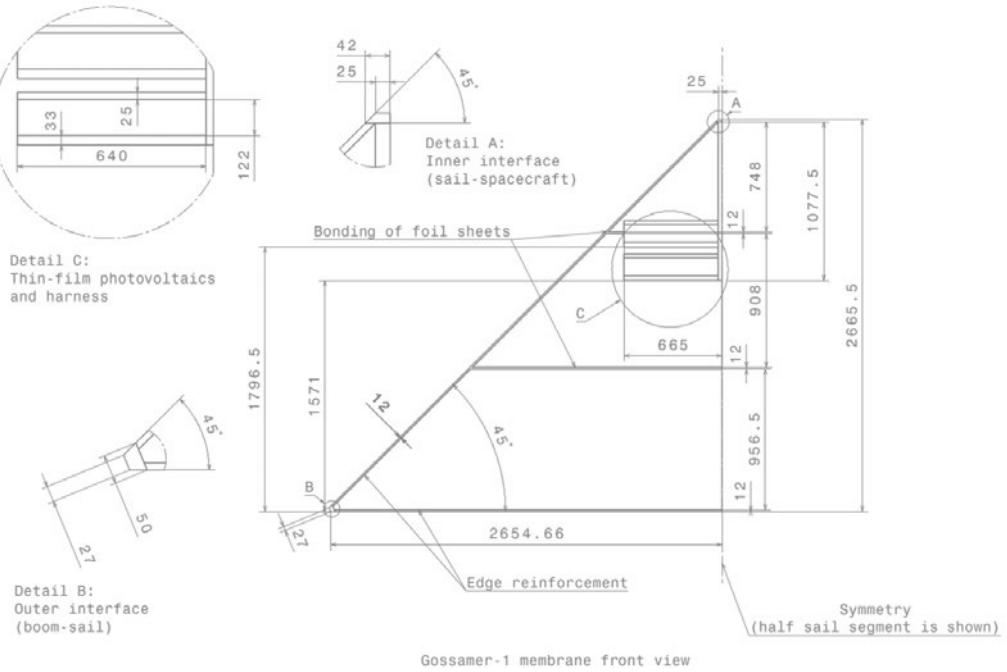


Figure 6.22: Drawing of the simplified geometry of the Gossamer-1 membrane used for the finite-element analysis. Note that only the half sail segment is shown and that the sail is symmetric to the height of the triangular-shaped full sail segment.

### 6.4.1 Analysis of the deployed Gossamer-1 membrane

For the analysis of the membrane deformation and the stress in the membrane under pressure loads such as drag and solar radiation pressure, a finite element model is used. It was implemented in ANSYS Workbench 15. The sail geometry, including areas with thin film photovoltaics, was modeled with the CATIA V5R20 Computer-Aided Design (CAD) tool. From that model a simplified version for the analysis was derived. The geometry is shown in Figure 6.22. The simplified model only shows one half of a sail segment. When further processed in the finite element analysis the symmetry of the segment was used to reduce computational effort. The Catia CAD model, which only consists of surfaces, was imported into the ANSYS Workbench. This way, the software automatically applies shell elements to the areas. The sail is very thin, especially compared to its other dimensions. In consequence, it is common for those structures to use two-dimensional shell elements instead of modeling the complete body, which would also require very small elements to resolve the thickness properly and in consequence would dramatically increase the computational effort. Figure 6.23 gives an overview of the finite element model. When tensioning such a thin membrane through the corners, it will always result in a wrinkled surface. In a static case, the wrinkling pattern has to result in an equilibrium between internal and external forces. In addition, the wrinkles will appear such that an energy minimum of strain energy is achieved. The formation of wrinkles is comparable to the buckling of a shell. If the membrane is perfectly aligned in its plane, relatively high compression loads can be carried, but the smallest out-of-plane deformation leads to a loss of stability with increasing out of plane deformations. This sudden change in compression stiffness leads to the formation of wrinkles so that the compression loads are reduced. Such a process with a change of stiffness due to the deformation is nonlinear and requires a nonlinear finite element analysis. In the analysis at hand, it was decided to use an implicit simulation. If the model converges in an equilibrium state, it is likely representing the real physical processes. The alternative would be an analysis with explicit integration of the structural differential equations over time (e.g. with the software LS-DYNA). This kind of simulation needs

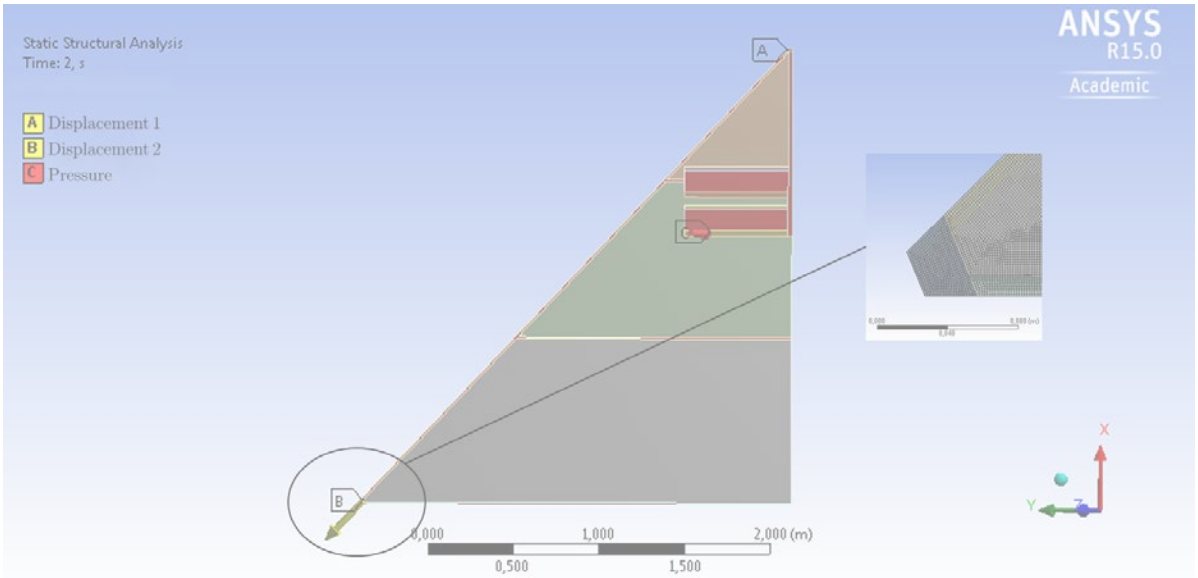


Figure 6.23: Geometry transferred into a finite element shell model in ANSYS 15. It is meshed homogeneously with quadratic shell elements of edge length $1.5 \times 10^{-3}$ m. At the inner edge, the displacement is set to zero. At the outer edge the displacement in a negative x- and positive y-direction is set to $1.3 \times 10^{-5}$ m. Pressure is applied along the z-direction on all surfaces with $10^{-2}$ Pa.

to be treated with more care regarding its interpretation.

In order to resolve the wrinkling pattern in such a membrane, a very fine mesh is required so that the geometry of one wrinkle is at least represented with four elements. If the mesh cannot represent the wrinkling, it leads to a non-converging model. This means the algorithm cannot find the equilibrium between internal and external forces because the equilibrium is reached by the wrinkling, which cannot be represented with elements that are too big. The stronger the tension in the membrane, the finer the wrinkling gets and in consequence, a finer mesh is needed for the model to converge. For the loading considered here, elements with an edge length of $1.5 \times 10^{-3}$ m were required.

The analysis is run in two steps. First, the membrane is pretensioned in plane and in a second step the pressure is applied. When the membrane is pretensioned, no wrinkling occurs because the model of the membrane is perfectly aligned in the membrane plane and thus can be loaded with compression loads. Then, if a small distortion is applied, in this case due to the pressure, the wrinkling occurs. The Gossamer-1 sail is only slightly tensioned. It is intended to maintain a load of approximately 2 N at the sail boom interfaces. The load is applied by a displacement at the outer corner of $1.3 \times 10^{-5}$ m in both x- and y-direction along the cathetus of the sail triangle (note that only the half triangle is shown in the pictures). The pretension is done in one load step. The simulation was intended to cover a pressure of up to $10^{-2}$ Pa in order to take the orbit drag loads into account. The load was applied in 23 substeps and overall 56 iterations were required by the algorithm to find a converged solution.

The Young's modulus $E$ considered for the different areas of the segment are given in Table 6.5. It was estimated as a mean value of the layers in one area. Each layer consists of a material with a Young's modulus $E_i$ and has a thickens of $d_i$, and the mean Young's modulus is thereby calculated as

$$E = \frac{\sum_i E_i d_i}{\sum_i d_i} \tag{6.40}$$

Table 6.5: Material Parameters, estimated by employing the Young's modulus of Upilex-S

| Sail Area | Thickness [m] | Young's modulus [Pa] |
|---|---|---|
| Upilex-S foil with aluminum | $7.7 \times 10^{-6}$ | $1.26 \times 10^{10}$ |
| Thin-film Photovoltaic | $8.9 \times 10^{-5}$ | $0.71 \times 10^{10}$ |
| Photovoltaic and Harness | $1.3 \times 10^{-4}$ | $1.85 \times 10^{10}$ |
| Mid-Harness | $6.9 \times 10^{-5}$ | $4.14 \times 10^{10}$ |
| Edge reinforcement / Sheet bonding | $7.5 \times 10^{-5}$ | $2.57 \times 10^{10}$ |
| Corner reinforcement | $5.0 \times 10^{-5}$ | $4.07 \times 10^{10}$ |

The stress according to the finite element analysis is shown in Figure 6.24. Considering an ultimate tensile strength of 657 Mpa for Upilex-S (see Table 3.1), the maximum von Mises stress, shown in Figure 6.24(a), is still one order of magnitude smaller. Therefore, the stress due to the mission loads is well inside tolerable load limits. Figure 6.24(b) shows the stress in the direction perpendicular to the folding lines. This stress is a measure of how far the folding lines are opening and is an input for the analysis shown in Section sec:foldinglines.

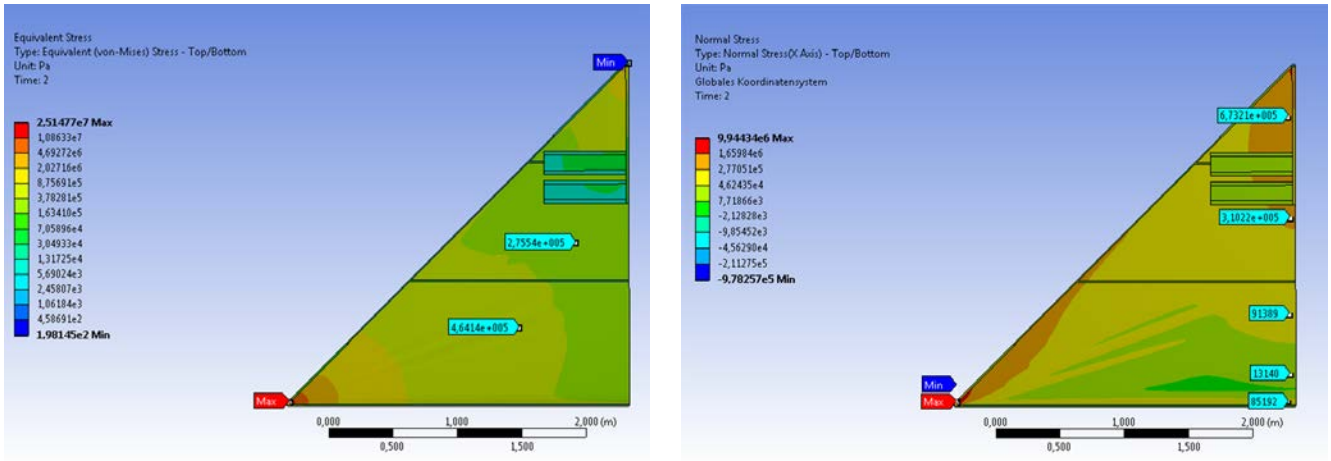


(a) Von-Mises stress.

(b) Stress in x-direction (perpendicular to folding line).

Figure 6.24: Resulting stress according to finite element analysis.

The force reaction at the outer corner of the sail is transferred through the sail boom interface to the booms. Therefore it is of particular interest for the sizing of booms and interfaces. It is shown in Figure 6.25.

The deformation according to the finite element analysis is shown in Figure 6.26. The biggest deformation appears in the middle of the hypotenuse of the segment. For the pressure load of $10^{-2}$ Pa and the relatively low pretension of about 2 N at the sail corner, the deformation in out-of-plane direction at this point is about 10 mm. Small wrinkles in the area along the angle bisecting between hypotenuse and cathetus are forming.

The data achieved with the finite element analysis is further processed in order to generate a simplified model for attitude simulations of the sail in a LEO. Therefore, the maximum out-of-plain displacement is described with a fitting function based on the results of the finite element analysis as

$$z_{max} = -0.11 \cdot \sqrt{p} \ . \tag{6.41}$$

Here, $z_{max}$ is the out-of-plane displacement, $p$. This function and the finite element results are shown in Figure 6.27. For very low orbits below about 250 km the pressure exceeds $10^{-2}$ Pa and

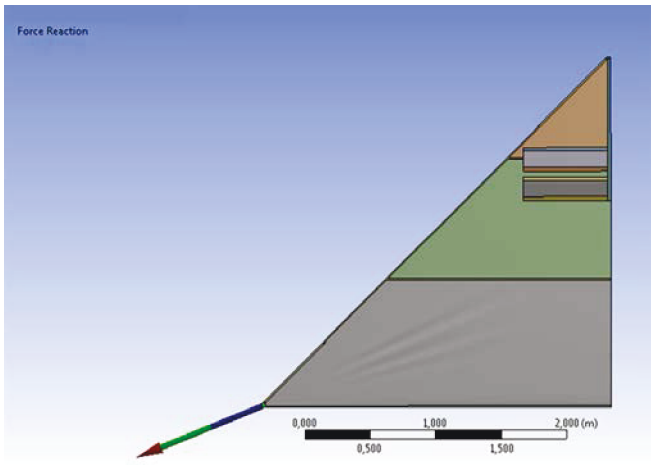


(a) Visualization of reaction force.

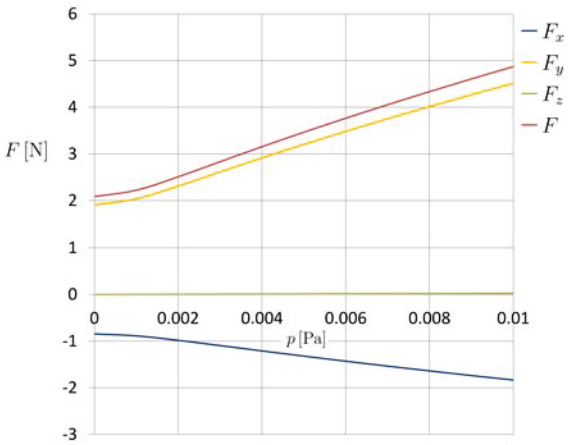


(b) Progression of reaction force with increasing pressure.

Figure 6.25: Reaction force at the outer corner.

Equation 6.41 can be used for an extrapolation. Figure 6.28 shows the simplified structure of the deployed sail used for the attitude simulation. In this model the central edges of each quadrant can move along the out-of-plane direction according to Equation 6.41. The attitude simulations are presented in Pirovano et al. (119).

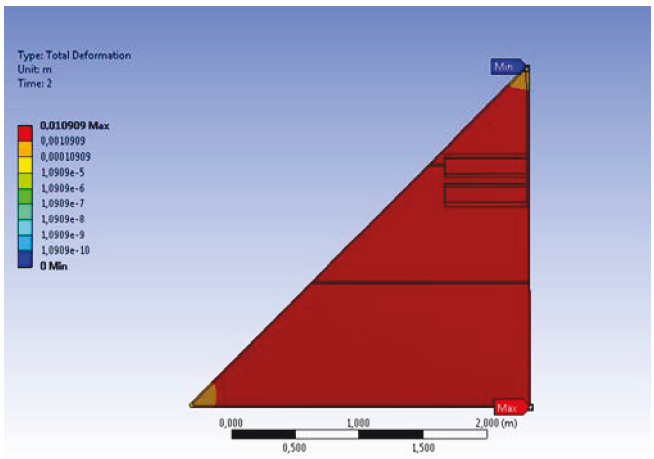


(a) Total deformation

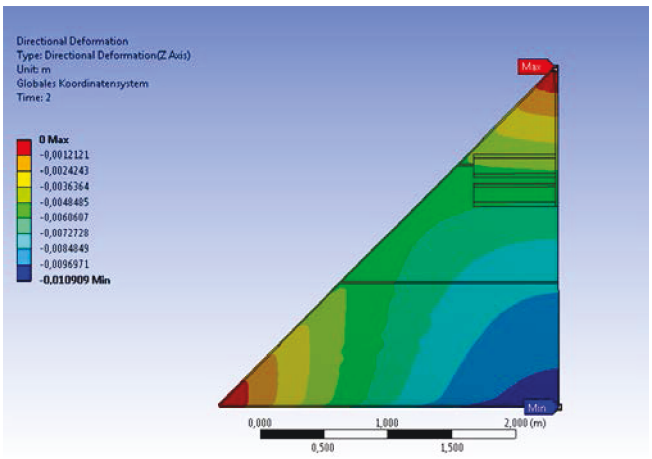


(b) Out-of-plane Deformation

Figure 6.26: Resulting deformation according to finite element analysis.

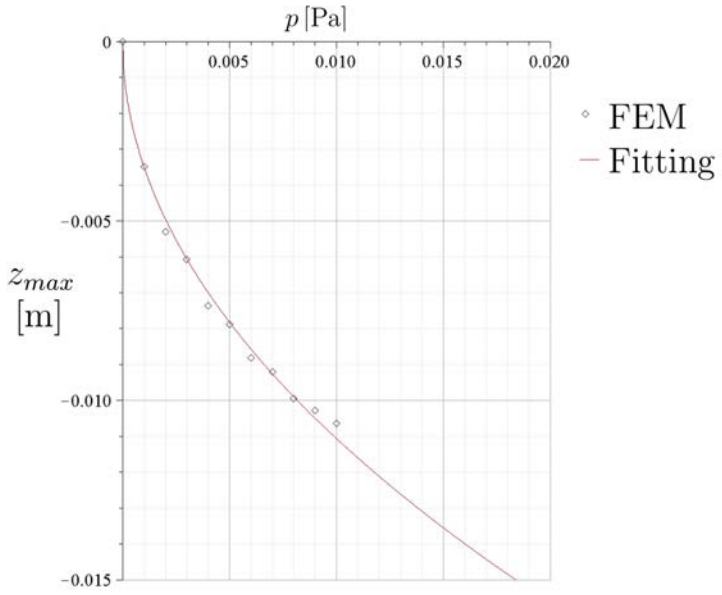


Figure 6.27: Curve fitting according to Equation 6.41 for the maximum out-of-plane deformation.

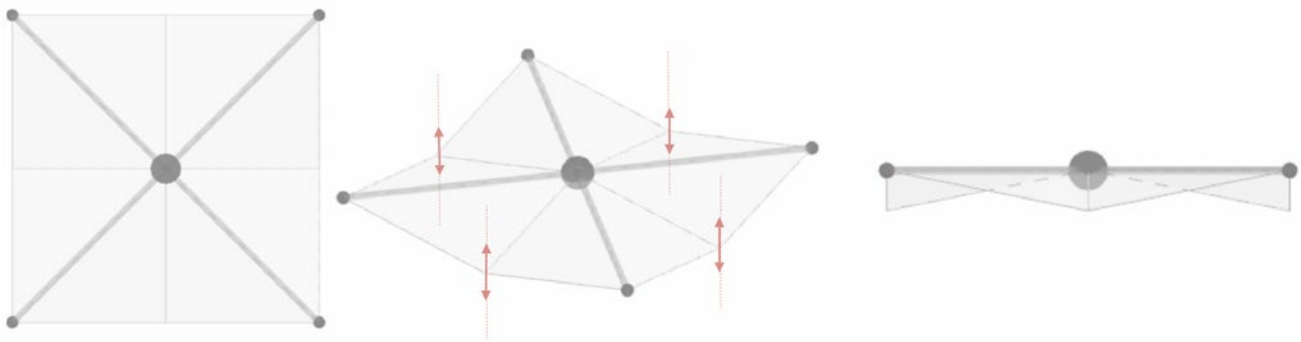

Figure 6.28: Simplified model of the sail used for dynamics simulations.

## 6.5 Analysis of folding lines

When implementing the folding, plastic deformations of the foil, referred to as folding lines, occur. This areas appear to be a critical point in the current design because the coatings might get destroyed in such a folding line and the geometry might lead to reflections of the incident light that could cause a temperature increase. The folding line geometry is determined by microscope measurements shown in Section 6.5.1, and by geometrically analyzing the path of rays the impact on the thermal design is evaluated Section 6.5.2.

### 6.5.1 Measurement of folding line geometry

In order to analyze the folding lines in more detail, the geometry of these folding lines was measured with microscopes. For this purpose samples as shown in Figure 6.30 with a width of 40 mm and a

Figure 6.29: Folding line.

length of 200 mm with a folding line in the middle were prepared. The folding lines of the samples were impressed with a standard weight of 500 g as shown in Figure 6.30(a). The weight was placed on the folding line for five minutes. A thin metal sheet was attached with the transfer adhesive to the sample edges with two threads that allow a uniform tensioning of the sample.

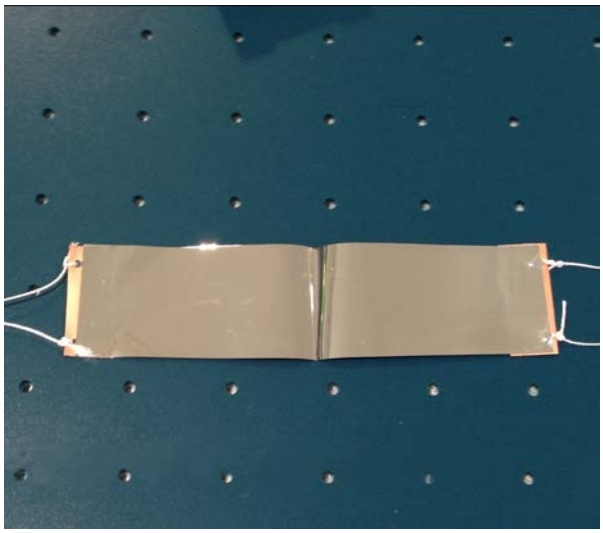

(a) Sample of Upilex-S 7.5 $\mu$m coated with 100 nm aluminum on both sides with a folding line.

(b) Defined folding of the specimen using a 500 g standard weight.

Figure 6.30: Sample for folding line investigation.

The geometry of an untensioned folding line was measured with a Keyence VR-3200 optical microscope. The microscope generates an ASCI file with Cartesian surface coordinates with a varying resolution of approximately between $10^{-2}$ and $10^{-1}$. Figure 6.31(a) shows a visualization of the surface coordinate points of the middle section of the sample with a width of about 30 mm and a length of about 100 mm. These surface coordinates were then further processed to a surface CAD model shown in Figure 6.31(b). For possible further analysis a measurement along a line in the middle of the sample was fitted to a function of type

$$f_i(x) = -K_0 \cdot \exp(-K_1 \cdot x^2) + K_0 \tag{6.42}$$

This function can also be used to approximate the smallest opening angle $\psi$ of the folding line at

(a) Visualized coordinate points of measurement with Keyence VR-3200 optical microscope.

(b) Processed CAD surface model.

Figure 6.31: Measurements of folding lines with Keyence VR-3200 optical microscope.

the point where $f_i$ has the highest slope at

$$\frac{d^2 f}{dx^2} = 0$$
$$\Rightarrow x_{\alpha_{f,min}} = \pm \frac{\sqrt{2}}{2 \cdot K_1} \ . \tag{6.43}$$

The opening angle is given by

$$\psi = 2 \cdot \left[ \pi - tan^{-1} \left( \frac{df(x_{\alpha_{f,min}})}{dx} \right) \right]$$
$$= \pi - 2 \cdot tan^{-1} \left( K_0 \cdot \sqrt{2 \cdot K_1} \cdot e^{-0.5} \right) \tag{6.44}$$

For the untensioned sample the function describes the geometry with a standard deviation of 0.3 as

$$f_0(x) = -4.66\,\text{mm} \cdot \exp(-0.17 \frac{1}{\text{mm}} \cdot \text{x}^2) + 4.66\,\text{mm} \ . \tag{6.45}$$

The opening angle according to Equation 6.44 is 62.5°. The geometry and the fitting function for the untensioned sample is shown in Figure 6.32. It needs to be pointed out that the sample

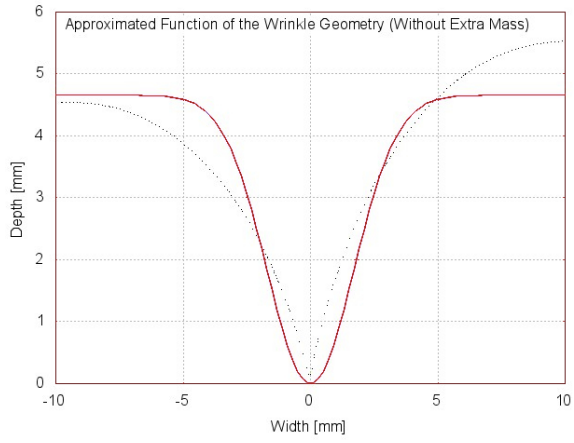


Figure 6.32: Measured geometry of the folding line in the middle of the sample and the fit function according to Equation 6.45 for an untensioned sample.

was apparently a little tilted during the microscope measurement. This led to the relatively high deviation of the fitting function. For future analysis the measure points could be orated around the zero point such that the depth of the folding is equal on both sides.

In order to get an impression of the microscopic nature of tensioned folding lines and the coating inside a folding line, a scanning electron microscope from the IWT (Siftung und Insitut für Werkstofftechnik) in Bremen was used. The generated images offer information about the topography of the sail's surface, and especially of the folding lines. The topography of folding lines tensioned with different force was measured employing a sample holder specifically designed for that purpose. The sample holder and the pretensioning principle is shown in Figure 6.33. Two weights mounted on either side of the sample apply the load. The weight, and thereby the

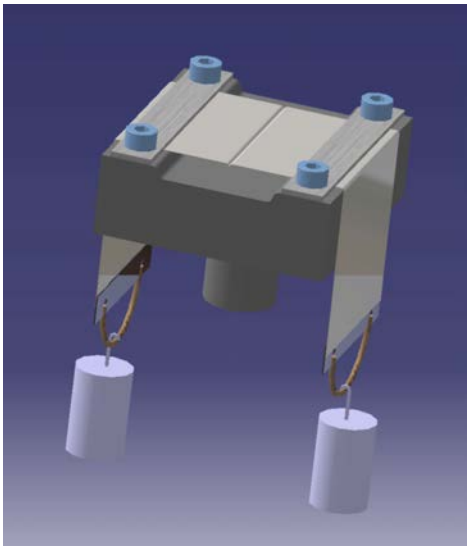

Figure 6.33: Sample holder for the fixation of a samples with a pretensioned folding line.

pretensioning is chosen so that it is in the order of the results from the finite element simulation (see Section 6.4.1). Two samples were evaluated one pretensioned with 1 g and one pretensioned with 125 g on each side. The weight of the sample's overlap with a metal sheet adds another 0.44 g on each side. This results overall in a tension of $9.17 \cdot 10^4$ Pa for the first sample and $4 \cdot 10^6$ Pa for the second sample. After the load is applied, the pretensioned sample is fixed by tightening the brackets on top of the sample holder. The weights are disassembled and the overlap of the sample is fixed with Kapton tape on the side of the sample holder. The prepared sample as shown in Figure 6.34(a) is then mounted in the microscope's vacuum chamber (see Figure 6.34(b)) and the measurement is started.

Figure 6.35 shows a three-dimensional picture generated by the electron microscope measurement. The picture shows the bottom of the folding line of the sample that was tensioned with 1 g on each side. Inside the wrinkle some creased lines due to the folding and general surface roughness are visible. The complete measured geometry along a line in the center of both samples is shown in Figure 6.36. For the sample loaded with the 1 g, weights the function describes the geometry with a standard deviation of 0.044 as

$$f_{1\,\mathrm{g}}(x) = -0.597\,\mathrm{mm} \cdot \exp\left(-2.48 \frac{1}{\mathrm{mm}^2} \cdot \mathrm{x}^2\right) + 0.597\,\mathrm{mm} \tag{6.46}$$

with an opening angle according to Equation 6.44 of 102°. For the sample loaded with the 125 g weights the function describes the geometry with with a standard deviation of 0.015 as

$$f_{125\,\mathrm{g}}(x) = -0.059\,\mathrm{mm} \cdot \exp\left(-14.275 \frac{1}{\mathrm{mm}^2} \cdot \mathrm{x}^2\right) + 0.059\,\mathrm{mm} \tag{6.47}$$

with an opening angle according to Equation 6.44 of 158°.

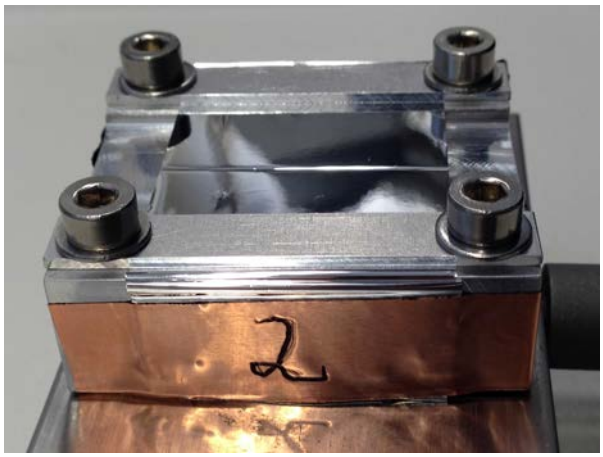

(a) Sample tensioned with a weight of 250 g fixated with the brackets on the sample holder.

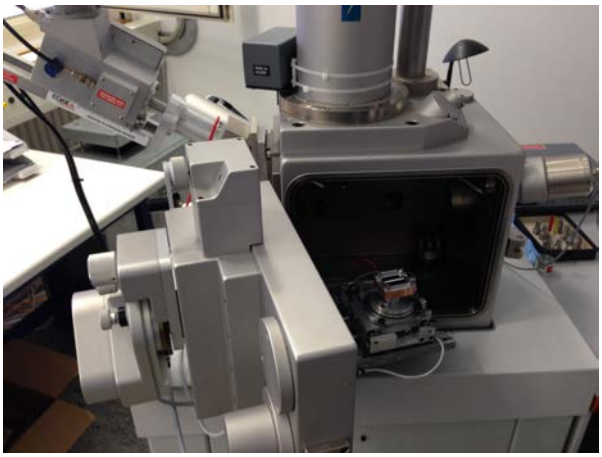

(b) Scanning electron microscope of the IWT Bremen with sample holder and sample mounted inside the microscope's vacuum chamber.

Figure 6.34: Sample mounted for microscope investigation.

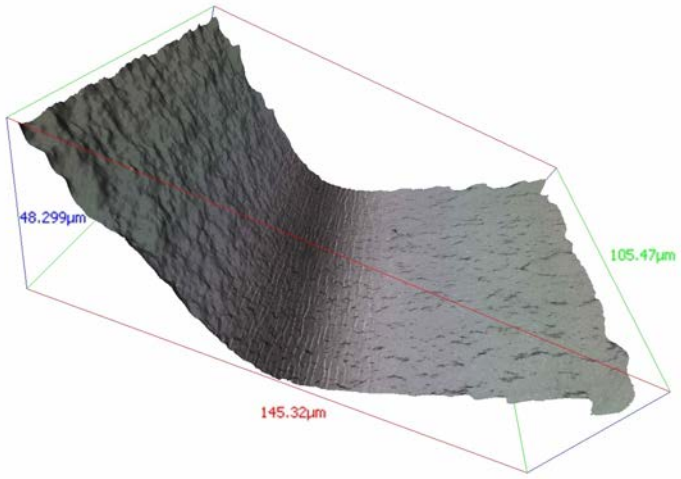


Figure 6.35: Three-dimensional picture of a wrinkle minimum

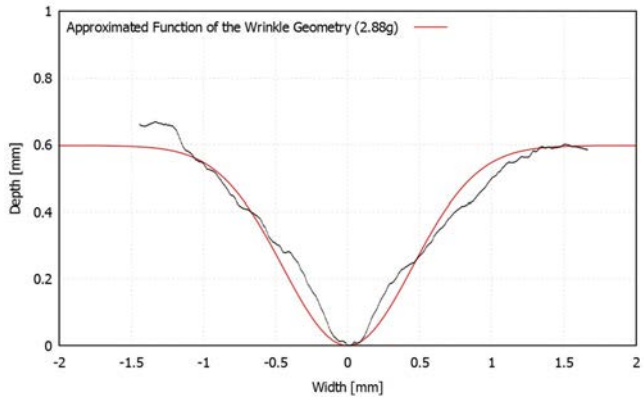


(a) Best-fit curve (red) according to Equation 6.46 of the geometry of the wrinkle (black) which was stretched with a total mass of 2.88 g.

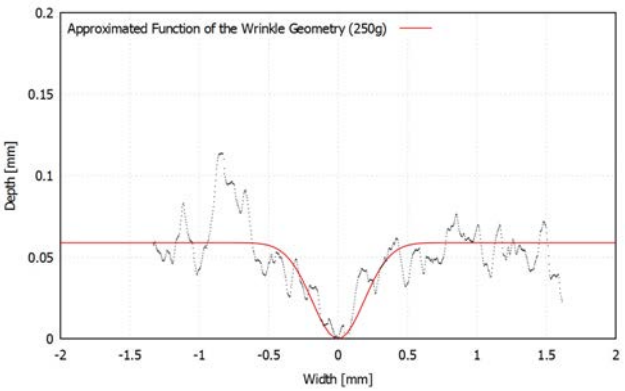


(b) Best-fit curve (red) according to Equation 6.47 for the geometry of the wrinkle which was stretched with a total mass of 250 g.

Figure 6.36: Measured geometry of the folding line in the middle of the sample and the fit function according to Equation 6.42.

### 6.5.2 Hot spots in folding lines

Inside the folding line, multiple reflections of the sunlight can cause a local temperature increase. These hot spots depend on the angle of incident of the light and the folding line geometry, which depends on the tension state of the membrane. Figure 6.37 illustrates the phenomenon. In the following sections it is briefly described.

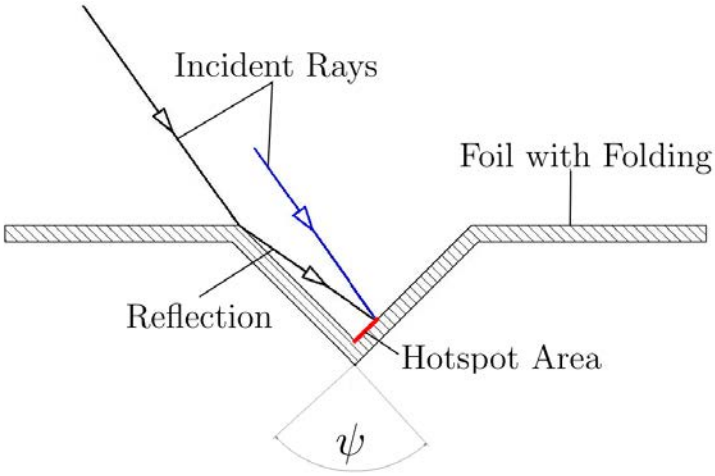


Figure 6.37: Hot spot (red line) due to a reflection inside a folding line.

In a simplified approach, the path of rays is analyzed for the hot case scenario described in Section 3.1.4 with a sail membrane directed towards the Sun. The temperature increase inside

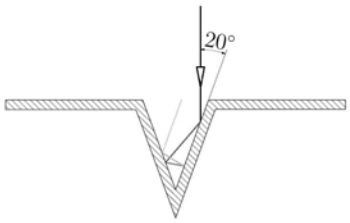


(a) Multiple reflections for small opening angles $\psi \leq 90°$, here $\psi = 40°$

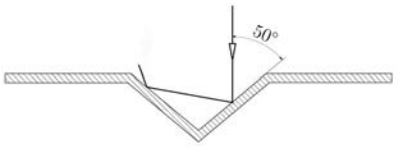


(b) Two reflections for medium opening angles $\psi \geq 90°$, here $\psi = 100°$

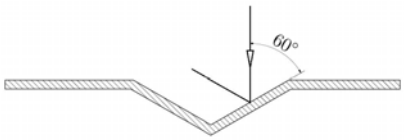


(c) Only a single reflection (not hot spot) for opening angles $\psi \geq 120°$, here $\psi = 120°$.

Figure 6.38: Path of rays for different opening angles of the folding line.

a folding line can be estimated under the simplified assumption that infrared radiation does not significantly contribute to the temperature increase and that the infrared emission does not change (the areas can radiate the heat without being in view of each other). In this case the equilibrium temperature according to Equation 6.48 needs to be supplemented for the reflected sun light $q_\rho$ as

$$\begin{aligned} T_{hotspot} &= \left( \frac{(q_s + q_a) \cdot cos\left(\frac{\pi}{2} - \frac{\psi}{2}\right) + q_{IR} + q_\rho}{2A_s\epsilon_t\sigma} \right)^{\frac{1}{4}} \\ &= \left( \frac{A_s\alpha_S S \cdot (1+0.3) \cdot cos\left(\frac{\pi}{2} - \frac{\psi}{2}\right) + \epsilon_t F_{e,s_h} A_e I_{e,IR}}{2A_s\epsilon_t\sigma} + \right. \\ &\qquad \left. \frac{(1-\alpha_S) \cdot A_s\alpha_S S \cdot (1+0.3) \cdot cos\left(\frac{\pi}{2} - \frac{\psi}{2}\right) \cdot cos(\frac{3}{2}\psi - \frac{\pi}{2})}{2A_s\epsilon_t\sigma} \right)^{\frac{1}{4}} \end{aligned} \tag{6.48}$$

Figure 6.39 shows the estimated temperature difference inside a folding line.

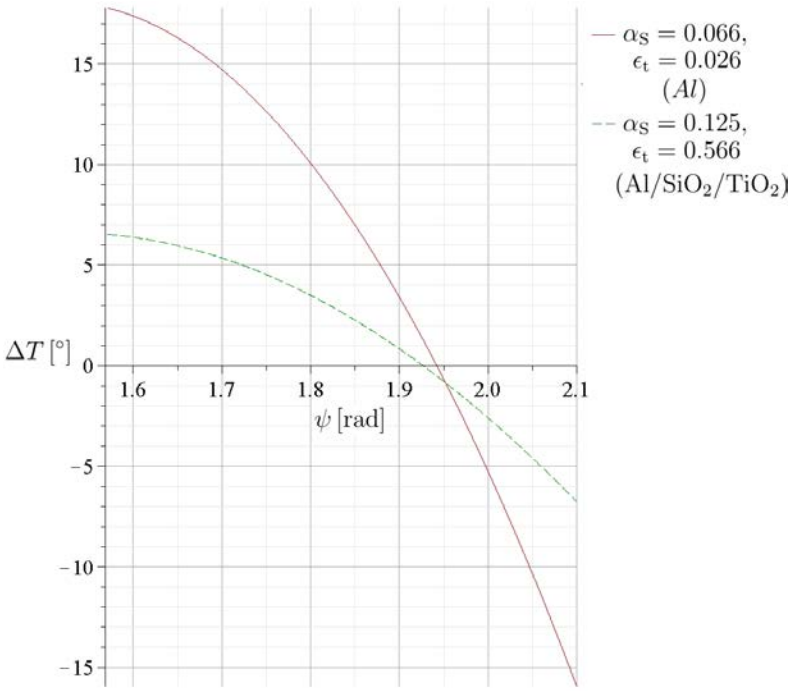


Figure 6.39: Temperature difference due to two reflections in the folding line. Positive values indicate a temperature increase.

## 6.6 Conclusion

On the example of the Gossamer-1 project several membrane aspects were analyzed. The overall concept of crossed booms already imposed the use of triangular segments with a load introduction in the corners.

A theoretical mechanical analysis of the stowed membrane under launch loads is not presented and also for future work this will be difficult to achieve due to the challenge of modeling several layers of folded and coiled foil pressed on each other with friction between those layers. In consequence, additional tests presented in Section 7.2.2 were made in order to verify the integrity of the stowed sail segment under launch loads.

The mathematical modeling of the stowing and deployment geometry presented in Section 4.2 combined with the loads introduced by the mechanisms as described in Section 5.2 allows a modeling of the deployment loads and their progression. The peak load of a little more than 3.7 N appears at the end of the deployment. In addition, the moments acting on the boom crossing point are presented. The pressure load due to drag in very low orbits between 200 km and 300 km in altitude is on the order of $10^{-2}$ Pa. Compared to the solar pressure force at 1 AU with $9 \cdot 10^{-6}$ Pa, the drag force is the dominant factor in such low orbits. Even for solar sails that fly closer to the Sun, the solar radiation pressure will be lower compared to the drag force in LEO (about $10^{-4}$ N at 0.3AU).

For the load introduction the more simple design of a direct introduction in the corner without an extra rigging was chosen. While the presented rigging could in principle generate a more uniform stress distribution and thereby also reduce the wrinkling due to the tensioning of the sail, there is no requirement, neither for Gossamer-1 nor for a possible solar sail, that would justify the increased complexity. In principal, a reduction of wrinkling and a therefore a flatter surface would increase a solar sail's performance by better reflecting the light. This effect is considered to be very small because the projected area to the Sun is nearly not changing. Sacrificing sail area for curved edges reduces the overall performance of a solar sail significantly and must be avoided. In principal, a rigging could be used without curved sail edges to even the tension state of the

membrane, but again the benefit would be small and the disadvantage of additional weight would likely dominate. In consequence, a direct force introduction into the sail corners is recommended. It should be noted that especially with respect to the attitude control, which has not yet been analyzed, requirements with respect to the surface quality could arise in order to keep disturbance torques low. This aspect might need further analysis in future work.

When analyzing the deployed sail under pressure loads with a finite element model, it is found that the reaction force transferred through the interfaces can be up to nearly 5 N. The loads during deployment and due to drag transferred through the interfaces to other structural components such as the booms are on the order of several Newtons and the deployment loads are smaller than the loads expected due to atmospheric drag.

The analysis of the folding lines reveals that, even with the low pretensioning of the sail, only two reflections may appear in a folding line. The local temperature increase due to the reflections compared to the flat sail is estimated at about 7 K. Inside the folding line a cracking of the coating is visible. It can be assumed that the protective properties of the coating deteriorate in this area, and due to the decrease in reflection, a change in the thermo-optical properties might also be present. The folding lines are considered to be a weak link in the current design. For a short-term mission, this can be tolerated, but for a long duration in the LEO environment or a solar sail mission, the design needs improvement, maybe in the way of a stripped design as shown in Figure 6.2.

The crack propagation behavior of the membrane is considered to be a critical design driver because micrometeorites and space debris are likely to accrue on large membranes during a long lifetime. Yet, it was not possible to present such an analysis here. Such an analysis is very specific and requires tests in order to determine material properties. The first results of an analysis made within the ESA drag sail project ADEO indicate that for the low tension of the membrane, a crack propagation might not be present and it might be that future analyses reveal a maximum stress in the membrane that should not be exceeded in order to avoid crack propagation.

# Chapter 7

# Manufacturing, integration and testing

For the verification of the sail membrane as well as its stowing and deployment, strategy bread boards and engineering models were built. The hardware was subjected to an extensive test campaign that ranged from component level to system level tests. The manufacturing and integration of the Engineering-Qualification Model (EQM) components are presented in Section 7.1 and the tests conducted are described in Section 7.2.

## 7.1 Manufacturing and integration

For the verification of the deployment strategy hardware was build on different levels of complexity. At first, the stowing and deployment process was evaluated with different engineering models that were modified several times. In a next step an EQM of one BSDU with a boom and two sail segments was built for the verification in simulated launch and space environment (see Section 7.2.4). The EQM hardware is the latest iteration of the Gossamer-1 hardware. A description of the membrane manufacturing as well as the mechanism and membrane integration is given in the following sections.

### 7.1.1 Membrane manufacturing

The main membrane material is the Upilex-s coated with 100 nm aluminum on both sides. The material is delivered on a roll with a width of 1.016 m. All bonding processes were made with the transfer adhesive tape 966 with adhesive 100 of the company 3M. The manufacturing is made according to the design presented in Section 6.2. The manufacturing drawings are provided in Appendix C.

Two sail segments were built, one with CIGS photovoltaic (see Chapter 6) and one with photovoltaic dummies. Figure 7.4 gives an impression of the manufacturing process. At first, the sheets geometry is cut out of the foil with an extra length for the edge reinforcement (see Figure 7.1(a)). The manufacturing of sheet three, that later holds the photovoltaic is shown in Figure 7.1(a). In the places where the photovoltaics are placed, the cut-outs are made (see Figure 7.1(b)). In order to prevent short-circuits between the harness and the aluminum coating the harness base sheet is implemented, made from an uncoated 12 $\mu$m Upilex-S foil (see Figure 7.1(c)). Along the height of the triangular segments, the harness is bonded through foil hinges to provide the possibility of relative movement between the harness and the main foil (see Figure 7.1(d)).

At the point where the harness turns 90° to the photovoltaic areas, the flexible PCB is cut int the middle, providing one part for the left and one for the right side of the photovoltaic segment (see Figure 7.1(e)). In order to prevent further cracking of the material along the cut, the transition zone was made with a circular punch out. The 90° folding was made, unnecessarily, with sharp folding lines. This can lead to cracks of the conducting path which should be avoided

in future designs. Instead, the harness should just softly be bend over and for further safety thin non-conducting tubes possibly made of polyimide can be glued along the bending line. In a next step, the photovoltaics are attached to segment three such that the backside is facing through the cut outs and the photovoltaics are electrically contacted to the harness. At last all segments are bonded together. Figure 7.1(f) shows the EQM segments with CIGS photovoltaic.

(a) Manufacturing of four sheets with edge reinforcement.

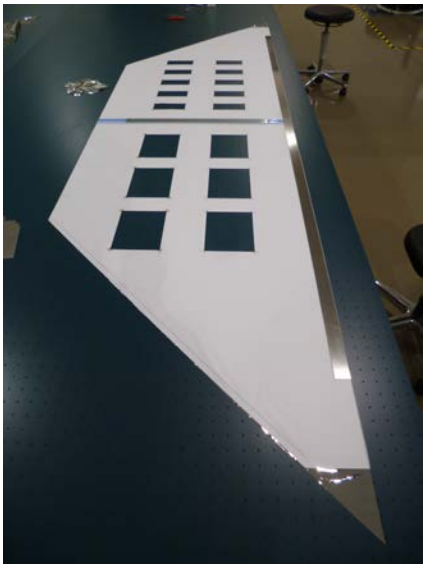

(b) Cut outs for photovoltaic modules.

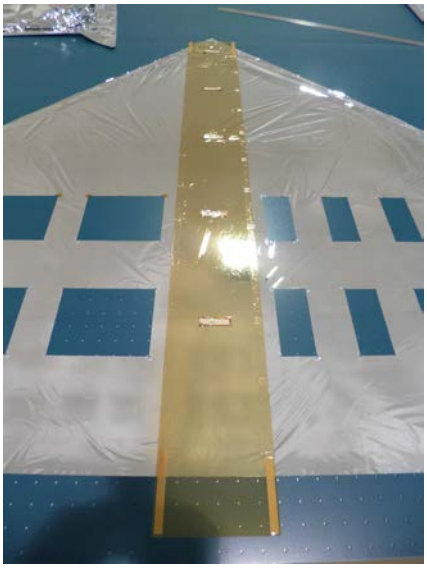

(c) Harness base-sheet as an electrical isolator.

(d) Attachment of the harness with foil hinges.

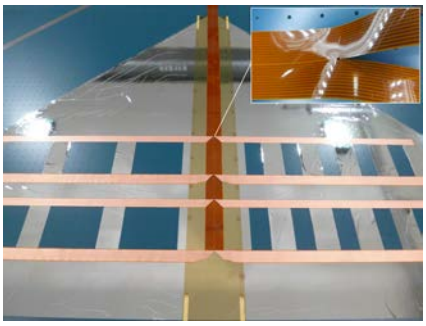

(e) Folding the harness over 90° for a routing along the photovoltaics.

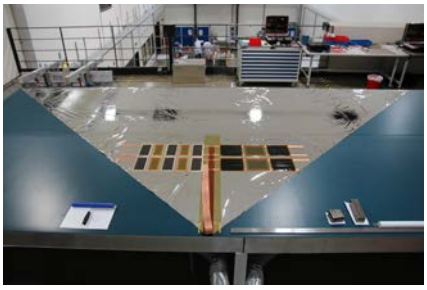

(f) EQM sail segment with CIGS photovoltaic.

Figure 7.1: Sail membrane manufacturing.

### 7.1.2 Mechanism integration

The integration of all components was made in an ISO 8 clean room environment. In a first step sub-components like electronics, the BWM, Boom Hub, launch locks were pre-assembled and prepared for the final integration into the BSDU. The rooting for the harness was finalized, and cable tie mounts were mounted with adhesive on the main structure. Figure 7.2 gives an impression of that integration work. All screws were tightened with a torque wrench and additionally locked with adhesive. At last the boom was coiled on the boom hub inside the BSDU and the sail segments were integrated.

### 7.1.3 Membrane integration

After the BSDU integration, the sails are stowed and mounted on the BSDUs. A method has been developed which ensures that the sail segments are always stowed in the same way, and

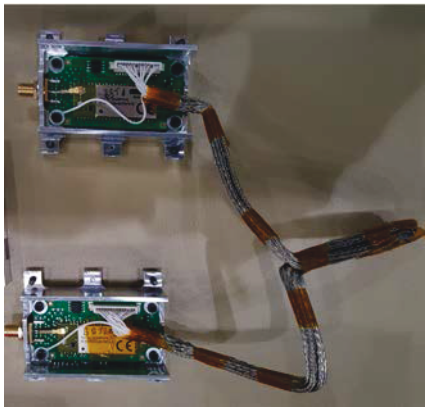

(a) Bluetooth electronics.

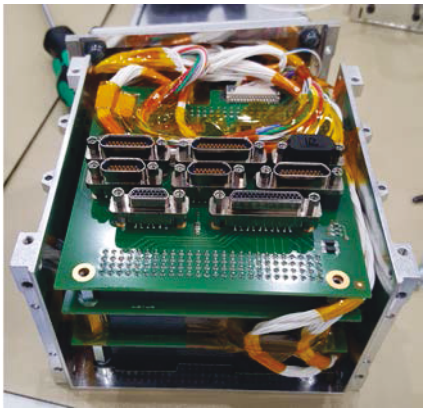

(b) Main electronics including power system, communication, and on-board computer.

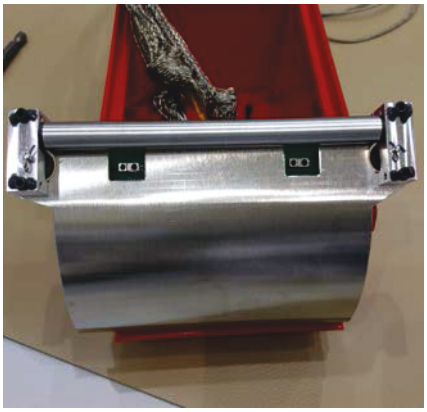

(c) Part of boom guide with mounted optical sensors for deployment length measurement.

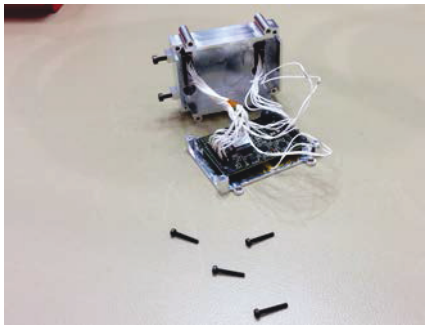

(d) Motor electronics.

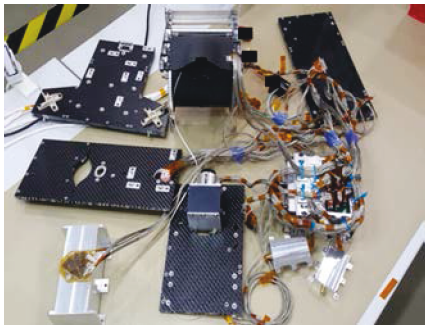

(e) Pre-assembled BSDU parts with all mechanisms and electronics.

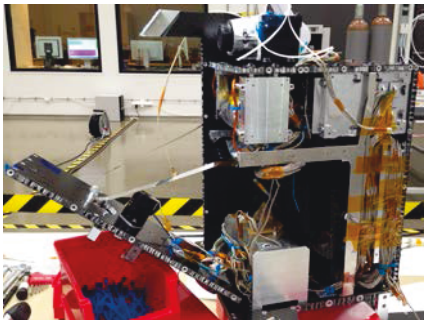

(f) BSDU during final integration process.

Figure 7.2: BSDU integration in ISO 8 clean room environment

consequently the same configuration is always obtained in a reproducible manner. This is always an important aspect when developing hardware for space applications. It must be ensured that the tested and qualified configurations are also achieved for the flight hardware. For this purpose two identical tools were built that allow the coiling of the sail segments on the spools with a defined torque, it is shown in Figure 7.3. The tools use a hysteresis brake that transfers a defined torque when coiling the sail onto the spool. The drive side always rotates significantly faster than the output side. The folded sail segment is coiled while the tool is slowly moved forward. The integration process is shown in Figure 7.4.

In a first step, the sail segments are manually folded (see Figure 7.4(a)). Long rulers were used for fixation and as guide edge for the folding. The sail segments were folded starting from the hypotenuse. For each fold, the remaining segment was pulled further to the hypotenuse. After the folding, the first half of the segment is coiled on one spool with using one of the integration tools. The coiled half of the segment remains on the integration tool and is additionally fixated with Kapton tape (see Figure 7.4(b)). In a next step the second half of the segment is coiled on another spool in the same way (see Figure 7.4(c)). Care must be taken not to loosen the coiled segment again or to change the configuration in any other way. Therefore the coiled sail is also fixated with Kapton tape on the spool. After placing the spools with the sail segment into the bearings of the BSDU or a test adapter, respectively, the segments are again preloaded (see Figure 7.4(e)) before the launch locks are engaged (see Figure 7.4(f)). The preload is achieved by applying a torque of 0.14 Nm to the spool, and then further rotating the spool to the next position in which the launch lock can engage into the gear.

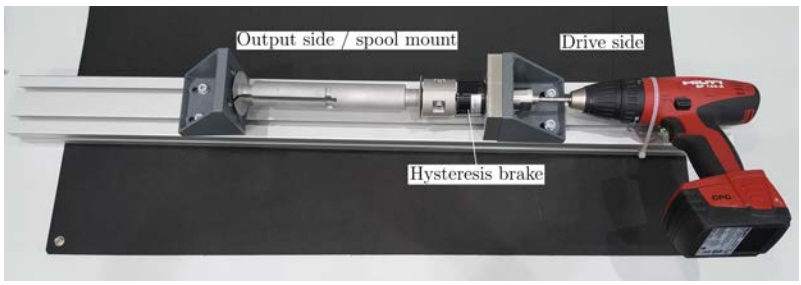


Figure 7.3: Integration tool for sail stowing. A hysteresis coupling separates the drive side from the actual spool rotation on the output side. Only a torque of 0.14 Nm is transferred.

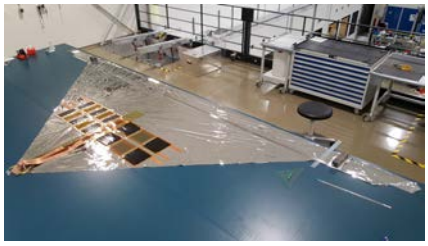

(a) Folding of the sail segment (manually) from the hypotenuse to the inner edge.

(b) Coiling one half of the sail segment on the first spool using one of the integration tools.

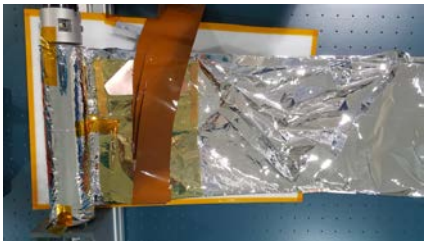

(c) The first half of the segment is fixated on the first integration tool.

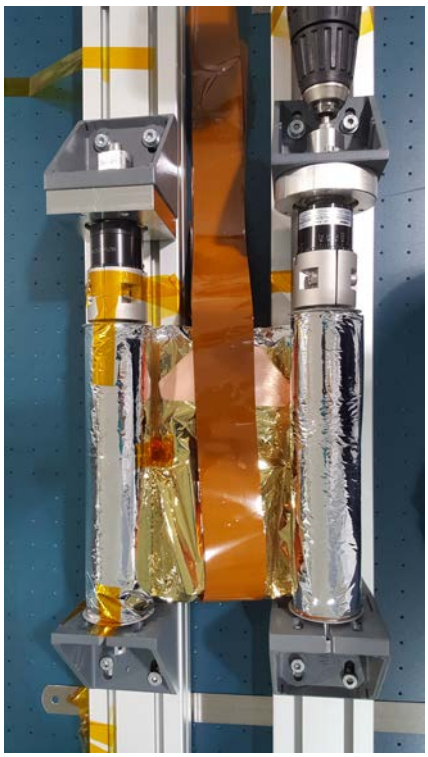

(d) The second half of the sail segment is coiled on the second spool using the second integration tool.

(e) The spools are mounted on the deployment units (or test adapter, respectively). Before engaging the launch locks, the configuration is preloaded.

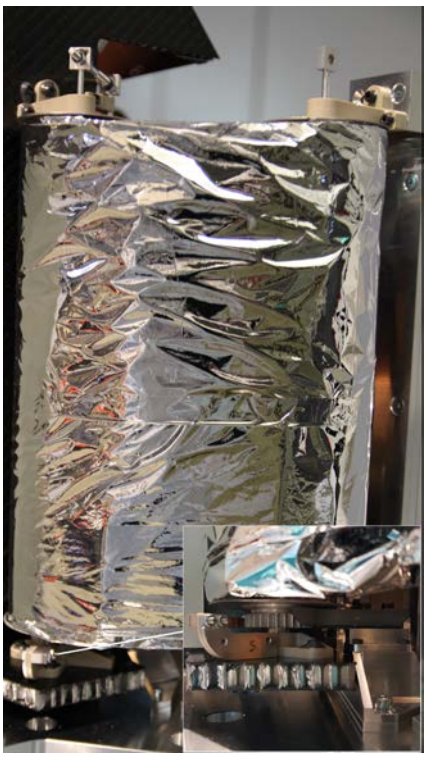

(f) While applying the preload, the launch locks are engaged into the gear on the downside of the sail spool.

Figure 7.4: Sail integration.

## 7.2 Verification tests

Several tests were carried out in order to verify the functionality of the materials, components as well as the deployment strategy on a system level. Whenever it was possible and reasonable, a test-as-you-fly approach was pursued. This means that the different tests were carried out such that they followed as closely as possible the same order of occurrence of loads as experienced in a real launch and mission. The tests are presented here with a focus on the sail membrane subsystem and the stowing and deployment strategy. A complete assessment of the Gossamer-1 system performance under these tests cannot be carried out at this point since this would require the participation of all subsystem responsible persons. This is considered to be out of the scope of the work presented here.

In the precursor projects (DLR (99)) the adhesive was already tested in a temperature range between -142°C and 98°C. In addition to thermal-vacuum tests carried out in this precursor project, samples of the foil bonded with adhesive were tested for temperature dependent adhesion failure at elevated temperatures and static mechanical loads (see Section 7.2.1). The verification was completed with thermal-cycling tests carried out by the company HTS within the joint ESA project Deployable Membrane.

The membrane stowing and deployment technique was first verified on subsystem level (see Section 7.2.2). A mechanical representative sail was mounted on a test adapter and subjected to different mechanical loads followed by venting and deployment tests.

In order to verify the deployment on system level, an engineering model of the deployment with avionics and simulated space to ground interface was tested under ambient conditions (see Section 7.2.3). The engineering model employed two sail segments without photovoltaics or dummies in order to reduce gravity loads. This test data is further used to establish a force and torque budget for the sizing of the deployment unit's motor.

The tests were supplemented by a complete test-as-you-fly cycle with an engineering-qualification model of the deployment unit. The tests included vibration testing, fast venting, thermal-vacuum cycles and a laboratory deployment (see Section 7.2.4).

### 7.2.1 Adhesive thermal tests

The test focus was on the thermal resistance of the transfer adhesive tape 966 with adhesive 100 from the company 3M that was used for the manufacturing of the sail (see Chapter 6). For the test, eight strips of Upilex-S foil with a width of 3 cm were manufactured (four were subjected to the thermal test). The edges were folded over and bonded with the same adhesive as reinforcement against cracks. The ends of the stripes were folded to the middle and bonded with the transfer adhesive such that a loop was present on both ends. The test setup in the furnace is shown in Figure 7.5(a) and side view of the sample is shown in Figure 7.5(b). On the top side, the samples were mounted in a small test rig and on the lower side, a weight was mounted in the loop such that the bonding area of 3 cm × 1 cm was loaded with shear force.

The test was carried out at the FH Aachen University of Applied Sciences as part of a collaboration on the Compass-2 drag sail. The bonding areas were loaded with different weights. According to the data sheet (see 3M, Industrial Adhesives and Tapes Division (120)) the limit shear load on stainless steel at 230°C is 0.61 $\mathrm{Ncm^{-2}}$. For a bonding area of the samples with 3 $\mathrm{cm^2}$, this corresponds to a weight of approximately 200 g. Sample four was loaded with a weight of 400 g introducing a load twice as high as the specified limit load. The other samples were loaded with 200 g (sample three), 100 g (sample one) and 50 g (sample two).

Figure 7.5(c) shows the temperature measured in the furnace at the height of the bonding area of the samples. The samples were heated up to 150°C. After a dwell time of one hour the samples were further heated up to 200°C, and after another hour of dwell time the temperature

(a) Test rig, samples (3 cm width) and weights inside the furnace.

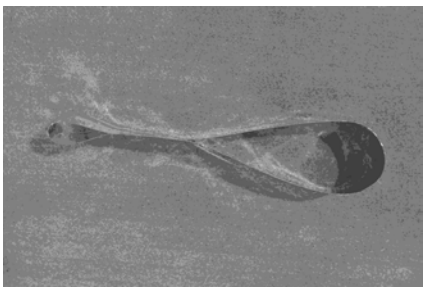

(b) Sample side view.

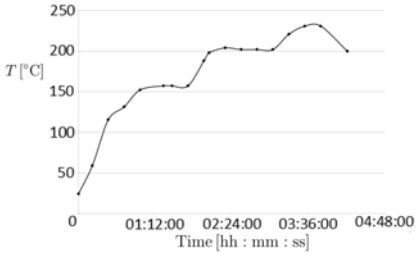


(c) Temperature during test.

Figure 7.5: Thermal test of transfer adhesive.

was increased to 230°C. The highest temperature was kept for another 30 min.

Figures 7.6(a) and 7.6(b) show the tested samples before and after the test. Triangular markers made of a temperature resistant Kapton tape were attached to the samples. The sample number is specified by the amount of Kapton dashes and the triangular markers pointing to the edge of the adhesive bond. In case the bond would open, this helps in visualizing the process. However, there was no separation of the bonded area present. The temperature limit is still not known but according to this test it is above 230°C.

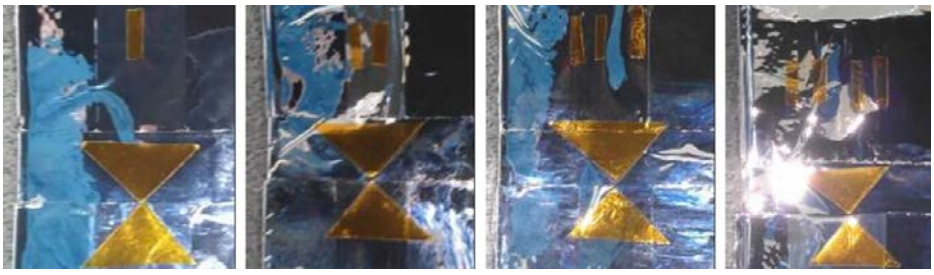

(a) Before heating.

(b) After heating.

Figure 7.6: Comparison of test samples before and after heating.

Additional thermal tests were conducted by the company HTS within the joint European Space Agency (ESA) project Deployable Membrane. In this test the successor product of the adhesive 966 named transfer tape 9460 was used. It is nearly identical to the previous product but according to the company has a slightly higher thermal stability. HTS tested the samples in 20 thermal cycles between −90°C and +220°C. The temperature profile is shown in Figure 7.7(a). The test setup is shown in 7.7(b). The samples were only loaded with an unknown but very small load due to the weight of the clamps visible in the picture. The samples survived the thermal-cycling test and further mechanical testing confirmed the applicability of the adhesive tape for the space sail application.

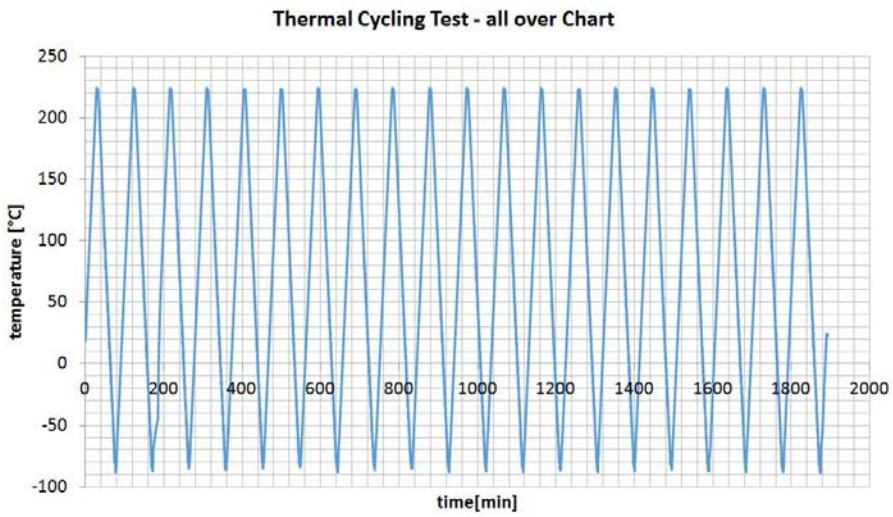


(a) Thermal cycles.

(b) Test setup for thermal cycling

Figure 7.7: Deployable Membrane thermal cycling tests (courtesy of HTS GmbH).

### 7.2.2 Sail breadboard tests

Pre-qualification tests were performed with a sail segment stowed on engineering models of the sail spools. The sail was built as mechanically flight representative. Thin film photovoltaics as such were not included, but were simulated by suitable mechanically-representative dummies made from flexible PCB material, i.e. copper-polyimid laminates of suitable dimensions (Figure 7.8(a)). The electrical harness on the sail was made using high-quality industrial Polytetrafluorethylen (PTFE)-insulated AWG28 litz wire loosely bundled. The wire type used was previously qualified at system level for MASCOT (Ho et al. (121)). Note that these wires were replaced by a flexible PCB harness for the engineering-qualification model (see Section 7.2.4).

Tests were performed as a representative cycle starting with the shaker test followed by centrifugal acceleration, fast decompression, and finally deployment under ambient conditions. The tests were also presented in Seefeldt et al. (101). Test loads were based on the launcher load envelope as specified in Appendix A.

All tests were conducted with a test adapter specially designed for those tests. The adapter is shown in Figure 7.8(b). Regarding the sail spools the adapter provides a bearing and locking mechanism representative to the Gossamer-1 system design. For final functional verification, the sail package and sail spools were then transferred to the deployment test rig that uses linear drive units as a replacement for the booms and deployment unit.

#### Breadboard vibration test

The sail breadboard mounted on the test adapter was subjected to sinusoidal and random loads. The first eigenfrequencies were expected at approximately 350 Hz, which is well above the frequencies of the sinusoidal loads. In consequence the sinusoidal loads tested were chosen according to the launcher loads (see Appendix A) and no further amplification needed to be considered. The vibration spectra for the random loads were chosen according to preliminary FEM simulations made by colleagues responsible for the structural design of Gossamer-1 (see Hillebrandt et al. (114)). The analysis revealed structural amplifications of the loads introduced to the launch adapter. The power spectral density has a peak of $100\,\mathrm{g}^2/\mathrm{Hz}$ at 100 Hz for the $x$-axis as well as the $y$-axis and a peak of $150\,\mathrm{g}^2/\mathrm{Hz}$ at 110 Hz. The root mean square acceleration is $25.15\,\mathrm{G}_{\mathrm{rms}}$

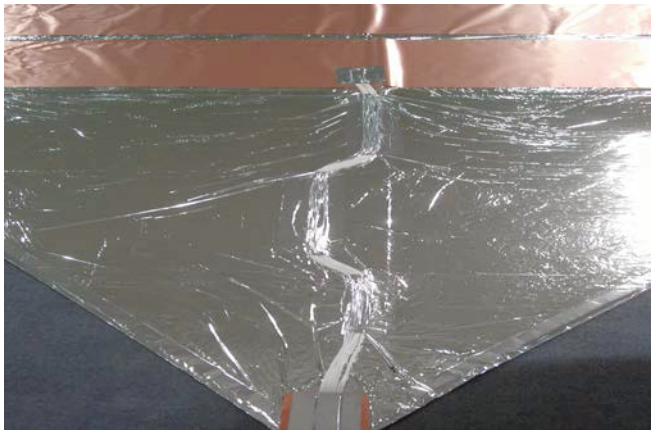

(a) Sail with flexible PCB dummies and cables.

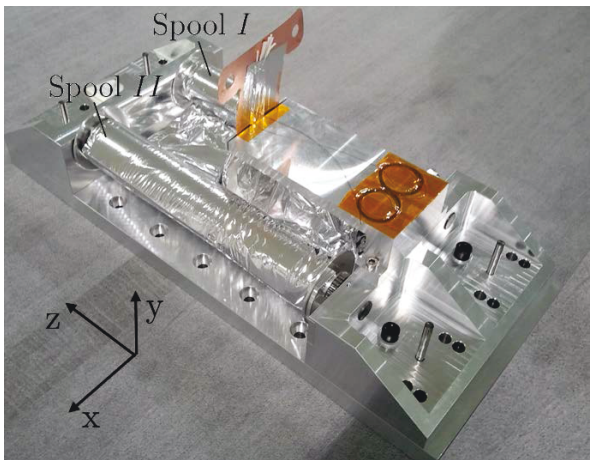


(b) Sail package mounted on test adapter.

Figure 7.8: Gossamer-1 sail segment breadboard model for testing the stowing and deployment technique.

for the $x$-axis, 21.87 $G_{rms}$ for the $y$-axis, and 46.36 $G_{rms}$ for the $z$-axis. The loads present at the sail spools according to that simulation were reproduced and partly exceeded during the vibration test. The test setup is presented in Figure 7.9. The accelerations were measured on the sail spool flange near the spool axis.

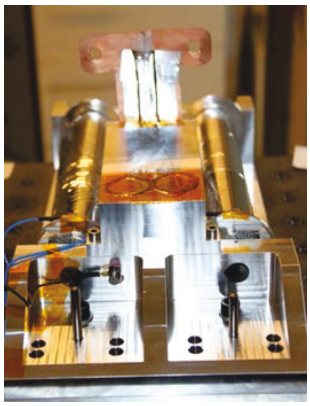

(a) $x$-axis.

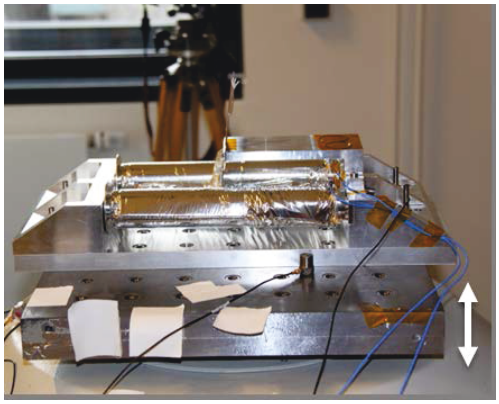

(b) $y$-axis.

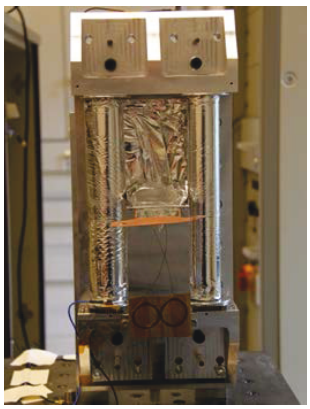

(c) $z$-axis.

Figure 7.9: Gossamer-1 sail segment breadboard vibration test setup.

The response to the sinusoidal loads is given in Figure 7.10(a). Figure 7.10(b) shows the response on the random loads. At the point of measurement the loads basically followed the excitation. This was expected because this point is near the bearing and mounting point of the sail spools. The eigenfrequencies measured are presented in Table 7.1. The mounting and locking of the spools does not pretension the configuration. It was expected that the eigenfrequencies would decrease due to settle effects . The sail package passed vibration testing without any visible change of the configuration.

### Breadboard static acceleration test

During a real launch, the vibration loads and the static acceleration loads are superimposed. The high acceleration test was performed in order to ensure that even the high accelerations in the vibration spectrum will not lead to slipping between the foil layers, which could lead to a slipping of the sail package on the sail spool. In a first step, a centrifuge test was made, applying an

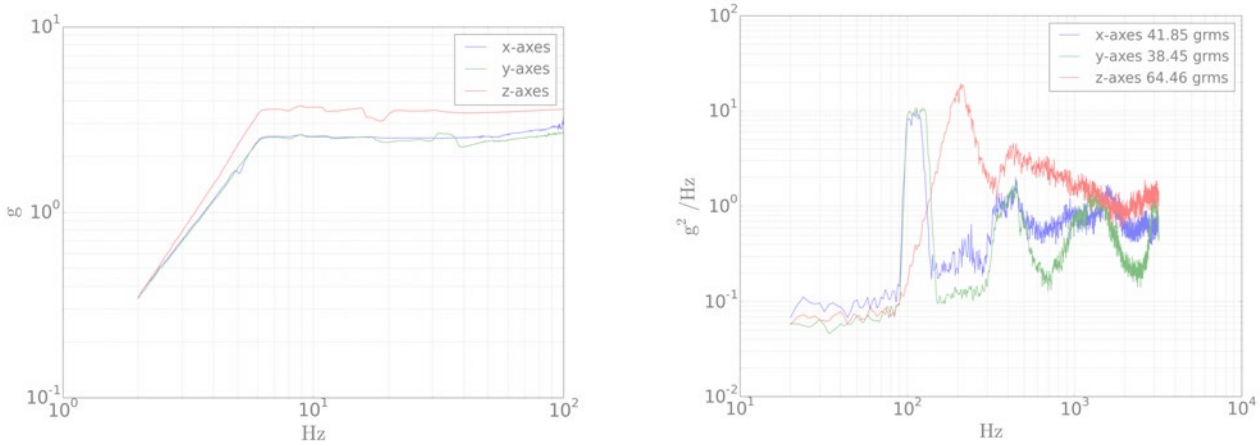


(a) Response to sinusoidal loads.

(b) Response to random loads.

Figure 7.10: Gossamer-1 sail segment breadboard vibration test response.

Table 7.1: First eigenfrequencies of the breadboard before and after vibration testing.

| Spool, axis | First eigenfrequency | |
|---|---|---|
| | Before vibration test | After vibration test |
| Spool $I$, $x_v$-axis | 516.0 Hz | 465.2 Hz |
| Spool $I$, $y_v$-axis | 465.2 Hz | 465.2 Hz |
| Spool $I$, $z_v$-axis | 345.1 Hz | 273.0 Hz |
| Spool $II$, $x_v$-axis | 325.5 Hz | 351.2 Hz |
| Spool $II$, $y_v$-axis | 357.5 Hz | 287.8 Hz |
| Spool $II$, $z_v$-axis | 347.1 Hz | 339.1 Hz |

acceleration of 30 g on every axis. Furthermore, a second test was made with 90 g, along the spools axes. The different test runs are summarized in Figure 7.11. With the high acceleration test of 90 g about $2\sigma$ standard deviation of the maximum vibration acceleration were covered in the test. There was no visible deformation of the sail package investigated during and after the centrifuge tests.

### Breadboard venting test

During the ascent of the rocket the pressure gradient from the inside of the fairing to the outside increases and the air is vented out of the fairing. A venting test was conducted in order to ensure that the air can be vented out of the stowed sail segment without causing any kind of destruction. The test setup is depicted in Figure 7.12(a) and the breadboard inside the venting chamber is shown in Figure 7.12(b).

The Gossamer-1 project had to deal with a number of uncertainties regarding possible launch vehicles. This included, for example, the possibility of a Shtil' launcher that is a modified military missile of the Russian Navy. While very little information about the launcher was available, it was clear that such a launcher would accelerate faster and therefore the pressure drop would be higher. The pressure decrease chosen for the venting test as shown in Figure 7.12(c) was therefore much stronger than what would be expected for conventional launch vehicles like the VEGA (Arianespace (122))or Ariane 5 (Arianespace (123)) launcher.

The most critical phase is during the first few seconds when most of the air is vented. After 75 seconds 99% of the air is vented and the further decrease has no effect on the stowed sail segment. During the test, very small movements of the outer foil layer were visible. There was no visible

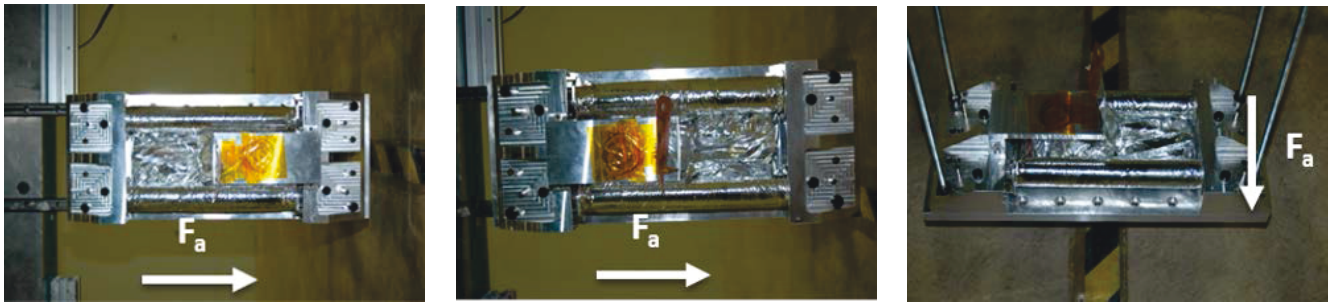


(a) Run 1: $+z$-axis, 30 g (b) Run 2: $-z$-axis, 30 g (c) Run 3: $+x$-axis, 30 g

(d) Run 4: $-x$-axis, 30 g (e) Run 5: $+y$-axis, 30 g (f) Run 6: $+y$-axis, 90 g

Figure 7.11: Static acceleration test on a centrifuge with the breadboarded of a stowed sail segment.

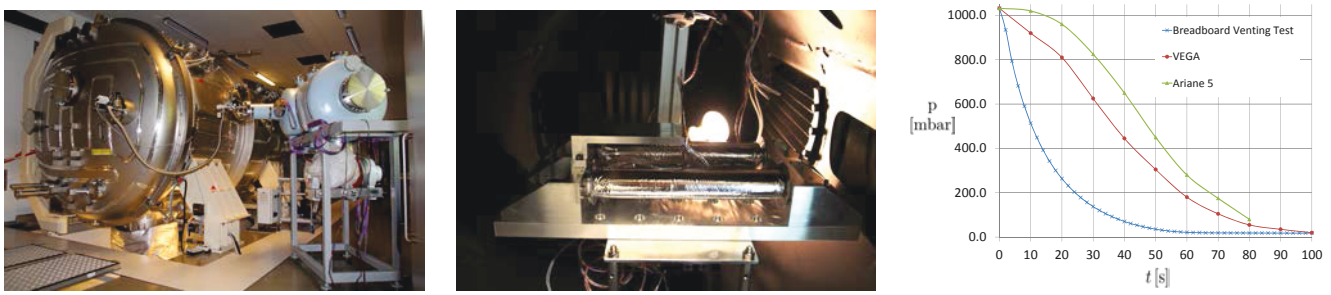


(a) Venting test, big space simulation chamber on the left and small venting chamber on the right.

(b) Test setup of the fast decompression.

(c) Pressure progression during venting test and comparison to launchers.

Figure 7.12: Sail segment breadboard venting test.

deformation nor damage of the sail package observed during and after the venting test.

### Breadboard deployment test

As a last step in the breadboard testing it was deployed employing linear drive units instead of booms and deployment units. Two linear drives (4.5 m maximum length each) at right angles with sail spools mounted on them were used to deploy one sail segment (Figure 7.13). Deployment took place via computer-controlled movement of the linear drives. Different deployment speeds as well as speed profiles could be tested. The breadboard sail segment was deployed within about 10 minutes.

All mechanical interfaces and the segment itself stayed intact throughout the tests described. After the first stowing and deployment process, several wrinkles on the surface of the segment are visible. This would slightly decrease the reflectivity and thereby the efficiency of a solar sail.

In a next step this test rig was extended in order to deploy two sail segments with one boom and one BSDU. This test setup also enables a system level test including mechanisms, electronics and implemented logic. These deployment tests are presented in Sections 7.2.3 and 7.2.4.

Figure 7.13: Deployment test of one sail segment alone without Booms and BSDU. The photovoltaic mass dummies are directed to the bottom side of the sail.

### 7.2.3 System level deployment test

System level deployment tests used two linear drives arranged in a line, simulating one full boom diagonal of a Gossamer-1 configuration with a boom and BSDU tested at right angles between them (Figure 7.14). The boom was mounted to a Boom-Spacecraft Interface (BSI) and was deployed by a fully functional BSDU engineering model. The BSDU was supported by a test rig, which glides on air bearings to provide minimum friction in order to allow free BSDU and boom movement within the sail plane. On each linear drive, a sail spool was mounted on top of a three-axis force sensor. The BSDU was fully equipped including the sail spools at its sides. One boom and both adjacent sail segments could thereby be deployed in this setup, designated as one-boom-two-sail-segment system level testing. The BSDU was controlled by the on-board wireless communications with a fully functional CSCU electronics system as the counterpart, which in turn was connected to the electronic ground support equipment and suitable control interfaces. The acquisition of sensor data as well as BSDU camera images was implemented. Commands and data were transferred via the on-board wireless communications system from the BSDU to the CSCU.

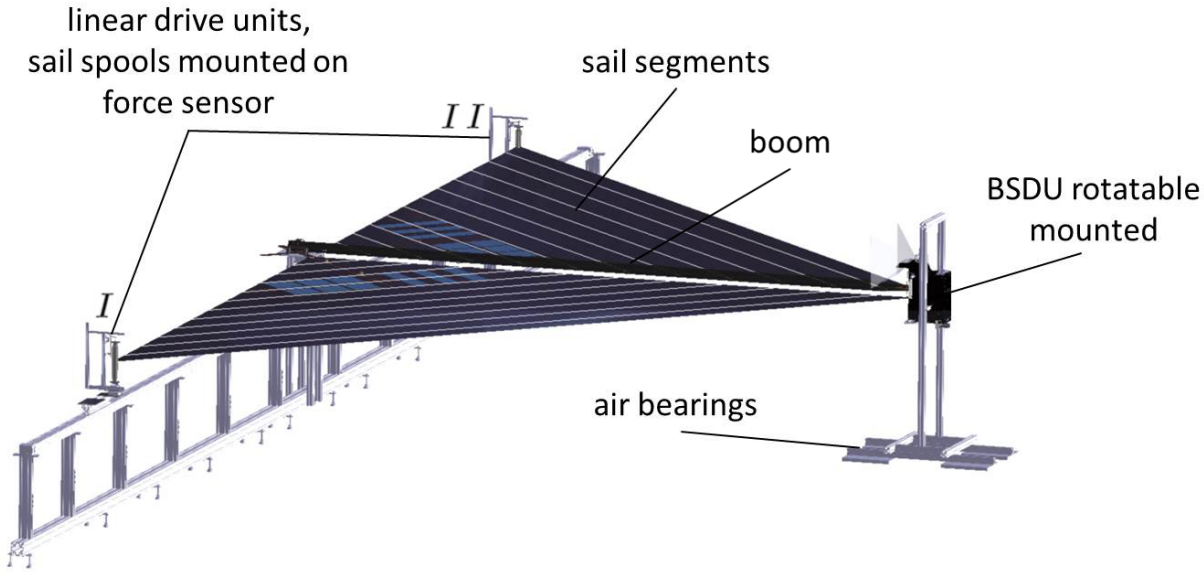


Figure 7.14: Test rig for the deployment of two sail segments together with one boom by employing the Gossamer-1 deployment mechanisms. In correspondence to Figure 4.20, forces measured are differentiated with the subscribes $I$ and $II$ depending on the linear drive.

The deployment test with its different phases as described in Seefeldt et al. (9) is shown in Figure 7.15. The deployment (Phase 4) is shown in Figure 7.15(b), followed by the separation (Phase 5) in Figure 7.15(c) and the BSDU jettison (Phase 8) in Figure 7.15(d). In addition, Figure 7.15(e) shows an image acquired by the BSDU on-board camera during the deployment test.

(a) Deployment start - Phase 4.

(b) Acquiring picture with on-board camera (Figure 7.15(e)).

(c) Sail completely deployed, BSDU Separation - Phase 5

(d) BSDU jettison - Phase 8

(e) Picture taken with the Gossamer-1 on-board camera.

Figure 7.15: Gossamer-1 deployment test in progress.

In the same way as in the boom pull-out, the sail spools and sail deployment also introduce additional forces when pulling the sail off of the sail spool. These forces were measured during deployment by force sensors placed between the two linear drive units and their corresponding sail spool mounts. Data was recorded as a function of time, and thereby as a function of deployment phases ranging from stowed configuration up to final jettison of the BSDU.

Results obtained for one of these sensors are shown in Figure 7.16. Maximum values were observed at 2.2 N. This applies to one sail spool. As one BSDU has to pull off the sail halves from two sail spools, this force must be considered twice in the budget, resulting in 4.4 N.

The sail pull-off measurements showed a fast oscillation caused by the leaf spring brake at the sail spool. The oscillations are roughly about 1.3 N, which is in agreement with the leaf springs used for this engineering model. Besides a smaller amount of friction between the tip of the spring and the gear, this mainly represents the deformation of the spring. The general trend of an increasing force during the sail deployment is due to two main effects. The diameter of the sail coiled on the spool is reducing. At the beginning, the diameter of the coiled sail is about 50 mm, and at the end it is the spool diameter of 35 mm. This in turn leads to a force increase of about 0.4 N. In addition, the deployed sail introduces tension forces, especially when deployed in the laboratory under gravitation. The highest forces appear at the point shortly before the sail is completely deployed and when jettisoning the BSDU. At both times the force is about 2.2 N.

The oscillating force is present up to the point where the BSFR is locked into the boom, which, due to the design, occurs just after having pulled the sails completely off of the sail spools. When the last tip of the sail segment slips off of the spool, the sail gets a little more slack. As the sail is

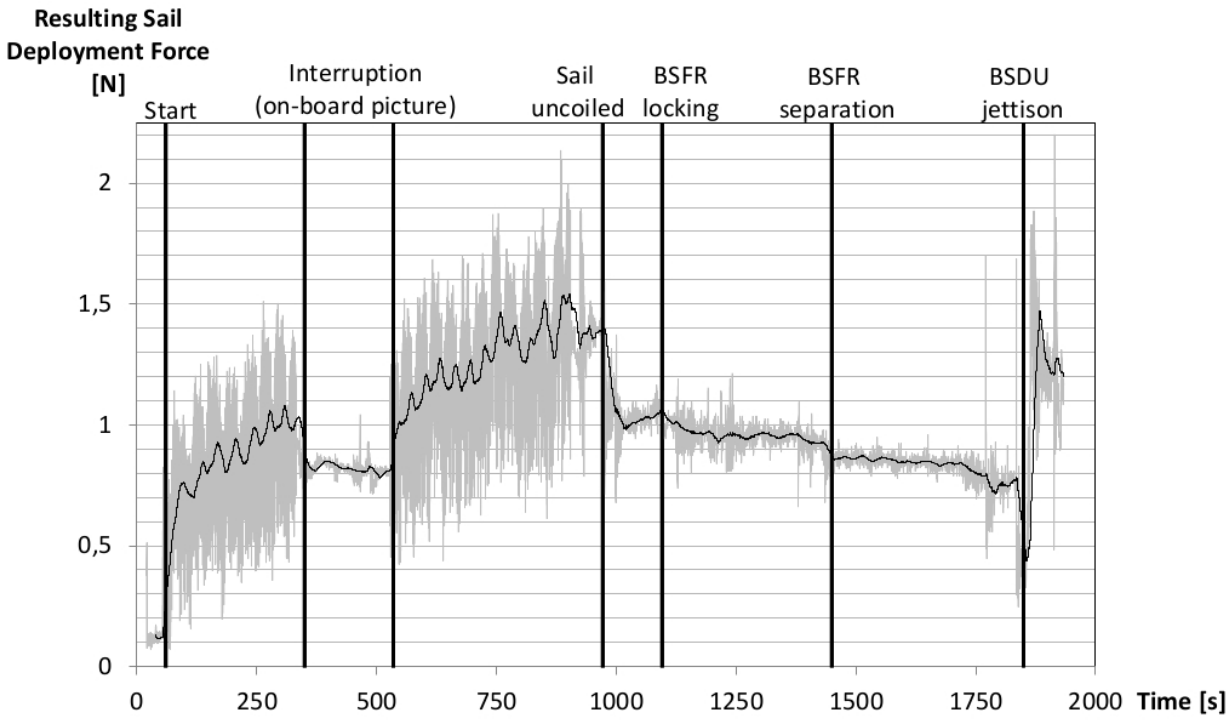


Figure 7.16: Measured total deployment forces at linear drive *II* during laboratory deployment test. Measured at 12.5Hz sampling rate, the black graph represents the moving average for every 255 data points.

less tensioned at that point, a decrease of approximately 1 N appears. After having pulled off the sail completely, only more or less constant force is observed, which is equal to the tension force applied to the sails. After the separation of the BSDU from the BSFR, the force measured reduces slightly, indicating that due to the additional flexibility of the BSFR interface, the sail tension is also slightly reduced. Final and stronger oscillations towards the end of the measurement are caused by perturbations due to the BSDU rolling off of the boom (jettisoning).

### Deployment force budget results and motor sizing

For the motorizing a deployment force budget and a torque budget is established. The forces that are not sail related are taken from Straubel et al. (106) the sail deployment forces are taken from Figure 6.11. The force budget is also presented in Seefeldt et al. (9). Forces purposely added by the sail spool and boom hub leaf spring brake add up to $5.2\,\mathrm{N} + 2.6\,\mathrm{N} = 7.8\,\mathrm{N}$, whereas the major friction-related contributions of the boom deployment add up to 6.6 N. In addition, the laboratory sail deployment introduces forces of 1.8 N. This is mainly gravitation related, but also includes an unknown fraction of friction force of the sail spool mechanisms. These forces transform into the required drive torque at the gear's axis through multiplication with the radius of the belt winding mechanism's spool of 20 mm. The torques were multiplied with uncertainty and safety factors according to the ECSSS EST01 standard ECSS (124). Table 7.2 provides an overview of the torque budget for the motor. Figure 7.17 shows the measured contributions to the full force budget.

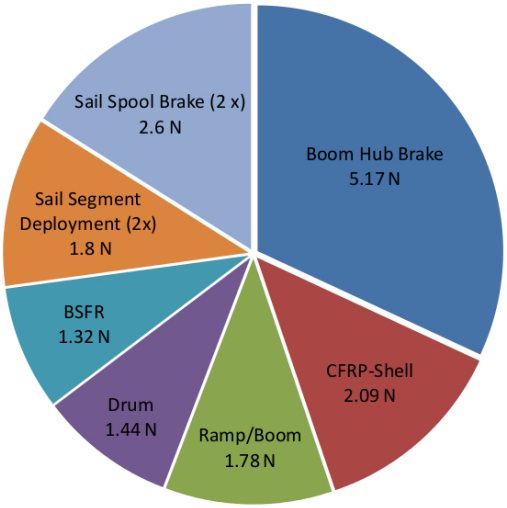


Figure 7.17: Composition of the deployment force that is introduced through the BWM (see Section 5.1).

Table 7.2: Overview of the torque budget for the motor sizing. The translation of the force budget to a torque budget considers a diameter of 40 mm of the BWM spool. Uncertainty and design factors according to the ECSS standard ECSS (124) are considered.

| Component/Type | Torque [Nm] | Uncertainty Factor | Design Torque [Nm] |
|---|---|---|---|
| Boom Hub Brake / Spring | 0.1034 | 1.2 | 0.1241 |
| CFRP-Shell / Friction | 0.0418 | 1.5 | 0.0627 |
| Ramp/Boom /Friction | 0.0356 | 1.2 | 0.0427 |
| Drum Friction | 0.0288 | 1.5 | 0.0432 |
| BSFR / Friction | 0.0264 | 1.5 | 0.0396 |
| Sail Spool Brake / Spring | 0.0520 | 1.2 | 0.0624 |
| Sail Deployment / Gravity, Friction | 0.0360 | 1.5 | 0.054 |
| Inertia | 0.0020 | 1.1 | 0.0022 |
| Sum | 0.3260 | (1.3) | 0.4309 |
| Design Torque Safety Factor 2 | | | 0.8618 |

### 7.2.4 Qualification tests

According to the design presented in Chapter 5, a BSDU was build in order to carry out the first environmental tests. This EQM was subjected to a complete test cycle including mechanical vibration testing, venting, thermal-vacuum cycles and ambient deployment (in this order). The EQM included all mechanisms, electronics, two sail segments and one boom. Due to reasons of funding it did not include a battery and operational photovoltaic arrays on the BSDU walls. Instead mass dummies for these components were used and the power supply came through the EGSE plug on the backside of the BSDU. The EQM was mounted on a test adapter using the hold down and release mechanisms as presented in Section 5.3. The adjacent sail spools that would be mounted on the other BSDUs were mounted on this test adapter in the same way as they would be on these BSDUs. The EQM mounted on the test adapter just before testing is shown in Figure 7.18.

The Gossamer-1 project suffered from a lack of resources, which also had a negative effect on the development of key components. The internally developed booms as well as the boom guiding

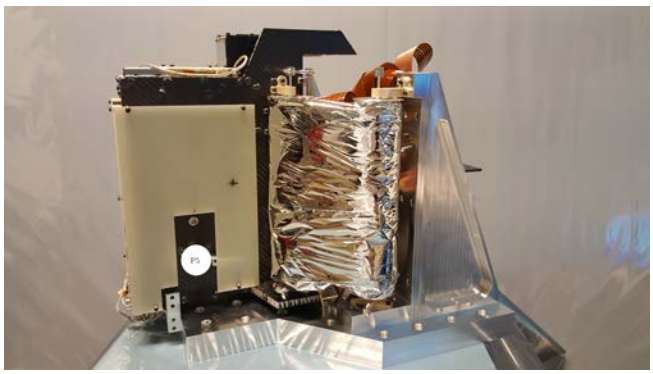

(a) View of the BSDU side on which the sail membrane with functional photovoltaics is mounted.

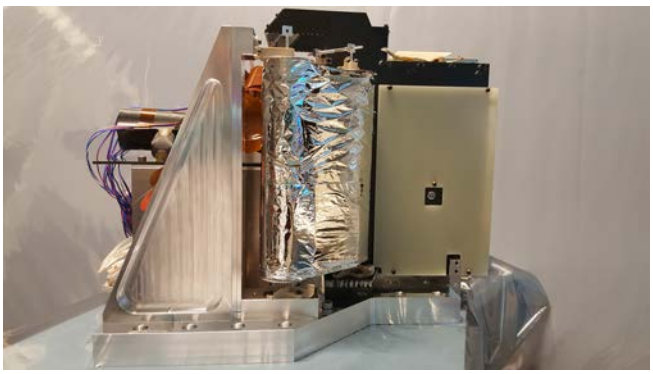

(b) View of the BSDU side on which the sail membrane with photovoltaic dummies is mounted.

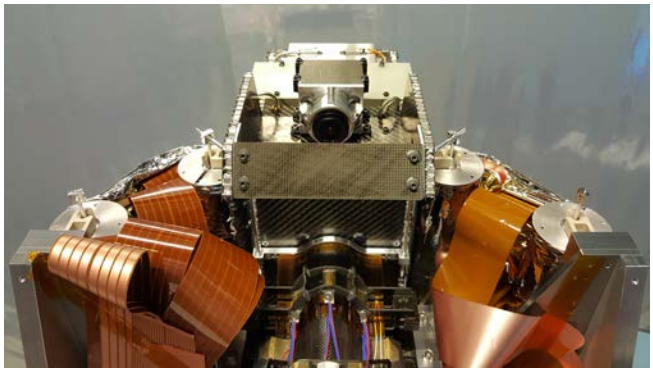

(c) Front view (from CSCU).

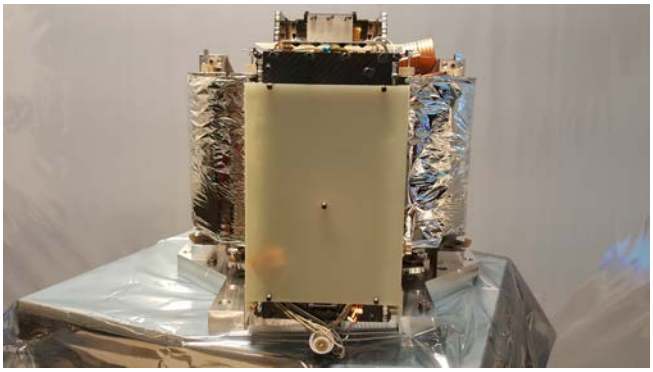

(d) Back view (towards CSCU).

Figure 7.18: Gossamer-1 BSDU EQM mounted on the test adapter that represents the CSCU.

inside the deployment require further attention. Due to procurement problems with the high quality preprags of the CFRP material used for the manufacturing of the booms, these booms are very brittle compared to the previously manufactured booms. In particular, the boom flanges tend to crack and delaminate. The delamination problem accrued due to a warp in the manufacturing tools which were in use for many years and are currently being replaced. Within the Gossamer-1 project these problems were not solved. As a result, only one fragile boom was available for the EQM test campaign while the original test plan considered the use of three booms (one engineering model for preliminary testing, one EQM boom and one EQM spare). During the first preliminary functional tests, the one available boom cracked and got jammed inside the deployment unit. Repairing the damaged boom required shortening it, so that it unavoidably became too short to test the separation of the BSFR from the BSDU and also the BSDU jettisoning. Both phases could therefor not be tested due to the unavailability of suitable booms.

### EQM vibration test

For the first vibration test with the EQM model, the expected launch loads (see Appendix A) were directly transmitted into the test adapter. For the full Gossamer-1 configuration the loads would be transferred through the CSCU to to the BSDUs. Additional structural amplification is to be expected. This has not yet been fully analyzed nor tested on system level. Such higher loads were tested on subsystem level (see Section 7.2.2). The test setup during vibration testing is shown in Figure 7.19.

In contrast to the preliminary analysis presented in Seefeldt et al. (9) the first eigenfrequencies of the EQM are significantly lower. A more detailed FEM analysis that took flexibility of the interfaces into account is presented by Boblenz (125). It reveals the first eigenfrequencies at 76.5 Hz and 83.2 Hz

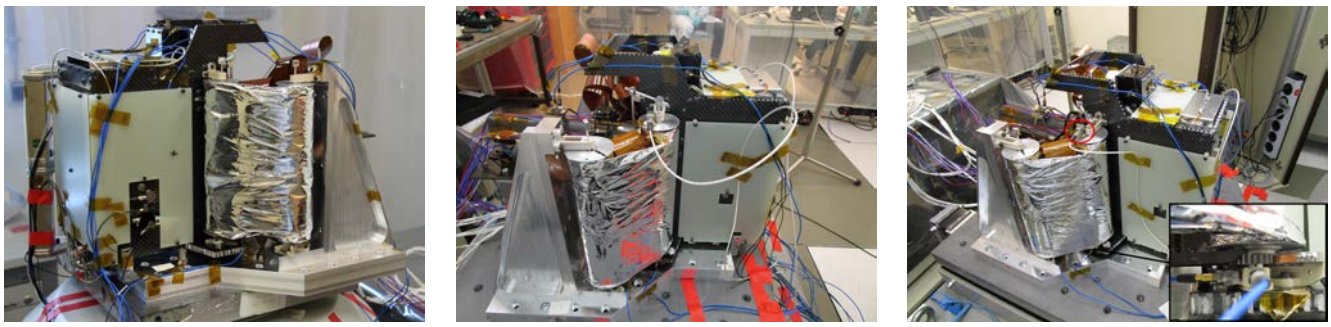

(a) Vibration test $z_s$-axis. (b) Vibration test $y_s$-axis. (c) Vibration test $x_s$-axis.

Figure 7.19: Gossamer-1 BSDU vibration test. The sensor on top of the spool is highlighted with a red circle. Another sensor was mounted right beneath the spool on the primary structure.

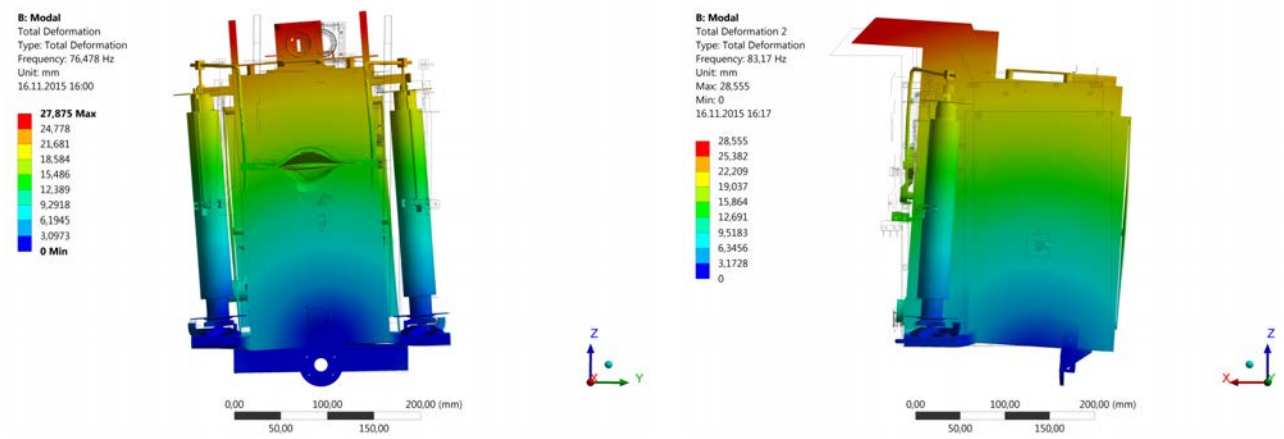


(a) First global mode at 76.5 Hz. (b) Second global mode at 83.2 Hz.

Figure 7.20: Gossamer-1 EQM eigenmodes Boblenz (125).

When testing folded and coiled foils it is not possible to attach acceleration sensors directly to the foil. The mass of the sensor itself would obviously significantly influence the behavior of the foil. By that reasoning, the acceleration sensors were only mounted on solid structures such as the sail spool. The sensor at the sail spool (see Figure 7.19(c), highlighted with the red circle) gives an impression of the loads transferred to the folded and coiled sail segment. Figure 7.21(a) shows the response of the sail spool on the sinusoidal loads, and Figure 7.21(b) shows the response to the random loads.

The hold down and release mechanisms are not designed to pretension the configuration according to the launch loads. This is usually done for standard spacecrafts in order to prevent any relative movement between parts. In the field of small satellites, this is often difficult to implement because mass and size constraints just do not allow such a stiff structural design. Extensive testing, as presented here, is then required for the functional verification of mechanisms like the sail spool launch lock. The first global eigenfrequencies and their change throughout the vibration testing are shown in Table 7.3.

Table 7.3: The first eigenfrequencies measured at the sail spool are the global eigenfrequencies.

| Axis | Eigenfrequency (Quality factor) | | |
|---|---|---|---|
| | Before test | After sinusoidal loads | After random loads |
| $x_s$ | 60 Hz (Q=10) | 61 Hz (Q=10) | 61 Hz(Q=10) |
| $y_s$ | 62 Hz (Q=14) | 62 Hz (Q=17) | 63 Hz (Q=14) |
| $z_s$ | 305 Hz (Q=7) | 381 Hz (Q=5) | 237 Hz (Q=5) |

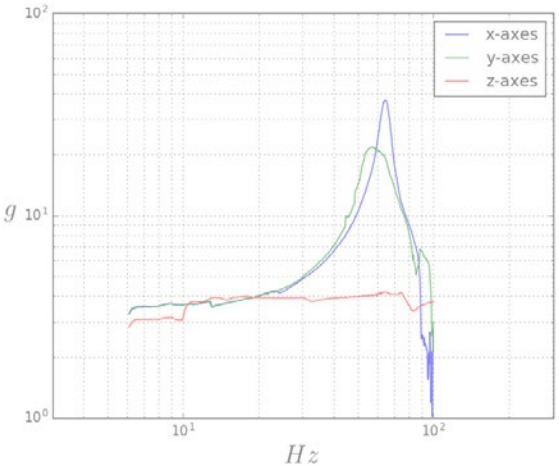


(a) Sail spool response to sinusoidal loads.

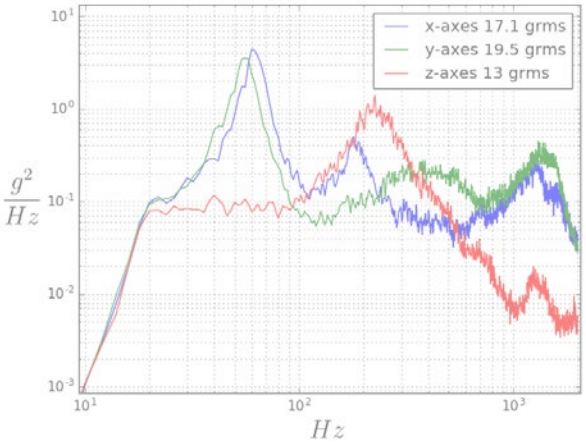


(b) Sail spool response to random loads.

Figure 7.21: Accelerations measured on the sail spool during the EQM tests.

### EQM venting test

The test was conducted in the same manner as the test with the sail segment breadboard (see Section 7.2.2). The test setup with the EQM is shown in Figure 7.22(a), and the pressure progression in the venting chamber, together with the fairing pressure of the VEGA (Arianespace (122)) and Ariane 5 (Arianespace (123)) fairing during launch for comparison, is given in Figure 7.22(b).

(a) Gossamer-1 BSDU venting test.

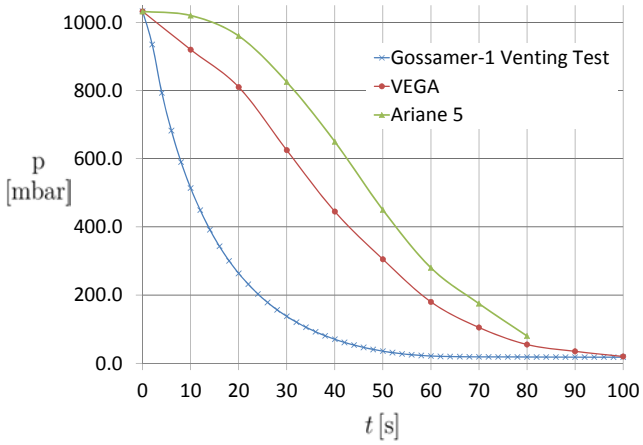


(b) Pressure progression during venting test and comparison to launchers.

Figure 7.22: Gossamer-1 BSDU EQM venting test.

During the venting test a very small movement in the outer foil layer was visible. The membrane, as well as the whole EQM successfully passed the venting test. There was no visible deformation in the membrane present after the venting test. The test campaign was then continued with thermal-vacuum cycling.

### EQM thermal-vacuum test

In a first thermal-vacuum test, three cycles between roughly +50°C and −40°C were tested. The test setup is presented in Figure 7.23(a) and the temperature progression is shown in Figure 7.24. The BSDU was still mounted on the test adapter, but in addition, a board with rolls was mounted underneath it. On every hot and cold plateau a functional check of the electronics was

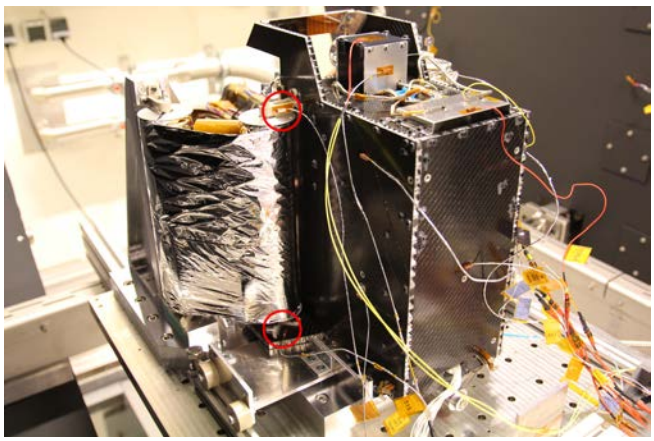

(a) Test setup for thermal vacuum cycles.

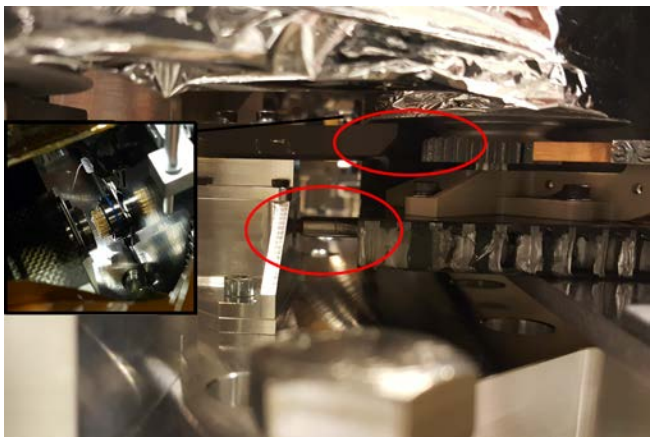

(b) BSDU/CSCU separation.

Figure 7.23: Gossamer-1 BSDU EQM thermal-vacuum test. Sensor positions are highlighted with a red circle.

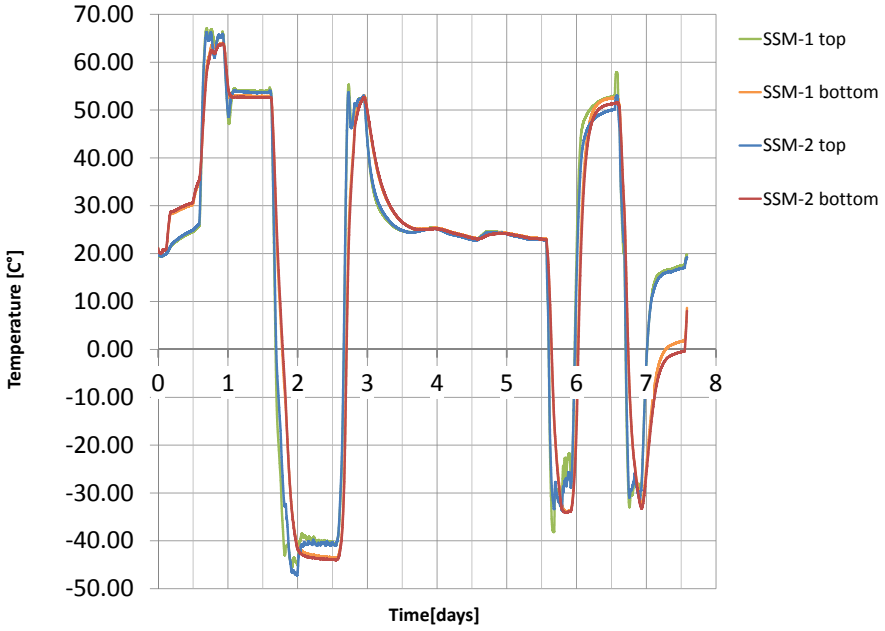


Figure 7.24: Temperatures of the sail spool.

made, and the motor was activated but not rotated. Actual thermal-vacuum deployment was not made. After the thermal cycling, the hold down and release mechanisms were activated and the separation of the BSDU was executed. During the separation, the BSDU rolled a few centimeters on the board.

The functional check out of the electronics worked well and the motor also always responded. The hold down and release mechanisms all worked, but the safety cap of the frangibolt was not sufficiently sized and was destroyed by the cracking bolt.The separation after the thermal cycling also worked smoothly. The locking pins between BSDU and CSCU separated, the sail spool locking disengaged and the umbilical plug disconnected. Before the test campaign, the separation forces were measured with a force gauge under ambient conditions to be between 13 N and 18 N. The deployment unit that was already released was then mounted on the deployment test rig and the deployment was continued under ambient conditions.

**EQM deployment test**

For the deployment test, the same test setup was used as before for the engineering model (see Section 7.2.3). In preparation for the test, the force required to move the air-bearing test rig was measured with a force gauge to be 11 N at maximum. This is still significant compared to the overall deployment forces, but a further reduction with this test rig was not possible.

In order to get a better understanding of the composition of the measured forces, the forces required to rotate the spools (including the brake) mounted on the linear drive units were measured. A rope was coiled on the spool and pulled off by the drive units moving with 4 mm/s for one meter travel distance as shown in Figure 7.25. The original measurement took 12.5 force measurements per second. Figure 7.26(a) shows the data as a function of the spool rotation angle $\alpha$, which is received by multiplication of the deployment speed with the measurement time. The measurement shows the characteristic as predicted with Equation 5.13 (see Figure 6.9(a)). With a periodicity of 0.2 rad, the force is oscillates. After the maximum force is reached, there is a sharp decrease in the force as the spring snaps to the next gear tooth. When the force increases, the friction between the rough gear surface and the spring causes some local force peaks. Furthermore, manufacturing and assembling tolerances cause a deviation between the two spool brakes measured. The complete measurement, shown in Figure 7.26(b) as a function of the spool rotations, also shows an oscillation per spool rotation. This is also likely because of manufacturing tolerances which are present in both spools due to the same production process (3D-printing) and possible misalignment of the spool in the bearings. According to the predicted forces, the maximum should appear at 1.99 N and the minimum at 1.1 N. Although the amplitude of 0.5 N (1 N between minimum and maximum force) is reproduced well, the minimum and maximum forces vary slightly. While generally higher forces were expected due to friction (not considered in the model), the impact of the inaccuracies of the geometry is apparently much stronger. During one oscillation, the peak of the forces can be up to 2.6 N and the minimum can decrease down to 0.3 N. Taking the impact of the geometric tolerances of the hardware into account, the model is still considered to be sufficiently accurate for the design and sizing process, which usually includes safety factors anyway.

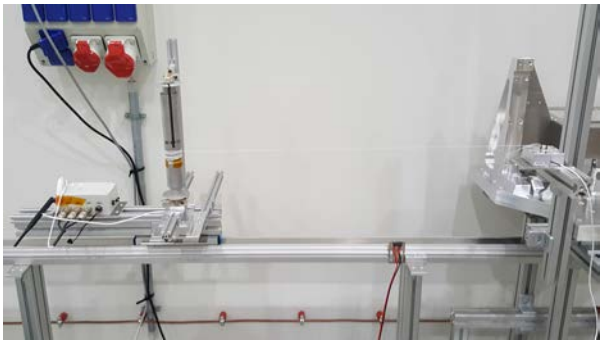

Figure 7.25: Measurement of the spool brake forces. The spool is moved by the linear unit to the left. Thereby, a thin rope that is connected to a force gauge on the right is uncoiled from the spool.

For the deployment of the sail segments with photovoltaics and mass dummies, it was necessary to support the sail segments. The gravity load would otherwise just uncoil the sail segments and due to the high load, there would also be a risk of destroying the interfaces of the sail to the central unit and the boom. The laboratory EQM deployment is shown in Figure 7.27. During the deployment test several interruptions took place in order to perform functional checks and in order to position and adjust the support structures:

- Event at $t_1$ - interruption after deploying the first centimeters from the BSDU so that the deployed length on the linear units and on the BSDU is equal.

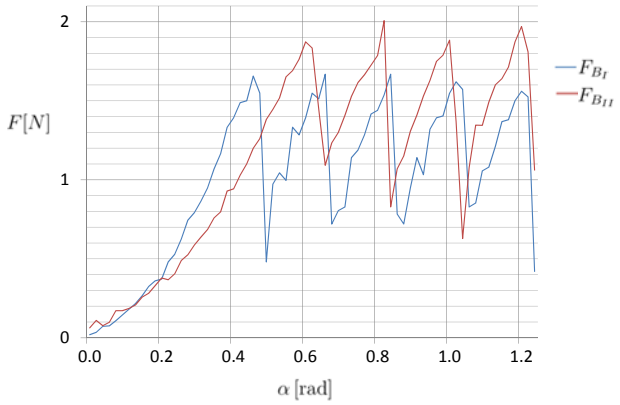


(a) Details of the measured brake force at the beginning of the measurement.

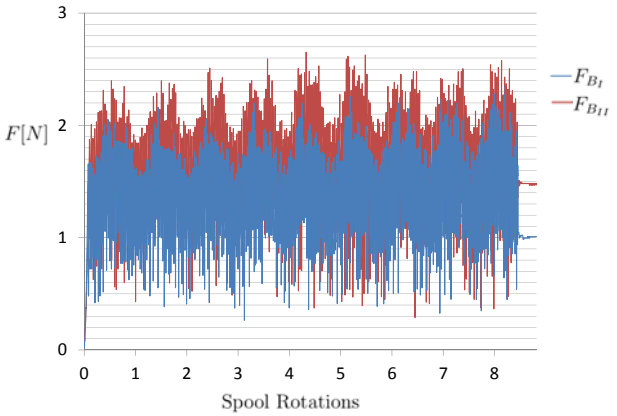


(b) Complete measurement of the brake force.

Figure 7.26: Force measurement of the brake forces of the spools mounted on the linear drives.

- Event at $t_2$ - interruption for system check,
- Event at $t_3$ - adjusting the support for the photovoltaic area below the sail spools so that it is partly supported during deployment,
- Event at $t_4$ - full support of photovoltaic area,
- Event at $t_5$ - adjusting the support for the whole sail segment below the sail spools so that it is partly supported during deployment,
- Event at $t_6$ - full support of sail segment,
- Event at $t_7$ - sail tensioning before sail separation.

The deployment forces and the angles of attack are shown in Figures 7.28 and 7.29. In contrast to the model presented in Section 4.2, the deployment under gravitation causes additional loads. The gravity load directly increases the forces in $z_s$-direction. Additionally the loads in $y_s$-direction increase due to the slag of the membrane between the two spools from which a segment is uncoiled.

The general progression shows that the total force is in the order of the brake force until the segments are spanned against the gravity loads. Every time the segment is additionally supported, the forces decrease (depending on the amount of support provided). This can be observed well after $t_3$ when the deployed parts of the segment are well-sported. Just after this event, the deployment forces are close to the prediction that did not take gravity loads into account (see Figure 6.11). When the sail is again partly unsupported the forces increase again (at approximately 6.5 min). Close to the end of the deployment, the support is adjusted again and the segments are laying on the support. When the fully deployed segments are then tensioned against the gravity loads, the highest forces appear.

Gravity loads are also reflected in the force angles. The angle $\zeta$ is always negative, meaning that the force always points downwards in the direction of the gravity load. When the deployed parts of the sail segments are supported, this angle gets closer to zero as the gravity load is carried by the support instead of the being transferred to the sail spools. When the support is compensating for the gravity load, the force transferred through the hypotenuses is decreasing, which in turn decreases the absolute value of angle $\delta$. That reflects that the forces are transferred more through the cathetus as expected according to Section 4.2 for deployment in a zero gravity environment.

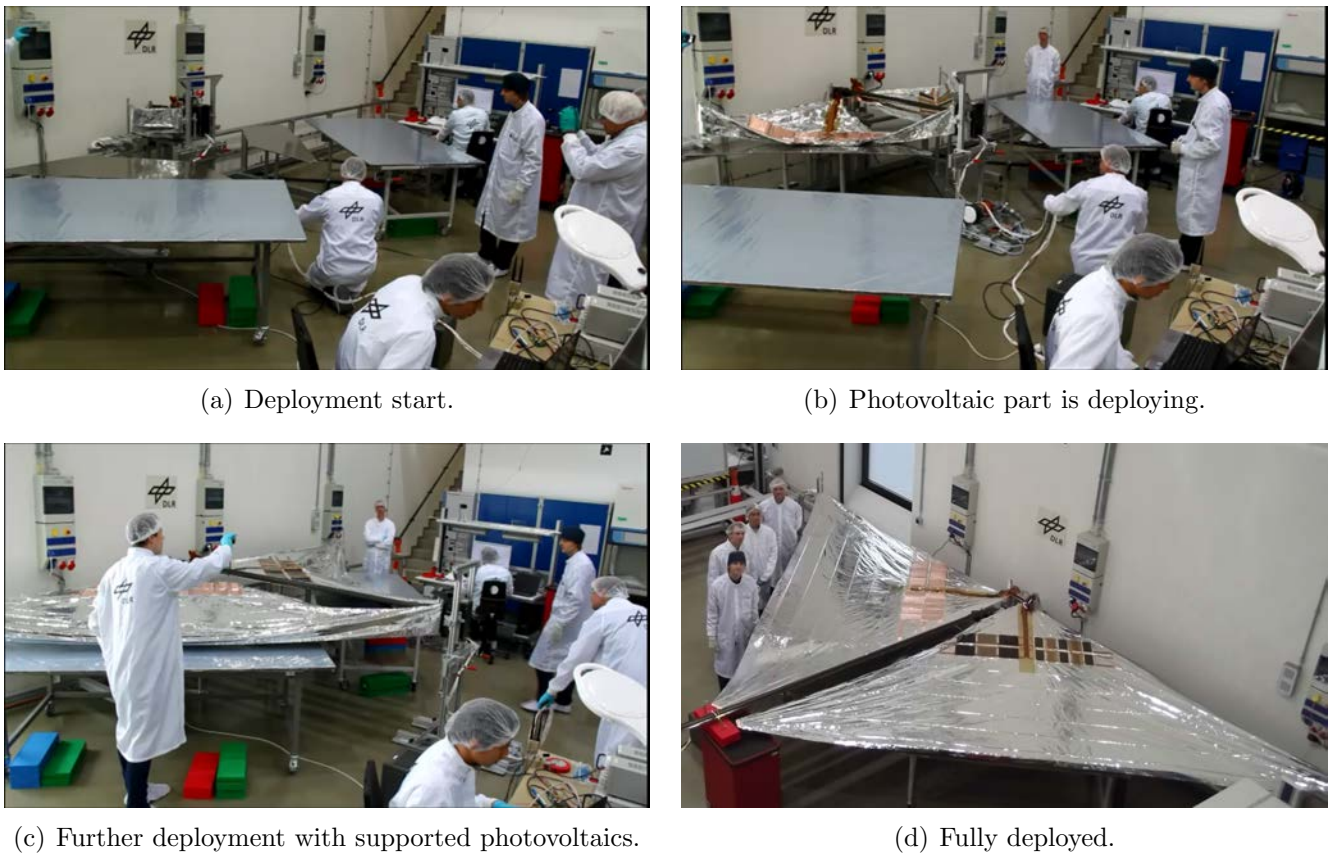

(a) Deployment start.

(b) Photovoltaic part is deploying.

(c) Further deployment with supported photovoltaics.

(d) Fully deployed.

Figure 7.27: Gossamer-1 deployment test with BSDU-EQM in progress.

Due to the spool brake the fast oscillations are present during the deployment, but only when the sail segment is well-supported (e.g. just after $t_2$ and $t_3$) is the amplitude the same as it is for the brake force (see Figure 7.26). The slag of the segment between the two spools from which it is deployed and the wavering of the sail between these spools increases the amplitudes.

As described in the introduction of Section 7.2.4, the tests with the EQM had to be conducted with only one boom that was shortened during repair after a problem during the first functional test. The separation was therefore tested after the deployment unit had passed the normal locking position by about 20 cm. While forces were not measured, it needs to be stated that the separation was not smooth. In a first functional test that is not further described here, the separation was investigated with the stiff linear drives instead of a flexible boom and with a stiff mounting point instead of the BSFR. While the separation with such a stiff setup worked well, the interaction between the separating sail interface with the BSFR that tilted due to the sail tension loads led to clamping during the separation. This significantly increased the forces required for the separation process. This point needs further development work. The following points can potentially improve the design

- better fixation of the interface on the boom in order to reduce tilting of the fixation ring,
- increasing the insert of the sail interface that is mounted inside the spool to about one quarter of the spool's circumference,
- increaseing the bearing diameter would allow an easier adjustment of the geometry to ensure that interface can slip out of the bearing easily,
- it could further be considered to allow an rotation of the interface between sail and BSFR.

A further elaboration of these design features must be carried out in possible future projects.

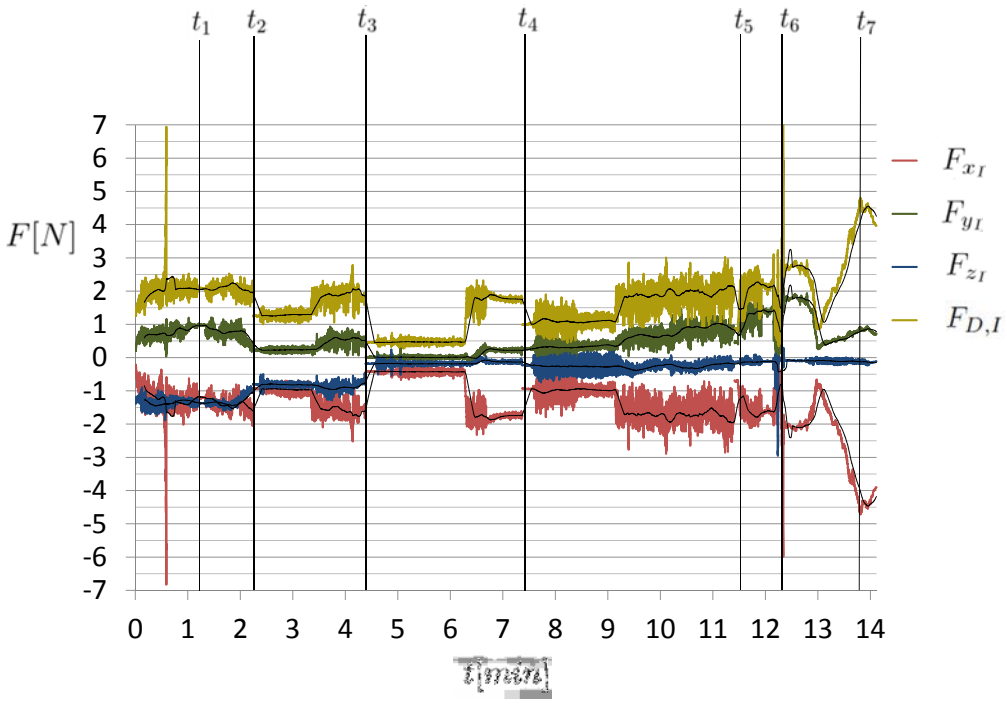


(a) Measured deployment forces $F_{D_I}$ and components.

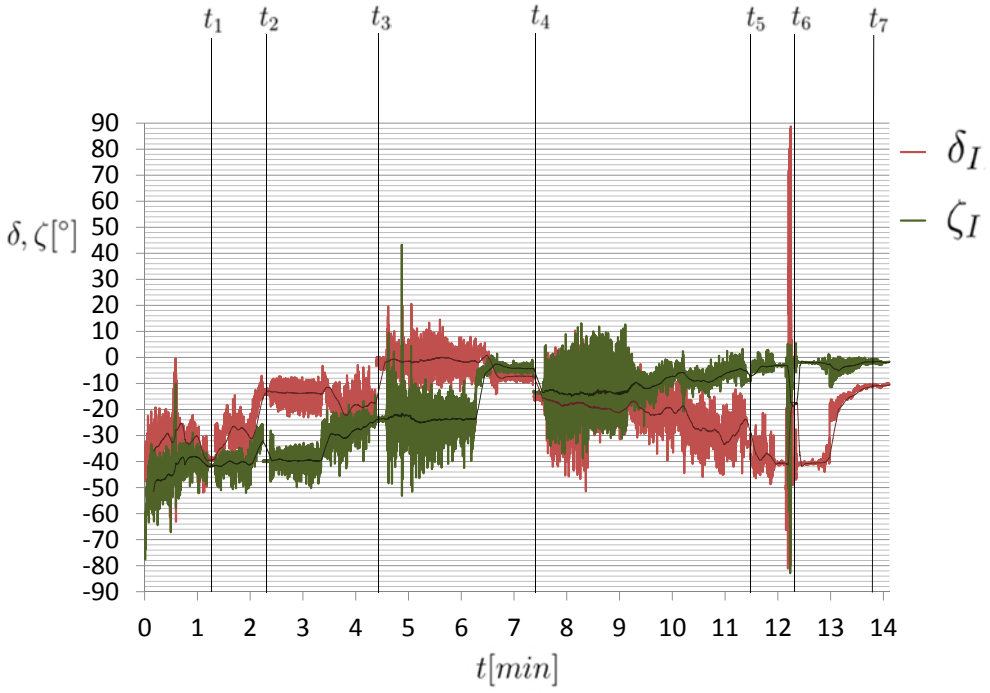


(b) Angles of atack of $F_{D_I}$.

Figure 7.28: Measured deployment forces during ambient deployment with linear drive units, measured for the segment with dummy photovoltaics (geometrical conventions see Figure 4.20, subscribe $I$)

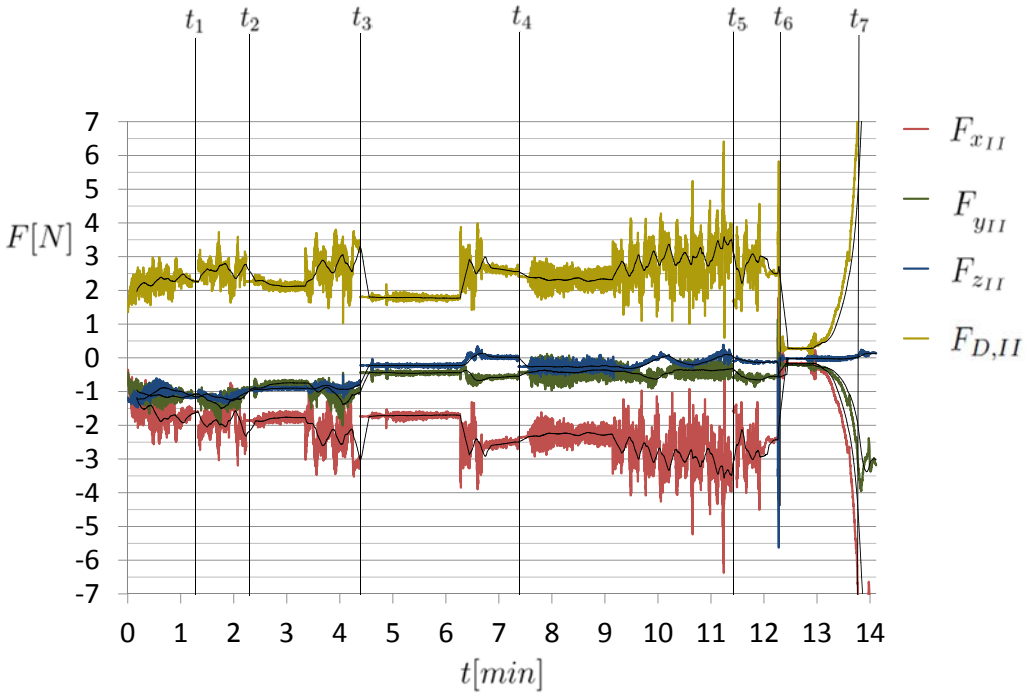


(a) Measured deployment forces $F_{D_{II}}$ and components.

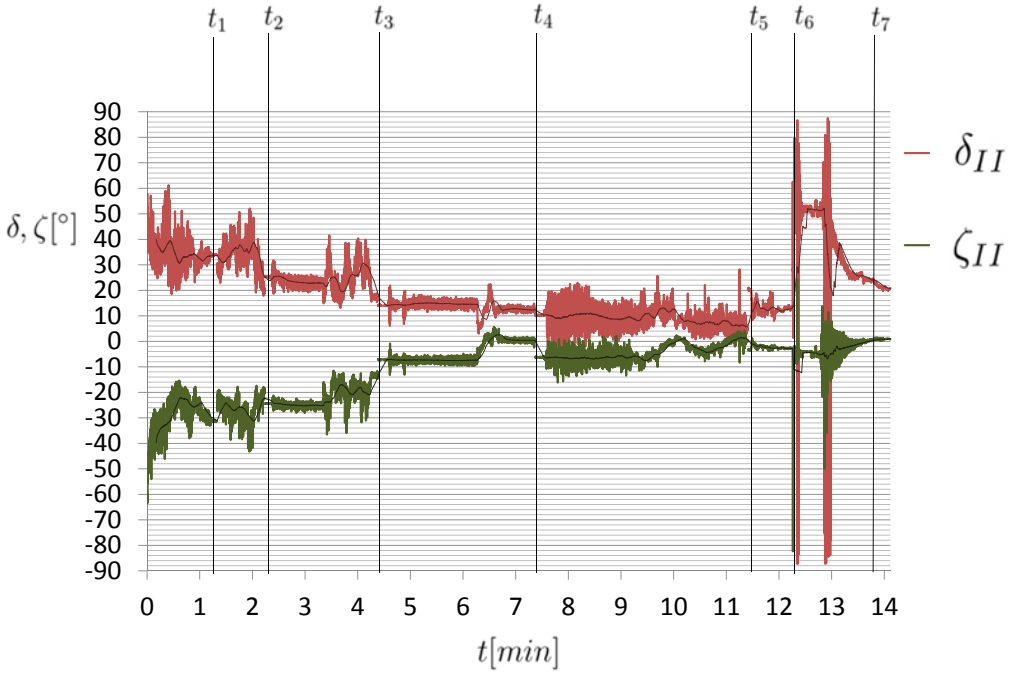


(b) Angles of atack of $F_{D_{II}}$.

Figure 7.29: Measured deployment forces during ambient deployment with linear drive units, measured for the segment with dummy photovoltaics (geometrical conventions see Figure 4.20, subscribe $II$)

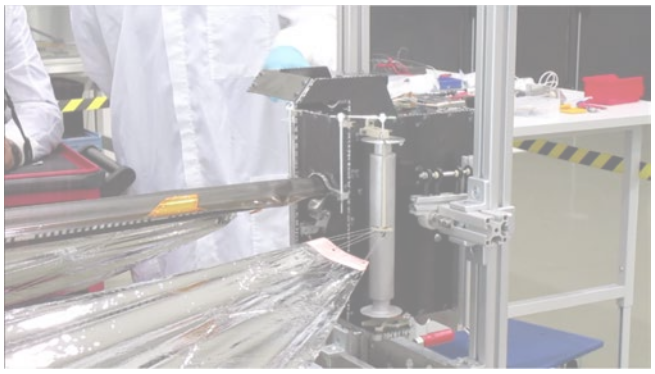

(a) Sail spool is just before separation.

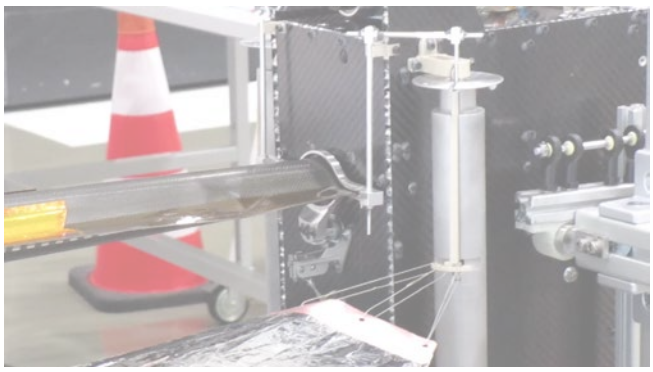

(b) ERM was activated separation started.

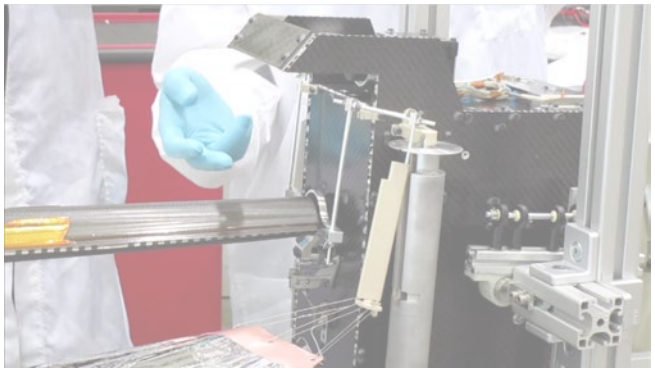

(c) Further separation, fixation ring and sail interface getting tilted.

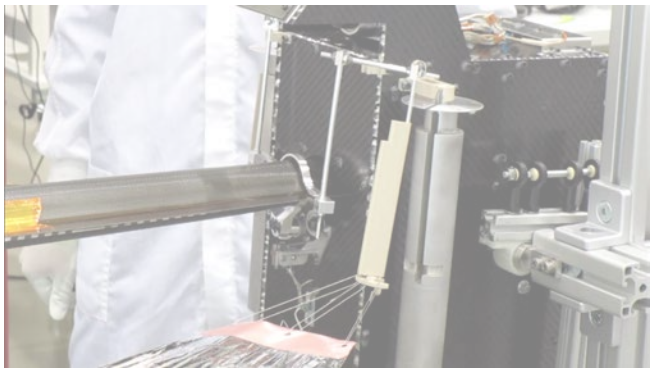

(d) Sail segments are fully separated.

Figure 7.30: Separation of the sail segments from the deployment unit. Note that due to the problems with the boom (see introduction Section 7.2.4) the deployment unit has already passed the locking point (orange wings at the boom flanges) when the separation took place. The fixation ring with the sail interface tilted due to the sail tension loads, which increased the separation forces.

## 7.3 Conclusion

The manufacturing of the sail membrane and integration was established at DLR's Institute of Space Systems in an ISO 8 clean room environment. Bread boards and engineering models according to the designs presented in Sections 5 and 6.2 were manufactured and subject of tests ranging from component level to system level.

With additional simple thermal tests it was demonstrated that the foil and the adhesive can withstand the temperatures that are expected with a purely aluminum coated foil in an Earth orbit. Using materials that can withstand the space environment, a first breadboard of the sail was subject to environmental and deployment testing. The stowed segment withstood the vibration loads that are expected to occur for the Gossamer-1 configuration during launch. The stowed segment also passed a test with high static accelerations on a centrifuge. After subjecting the breadboard to these mechanical loads it was verified that the air can be vented out of the stowed sail segment. A deployment after these tests showed that the sail segment and its mechanical interfaces were intact.

The deployment process, and especially the interaction between two sail segments, a boom and the deployment unit, was investigated during a laboratory deployment. This test also included the electronics and software of the Gossamer-1 system in order to demonstrate a system level functionality. Deployment on system level employing the deployment test rig presented could be successfully demonstrated to be robust, controllable and at no time at risk of entangling. The latter is guaranteed by the folding concept, which ensures that at each stage of deployment only

a minimum length of sail is released. Boom, BSI and BSDU proved to be strong enough to drive the combined deployment of booms and sail segments together under ambient conditions on the test rig. No negative interference between boom deployment and sail deployment was observed. Functionality of all mechanisms involved could be demonstrated. Functionality of all electronics involved could be demonstrated, i.e. wireless control, deployment logic, data acquisition, image acquisition (see Figure 7.15(e) for an image acquired by the BSDU's on-board camera during deployment) and a ground segment representative control via the electronics ground support equipment could be demonstrated.

Tests conducted with an EQM model of the deployment unit confirmed in principle the results of the breadboard tests and the tests conducted with the Engineering Model (EM) for the deployment unit during the system level deployment. With respect to the mechanical loads, it needs to be pointed out that the vibration loads were relatively low, as amplifications of the CSCU structure were not taken into account. The sail segments and the stowing strategy withstood the loads and were successfully deployed afterward. The vibration testing also showed a change of eigenfrequencies in the configuration of the sail and sail spools that were not pretensioned. This was expected due to the relative movement of parts and settling of the components. Additionally, the eigenfrequencies were lower than originally envisaged (compare Tables 7.1 and 7.3). This is due to additonal flexibiltiy of the bearings that was not considered in the FEM analysis. With respect to the separation of the sail segments from the BSDU, an interaction between the BSFR that was not well-mounted and the flexible sail interface led to clamping, which significantly increases the separation forces. It seems to be possible to adapt the design in order to avoid this clamping.

Besides the only membrane-related aspects of the deployment mainly discussed here, the weakest link of the deployment is currently the boom, especially with the material quality problems that were present at the end of the project when manufacturing the booms for the EQM. The booms allow for high deflections on the order of tenths of centimeters, even for low lateral loads on the order of several Newtons. Interactions within the sail plane due to forces on this order of magnitude are compensated by the test rig because the air-bearing setup itself requires up to 11 N for sliding. Deflections out of the sail plane are completely prevented in the used test rig even though the BSDU was rotatably mounted. It is expected that during deployment the boom, due to its flexibility, would constantly be deflected in an oscillating manner according to the force progression as predicted in Section 4.2.

# Chapter 8

# Discussion and conclusion

With the precursor CubeSat projects and the state-of-the-art review presented in Chapter 2, two main topics for the research on deployable gossamer structures were identified. On the one hand, the technology must provide means to control and automatize the deployment process, and on the other hand, further qualification of it is required to enable first space missions.

Pursuing those goals required, in a first step presented in Chapter 3, the determination of requirements imposed by the space environment in which the system would have to operate. This provides the basis for the following selection of proper membrane materials. The environment differs depending on the mission considered. While for a LEO technology demonstrator like the Gossamer-1, the environment is mainly characterized by AO and VUV radiation, a solar sail mission in interplanetary space has to consider the effect of corpuscular radiation on the materials and of course VUV radiation. Additionally, for a solar sail it is important to have a highly specular reflective material and to preserve the reflectivity throughout the mission, while these aspects are not as important for a short-term deployment technology demonstration in an Earth orbit without actually solar sailing. As substrate material, polyimides are considered because of its superior mechanical properties and thermal resistance. It is shown that for the LEOs an off-the-shelf product like the aluminum coated Upilex-S foil is suitable, although the aluminum coating reaches relatively high temperatures of about 200°C. For a solar sail, a coating system made of aluminum, silicon oxide and titanium oxide with a thickness of 100 nm for each layer is identified as a material that provides a good protection of the substrate against radiation and its thermo-optical properties yield for significantly lower temperatures. This could potentially enable solar sail missions with trajectories much closer to the Sun ($< 0.5\,\mathrm{AU}$). It needs to be pointed out that lower temperature also increases the formation of hydrogen bubbles due to proton radiation and thereby the reflectance decreases. This is a complex process influenced by multiple parameters like temperature, flux, dose and proton energy. In addition the degradation behavior of the coating systems presented here differs from those of pure aluminum. For a certain mission respectively trajectory the coating can be adjusted such that a certain temperature range. For the temperature profile and the proton flux that is expected on a certain trajectory, material degradation experiments with different proton energies needs to be carried out in a facility like the Complex Irradiation Facility at DLR's Institute of Space Systems in order to qualify the material for a certain mission.

In Chapter 4 deployment strategies are evaluated, and it is found that with respect to the requirement of a controlled deployment, the strategies found in former projects had disadvantages.The motivation to deploy the sail segment from spools that move away from the sail center is to have a mechanically stable configuration without much slack in the membrane. All investigated stowing strategies that stow the sail in its center have this disadvantage. As explained, that comes with a risk that during a slow deployment, the sail drifts and gets entangled. In order to realize a controlled deployment, in the way that it can be stopped and resumed at any time while

always providing a mechanically stable configuration, a deployment strategy for large membrane structures is proposed in Section 4.2. The stowing and deployment geometry and the resulting force vector is modeled mathematically. This model is idealized in the sense that it does not take any wrinkling of the membrane into account. When coiling a real membrane, the folded layers are coiled onto different radii, which results in the wrinkling of the layers directed more to the inside. While this effect can be tolerated for the thin foils considered for solar sailing, it causes problems when coiling thicker thin-film photovoltaics that cannot wrinkle without destruction. The equations developed are used to predict the progression of deployment loads in Section 6.3.2.

For the proposed deployment strategy, mechanisms have been designed within the Gossamer-1 project as presented in Chapter 5. These mechanisms ultimately enable the deployment and allow further studies of the deployment process. This especially includes a spool mechanism onto which the folded sail is coiled. This mechanism provides a brake that prohibits a premature uncoiling of the sail. Furthermore, it allows a separation of the sail after the deployment so that the deployment units can be jettisoned in order to achieve the ultimately lightweight sail craft.

For the Gossamer-1 configuration, the membrane design and the deployment process are further studied in Chapter 6. The design of the Gossamer-1 membrane is presented in Section 6.2. One segment is a rectangular triangle with a hypotenuse of 5.3 m. It is manufactured out of four single sheets of the Upilex-S foil. The photovoltaics are located nearby the inner edge together with the harness that is routed along the height of the triangle to the center of the sail or the spacecraft bus, respectively. Considering this design and the Gossamer-1 mechanisms, several load were evaluated.

With the mathematical model of the deployment geometry, the progression of the deployment loads are described. When analyzing the stowing geometry in detail it is revealed that for the deployment process studied here the sail is also not fully tensioned. The slack of a few centimeters of the deploying hypotenuse and the layers folded alongside is small compared to the previous approach where the segments were coiled in the center, and it seems that there is no risk of entanglement. Considering the long booms are more sensitive to bending loads, the hypotenuse slack of a few centimeters might even have the positive effect of reducing this load case. The modeling of the oscillating load (see Section 5.2) in combination with the folding geometry revealed a sensitivity of the resulting load to the symmetry or synchronicity of the deployment of the sail segments coiled on the two spools on each side of the boom. A small difference in the spool rotations causes a significantly different load case. If the deployment would be ideally synchronous, only the moment around the $y_b$-axis would appear, while for a more realistic deployment, the significantly higher moment around the $z_b$-axis as well as a torque around the $x_b$-axis is present. For a more asynchronous deployment in which the uncoiling points on the spools differ significantly, a similar effect is expected due to the oscillation caused by the zig-zag folding, which has not been analyzed yet.

The analysis presented does not take into account any effects of gravity forces present in a laboratory deployment as presented in (9). For such a horizontal deployment, the gravity force pulls the sail down and thereby also tensions the hypotenuse of the deploying sail segment. Assuming that the gravity load would not exceed the spool brake torque during the deployment process (in which case the sail would uncoil independent of the deployment process), the hypotenuse and the folded layers alongside would bend through like a catenary. This would then introduce a load through the hypotenuse, which would increase load angle $\delta$. The direct gravity load increases the $z_b$ forces, thereby increasing the angle $\zeta$. Anyway, for the deployment of the heavier sail membrane with photovoltaics, a supporting structure is required for the compensation of gravity loads.

The elasticity of the booms and their influence on the deployment process is not reflected in the current analysis. The booms considered for the Gossamer-1 deployment are very flexible (see (9)). With progressing deployment, the bending loads will lead to a significant deflection of at least several centimeters. That means that the deployment of all segments is coupled. It is

expected that during deployment, the booms will constantly change the deflection according to the loads subjected to them. This aspect requires further analysis.

While the focus of the presented work was the analysis of the Gossamer-1 stowing and deployment strategy, the coiling of the sail in the opposite direction is also briefly introduced in Section 4.2.1. The main reason to choose the coiling direction was the reduction in the boom bending loads. Nevertheless, coiling the folded sail segments such that the opening of the folds is directed towards the outside would lead to a more compact stowing volume because the folded sail segment can be coiled a little further, as the interface is located on the outside of the coil.

The deployed configuration is analyzed with a finite element model in Section 6.4.1. It reveals very low stress in the membrane and interface loads between two and five Newton depending on the pressure (drag or radiation pressure), and a maximum billowing of a little more than a centimeter for high drag loads of about $2 \cdot 10^{-2}$ Pa that are present in an orbit height of about 200 km. The low stresses and interface loads show that the structural integrity of the membrane can easily be achieved and the interface loads can be used for the structural design and sizing of the booms. The results are further used for a simplified model that incorporates pressure-dependent billowing for attitude simulations.

The microscope analysis of the folding lines presented in Section 6.5 reveals the weak link of the current membrane design. The coating shows cracks inside the folding line which weakens its protective properties. Additionally, multiple reflections inside the folding line can lead to a local temperature increase, or a hot spot. The geometry of the folding line was measured for different tension states and it is shown that even for the low stress present in the membrane with the current design only two reflections in the membrane are possible. This leads to a temperature increase of about 18°K for an aluminum coated foil.

Two sail segments and the deployment mechanisms were manufactured and integrated under ISO 8 clean room conditions. The hardware and test deployment process was verified in an extensive test campaign presented in Chapter 7. The tests ranged from component level to system level and included mechanical vibration, static acceleration, fast decompression, thermal vacuum and laboratory deployment tests. The tests show the general functionality of the deployment process in the space environment simulated in the test laboratories. Therefore it can be concluded that the membrane related aspects of the deployment technology are on TRL six for a 25 $m^2$ LEO deployment demonstrator. However, it should not be concealed that with the first prototypes built there is still room for an optimization of the components. While functionality was demonstrated in the tests, an increase of robustness might be one goal in the further development of mechanisms and booms. With respect to the membrane a striped design could be considered in order to avoid the folding lines but this would only be required for long-term missions, especially in the LEO environment. For a solar sail it could also be concluded that this is only a point of optimization and increase in the overall lifetime that might not be required for a first solar sail. Especially not if the lifetime is significantly more limited by other components, such as a possible attitude control system.

Materials, mechanisms, and a stowing and deployment strategy are presented that enable the controlled and autonomous membrane deployment for space sails. While the analysis presented is applied on a sail with a size of about 5 m × 5 m, it allows an analysis of other configurations as well. This is of particular interest because currently-considered solar sails are about one order of magnitude larger. The deployment strategy is scalable and materials are available that can be used for bigger solar sails as well. Additionally, Appendix B outlines the potential of the currently available technology and its applicability for first missions.

# Chapter 9

# Outlook

Degradation of the foils reflective properties is a major concern for a solar sail. As described, the degradation process is complex and influenced by multiple parameters. In consequence, a combined degradation/mission analysis is proposed. A mission with multiple near earth object rendezvous is often considered as a first solar sail mission and would be a good candidate for further studies.

For such a mission a sail of at least 30 m × 30 m is required. With the tools provided here, a detailed design for this size needs to be implemented and a delta-qualification of the hardware is required.

In order to be able to better evaluate the deployment process under gravity conditions, this aspect could be incorporated in the mathematical model that is derived in this Chapter 4.2.This may be carried out analyzing the configuration in a similar way to a catenary.

The testing showed the suitability of the components for space applications. Still, the robustness of the system and its components could be increased. While the membrane itself is already robust and no failures were observed during several tests, the interaction between the different mechanisms sometimes lead to clamping during the separation process. Simple design changes that could avoid this behavior were already identified and should be implemented in the future.

The membrane deployment technology in Europe and especially the solar sail technology has been significantly advanced withing the Gossamer-1 project and related projects. Even more importantly, critical design factors, analysis strategies and the required tools are now available and can be used for the further development of systems for deployable gossamer structures. If the political support and funding is provided, there is nothing to prevent the development of full-scale solar sails.

# Appendix A

# Launch loads according to Gossamer-1 launcher survey

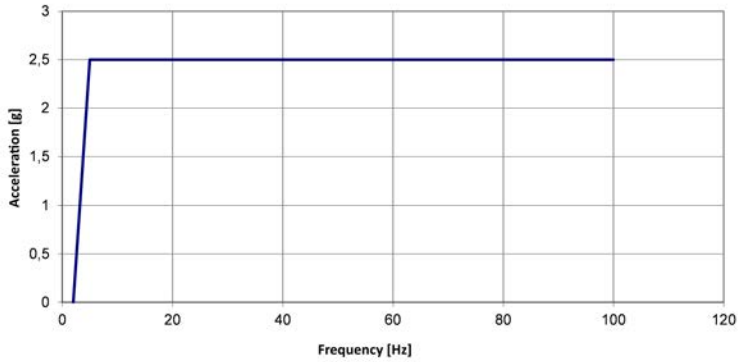


Figure A.1: Lateral sine vibration loads derived from launcher envelope.

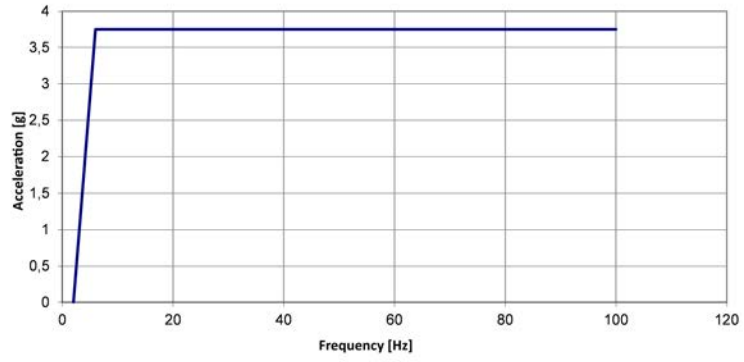


Figure A.2: Longitudinal sine vibration loads derived from launcher envelope.

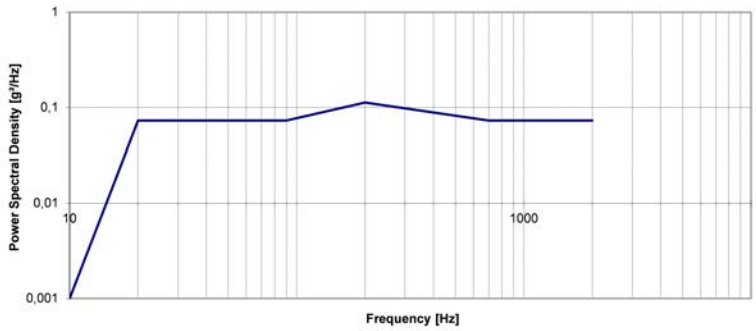


Figure A.3: Random vibration loads derived from launcher envelope ($G_rms = 12.4$).

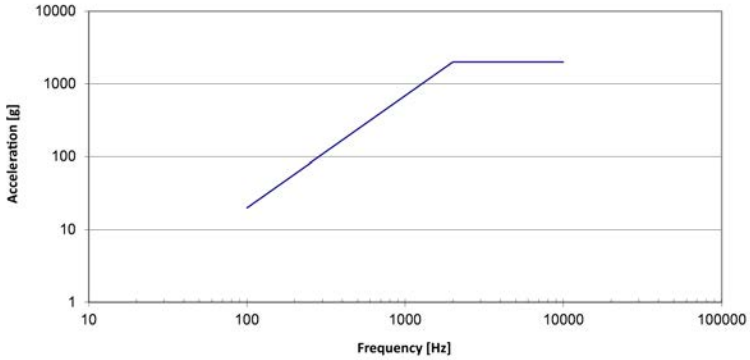


Figure A.4: Shock loads derived from launcher envelope.

# Appendix B

# Gossamer-1 technology performance

With the Gossame-1 technology, the pure sail mass (membrane and booms) as a function of the edge length of the rectangular sail is given in Figure B.1. The mass of the booms used for the Gossamer-1 project is 40 g/m. For Gossamer-2 with 20 m × 20 m it is expected to be 90 g/m and for a Gossamer-3 150 g/m. The boom mass for differently sized sails is linearly interpolated and extrapolated for big sails. The mass of the membrane includes 7.5 $\mu$m polyimide film and the required amount of adhesive for the considered sail size. An often used performance parameter

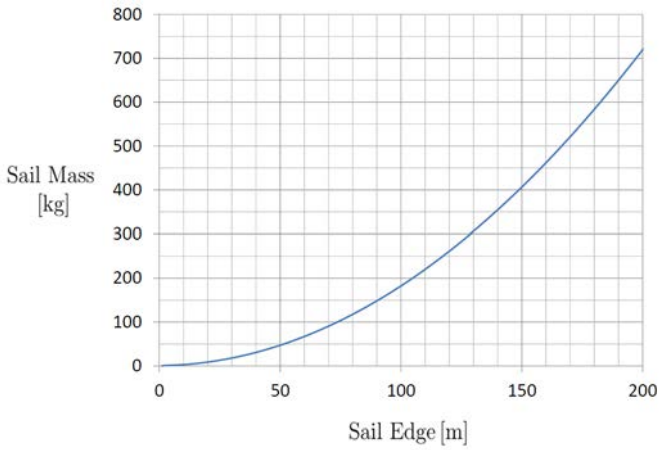


Figure B.1: Sail mass as a function of the edge length of the rectangular sail.

of solar sail is the characteristic acceleration. It is the acceleration which it would be present at 1 AU distance from the Sun when perpendicular irradiated. It is calculated according to Equation 6.20 as

$$a_c = \frac{p_{\mathrm{S,res}} \cdot A}{m} = \frac{S \cdot A}{c \cdot m} \cdot (1 + r_s) \ . \tag{B.1}$$

With the mass estimation, it is possible to also estimate the characteristic accelerations as shown in Figure B.2. The characteristic acceleration is calculated for a reflectivity of 90%. Missions considering multiple near earth object rendezvous as proposed in Peloni et al. (12) and Dachwald et al. (126) would require sails with an characteristic acceleration between 0.1 mm/s$^2$ and 0.2 mm/s$^2$. This can be achieved by sails with an edge length of about 30 m considering a bus and payload mass of about 50 kg. While further development is of course required, this is possible with the sail technology available.

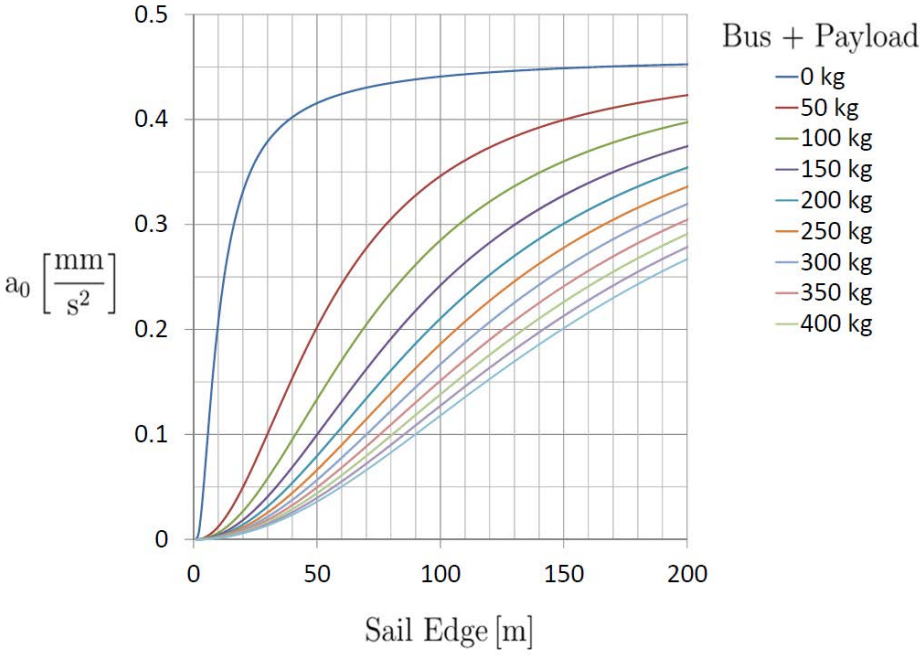


Figure B.2: Characteristic acceleration for different masses of bus and payload. This mass is considered in addition to the sail mass.

# Appendix C

# Gossamer-1 membrane manufacturing documents

- Sail quadrant assembly overview
- Sheet one
- Sheet two
- Sheet three
- Sheet four
- Electrical harness one
- Electrical harness two
- Measurement harness one
- Measurement harness two
- Harness base sheet
- Harness mounting hinges
- Interfaces
- Assembly step one
- Assembly step two
- Assembly step three
- Assembly step four
- Assembly step five
- Assembly step six
- Assembly step seven
- Assembly step eight
- Assembly step nine

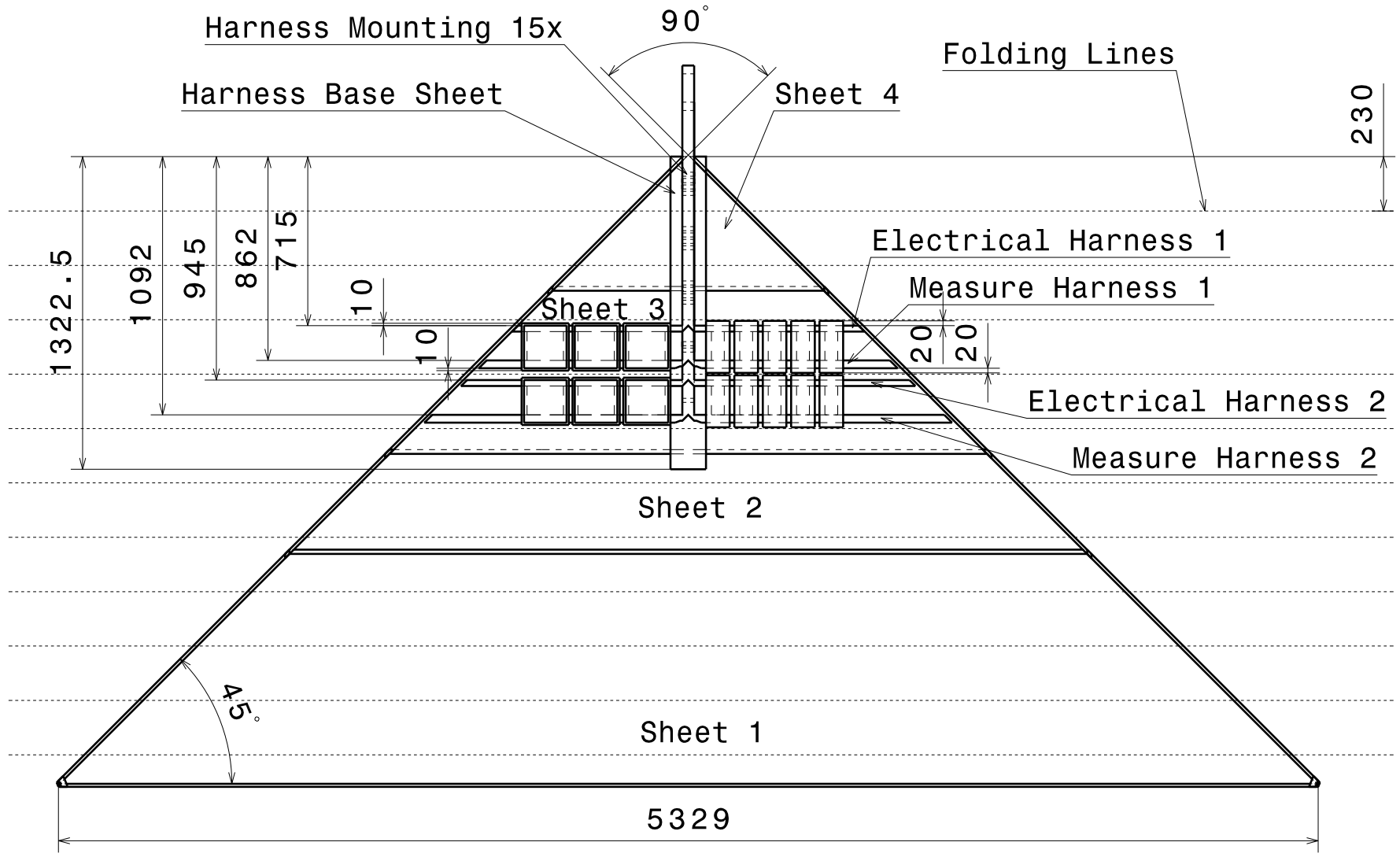


Front View

| Verwendung | | | |
|---|---|---|---|
| Idx | Aenderung | Datum | Name |

| | | | |
|---|---|---|---|
| Projekt: Gossamer-1 | Auftrags-Nummer | Mass-Stab: 1:20 | Net. Gewicht |
| Baugrpuppe: Sail Quadrant | | | Material-Nummer: Upilex S 7.5 um |
| | Datum | Name | Werkstoff: Pi |
| Bearb. | Seefeldt | 12/08/2015 | Benennung: Sail Assembly - Overview |
| Gepr. | | | |
| Norm. | | | |
| Freig. | | | |
| DLR | | | Zeichn.-Nr.: A3 |
| Ursprung | | | Ersatz fuer: / Ersatz durch: |
| | | | NN Nr. |
| | | | NN Bl. |

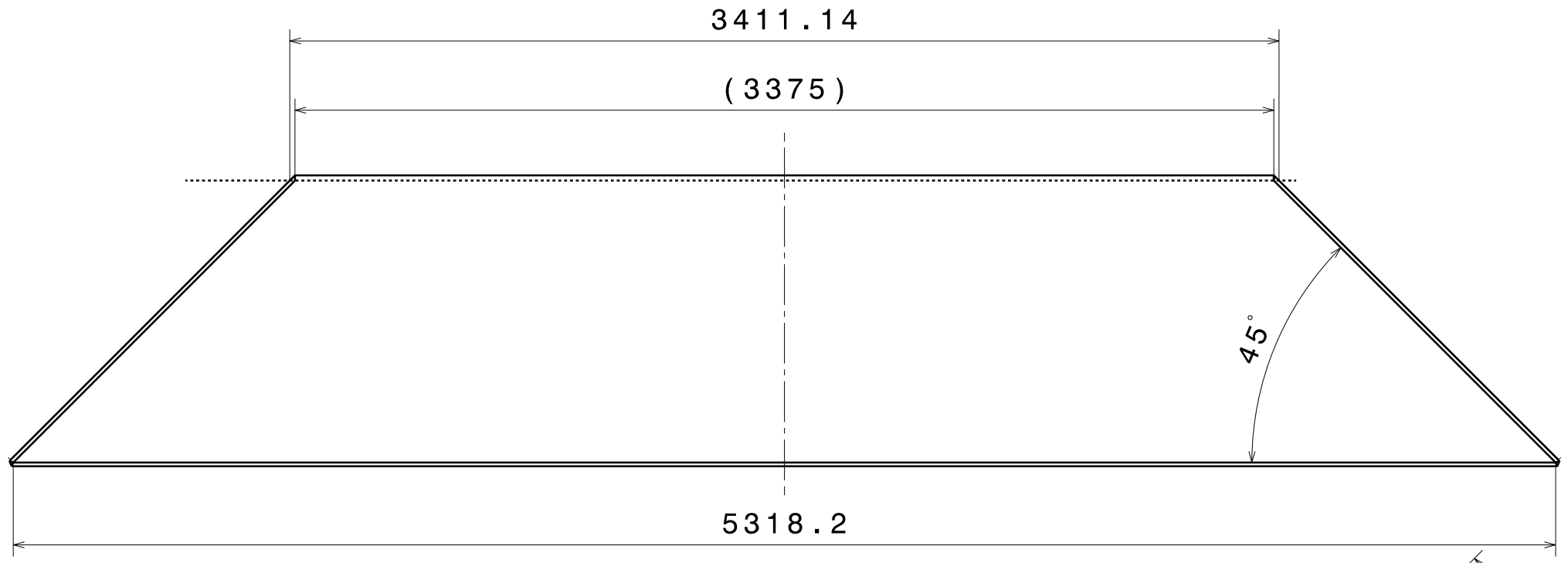


Front view with folded edges
Scale: 1:20

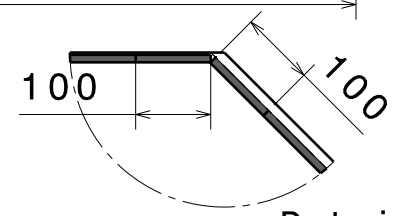


Detail B
Scale: 1:10

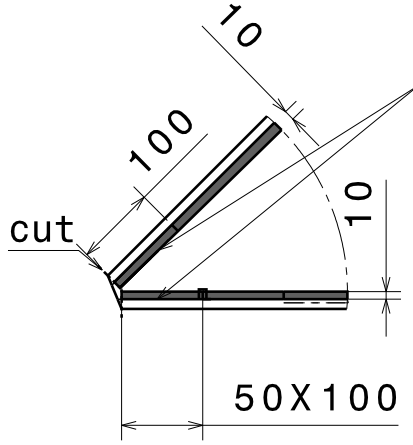


Detail A
Scale 1:10

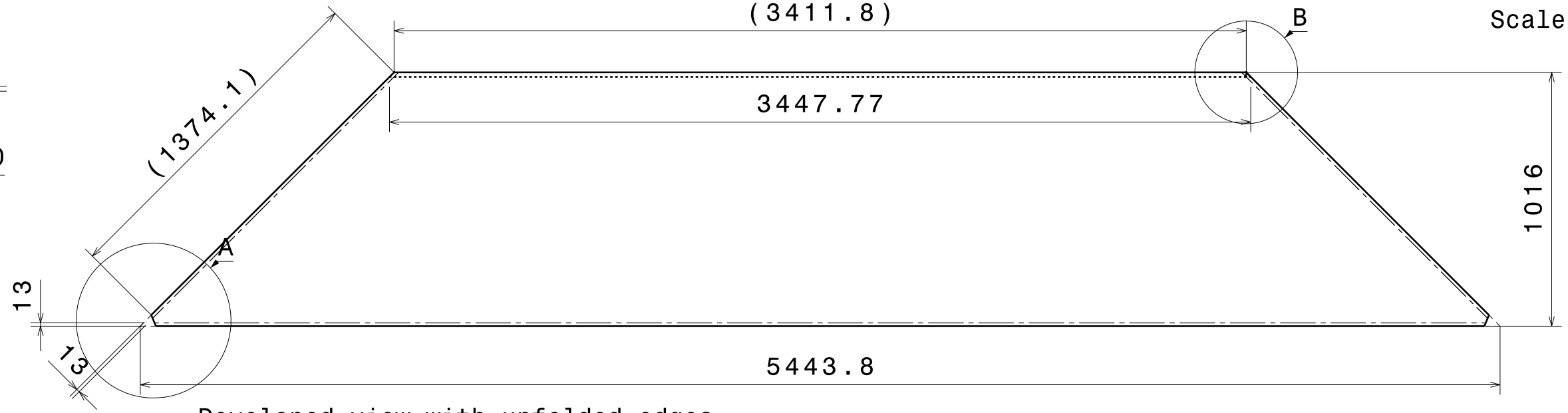


Developed view with unfolded edges
Maßstab: 1:20

| | | | |
|---|---|---|---|
| Idx | Aenderung | Datum | Name |

| | | | |
|---|---|---|---|
| Verwendung | | | |
| Projekt Gossamer-1 | Auftrags-Nummer | Mass-Stab 1:20 | Net. Gewicht |
| Baugrpuppe Sail Quadrant | | | Material-Nummer Upilex S 7.5 µm |
| | Datum | Name | Werkstoff Pi |
| Bearb. | Seefeldt | 12/08/2015 | Benennung |
| Gepr. | | | Sheet Sheet 1 |
| Norm. | | | |
| Freig. | | | |
| DLR | | | Zeichn.-Nr. A3 |
| | | | NN Nr. |
| | | | NN Bl. |
| Ursprung | Ersatz fuer: | Ersatz durch: | |

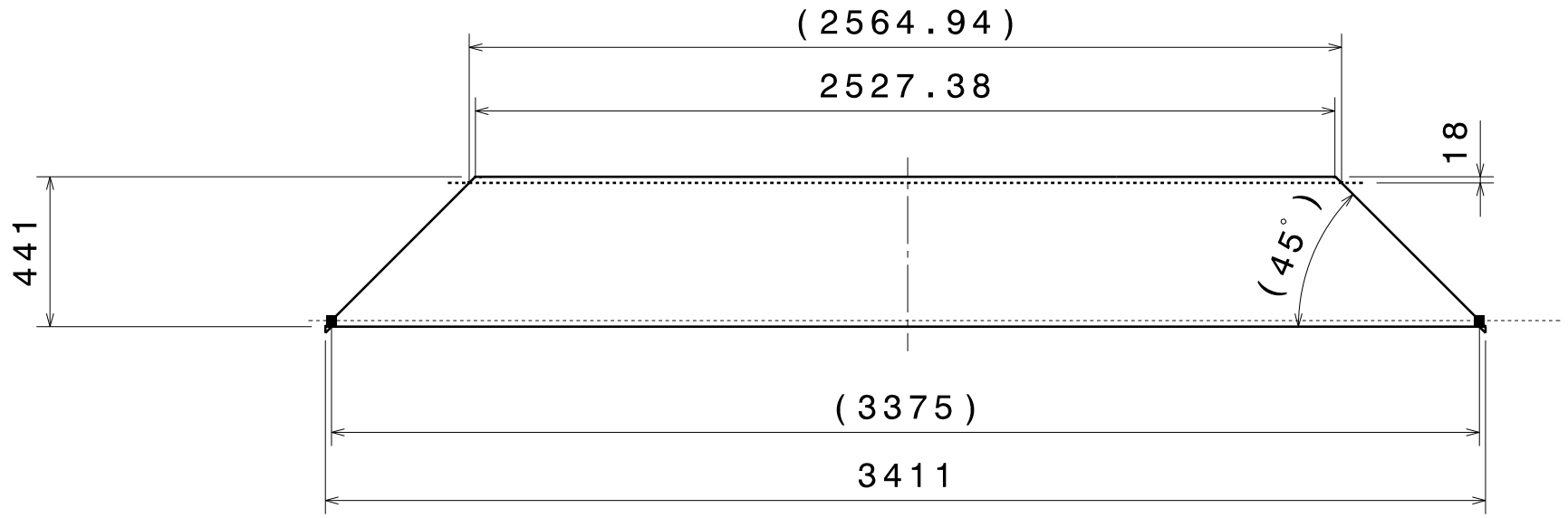


Front view with folded eges
Scale: 1:20

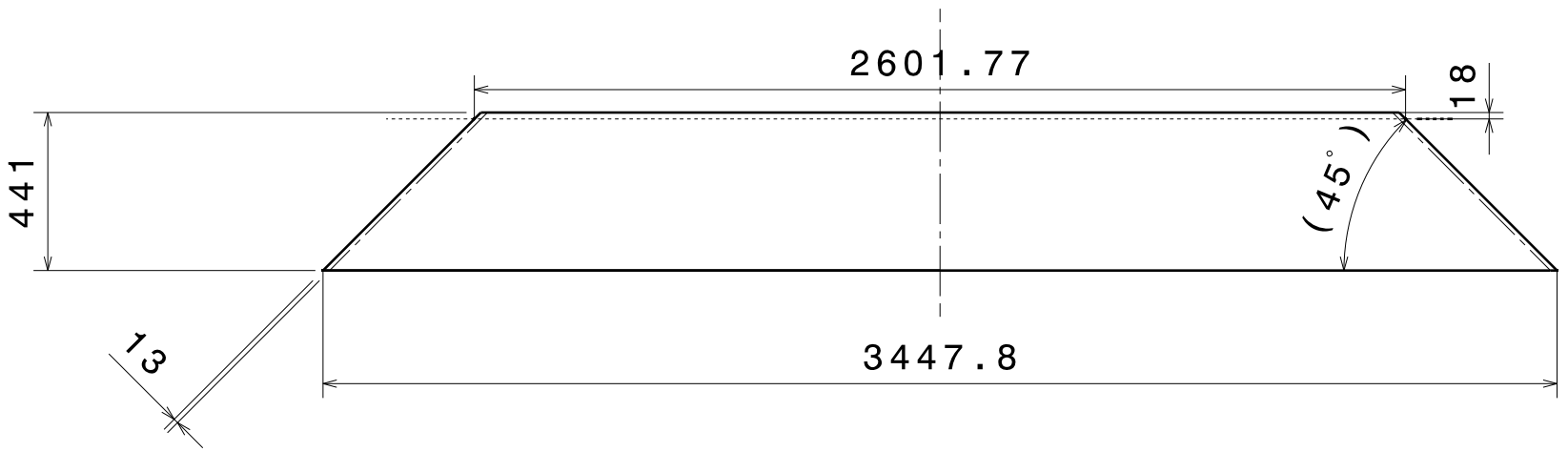


Developed view with unfolded edges
Scale: 1:20

| | | | |
|---|---|---|---|
| Verwendung | | | |
| Idx | Aenderung | Datum | Name |

| | | | |
|---|---|---|---|
| Projekt: Gossamer-1 | Auftrags-Nummer | Mass-Stab: 1:20 | Net. Gewicht |
| Baugrpuppe: Sail Quadrant | | | Material-Nummer: Upilex S 7.5 µm |
| Werkstoff: Pi | Datum | Name | |
| Bearb. | Seefeldt | 12/08/2015 | Benennung: Sheet 2 |
| Gepr. | | | |
| Norm. | | | |
| Freig. | | | |
| DLR | | | Zeichn.-Nr. / A3 / NN Nr. / NN Bl. |
| Ursprung | | | Ersatz fuer: / Ersatz durch: |

## Reinforcement Patch

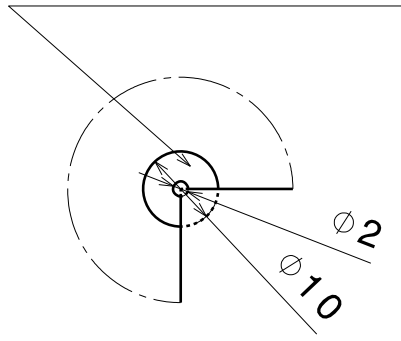


Detail C
Corner reinforcement
(to be applied on
all corners)
Scale: 1:1

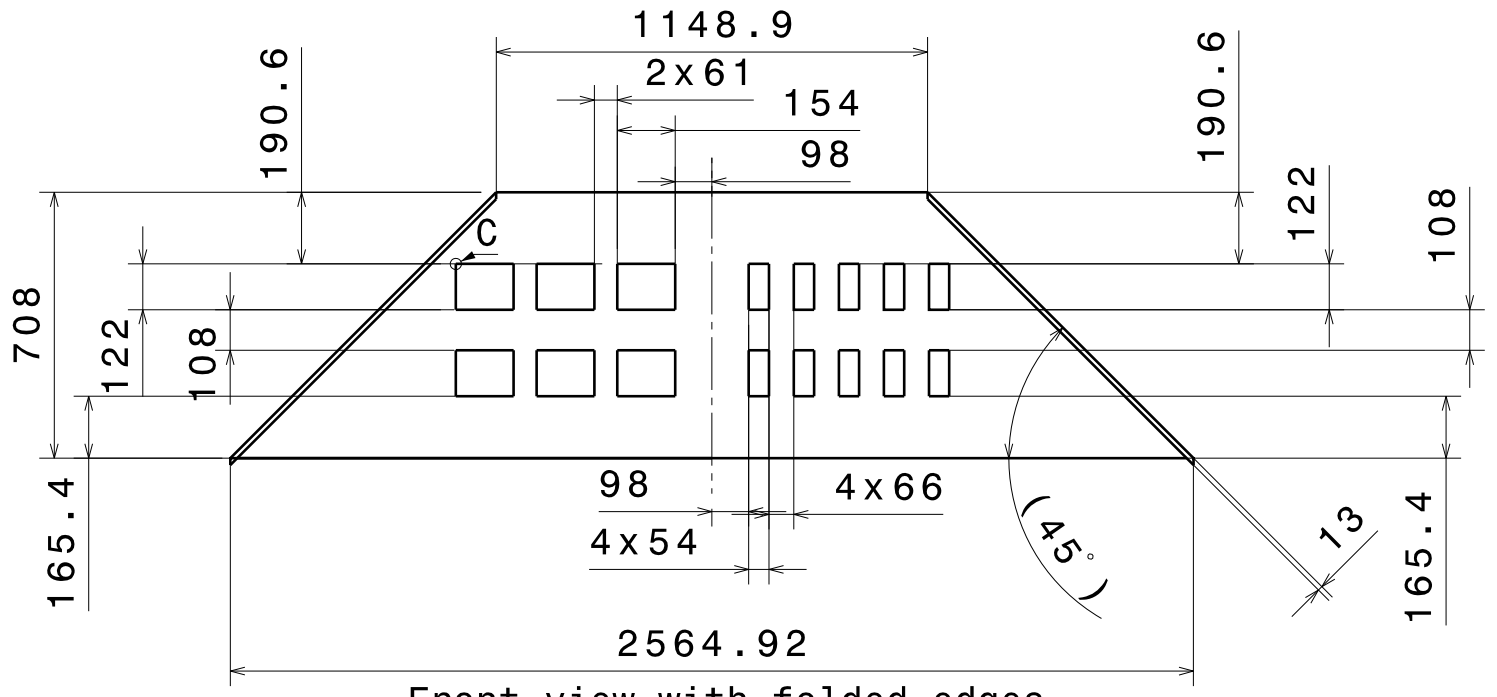


Front view with folded edges
Scale:1:20

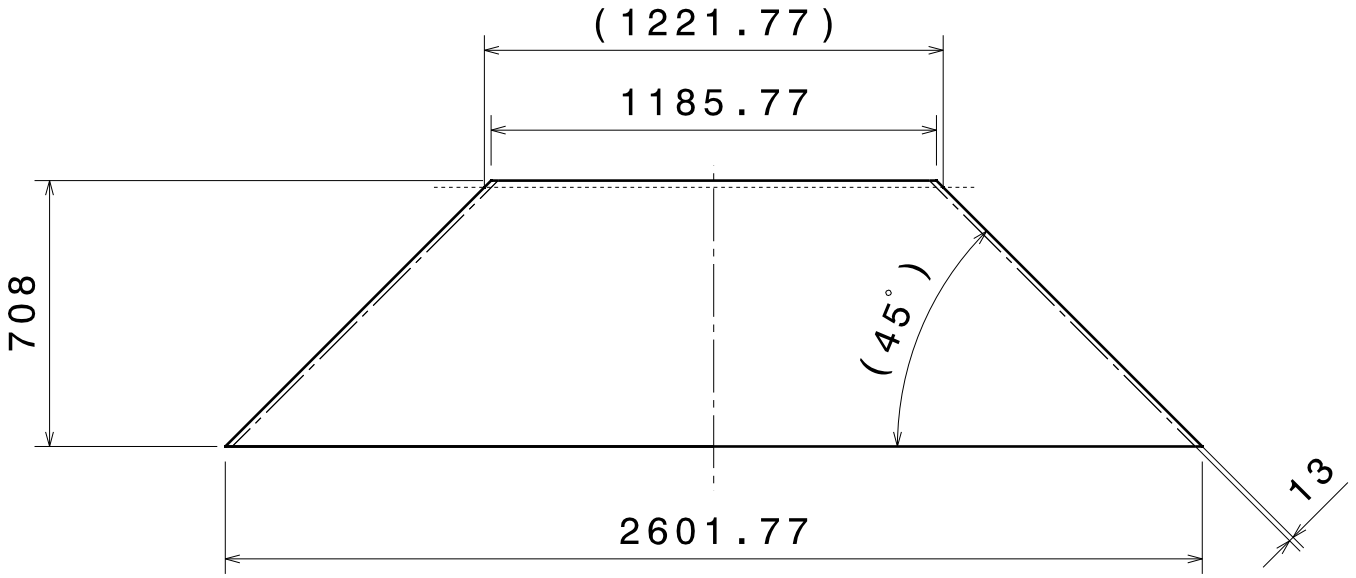


Developed view with unfolded edges
Scale: 1:20

| Verwendung | | | |
|---|---|---|---|
| | | | |
| | | | |
| | | | |
| | | | |
| | | | |
| | | | |
| | | | |
| | | | |
| Idx | Aenderung | Datum | Name |

| | | | |
|---|---|---|---|
| Projekt Gossamer-1 | Auftrags-Nummer | Mass-Stab 1:20 | Net. Gewicht |
| Baugrpuppe Sail Quadrant | | | Material-Nummer Upilex S 7.5 um |
| | Datum | Name | Werkstoff Pi |
| Bearb. | Seefeldt | 12/08/2015 | Benennung |
| Gepr. | | | Sheet 3 (PV) |
| Norm. | | | |
| Freig. | | | |
| DLR | | | Zeichn.-Nr. A3 |
| | | | NN Nr. |
| | | | NN Bl. |
| Ursprung | Ersatz fuer: | Ersatz durch: | |

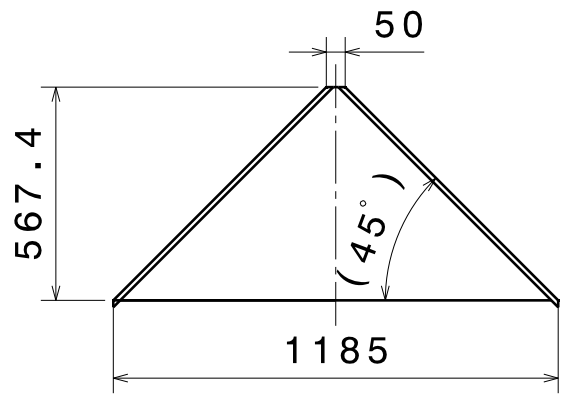


Front view with folded edges
Scale: 1:20

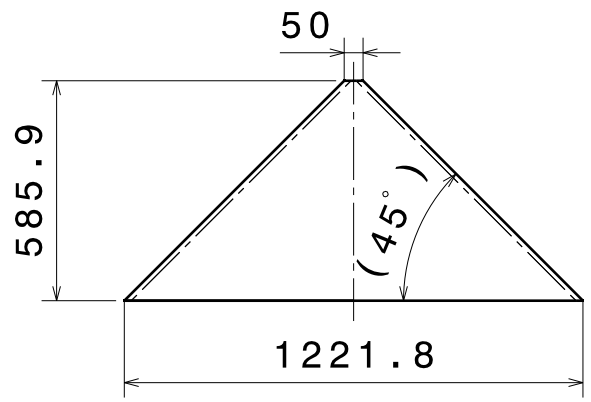


Developed view with unfolded edges
Scale: 1:20

| | | | |
|---|---|---|---|
| Verwendung | | | |
| Idx | Aenderung | Datum | Name |

| | | | |
|---|---|---|---|
| Projekt: Gossamer-1 | Auftrags-Nummer | Mass-Stab: 1:20 | Net. Gewicht |
| Baugrpuppe: Sail Quadrant | | | Material-Nummer: Upilex S 7.5 µm |
| | Datum | Name | Werkstoff: Pi |
| Bearb. | Seefeldt | 12/08/2015 | Benennung: Sheet 4 |
| Gepr. | | | |
| Norm. | | | |
| Freig. | | | |
| DLR | | | Zeichn.-Nr. |
| Ursprung | | | Ersatz fuer: / Ersatz durch: |

A3
NN Nr.
NN Bl.

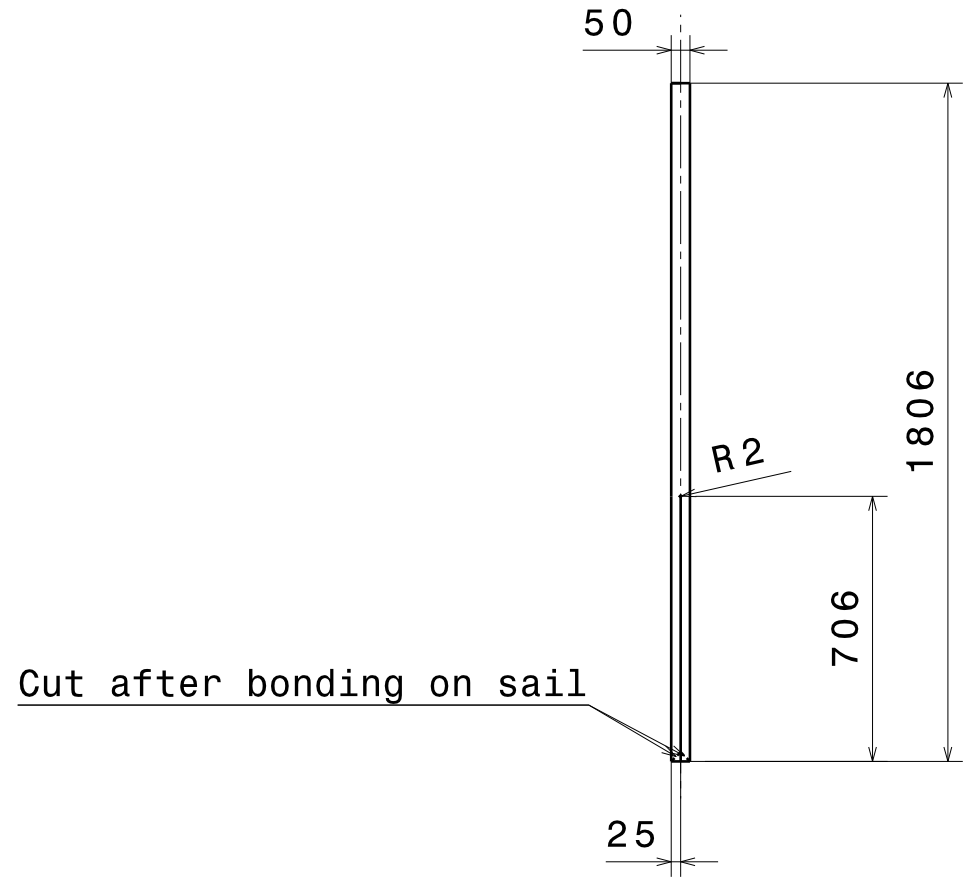


Developed View

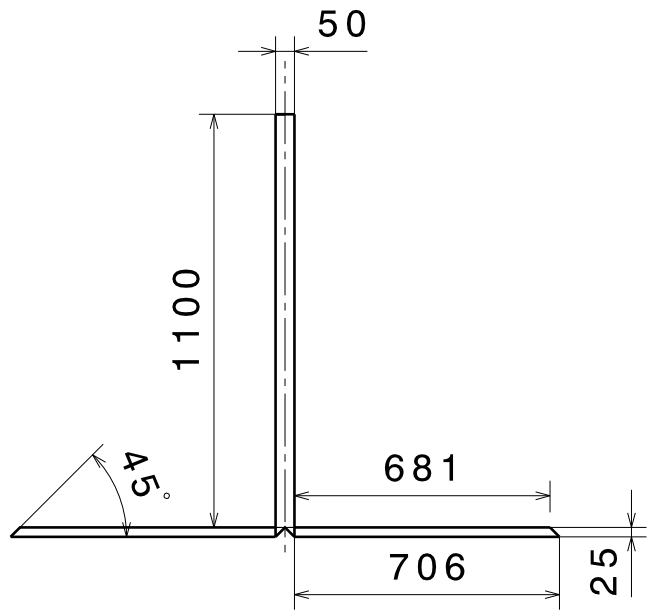


Front View

| | | | |
|---|---|---|---|
| Verwendung | | | |
| | | | |
| | | | |
| | | | |
| | | | |
| | | | |
| | | | |
| | | | |
| | | | |
| Idx | Aenderung | Datum | Name |

| | | | |
|---|---|---|---|
| Projekt: Gossamer-1 | Auftrags-Nummer | Mass-Stab: 1:20 | Net. Gewicht |
| Baugrpuppe: Sail Quadrant | | | Material-Nummer: FlexPCB |
| Werkstoff: Pi, Cu | | | |
| Benennung: Electrical Harness 1 | | | |
| DLR | Zeichn.-Nr. | | A3 |
| | | | NN Nr. |
| | | | NN Bl. |
| Ursprung | Ersatz fuer: | Ersatz durch: | |

| | | |
|---|---|---|
| | Datum | Name |
| Bearb. | Seefeldt | 12/08/2015 |
| Gepr. | | |
| Norm. | | |
| Freig. | | |

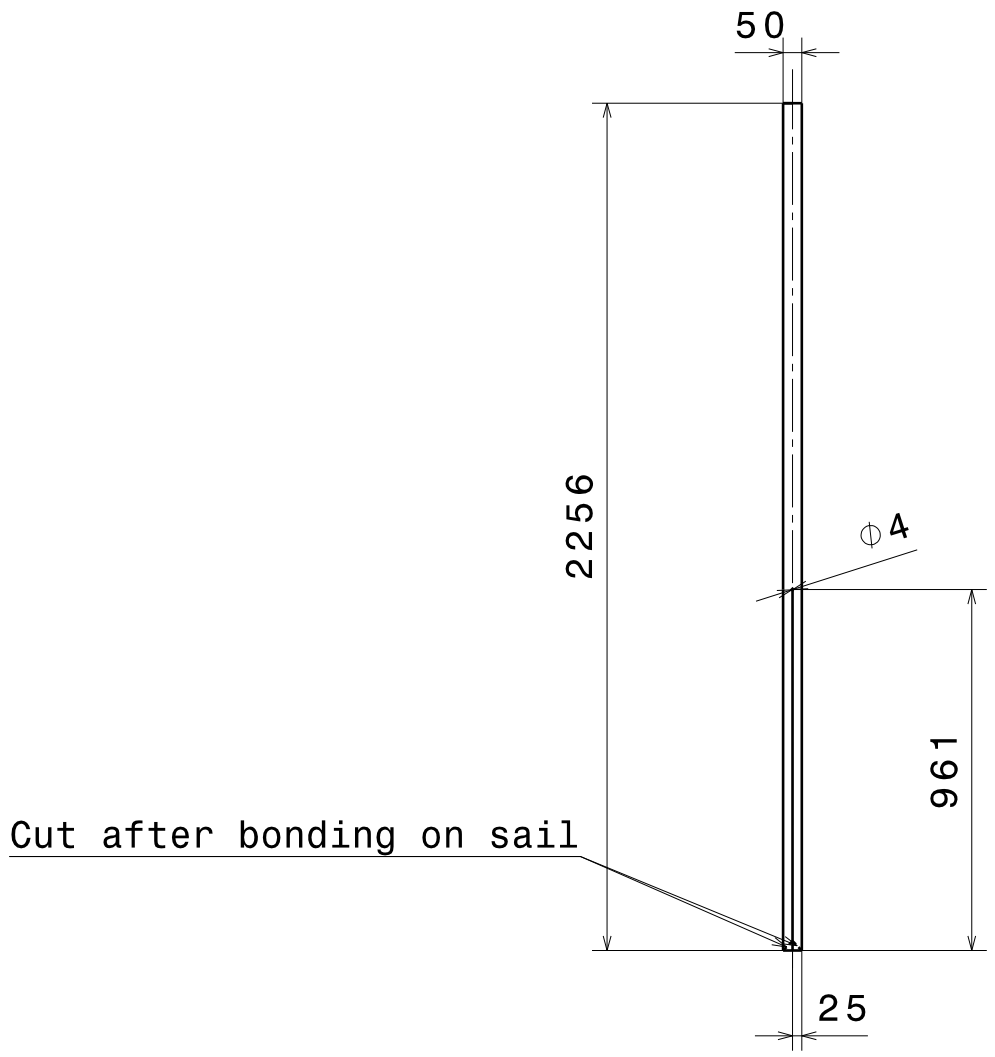


Developed View

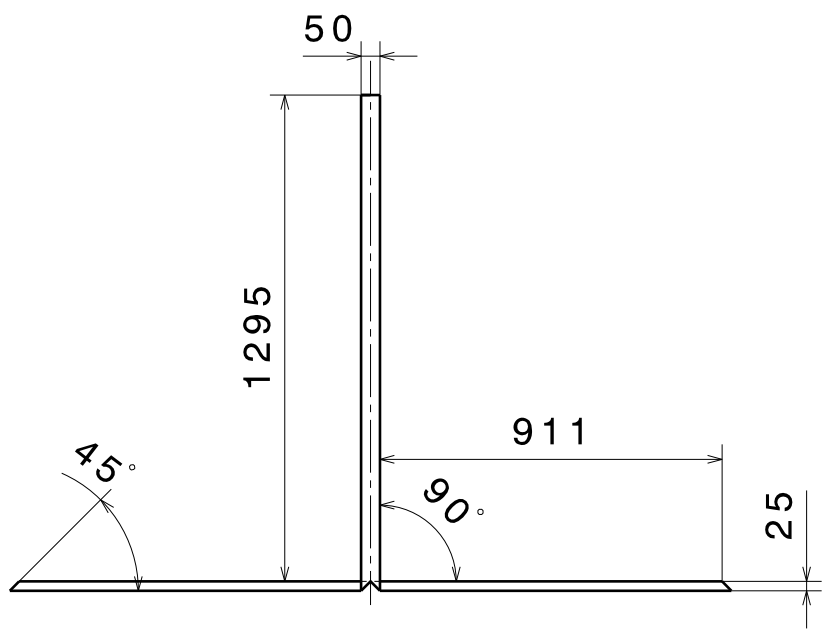


Front View

| Verwendung | | | |
|---|---|---|---|
| Idx | Aenderung | Datum | Name |

| | | | | |
|---|---|---|---|---|
| Projekt Gossamer-1 | | Auftrags-Nummer | Mass-Stab 1:20 | Net. Gewicht |
| Baugrpuppe Sail Quadrant | | | | Material-Nummer FlexPCB |
| | Datum | Name | Werkstoff Pi, Cu | |
| Bearb. | Seefeldt | 12/08/2015 | Benennung Electrical Harness 2 | |
| Gepr. | | | | |
| Norm. | | | | |
| Freig. | | | | |
| DLR | | | Zeichn.-Nr. | A3 |
| | | | | NN Nr. |
| | | | | NN Bl. |
| Ursprung | | | Ersatz fuer: | Ersatz durch: |

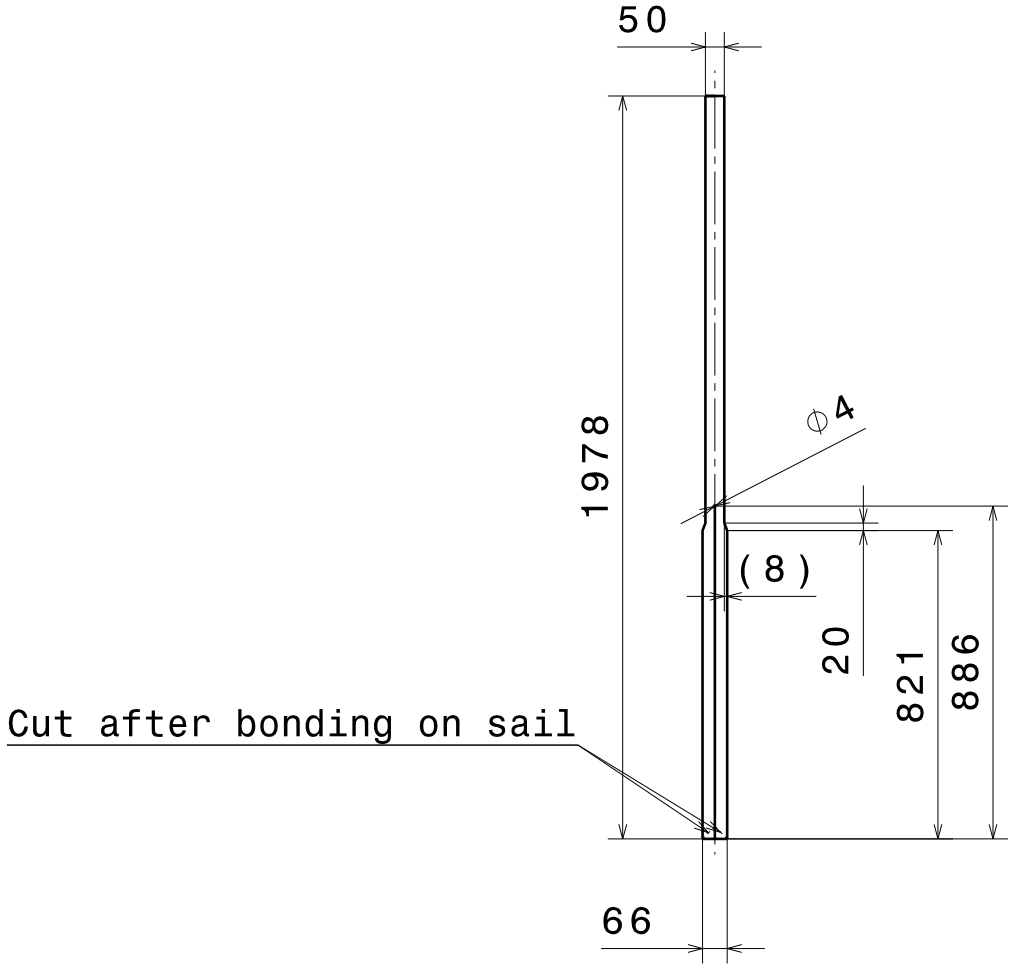


Developed View

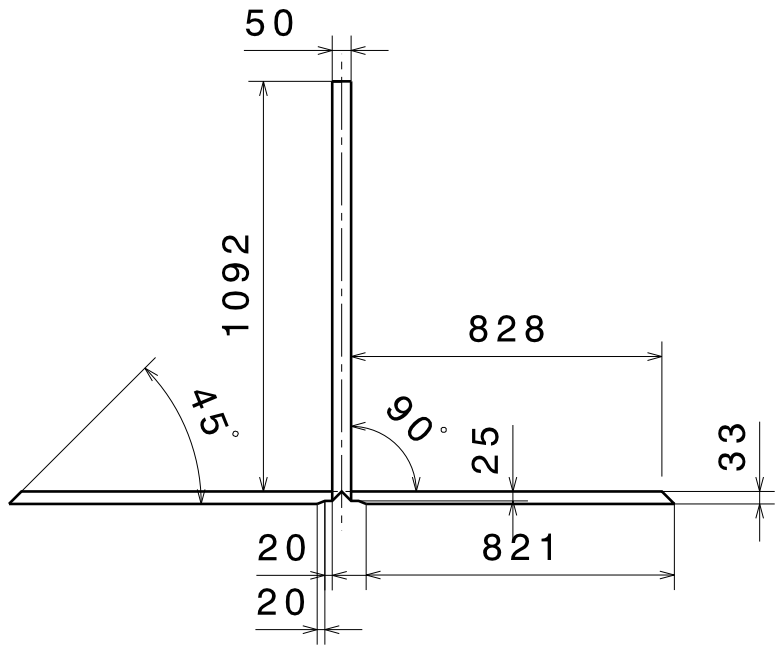


Front View

| | | | |
|---|---|---|---|
| Verwendung | | | |
| | | | |
| | | | |
| | | | |
| | | | |
| | | | |
| | | | |
| | | | |
| | | | |
| Idx | Aenderung | Datum | Name |

| | | | |
|---|---|---|---|
| Projekt: Gossamer-1 | Auftrags-Nummer | Mass-Stab: 1:20 | Net. Gewicht |
| Baugrpuppe: Sail Quadrant | | | Material-Nummer: FlexPCB |
| Bearb.: Seefeldt | Datum: 12/08/2015 | Name | Werkstoff: Pi, Cu |
| Gepr. | | | Benennung: Measure Harness 1 |
| Norm. | | | |
| Freig. | | | |
| DLR | | | Zeichn.-Nr. A3 |
| Ursprung | | | NN Nr. / NN Bl. |
| | | | Ersatz fuer: / Ersatz durch: |

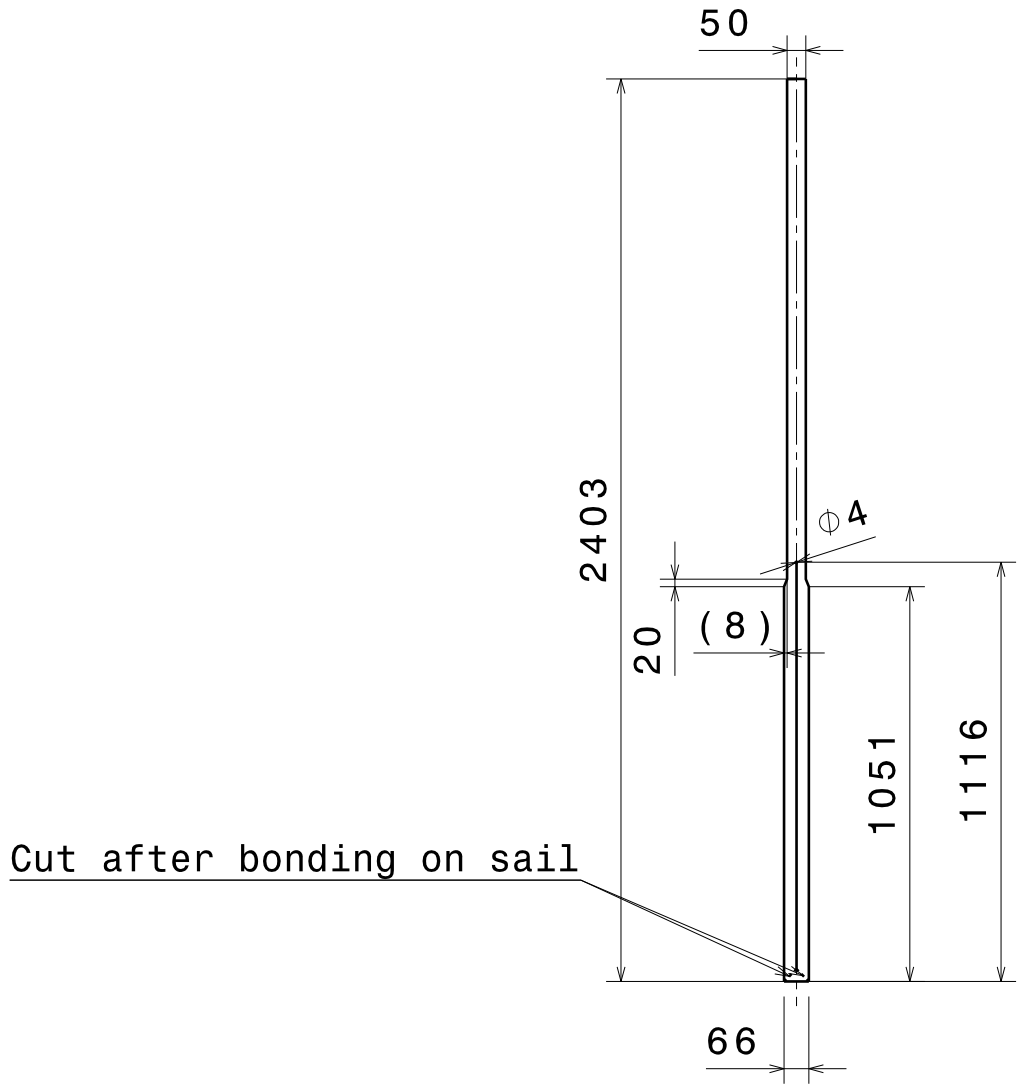


Developed View

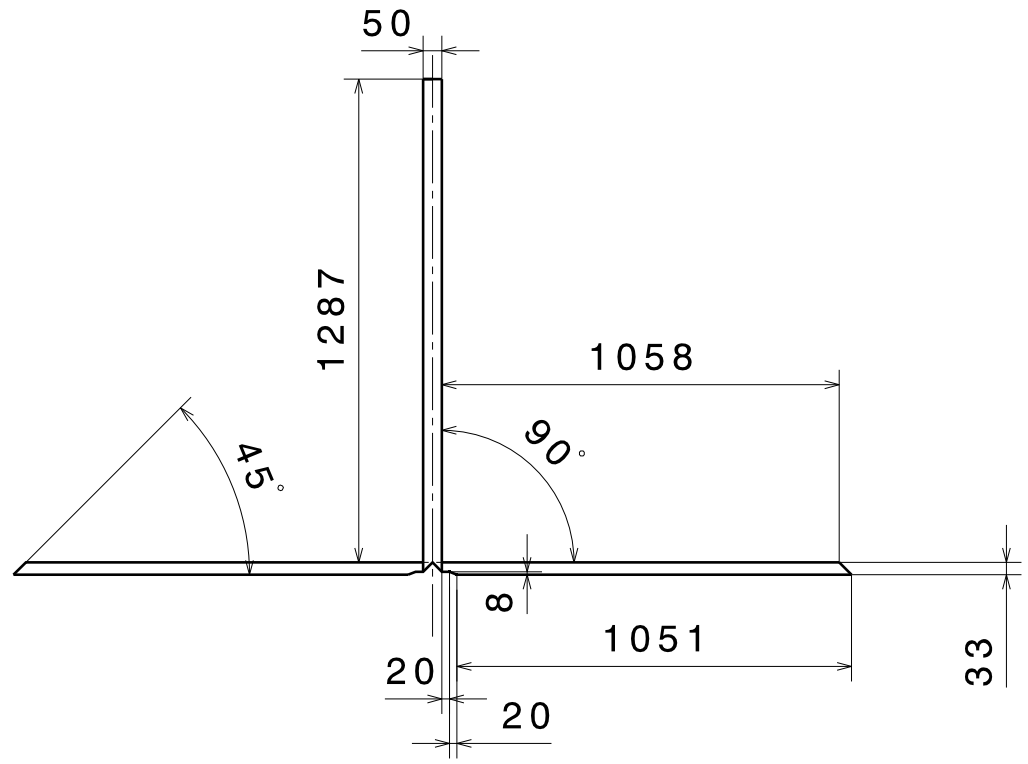


Front View

| | | | | | | | |
|---|---|---|---|---|---|---|---|
| Verwendung | | | | Projekt Gossamer-1 | Auftrags-Nummer | Mass-Stab 1:20 | Net. Gewicht |
| | | | | Baugrpuppe Sail Quadrant | | | Material-Nummer FlexPCB |
| | | | | | Datum | Name | Werkstoff Pi, Cu |
| | | | | Bearb. | Seefeldt | 12/08/2015 | Benennung |
| | | | | Gepr. | | | Measure Harness 2 |
| | | | | Norm. | | | |
| | | | | Freig. | | | |
| | | | | DLR | | | Zeichn.-Nr. A3 |
| | | | | | | | NN Nr. |
| | | | | | | | NN Bl. |
| Idx | Aenderung | Datum | Name | Ursprung | | | Ersatz fuer: Ersatz durch: |

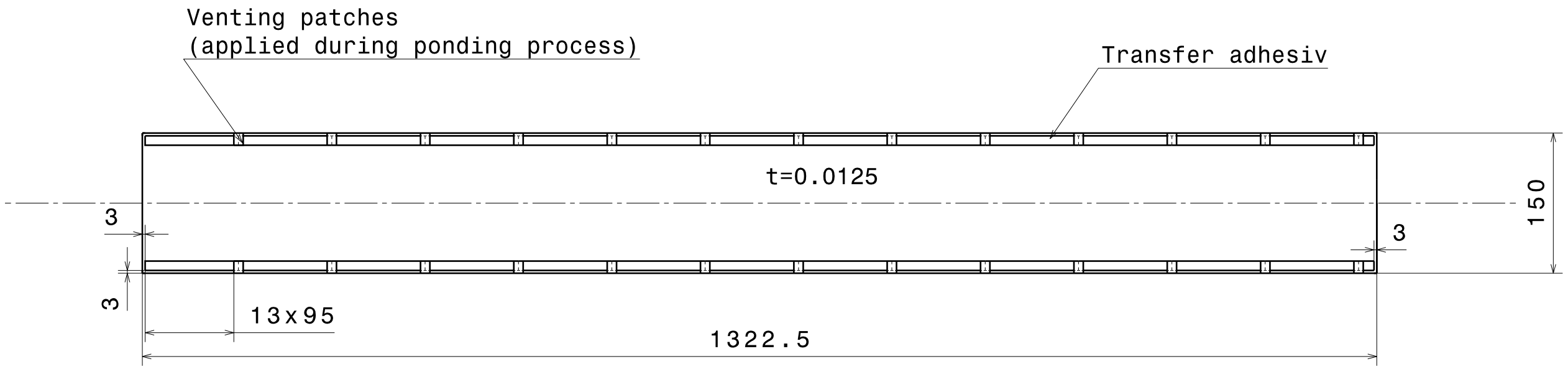


| Verwendung | | | |
|---|---|---|---|
| | | | |
| | | | |
| | | | |
| | | | |
| | | | |
| | | | |
| | | | |
| | | | |
| Idx | Aenderung | Datum | Name |

| | | | |
|---|---|---|---|
| Projekt Gossamer-1 | Auftrags-Nummer | Mass-Stab 1:5 | Net. Gewicht |
| Baugrpuppe Sail Quadrant | | | Material-Nummer Upilex S 12.5um |
| Werkstoff Pi | | | |
| Benennung Harness Base Sheet | | | |
| DLR | Zeichn.-Nr. | | A3 |
| | | | NN Nr. |
| | | | NN Bl. |
| Ursprung | Ersatz fuer: | | Ersatz durch: |

| | Datum | Name |
|---|---|---|
| Bearb. | Seefeldt | 12/08/2015 |
| Gepr. | | |
| Norm. | | |
| Freig. | | |

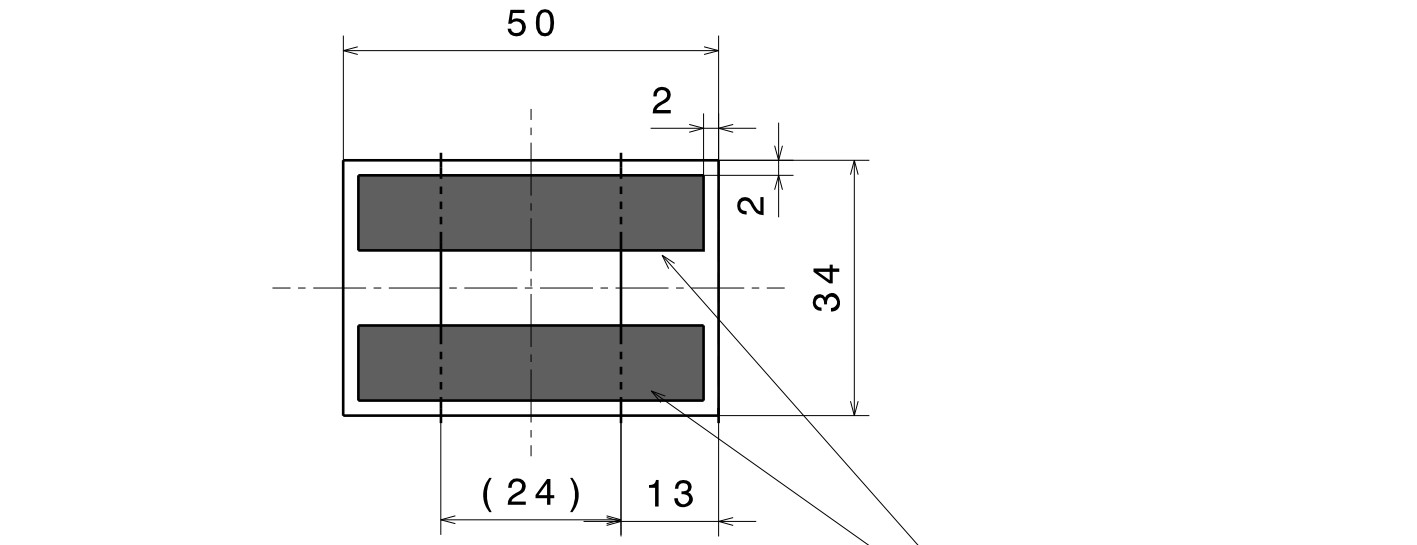


Front view
Scale: 1:1

Transfer adhesive

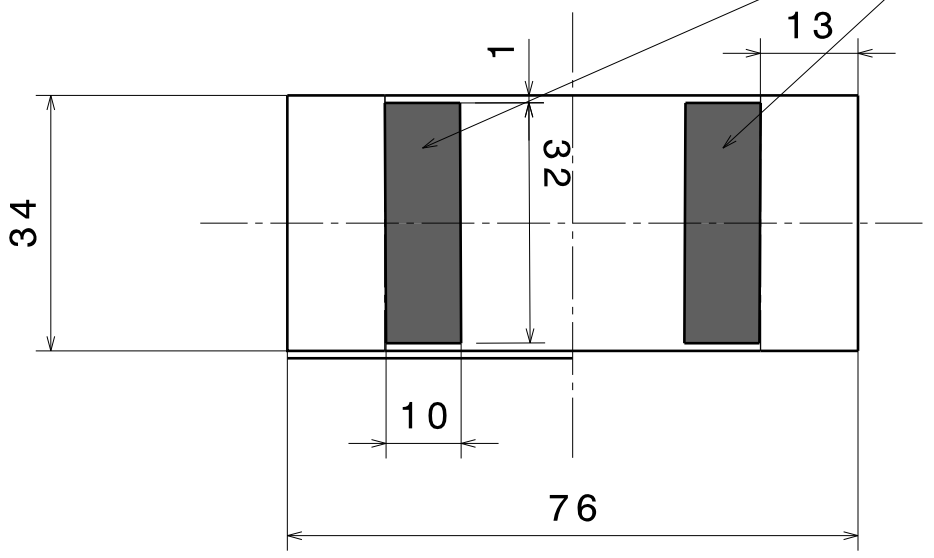


Developed view
Scale: 1:1

| Verwendung | | | |
|---|---|---|---|
| | | | |
| | | | |
| | | | |
| | | | |
| | | | |
| | | | |
| | | | |
| | | | |
| Idx | Aenderung | Datum | Name |

| | | | |
|---|---|---|---|
| Projekt: Gossamer-1 | Auftrags-Nummer | Mass-Stab: 1:20 | Net. Gewicht |
| Baugrpuppe: Sail Quadrant | | | Material-Nummer: Upilex S 7.5 µm |
| | Datum | Name | Werkstoff: Pi |
| Bearb. | Seefeldt | 12/08/2015 | Benennung: Harness Mounting |
| Gepr. | | | |
| Norm. | | | |
| Freig. | | | |
| DLR | | | Zeichn.-Nr. / A3 / NN Nr. / NN Bl. |
| Ursprung | | | Ersatz fuer: / Ersatz durch: |

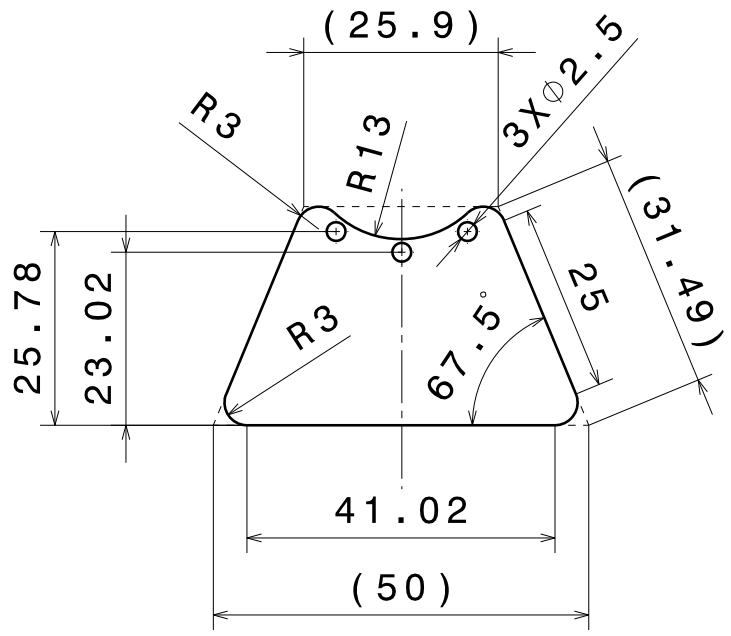


| Verwendung | | | |
|---|---|---|---|
| | | | |
| | | | |
| | | | |
| | | | |
| | | | |
| | | | |
| | | | |
| | | | |
| Idx | Aenderung | Datum | Name |

| Projekt | Auftrags-Nummer | Mass-Stab | Net. Gewicht |
|---|---|---|---|
| Gossamer-1 | | 1:1 | |

| Baugrpuppe Sail Quadrant | | | Material-Nummer |
|---|---|---|---|
| | Datum | Name | Werkstoff Pi, Cu |
| Bearb. | Seefeldt | 12/08/2015 | FLEX PCB |
| Gepr. | | | Benennung |
| Norm. | | | SSM Interface |
| Freig. | | | |

| DLR | Zeichn.-Nr. | A3 |
|---|---|---|
| | | NN Nr. |
| | | NN Bl. |
| Ursprung | Ersatz fuer: | Ersatz durch: |

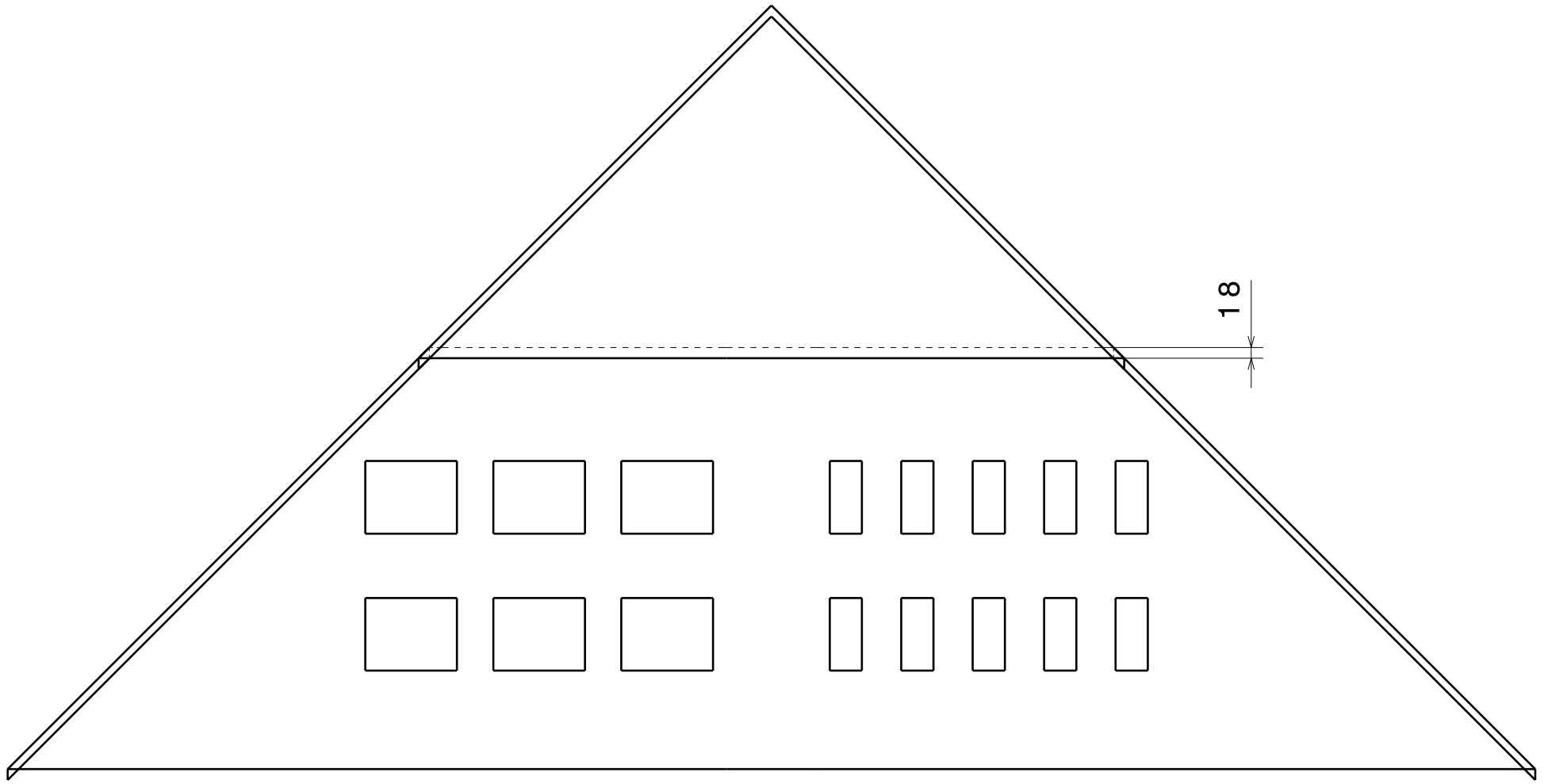


Front View

| | | | | | | | |
|---|---|---|---|---|---|---|---|
| Verwendung | | | | Projekt Gossamer-1 | Auftrags-Nummer | Mass-Stab 1:10 | Net. Gewicht |
| | | | | Baugrpuppe Sail Quadrant | | | Material-Nummer Upilex S 7.5 um |
| | | | | | Datum | Name | Werkstoff Pi |
| | | | | Bearb. | Seefeldt | 12/08/2015 | Benennung |
| | | | | Gepr. | | | Sail Assembly - Step 1 |
| | | | | Norm. | | | |
| | | | | Freig. | | | |
| Idx | Aenderung | Datum | Name | DLR | | | Zeichn.-Nr. A3 |
| | | | | | | | NN Nr. |
| | | | | | | | NN Bl. |
| | | | | Ursprung | | | Ersatz fuer: Ersatz durch: |

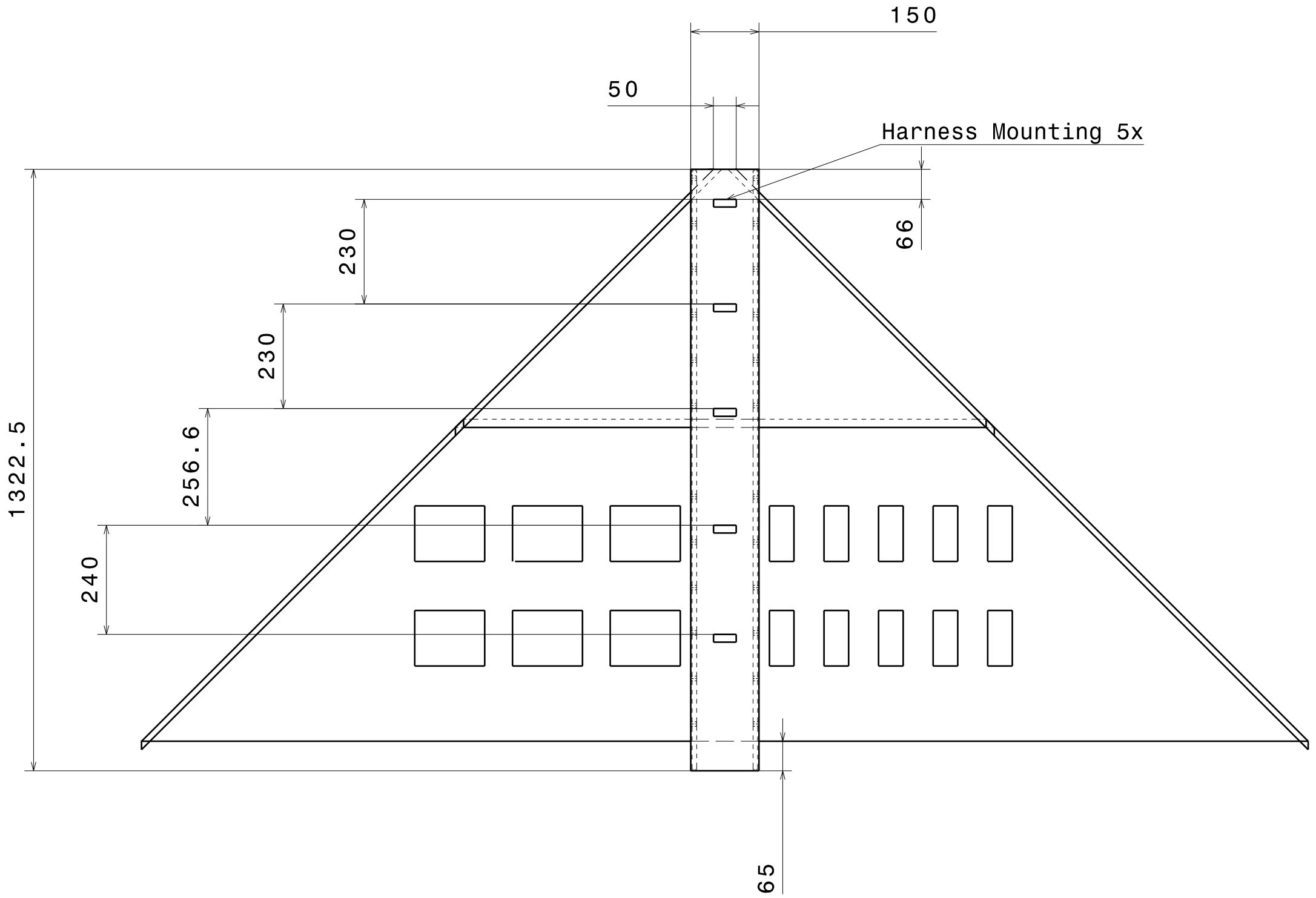


| Verwendung | | | | | | | |
|---|---|---|---|---|---|---|---|
| | | | | | | | |
| | | | | | | | |
| | | | | | | | |
| | | | | | | | |
| | | | | | | | |
| | | | | | | | |
| | | | | | | | |
| | | | | | | | |
| Idx | Aenderung | | Datum | Name | | | |

| Projekt | Auftrags-Nummer | Mass-Stab | Net. Gewicht |
|---|---|---|---|
| Gossamer-1 | | 1:20 | |

| Baugrpuppe Sail Quadrant | | | Material-Nummer |
|---|---|---|---|
| | Datum | Name | Werkstoff Pi |
| Bearb. | Seefeldt | 12/08/2015 | Upilex S |
| Gepr. | | | Benennung |
| Norm. | | | Sail Assembly - Step 2 |
| Freig. | | | |

| DLR | Zeichn.-Nr. | A3 |
|---|---|---|
| | | NN Nr. |
| | | NN Bl. |
| Ursprung | Ersatz fuer: | Ersatz durch: |

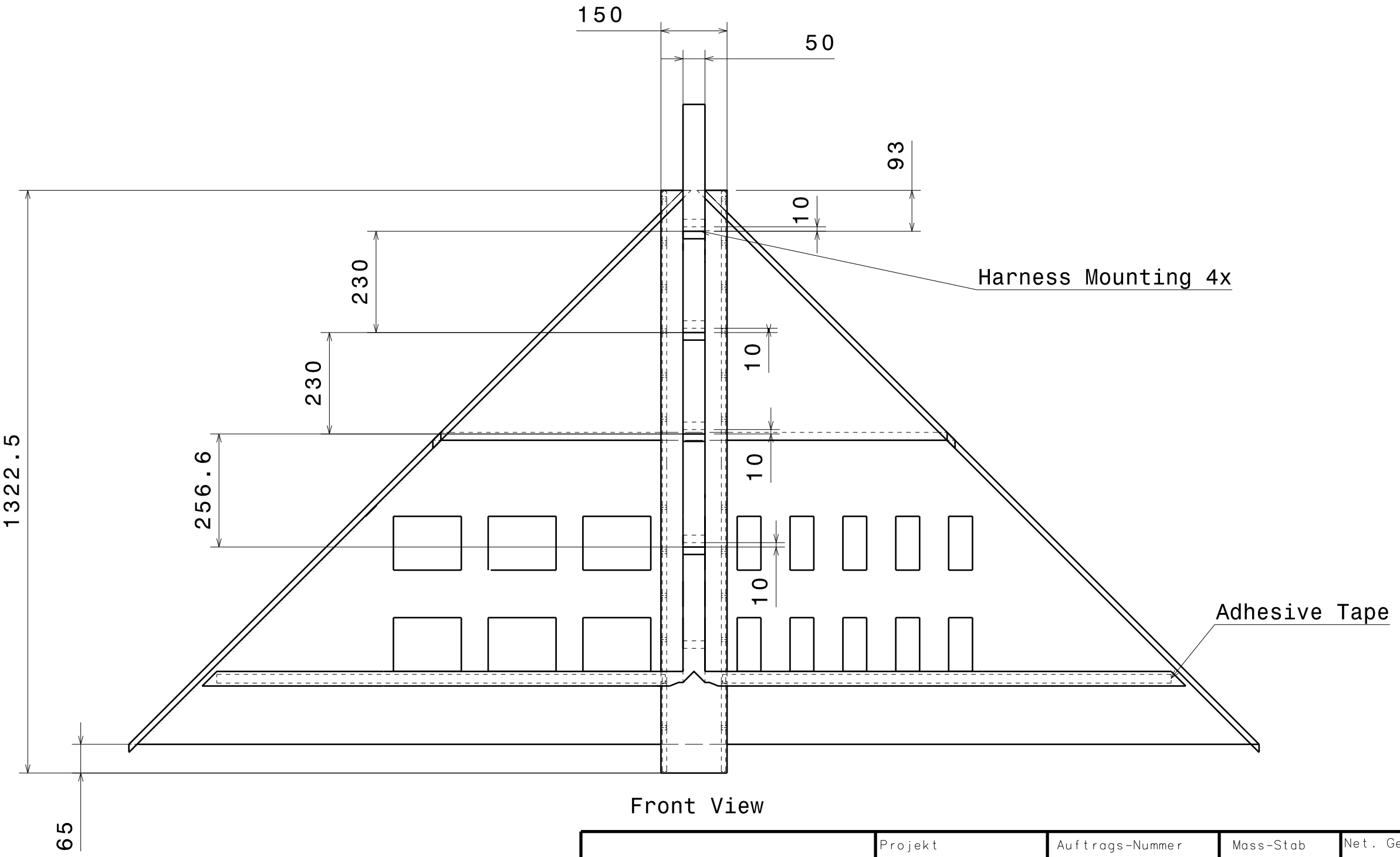


Front View

Verwendung

| Idx | Aenderung | Datum | Name |
|---|---|---|---|
| | | | |

| | | | |
|---|---|---|---|
| Projekt: Gossamer-1 | Auftrags-Nummer: | Mass-Stab: 1:10 | Net. Gewicht: |
| Baugrpuppe: Sail Quadrant | | | Material-Nummer: Upilex S, Flex PCB |
| | Datum | Name | Werkstoff: Pi, Cu |
| Bearb. | Seefeldt | 12/08/2015 | Benennung: Sail Assembly - Step 3 |
| Gepr. | | | |
| Norm. | | | |
| Freig. | | | |
| DLR | | | Zeichn.-Nr.: A3 |
| | | | NN Nr. |
| | | | NN Bl. |
| Ursprung | | | Ersatz fuer: Ersatz durch: |

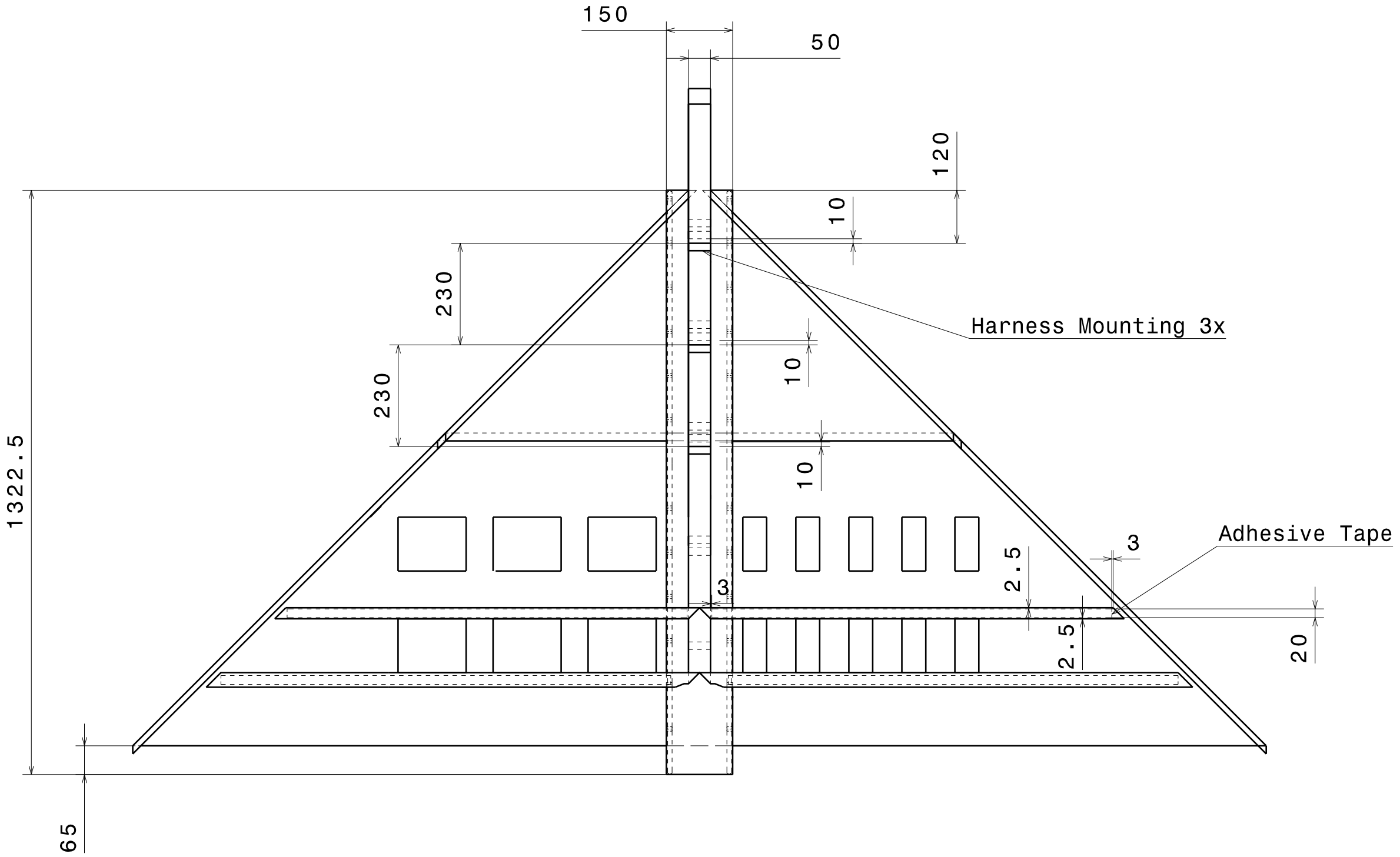


Front View

| | | | |
|---|---|---|---|
| Verwendung | Projekt: Gossamer-1 | Auftrags-Nummer | Mass-Stab: 1:10 |
| | Baugrpuppe: Sail Quadrant | | Net. Gewicht |
| | | Datum / Name | Werkstoff: Pi, Cu |
| | Bearb.: Seefeldt | 12/08/2015 | Material-Nummer: Upilex S, Flex PCB |
| | Gepr. | | Benennung: Sail Assembly - Step 4 |
| | Norm. | | |
| | Freig. | | |
| Idx / Aenderung / Datum / Name | DLR | Zeichn.-Nr. | A3 |
| | Ursprung | Ersatz fuer: | Ersatz durch: |
| | | | NN Nr. |
| | | | NN Bl. |

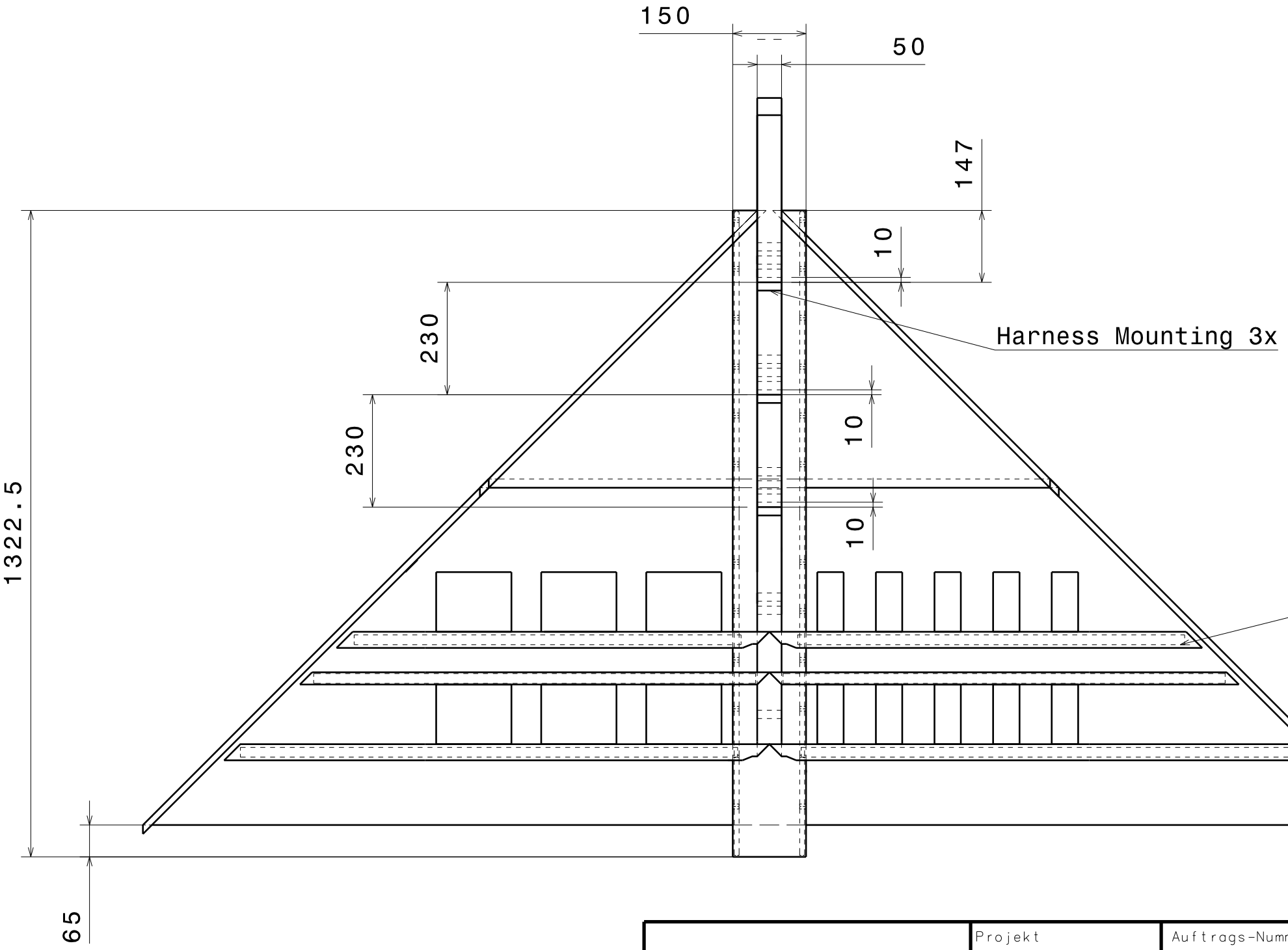


| | | | |
|---|---|---|---|
| Verwendung | | | |
| Idx | Aenderung | Datum | Name |

| | | | |
|---|---|---|---|
| Projekt: Gossamer-1 | Auftrags-Nummer | Mass-Stab: 1:10 | Net. Gewicht |
| Baugrpuppe: Sail Quadrant | | | Material-Nummer: Upilex S, Flex PCB |
| Werkstoff: Pi, Cu | | | |
| Benennung: Sail Assembly - Step 5 | | | |
| Zeichn.-Nr. | | | A3 |
| | | | NN Nr. |
| | | | NN Bl. |
| Ursprung | Ersatz fuer: | Ersatz durch: | |

| | Datum | Name |
|---|---|---|
| Bearb. | Seefeldt | 12/08/2015 |
| Gepr. | | |
| Norm. | | |
| Freig. | | |

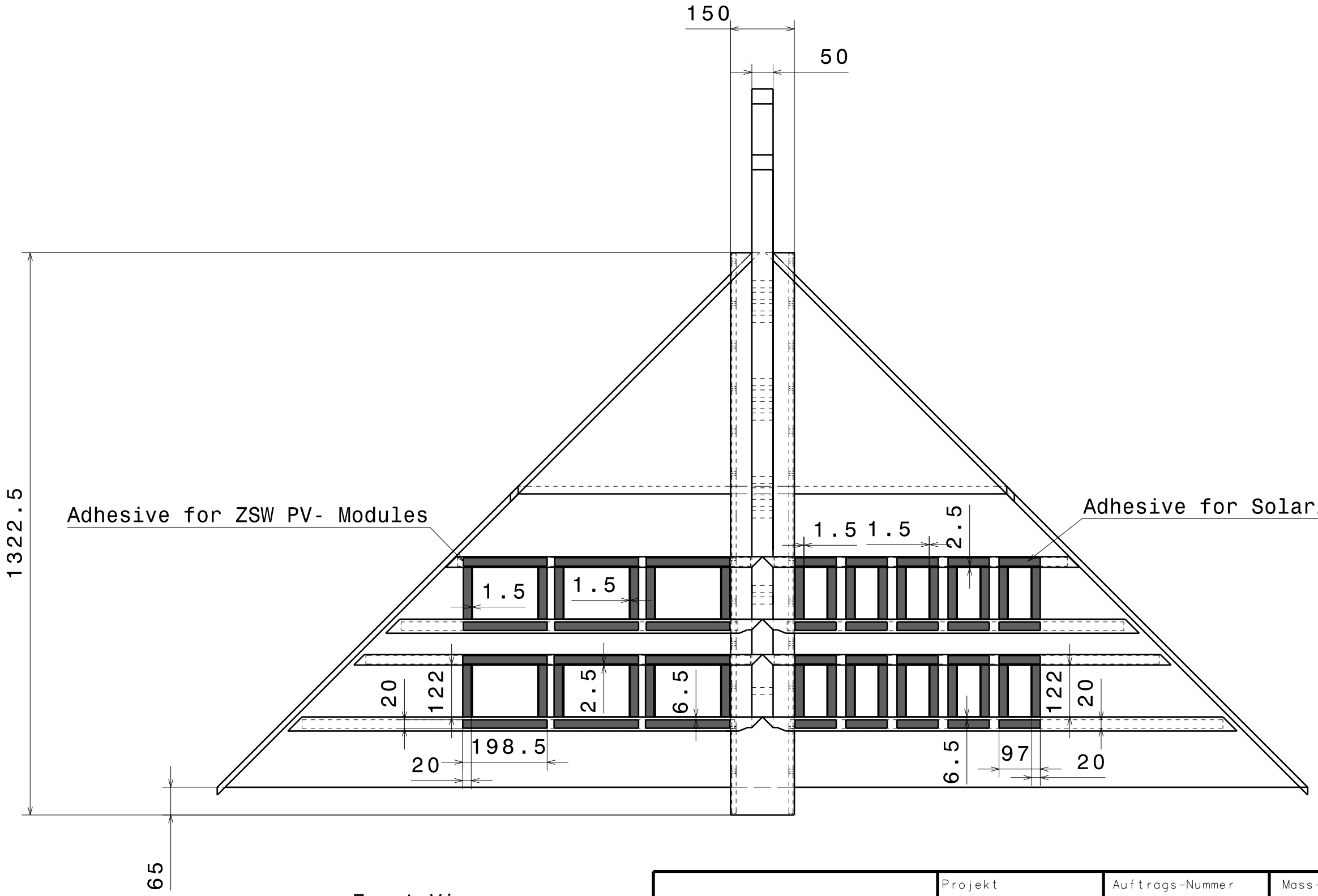


Front View

| Verwendung | | | |
|---|---|---|---|
| | | | |
| | | | |
| | | | |
| | | | |
| | | | |
| | | | |
| | | | |
| | | | |
| Idx | Aenderung | Datum | Name |

| | | | |
|---|---|---|---|
| Projekt: Gossamer-1 | Auftrags-Nummer | Mass-Stab: 1:10 | Net. Gewicht |
| Baugrpuppe: Sail Quadrant | | | Material-Nummer: Upilex S, Flex PCB |
| Werkstoff: Pi, Cu | | | |

| | Datum | Name |
|---|---|---|
| Bearb. | Seefeldt | 12/08/2015 |
| Gepr. | | |
| Norm. | | |
| Freig. | | |

Benennung: Sail Assembly - Step 6

DLR

Zeichn.-Nr.

A3

NN Nr.

NN Bl.

Ursprung

Ersatz fuer:

Ersatz durch:

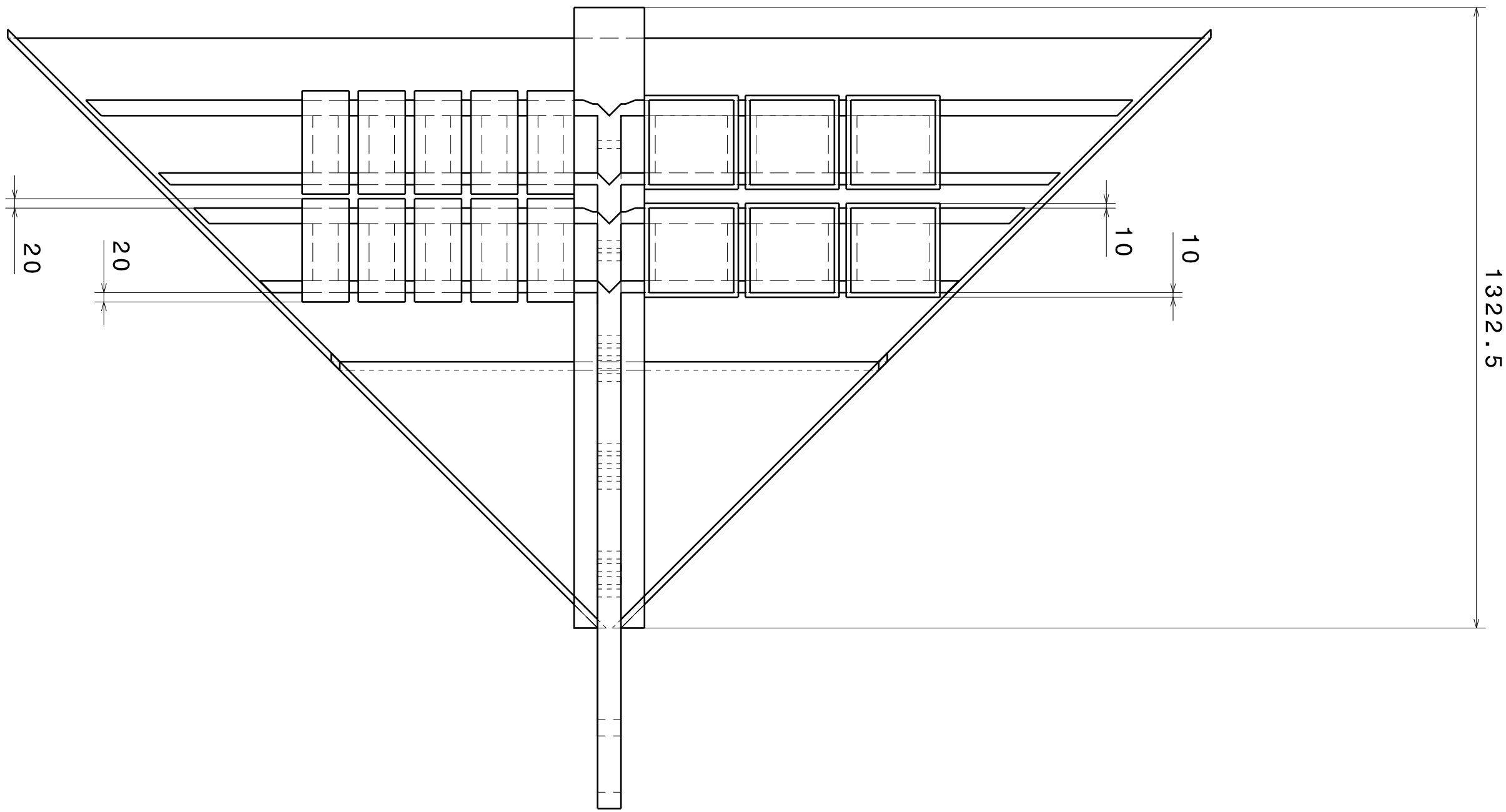


| Idx | Aenderung | Datum | Name |
|---|---|---|---|
| | | | |

Verwendung

| | | | |
|---|---|---|---|
| Projekt | Auftrags-Nummer | Mass-Stab | Net. Gewicht |
| Gossamer-1 | | 1:10 | |

| | | | |
|---|---|---|---|
| Baugruppe Sail Quadrant | | | Material-Nummer |
| | Datum | Name | Werkstoff Fi, Cu, CIGS |
| Bearb. Seefeldt | 12/08/2015 | | Benennung |
| Gepr. | | | Sail Assembly - Step 7 |
| Norm. | | | |
| Freig. | | | |

| | |
|---|---|
| Ursprung | Zeichn.-Nr. |
| DLR | A3 |
| Ersatz fuer: | NN Nr. |
| Ersatz durch: | NN Bl. |

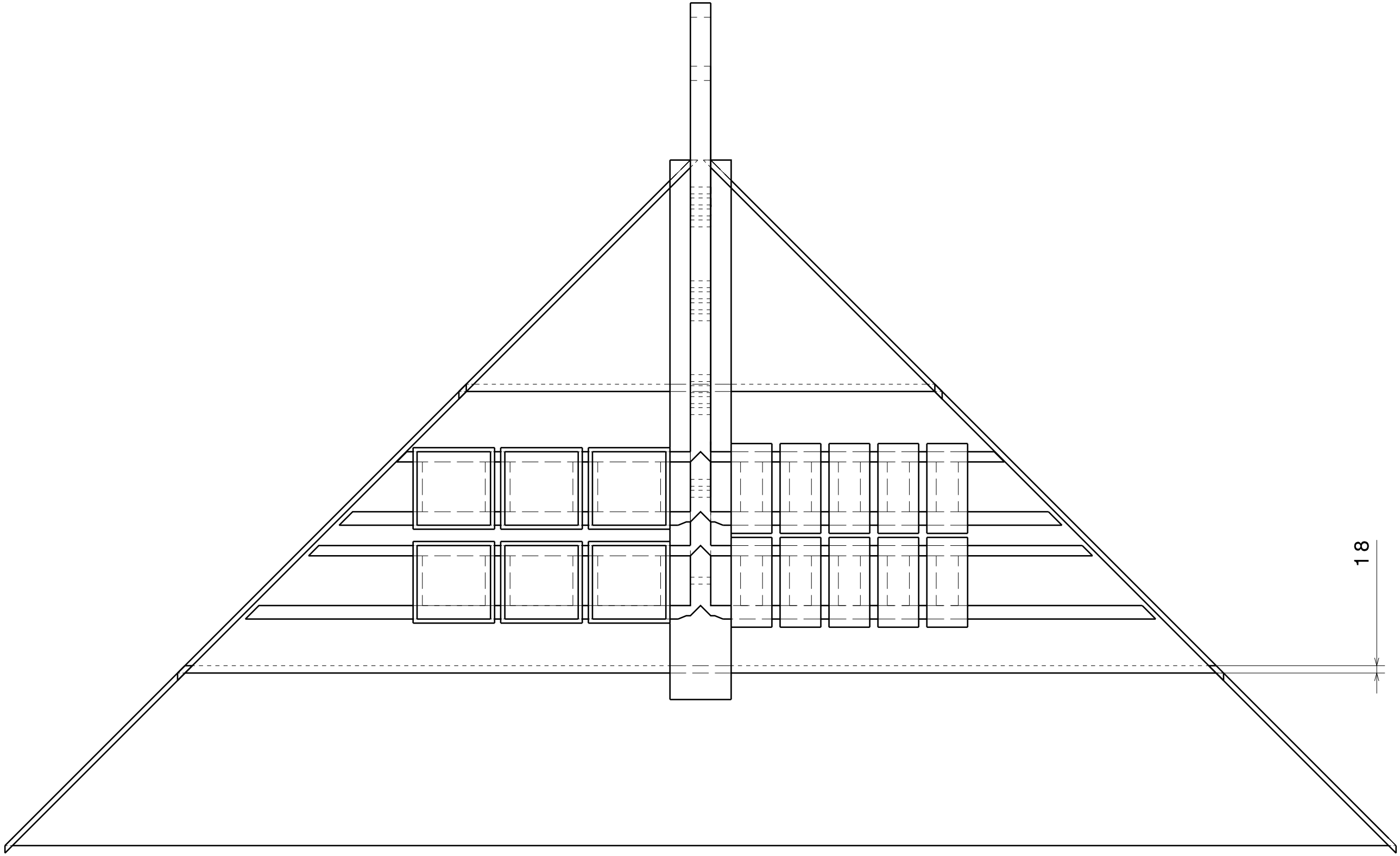


Front View

| | | | |
|---|---|---|---|
| Verwendung | | | |
| Idx | Aenderung | Datum | Name |

| | | | | |
|---|---|---|---|---|
| Projekt Gossamer-1 | | Auftrags-Nummer | Mass-Stab 1:10 | Net. Gewicht |
| Baugrpuppe Sail Quadrant | | | | Material-Nummer Upilex S, FlexPCB, CIGS |
| | Datum | Name | Werkstoff Pi | |
| Bearb. | Seefeldt | 12/08/2015 | Benennung Sail Assembly - Step 8 | |
| Gepr. | | | | |
| Norm. | | | | |
| Freig. | | | | |
| DLR | | | Zeichn.-Nr. | A3 |
| | | | | NN Nr. |
| | | | | NN Bl. |
| Ursprung | | | Ersatz fuer: | Ersatz durch: |

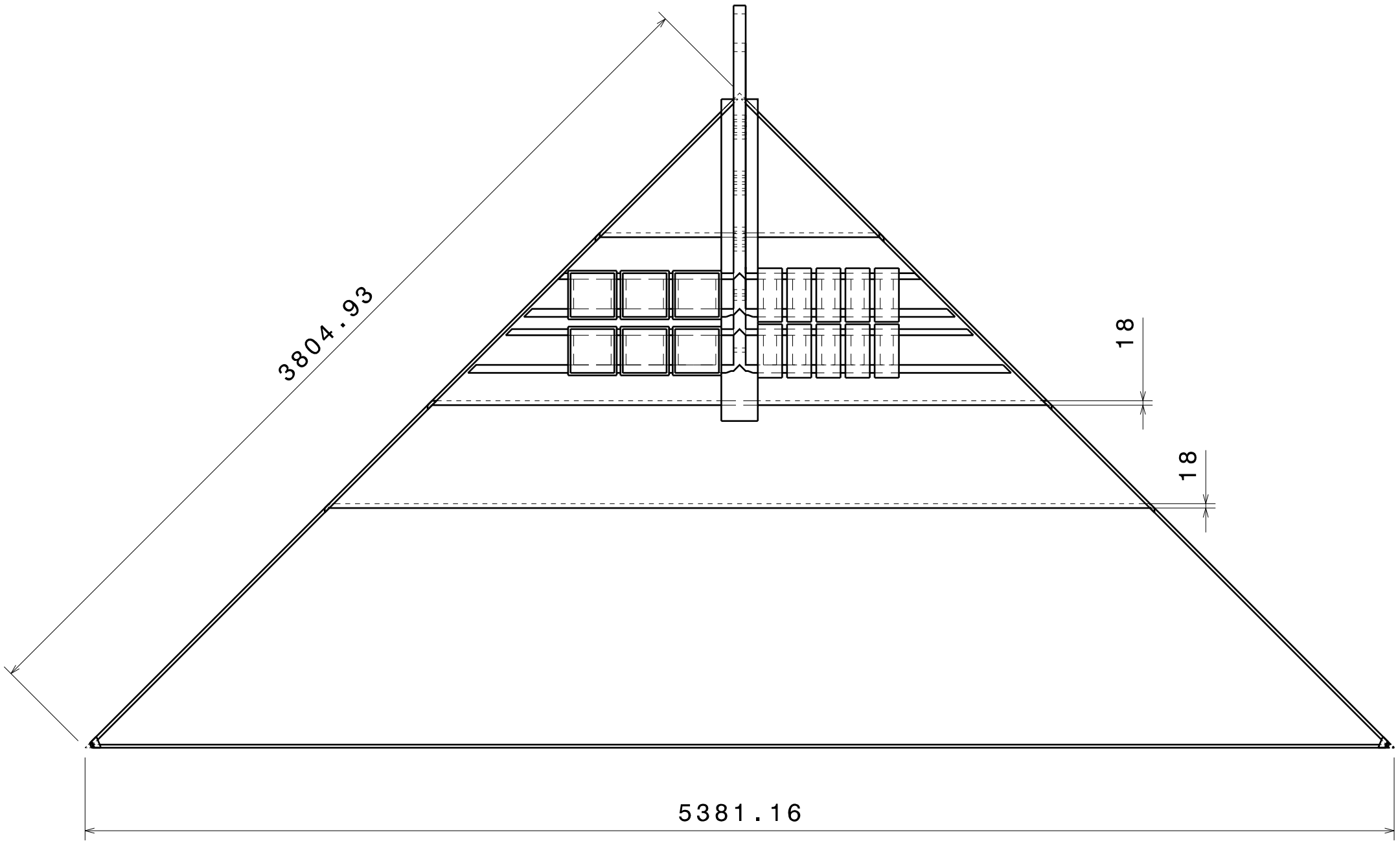


Front View

| Verwendung | | | |
|---|---|---|---|
| | | | |
| | | | |
| | | | |
| | | | |
| | | | |
| | | | |
| | | | |
| | | | |
| Idx | Aenderung | Datum | Name |

| | | | |
|---|---|---|---|
| Projekt<br>Gossamer-1 | Auftrags-Nummer | Mass-Stab<br>1:20 | Net. Gewicht |
| Baugruppe Sail Quadrant | | | Material-Nummer<br>Upilex S, FlexPCB, CIGS |
| | Datum | Name | Werkstoff Pi |
| Bearb. | Seefeldt | 12/08/2015 | Benennung |
| Gepr. | | | Sail Assembly - Step 9 |
| Norm. | | | |
| Freig. | | | |
| DLR | | | Zeichn.-Nr. A3 |
| | | | NN Nr. |
| | | | NN Bl. |
| Ursprung | | | Ersatz fuer: Ersatz durch: |

# Acknowledgments

Six years ago I prepared a diploma thesis for Professor Dr. Dachwald in cooperation with the Institute of Lightweight Design at RWTH Aachen University. He proposed pursuing the design of a small drag sail for the CubeSat Compass-2 of the University for Applied Sciences in Aachen. A few months later I was totally fascinated by the engineering challenge of deploying a relatively large sail out of a CubeSat segment. Professor Dr. Dachwald's field of research is, besides others, solar sailing and it was thanks to him that I came in contact with several DLR researchers that are working in this field and soon I was eager to pursue this research myself. Ever since, Professor Dr. Dachwald has inspired and motivated me to find my own way in the research and development of deployable gossamer space systems.

It was thanks to Dr. Biring, the former head of DLR's Institute of Space Systems, that I was able to carry out my research within the Gossamer-1 project. Dr. Spietz, head of the project, gave me great support in my everyday work, reviewed my findings and thereby enabled me to prepare my first publication. With Professor Dr. Braxmaier, I finally found my Ph.D. supervisor for whom I am very grateful. After a change of the institute's head, I was very pleased to find that the new head Professor Dr. Rittweger was also interested in the research and development of deployment systems. He allowed me to carry on with my research and now, after my Ph.D. thesis is finished, it has found its application in large deployable gossamer solar arrays. The extensive testing required for the verification of the deployment was carried out and supervised by Mr. Spröwitz, head of the Department of Mechanics and Thermal Systems.

Without the support, supervision, and reviews provided by all of the above-mentioned persons, it would not have been possible to carry out the work presented here. I am thanking every single one for giving me the chance to carry out my research, improve my professional skills and prepare my Ph.D. thesis.

I would also like to thank the Gossamer-1 team and my colleagues for the good cooperation and fruitful discussions. Special thanks go to my colleague Dr. Maciej Sznajder, who supported me with his expertise in material degradation and my colleague Norbert Tóth who developed the required electronics.

After I prepared my diploma thesis I had the privilege of being a part of the Space Sailors student group who carried out the development of a CubeSat drag sail and finally tested it on a REXUS sounding rocket in 2013. The commitment of that group to this project, despite many political problems, inspired and motivated me to carry on in this field of research, and I am proud that I had a part in this. For this, I thank the team, namely Christopher Fiebig, Wolfgang Bauer, Patrick Gerding, Kai Parow-Souchon, Anna Pongs and Matti Reiffenrath.

I would also like to thank the students who prepared their bachelor's and master's theses under my supervision and thereby also supported my own work. Specifically, these include Matthias Baader for his support in the mechanical analysis of the deployment mechanism, Lukas Steindorf for his support in the preparation of finite element models, and Christoph Auenmüller and Chris Nordmann for their support in thermal analysis. In the dissertation, the results from the supervision of the following students' works are included

- Matthias Baader, Detailed design and prototype construction of the Gossamer-1 Sail Spool Mechanism (2013)

- Lukas Maximilian Steindorf, Design and Parameter Evaluation of the Gossamer Solar Sail (2014)
- Chistoph Auenüller, Thermal analysis of wrinkled solar sail membranes (2014)

Finally, I would like to thank my family for their understanding while I dedicated such a tremendous amount of time to this work. Their constant encouragement to carry on and never give up were no less important for the success of this work than the professional support of my supervisors. For this, I especially thank my beloved wife who always takes care of me and I thank my father and stepmother, who made it possible for me to receive such a good education. For this, I feel privileged and I am most grateful.

# Nomenclature

| | |
|---|---|
| $A$ | Area (subscripts: $s$-sail, $e$-earth) |
| $A_F$ | Amplification factor |
| $C$ | Cathetus of sail segment |
| $CTE$ | Coefficient of thermal expansion |
| $C_d$ | Drag coefficient |
| $C_l$ | Lift coefficient |
| $C_p$ | Pressure coefficient |
| $E$ | Young's modulus |
| $EY$ | Erosion Yield |
| $E_p$ | Photon energy |
| $E_{AO}$ | Energy of atomic oxygen |
| $E_\lambda$ | Black body spectrum |
| $F_B$ | Brake force (subscripts: $min$-minimum, $max$-maximum) |
| $F_D$ | Deployment force (subscripts: $min$-minimum, $max$-maximum) |
| $F_{e,s}$ | View factor from earth to sail(subscripts: $c$-cold case, $h$-hot case) |
| $G_{rms}$ | Root mean square acceleration |
| $H$ | Hypotenuses of sail segment |
| $I$ | Geometrical moment of inertia |
| $I_A$ | Earth albedo |
| $I_\lambda$ | Intensity of an electromagnetic wave (subscript "0" indicates a point at the material's surface). |
| $I_{e,IR}$ | Infrared emission from the Earth |
| $I_{s,IR}$ | Infrared emission from the sail |
| $K$ | Constant |
| $L$ | Lever arm |

$M_D$ Deployment moment

$P_{\mathrm{S}}$ Total radiation power of the Sun

$R$ Electrical resistance or outer radius of the gear

$R_{\mathrm{S}}$ Average reflectance

$R_{\square}$ Surface resistance

$S$ Solar constant or solar spectrum, if described as a function of wavelength

$TML$ Total mass loss

$T_B$ Brake torque (subscripts: *min*-minimum, *max*-maximum)

$T_D$ Deployment torque (subscripts: *min*-minimum, *max*-maximum)

$T_c$ Cold case temperature

$T_g$ Glass transition temperature

$T_h$ Hot case temperature

$T_m$ Mission time

$T_{ip}$ Temperature in interplanetary space

$W$ Spring deflection (subscripts: *min* - minimum deflection, *max* - maximum deflection)

$\Delta\alpha$ Angle between uncoiling point of the cathetus and hypotenuses on the sail spool

$\Delta l_h$ Extra length of the deployed hypotenuses during deployment (slack)

$\Delta t_{AO}$ Change in material thickness due to atomic oxygen erosion

$\Delta z$ Engagement depth into the gear teeth (subscripts: *min*-minimum, *max*-maximum)

$\Phi_{AO}$ Atomic oxygen flux

$\Theta$ Opening angle between the cathetus of the deploying sail segment (subscripts 1 and 2 for the two possible coiling directions)

$\alpha$ Angle

$\alpha_{\mathrm{S}}$ Solar absorption

$\delta$ Angle between the angle of the cathetus of the sail segment (here 90°) and the opening angle during deployment

$\epsilon_{\mathrm{t}}$ Infrared emittance

$\gamma$ Tangent angle of logarithmic spiral

$\mu$ Friction coefficient

$\phi$ Angle between hypotenuses and cathetus of sail segment

$\rho$ Reflection coefficient

| | |
|---|---|
| $\rho_{CH}$ | Ratio between deployed cathetus and hypotenuses |
| $\sigma$ | Boltzmann constant |
| $\sigma_{uts}$ | Ultimate tensile strength |
| $\theta$ | Angle of incident |
| $\zeta$ | Angle between a force vector and its z-component |
| $a$ | Semi-major axis or acceleration |
| $c$ | Correction factor for the slope of the logarithmic spiral |
| $d$ | Depth |
| $d$ | Distance between boom tips, respectively the two sail spools of one sail segment |
| $i$ | Inclination |
| $l_b$ | Boom length |
| $l_c$ | Length of (deployed) cathetus |
| $l_h$ | Length of (deployed) hypotenuse |
| $l_s$ | Spring length |
| $m$ | Slope of the logarithmic spiral |
| $m_{AO}$ | Mass of atomic oxygen |
| $n_f$ | Number of folding lines |
| $n_z$ | Number of gear teeth |
| $p$ | Circular pitch of the gear |
| $p_d$ | Drag pressure |
| $p_{\mathrm{S}}$ | Solar radiation pressure |
| $q$ | Heat flux |
| $r_c$ | Cold case orbit radius |
| $r_e$ | Earth radius |
| $r_h$ | Hot case orbit radius |
| $r_i$ | Inner radius |
| $r_o$ | Outer radius |
| $t_l$ | Thickness of folded and coiled membrane layers |
| $t_s$ | Spring thickness |
| $u$ | Arc length of the spring deflection points (subscripts: $min$ - to point of minimum deflection, $max$ - to point of maximum deflection) |

$v_{AO}$ Velocity of atomic oxygen

$w$ Width of of folded sail

$x$ Cartesian coordinate (with applicable subscripts as defined in the text)

$y$ Cartesian coordinate (with applicable subscripts as defined in the text)

$z$ Cartesian coordinate (with applicable subscripts as defined in the text)

# List of abbreviations

**CAD** Computer-Aided Design

**BSDU** Boom and Sail Deployment Unit

**CSCU** Central Spacecraft Unit

**DLR** German Aerospace Center

**ESA** European Space Agency

**LEO** Low Earth Orbit

**MLI** Multi-Layer Insulation

**LEO** Low Earth Orbit

**BSDU** Boom and Sail Deployment Unit

**PCB** Printed Circuit Board

**PTFE** Polytetrafluorethylen

**BSI** Boom-Spacecraft Interface

**EQM** Engineering-Qualification Model

**CFRP** Carbon Fiber Reinforced Plastic

**BSFR** Boom Sail Fixation Ring

**EM** Engineering Model

**MLI** Multilayer Insulation

**CIGS** Copper Indium Gallium Selenide

**ISS** International Space Station

**SAR** Synthetic Aperture Radar

**VUV** Vacuum Ultra Violet

**UV** Ultra Violet

**AO** Atomic Oxygen

**ESD** Electrostatic Discharge

**EY** Erosion Yield

**GEO** Geostationary Orbit

**IR** Infrared

**NUV** Near Ultraviolet

**REXUS** Rocket Experiments for University Students

**TRL** Technology Readiness Level

**BWM** Belt Winding Mechanism

**ITO** Indium Tin Oxide

# List of Figures

# List of Tables

# Bibliography


[1] M. Leipold, C. Garner, R. Freeland, A. Hermann, M. Noca, G. Pagel, W. Seboldt, G. Sprague, and W. Unckenbold. Odissee, a proposal for demonstration of a solar sail in earth orbit. *Acta Astronautica*, 45(4-9):557–566, 1999.

[2] D. Agnolon. Study overview of a solar sail demonstrator: Geosail. An esa technology reference study, DLR/ESA, 2008.

[3] M. Leipold, M. Eiden, C. Garner, L. Herbeck, D. Kassing, T. Niederstadt, T. Krüger, G. Pagel, M. Rezazad, H. Rozemeijer, et al. Solar sail technology development and demonstration. *Acta Astronautica*, 52(2):317–326, 2003.

[4] M. Leipold, C. Widani, P. Groepper, C. Sickinger, and F. Lura. The european solar sail deployment demonstration mission. In *Proceedings of the International Astronautical Congress*, 2006.

[5] P. Seefeldt. Diploma Thesis, Development of a drag sail to avoid space debris in low earth orbits. *RWTH Aachen University, Institute of Lightweight Design*, 2010.

[6] P. Seefeldt, H.-G. Reimerdes, and B. Dachwald. Vorentwicklung eines Widerstandssegels zur Vermeidung von Weltraumrückständen in niedrigen Erdorbits. In *Proceedings of the Deutscher Luft- und Raumfahrtkongress*, 2011.

[7] N. Wolff, P. Seefeldt, W. Bauer, C. Fiebig, P. Gerding, K. Parow-Souchon, A. Pongs, M. Reiffenrath, and T. Ziemann. Alternative application of solar sail technology. In *Advances in Solar Sailing*, pages 351–365. Springer, 2014.

[8] J. Thoemel, F. Singarayar, T. Scholz, D. Masutti, P. Testani, C. Asma, R. Reinhard, and J. Muylaert. Status of the qb50 cubesat constellation mission. In *Proceedings of the 65th International Astronautical Congress, Toronto, Canada*, 2014.

[9] P. Seefeldt, P. Spietz, T. Spröwitz, J. T. Grundmann, M. Hillebrandt, C. Hobbie, M. Ruffer, M. Straubel, N. Tóth, and M. Zander. Gossamer-1: Mission concept and technology for a controlled deployment of gossamer spacecraft. *Advances in Space Research*, 2016.

[10] T. Sinn, P. Seefeldt, T. Riemer, S. Meyer, T. Spröwitz, H. R., S. Reershemius, M. Zander, T. L., K. D. Bunte, C. T., and T. D. Design, analysis and testing of the adeo passive de-orbit subsystem demonstrator. In *Proceedings of the 14th European Conference on Spacecraft Structure, Materials and Environmental Testing*, 2016.

[11] P. Seefeldt. A stowing and deployment strategy for large membrane space systems on the example of gossamer-1. *Advances in Space Research*, 2017.

[12] A. Peloni, M. Ceriotti, and B. Dachwald. Solar-sail trajectory design for a multiple near-earth-asteroid rendezvous mission. *Journal of Guidance, Control, and Dynamics*, pages 2712–2724, 2016.

[13] J. Bookless and C. McInnes. Control of lagrange point orbits using solar sail propulsion. *Acta Astronautica*, 62(2):159–176, 2008.

[14] M. Leipold, W. Seboldt, S. Lingner, E. Borg, A. Herrmann, A. Pabsch, O. Wagner, and J. Brückner. Mercury sun-synchronous polar orbiter with a solar sail. *Acta Astronautica*, 39 (1):143–151, 1996.

[15] C. R. McInnes. Solar sail mission applications for non-keplerian orbits. *Acta Astronautica*, 45(4):567–575, 1999.

[16] C. R. McInnes. Artificial lagrange points for a partially reflecting flat solar sail. *Journal of guidance, control, and dynamics*, 22(1):185–187, 1999.

[17] S. Carl G. Jr. Solar sail trajectories for solar polar and heliopause missions. *NASA Technical Reports Server*, 20000057299, 2000.

[18] J. D. Bernal. *The world, the flesh & the devil: an enquiry into the future of the three enemies of the rational soul*. Indiana University Press, 1969.

[19] R. M. Colon. *Solar Sailing, Technology, Dynamics and Mission Applications*. Springer-Praxis London, UK, 1999.

[20] M. Leipold, H. Fichtner, B. Heber, P. Groepper, S. Lascar, F. Burger, M. Eiden, T. Niederstadt, C. Sickinger, L. Herbeck, et al. Heliopause explorer, a sailcraft mission to the outer boundaries of the solar system. *Acta Astronautica*, 59(8):785–796, 2006.

[21] D. Lichodziejewski, J. Bladt, R. Pappa, B. Williams, and J. Rogan. Bringing an effective solar sail design to trl 6. In *39th AIAA/ASME/SAE/ASEE Joint Propulsion Conference and Exhibit*, page 4659, 2003.

[22] D. Lichodziejewski, J. West, R. Reinert, K. Slade, and K. Belvin. Development and ground testing of a compactly stowed inflatably deployed solar sail. In *45th AIAA/ASME/ASCE/AHS/ASC Structures, Structural Dynamics & Materials Conference*, page 1507, 2004.

[23] Space Service Holdings Inc. Sunjammer website. `http://www.sunjammermission.com`, 2014. Accessed: 11-11-2014.

[24] Y. Tsuda, O. Mori, R. Funase, H. Sawada, T. Yamamoto, T. Saiki, T. Endo, K. Yonekura, H. Hoshino, and J. Kawaguchi. Achievement of IKAROS, Japanese deep space solar sail demonstration mission. *Acta Astronautica*, 82(2):183–188, 2013.

[25] G. L. Matloff. The solar sail as planetary aerobrake. In *54th International Astronautical Congress of the International Astronautical Federation, the International Academy of Astronautics, and the International Institute of Space Law*, pages S–6, 2003.

[26] P. G. Harkness. *An aerostable drag-sail device for the deorbit and disposal of sub-tonne, low earth orbit spacecraft*. Phd thesis, Cranfield University, 2006.

[27] G. Bonin, J. Hiemstra, T. Sears, and R. Zee. The CanX-7 drag sail demonstration mission: enabling environmental stewardship for nano-and microsatellites. In *Proceedings of the Small Satellite Conference*, 2013.

[28] M. S. Murbach, K. M. Boronowsky, J. E. Benton, B. White, and E. Fritzler. The SPQR as an option for returning payloads from the ISS after the termination of STS flights. In *Proceedings of the 40th International Conference on Environmental System, AIAA-2010-6223*, 2010.

[29] ESA. About space debris. `http://www.esa.int/Our_Activities/Operations/Space_Debris/About_space_debris`, 2017. accessed: 07-04-2017.

[30] University of Surrey. Deploytech website. `https://www.surrey.ac.uk/ssc/research/space_vehicle_control/deploytech/science_and_tech`, 2014. Accessed: 05-07-2017.

[31] FH Aachen University of Applied Sciences. Compass CubeSat Project Website. `http://compass-project.de`, 2015. Accessed: 19-04-2016.

[32] M. Hillebrandt, S. Meyer, M. Zander, M. Straubel, and C. Hühne. The boom design of the de-orbit sail satellite. In *European Conference on Spacecraft Structures, Materials and Mechanical Testing*, 2014.

[33] L. Johnson, M. Whorton, A. Heaton, R. Pinson, G. Laue, and C. Adams. NanoSail-D: A solar sail demonstration mission. *Acta Astronautica*, 68(5):571–575, 2011.

[34] M. Pfisterer, K. Schillo, C. Valle, K.-C. Lin, and C. Ham. The development of a propellantless space debris mitigation drag sail for leo satellites. In *Proceedings of the 15th World Multi-Conference on Systemics, Cybernetics and Informatics, WMSCI*, pages 19–22, 2011.

[35] R. Freeland, G. Bilyeu, G. Veal, M. Steiner, and D. Carson. Large inflatable deployable antenna flight experiment results. *Acta Astronautica*, 41(4):267–277, 1997.

[36] R. Freeland, G. Bilyeu, G. Veal, and M. Mikulas. Inflatable deployable space structures technology summary. In *Proceedings of the IAF 49th Congress*, 1998.

[37] E. Im, M. Thomson, H. Fang, J. Pearson, J. Moore, and J. Lin. Prospects of large deployable reflector antennas for a new generation of geostationary doppler weather radar satellites. In *AIAA SPACE 2007 Conference & Exposition*, page 9917, 2007.

[38] J. Huang. The development of inflatable array antennas. *IEEE Antennas and Propagation Magazine*, 43(4):44–50, 2001.

[39] H. Fang, E. Im, U. Quijano, K. Wang, J. Hill, J. Moore, J. Pearson, C. Lui, and F. Djuth. High-precision adaptive control of large reflector surface. *Earth Science*, 2008, 2008.

[40] H. Fang, U. Quijano, V. Bach, J. Hill, and K.-W. Wang. Experimental study of a membrane antenna surface adaptive control system. In *52nd AIAA/ASME/ASCE/AHS/ASC Structures, Structural Dynamics and Materials Conference 19th AIAA/ASME/AHS Adaptive Structures Conference 13t*, page 1828, 2011.

[41] D. Gorinevsky and T. T. Hyde. Adaptive membrane for large lightweight space application. In *Proceedings of the SPIE Astronomical Telescopes and Instrumentation Conference and Exposition*, 2002.

[42] M. Straubel. Trade-off on large deployable membrane antennas. In *30th ESA Antenna Workshop on Antennas for Earth Observation, Science, Telecommunication and Navigation Space Missions*, pages 321–325, 2008.

[43] M. Straubel. *Design and Sizing Method for Deployable Space Antennas*. PhD thesis, University of Braunschweig, Deutsches Zentrum für Luft-und Raumfahrt eV, 2012.

[44] L. Datashvili, M. Lang, H. Baier, and T. Sixt. Membranes for large and precision deployable reflectors. In *Proceedings of European Conference on Spacecraft Structures, Materials & Mechanical Testing*, 2005.

[45] A. Luque and S. Hegedus. *Handbook of photovoltaic science and engineering*. John Wiley & Sons, 2011.

[46] P. A. Jones and B. R. Spence. Spacecraft solar array technology trends. *IEEE Aerospace and Electronic Systems Magazine*, 26(8):17–28, 2011.

[47] N. G. Dhere, S. R. Ghongadi, M. B. Pandit, A. H. Jahagirdar, and D. Scheiman. Cigs2 thin-film solar cells on flexible foils for space power. *Progress in Photovoltaics: Research and Applications*, 10(6):407–416, 2002.

[48] K. Otte, L. Makhova, A. Braun, and I. Konovalov. Flexible cu (in, ga) se 2 thin-film solar cells for space application. *Thin Solid Films*, 511:613–622, 2006.

[49] K. Shimazaki, M. Imaizumi, and K. Kibe. Sio2 and al2o3/sio2 coatings for increasing emissivity of cu(in, ga)se2 thin-film solar cells for space applications. *Thin Solid Films*, 516 (8):2218–2224, 2008.

[50] M. Günthner, M. Pscherer, C. Kaufmann, and G. Motz. High emissivity coatings based on polysilazanes for flexible cu (in, ga) se 2 thin-film solar cells. *Solar Energy Materials and Solar Cells*, 123:97–103, 2014.

[51] M. Pscherer, M. Günthner, C. A. Kaufmann, A. Rahm, and G. Motz. Thin-film silazane/alumina high emissivity double layer coatings for flexible cu (in, ga) se 2 solar cells. *Solar Energy Materials and Solar Cells*, 132:296–302, 2015.

[52] ESA. Hubble space telescope: Solar arrays delivered to nasa. *COSPAR Information Bulletin*, Volume 1986, Issues 106-107:91–92, 1986. doi: 10.1016/0045-8732(86)90113-0.

[53] D. J. Shayler and D. M. Harland. *The Hubble Space Telescope: From Concept to Success*. Springer, 2015.

[54] NASA. International space station - solar arrays. `https://www.nasa.gov/mission_pages/station/structure/elements/solar_arrays.html#.WEwmgH19G55`, 2013. Accessed: 10-12-2016.

[55] ESA. Hubble with its second set of ESA-designed solar blankets. `http://www.esa.int/spaceinimages/Images/2010/12/Hubble_with_its_second_set_of_ESA-designed_solar_blankets`, 2006. Accessed: 10-12-2016.

[56] NASA. STS-116 Shuttle Mission Imagery. `http://spaceflight.nasa.gov/gallery/images/shuttle/sts-116/html/iss014e10053.html`, 2006. Accessed: 10-12-2016.

[57] Alliant Techsystems Inc. (ATK). PHOTOS: ATK Validates New MegaFlex Solar Array Technology for NASA's Future Solar Electric Propulsion Missions. `http://www.americaspace.com/?p=59476`, 2014. Accessed: 10-12-2016.

[58] K. Seifart, W. Göhler, T. Schmidt, R. John, and S. Langlois. Deployable structure for flexible solar generators. In *Spacecraft Structures, Materials and Mechanical Testing 2005*, volume 581, 2005.

[59] S. Langendorf, S. Brunner, and K. Zajac. Design and testing of a flexible solar generator for on-orbit verification misison. In *13th European Conference on Spacecraft Structures, Materials & Environmental Testing*, volume 727, 2014.

[60] S. Multek Corporation. The red book. Data sheets, 2014.

[61] B. A. Banks, S. K. Miller, K. K. deGroh, and R. Demko. Atomic oxygen effects on spacecraft materials. *NASA Technical Report Server*, NASA/TM-2003-212484, 2003.

[62] P. Fortescue, G. Swinerd, and J. Stark. *Spacecraft systems engineering*. John Wiley & Sons, 2003.

[63] A. De Rooij. Exposure of silver to atomic oxygen. *ESA/ESTEC, EUROCORR (Moscow)*, 2010.

[64] A. Rooij. Corrosion in space–encyclopedia of aerospace engineering. *ESA-ESTEC, John Wiley & Sons., Ltd*, 2010.

[65] ECSS. ECSS-Q-ST-70-06C, particle and uv radiation testing for space materials. European Cooperation for Space Standardization, 2008.

[66] ASTM International. Astm e512-94, standard practice for combined, simulated space environment testing of thermal control materials with electromagnetic and particulate radiation. American Society for Testing and Materials, 2010.

[67] T. K. Minton, B. Wu, J. Zhang, N. F. Lindholm, A. I. Abdulagatov, J. O'Patchen, S. M. George, and M. D. Groner. Protecting polymers in space with atomic layer deposition coatings. *ACS applied materials & interfaces*, 2(9):2515–2520, 2010.

[68] E. Grossman and I. Gouzman. Space environment effects on polymers in low earth orbit. *Nuclear Instruments and Methods in Physics Research Section B: Beam Interactions with Materials and Atoms*, 208:48–57, 2003.

[69] P. A. Tipler and G. Mosca. *Physik: Für Wissenschaftler und Ingenieure*. Springer-Verlag, 2000.

[70] R. Y. Kezerashvili and G. L. Matloff. Microscopic approach to analyze solar-sail space-environment effects. *Advances in Space Research*, 44(7):859–869, 2009.

[71] M. Sznajder, U. Geppert, and M. Dudek. Degradation of metallic surfaces under space conditions, with particular emphasis on hydrogen recombination processes. *Advances in space research*, 56(1):71–84, 2015.

[72] M. Sznajder, T. Renger, A. Witzke, U. Geppert, and R. Thornagel. Design and performance of a vacuum-uv simulator for material testing under space conditions. *Advances in Space Research*, 52(11):1993–2005, 2013.

[73] B. Dachwald, V. Baturkin, V. Coverstone, B. Diedrich, G. Garbe, M. Görlich, M. Leipold, F. Lura, M. Macdonald, and C. McInnes. Potential effects of optical solar sail degradation on interplanetary trajectory design. In *Proceedings of the AAS/AIAA Astrodynamics Specialist Conference*, 2005.

[74] J. F. Ziegler. Srim software, 2013. www.srim.org.

[75] E. Verkhovtseva, V. Yaremenko, V. Telepnev, and F. Lura. Gas-jet simulator of solar vuv and soft x-ray radiation and irradiation effect on some material. In *International Symposium on Materials in Space Environment, 7 th, Toulouse, France*, pages 119–124, 1997.

[76] S. Heltzel, C. Semprimoschnig, and M. V. Eesbeek. Environmental testing of thermal control materials at elevated temperature and intense ultraviolet radiation. *Journal of Spacecraft and Rockets*, 46(2):248–254, 2009.

[77] A. Sharma and N. Sridhara. Degradation of thermal control materials under a simulated radiative space environment. *Advances in Space Research*, 50(10):1411–1424, 2012.

[78] ECSS. ECSS-Q-ST-70-09C, mesurements of thermo-optical properties of thermal control materials. European Cooperation for Space Standardization, 2008.

[79] M. Boyle. Department of defense world geodetic system 1984-it's definition and relationship with local geodetic systems. Technical report, DMA Technical Report 83502.2., Washington, DC, 1987.

[80] M. Donabedian and D. G. Gilmore. *Spacecraft thermal control handbook*. Aerospace Press, 2003.

[81] B. T. Chung and M. Naraghi. Some exact solutions for radiation view factors from spheres. *AIAA Journal*, 19(8):1077–1081, 1981.

[82] ECSS. ECSS-E-ST-20-06C, spacecraft charging. European Cooperation for Space Standardization, 2008.

[83] F. Smits. Measurement of sheet resistivities with the four-point probe. *Bell System Technical Journal*, 37(3):711–718, 1958.

[84] UBE Compant Ltd. Upilex-s. Data sheets Version: 031105, 2005.

[85] UBE Compant Ltd. Upilex films - data sheet, tcf-s-000, rev. a. Data sheets, 2002.

[86] O. Yano and H. Yamaoka. Cryogenic properties of polymers. *Progress in Polymer Science*, 20(4):585–613, 1995.

[87] Songhan Plastic Technology Co., Ltd. UBE Upilex 25S (25 micron) Polyimid Film. Material data list, 2016.

[88] M. Görlich and F. Lura. Patent de102007016368, sail foil for solar sailer., 2007.

[89] ECSS. ECSS-Q-70-71A-REV1, space product assurance. European Cooperation for Space Standardization, 2004.

[90] A. D. Rakić. Algorithm for the determination of intrinsic optical constants of metal films: application to aluminum. *Applied optics*, 34(22):4755–4767, 1995.

[91] H. Shimamura, E. Miyazaki, J. Ishizawa, R. Yamanaka, Y. Kimoto, S. Remaury, and P. NABARRA. Joint evaluation of space materials by CNES and JAXA. In *Proceedings of ISMSE-11*, pages 15–18, 2009.

[92] R. Kitamura, L. Pilon, and M. Jonasz. Optical constants of silica glass from extreme ultraviolet to far infrared at near room temperature. *Applied optics*, 46(33):8118–8133, 2007.

[93] E. M. Silverman. Space environmental effects on spacecraft: Leo materials selection guide. *NASA Contractor Report*, 4661, 1995.

[94] T. haltec GmbH. Tabel of emissivity of various surfaces for infrared thermometry, 2002.

[95] I. Gouzman, O. Girshevitz, E. Grossman, N. Eliaz, and C. N. Sukenik. Thin film oxide barrier layers: protection of kapton from space environment by liquid phase deposition of titanium oxide. *ACS Applied Materials & Interfaces*, 2(7):1835–1843, 2010.

[96] B. A. Banks, J. A. Backus, M. V. Manno, D. L. Waters, K. C. Cameron, and K. K. deGroh. Atomic oxygen erosion yield prediction for spacecraft polymers in low earth orbit. *NASA Technical Report Server*, NASA/TM-2009-215812, 2009.

[97] G. Jellison Jr., L. Boatner, J. Budai, B.-S. Jeong, and D. Norton. Spectroscopic ellipsometry of thin film and bulk anatase (tio2). *Journal of Applied Physics*, 93(12):9537–9541, 2003.

[98] A. A. Daniyan, L. E. Umoru, A. Y. Fasasi, J. O. Borode, K. M. Oluwasegun, and S. O. O. Olusunle. Electrical properties of nano-tio2 thin film using spin coating method. *Journal of Minerals and Materials Characterization and Engineering*, 2014, 2014.

[99] DLR. Solar sail deployment module; In-orbit demonstration; Sails development phase B. Technical report, German Aerospace Center (DLR), Institute für Strukturmechaik (Berlin), 2001.

[100] K. Miura. Method of packaging and deployment of large membranes in space. *JAXA Repository / AIREX*, 618:1, 1985.

[101] P. Seefeldt, L. Steindorf, and T. Spröwitz. Solar sail membrane testing and design considerations. In *European Conference on Spacecraft Structures, Materials and Mechanical Testing*, 2014.

[102] S. D. Guest and S. Pellegrino. Inextensional wrapping of flat membranes. In *Proceedings of the First International Seminar on Structural Morphology*, volume 25, 1992.

[103] D. De Focatiis and S. Guest. Deployable membranes designed from folding tree leaves. *Philosophical Transactions of the Royal Society of London A: Mathematical, Physical and Engineering Sciences*, 360(1791):227–238, 2002.

[104] O. R. Stohlman, J. M. Fernandez, V. Lappas, M. Hillebrandt, C. Hühne, and M. Straubel. Testing of the deorbitsail drag sail subsystem. In *54th AIAA/ASME/ASCE/AHS/ASC Structures, Structural Dynamics, and Materials Conference*, page 1807, 2013.

[105] H. Furuya, Y. Inoue, and T. Masuoka. Deployment characteristics of rotationally skew fold membrane for spinning solar sail. In *46th AIAA/ASME/ASCE/AHS/ASC Structures, Structural Dynamics and Materials Conference*, page 2045, 2005.

[106] M. Straubel, P. Seefeldt, P. Spietz, and C. Hühne. The design and test of the gossamer-1 boom deployment mechanisms engineering model. *AIAA2015-1837*, 2015.

[107] P. Seefeldt and P. Spietz. Patent 10 2016 101 430.3, raumfahrzeug-membranentfaltungssystem und verfahren zum betrieb desselben, 01 2016.

[108] J. M. Fernandez, V. J. Lappas, and A. J. Daton-Lovett. Completely stripped solar sail concept using bi-stable reeled composite booms. *Acta astronautica*, 69(1):78–85, 2011.

[109] H. Sakamoto, K. Park, and Y. Miyazaki. Evaluation of membrane structure designs using boundary web cables for uniform tensioning. *Acta Astronautica*, 60(10):846–857, 2007.

[110] F. Dalla Vedova, D. de Wilde, C. Semprimoschnig, G. Oger, H. Henrion, G. Janssen, M. Leipold, T. Girot, J.-B. Chemin, R. Vaudemont, et al. The solar sail materials project: Results of activities. In *Advances in Solar Sailing*, pages 509–524. Springer, 2014.

[111] F. Dalla Vedova, H. Henrion, M. Leipold, T. Girot, R. Vaudemont, T. Belmonte, K. Fleury, and O. Le Couls. The solar sail materials (SSM) project–status of activities. *Advances in Space Research*, 48(11):1922–1926, 2011.

[112] *Technocables datasheet*. Carl Stahl GmbH, 2016.

[113] J. T. Grundmann et al. Launch vehicle survey - gossamer-1 virtual launch vehicle user guide (gos-1-tn-024-rysk). Technical report, German Aerospace Center (DLR), 2013.

[114] M. Hillebrandt et al. Gossamer-1 design description (gos1-dd-001-rysek), 4.2 gos-1 structure. Technical report, German Aerospace Center (DLR), 2013.

[115] J. Anderson. *Hypersonic and High-temperature Gas Dynamics*. AIAA education series. American Institute of Aeronautics and Astronautics, 2006. ISBN 9781563477805.

[116] J. Wertz, D. Everett, and J. Puschell. *Space Mission Engineering: The New SMAD*. Space technology library. Microcosm Press, 2011. ISBN 9781881883166.

[117] M. Griffin and J. French. *Space Vehicle Design*. American Institute of Aeronautics & Astronautics, 2004. ISBN 9781600861123.

[118] ECSS. ECSS-E-ST-10-04C, space engineering, space environment. European Cooperation for Space Standardization, 2008.

[119] L. Pirovano, P. Seefeldt, B. Dachwald, and R. Noomen. Attitude and orbital dynamics modeling for an uncontrolled solar-sail experiment in low-earth orbit. In *ISSFD 2015: Proceedings of the 25th International Symposium on Space Flight Dynamics, Munich, Germany, 19-23 October 2015*. DLR, 2015.

[120] 3M, Industrial Adhesives and Tapes Division. *3M High Temperature Acrylic Adhesive 100*, 2014.

[121] T.-M. Ho, V. Baturkin, C. Grimm, J. T. Grundmann, C. Hobbie, E. Ksenik, C. Lange, K. Sasaki, M. Schlotterer, M. Talapina, et al. Mascot—the mobile asteroid surface scout onboard the hayabusa2 mission. *Space Science Reviews*, pages 1–36, 2016.

[122] Arianespace. *VEGA User's Manual*, 2014.

[123] Arianespace. *Ariane 5 User's Manual*, 2011.

[124] ECSS. ECSS-E-ST-01C. European Cooperation for Space Standardization, 2008.

[125] J. Boblenz. Bsdu fe-analyses. Technical report, German Aerospace Center (DLR), Institute of Composite Structures and Adaptive Systems, 2015.

[126] B. Dachwald, H. Boehnhardt, U. Broj, U. R. Geppert, J.-T. Grundmann, W. Seboldt, P. Seefeldt, P. Spietz, L. Johnson, E. Kührt, et al. Gossamer roadmap technology reference study for a multiple neo rendezvous mission. In *Advances in Solar Sailing*, pages 211–226. Springer, 2014.